

A Precision Measurement of the Proton Structure Function F_2 with the H1 Experiment

DISSERTATION

zur Erlangung des akademischen Grades
doctor rerum naturalium
(Dr. rer. nat.)
im Fach Physik

eingereicht an der
Mathematisch-Naturwissenschaftlichen Fakultät I
Humboldt-Universität zu Berlin

von
Herr Dipl.-Phys. Jan Kretzschmar
geboren am 18.12.1978 in Leipzig

Präsident der Humboldt-Universität zu Berlin:
Prof. Dr. Christoph Marksches

Dekan der Mathematisch-Naturwissenschaftlichen Fakultät I:
Prof. Dr. Christian Limberg

Gutachter:

1. Prof. Dr. Hermann Kolanoski
2. Prof. Dr. Max Klein
3. Prof. Dr. Thomas Lohse

eingereicht am: 31. Oktober 2007
Tag der mündlichen Prüfung: 4. Februar 2008

Abstract

The H1 detector at the HERA collider is a complex device to study the interactions of electrons and protons at a centre of mass energy of $\sqrt{s} = 320$ GeV. One of the main goals is to determine the substructure of the proton with the best possible precision. This is done measuring the inclusive deep-inelastic scattering cross section as a function of the kinematic variables Q^2 and x .

This work presents a new measurement of the inclusive deep-inelastic electron-proton scattering cross section using the data taken with the H1 experiment in the year 2000. The measurement is restricted to the region of low and intermediate inelasticities y , where the background is low. In this domain the reduced cross section is mostly identical to the proton structure function F_2 . About one order of magnitude in the photon virtuality, $10 \text{ GeV}^2 < Q^2 < 180 \text{ GeV}^2$, and three orders of magnitude in the Bjorken scaling variable, $1.3 \cdot 10^{-4} < x < 0.15$, are covered.

The accuracy in this range is limited by systematic uncertainties rather than statistics. Compared to the published results using the data from the years 1996/97, these uncertainties are reduced by a significant amount and a self consistent measurement is presented. The results were also reproduced in an independent analysis. The errors of the new measurement are typically in the range of 1.3 – 2.0%, which means a 30% improvement over the previously published results. None of the considered systematic error sources dominates the total uncertainty in the bulk of the measurement. Only at the highest x values, or equivalently lowest y , the measurement is limited by the achieved control over the measurement of the hadronic final state.

An unexpected but nevertheless important result is the observed discrepancy between the measurement and the previously published H1 results. A new analysis of the older data shows, that the data sets themselves are not responsible for this. It is also found, that assumptions made for the simulated event sample were wrong and therefore the published cross section measurement is biased by up to 3%. An approximate correction of the published data leads to a reasonable agreement of the old and the new measurement within their respective uncertainties.

Keywords:

Proton Structure, F_2 , Deep-Inelastic Scattering, H1

Zusammenfassung

Der H1-Detektor ist eines der komplexen Messinstrumente am HERA Beschleuniger. Er wurde gebaut, um die Wechselwirkung von Elektronen und Protonen bei höchsten Schwerpunktenenergien von bis zu $\sqrt{s} = 320$ GeV zu untersuchen. Ein wichtiges Thema ist die Bestimmung der Protonstruktur mit der bestmöglichen Genauigkeit. Zu diesem Zweck bestimmt man den inklusiven tief-inelastischen Wirkungsquerschnitt als Funktion der kinematischen Variablen x und Q^2 .

In dieser Arbeit wird eine neue Messung des tief-inelastischen Wirkungsquerschnitts vorgestellt. Dazu werden Daten analysiert, welche mit dem H1 Detektor im Jahre 2000 aufgezeichnet wurden. Die Messung ist beschränkt auf den Bereich mittlerer und niedriger Inelastizität y . In diesem Bereich ist der Untergrund gering und die Messung des reduzierten Wirkungsquerschnittes ist fast eine direkte Messung der Protonstrukturfunktion F_2 . Die Messung erstreckt sich über etwa eine Größenordnung in der Photon-Virtualität, $10 \text{ GeV}^2 < Q^2 < 180 \text{ GeV}^2$, und drei Größenordnungen in der Bjorken-Skalenvariablen, $1,3 \cdot 10^{-4} < x < 0,15$.

Die Genauigkeit ist hauptsächlich durch systematische Unsicherheiten limitiert. Im Vergleich zu den publizierten Ergebnissen mit den Daten aus den Jahren 1996/97 konnten diese Unsicherheiten signifikant reduziert werden. Es werden selbstkonsistente Resultate vorgestellt, die auch von einer unabhängigen Analyse bestätigt werden. Die Fehler der neuen Messung liegen meist im Bereich von 1,3 – 2,0%, was eine Verbesserung um etwa 30% gegenüber den bereits veröffentlichten Resultaten darstellt. Keiner der systematischen Effekte dominiert die Unsicherheiten für die Mehrzahl der Messpunkte. Nur bei höchstem x , oder äquivalent kleinstem y , beschränkt das Verständnis des hadronischen Endzustandes die erreichbare Genauigkeit.

Ein unerwartetes, aber gerade deshalb wichtiges Ergebnis ist die signifikante Abweichung der neuen Messung von der publizierten. Eine neue Analyse der alten Daten zeigt, dass diese Diskrepanz nicht in den Daten selbst liegt. Es wird weiterhin gezeigt, dass Annahmen über die simulierten Ereignisdaten, welche für die Analyse der alten Daten verwendet wurden, falsch waren. Der Effekt ist eine um bis zu 3% falsche Messung. Nach einer Korrektur dieses Effektes stimmen die alte und die neue Messung unter Berücksichtigung ihrer Unsicherheiten miteinander überein.

Schlagwörter:

Protonstruktur, F_2 , Tief-inelastische Streuung, H1

Contents

1	Introduction	1
2	Deep-Inelastic Scattering	3
2.1	Event Kinematics	3
2.2	DIS Cross Section	4
2.3	The Quark Parton Model	6
2.4	Quantum Chromodynamics	7
2.5	The Rise of F_2 towards Low x	11
2.6	Radiative Corrections to ep Scattering	12
2.7	Experimental Status	13
2.8	Motivation of this Analysis	14
3	The H1 Detector at HERA	17
3.1	The HERA Accelerator	17
3.2	The H1 Detector	18
3.2.1	Central and Forward Tracking Systems	19
3.2.2	Liquid Argon Calorimeter	21
3.2.3	Backward Detectors	22
3.2.4	Luminosity System	27
3.2.5	Trigger System	28
4	Basics of the Cross Section Measurement	31
4.1	Reconstruction of DIS Events	31
4.2	Monte Carlo Models	35
4.2.1	DJANGO	35
4.2.2	PHOJET	36
4.2.3	Detector Simulation	36
4.2.4	Radiative Corrections	37
4.3	Electron Identification and Background Processes	39
4.3.1	Electron Identification	39
4.3.2	Photoproduction Background	39
4.3.3	Non- ep Background	41
4.4	Covered Phase Space and Resolutions	43
4.4.1	Electron Method	44
4.4.2	Σ Method	46
4.4.3	Alternative Reconstruction Schemes	46
4.4.4	Acceptance and Phase Space	46

4.5	Cross Section and Structure Functions	49
5	Data Selection and Treatment	53
5.1	Data Sample and Run Selection	53
5.2	Event Reconstruction and Selection	54
5.2.1	SpaCal	55
5.2.2	Electron Tracking in the Backward Detectors	56
5.2.3	Event Vertex	58
5.2.4	Hadronic Final State	59
5.2.5	Phase Space Selection	59
5.3	Online Event Selection	60
5.3.1	Subtrigger Definition	60
5.3.2	Trigger Efficiency	61
5.3.3	Combining Prescaled Triggers	65
5.3.4	Event Selection on L4	67
5.4	Stability Studies	68
5.5	Vertex Analysis and Reweighting	69
5.6	Global Normalisation Effects	70
5.6.1	Global Trigger Options	71
5.6.2	Photon Detector Reanalysis	72
5.6.3	Correction for e -gas Background	72
5.6.4	Analysis of the Proton Beam Satellite Bunches	73
6	Detector Performance and Calibration	75
6.1	SpaCal Double Angle Calibration	75
6.1.1	Cell Gain Correction	77
6.1.2	Correction for Finite Cell Size	79
6.1.3	Time Dependent Correction	81
6.1.4	Correction for Losses in Dead Material	82
6.1.5	Final Corrections and Assessment	82
6.2	HFS Calibration and Tuning	85
6.2.1	Hadronic SpaCal	86
6.2.2	LAr Calibration	88
6.2.3	HFS Description in the DIS Analysis Sample	89
6.3	Alignment	92
6.3.1	Backward Detectors	92
6.3.2	CIP	93
6.4	BDC Efficiency	94
7	DIS Cross Section Results	97
7.1	Vertex Reconstruction Efficiency	97
7.2	Other DIS Event Selection Cuts	100
7.2.1	Cluster Based Selection Cuts	100
7.2.2	BDC Linking Efficiency	100
7.2.3	QED Compton Rejection Efficiency	102
7.2.4	Momentum Balance Selection Efficiency	103
7.3	Bin Selection	104
7.4	Control Distributions for the DIS Sample	104

7.5	Systematic Uncertainties	106
7.6	Results and Internal Consistency	110
7.6.1	The Measurement and Discussion of its Uncertainties	110
7.6.2	Consistency of the Electron and Σ Methods	112
7.6.3	Splitting the Measurement Samples	114
7.6.4	Alternative Reconstruction Methods	114
7.7	Context of the New Measurement	116
8	Analysis of the Published H1 Measurement	119
8.1	Comparison to Published Measurements	119
8.2	Reanalysis of the H1 1996/97 Data	121
8.2.1	Data Sample and Event Reconstruction	121
8.2.2	Trigger Setup and Performance	122
8.2.3	BDC Efficiency Correction	123
8.2.4	Control Distributions	123
8.2.5	Cross Section Result and Comparison	125
8.3	Influence of the Monte Carlo Samples	129
8.3.1	Radiative Corrections	130
8.3.2	Derivation of a Correction	130
8.3.3	Final Comparison of the Cross Section Measurements	133
9	Summary	137
A	SpaCal Cell Numbers	145
B	Cross Section Results	147

Chapter 1

Introduction

At least since the days of the ancient Greek philosophers men have thought about their existence and their relation to the world around them. More than 2000 years ago Democritus developed his ideas, according to which the world is made up of an unchangeable substance consisting of small *indivisible* particles, the *atoms*. These are *interacting* with each other and thereby can be rearranged into many different forms. The parallels to the modern view of the micro cosmos with its *elementary particles and the four fundamental interactions* are intriguing. Democritus was one of the first to explain nature in a form similar to our current understanding. However his reasoning is not completely satisfactory from a modern scientific perspective, which puts the emphasis on *experiments and objective measurements*.

Chemistry can explain the enormous wealth of substances in the world by the interactions of just about 100 different species of atoms. The regular behaviour of the atoms evident from the periodic table of elements hinted at their composed structure. Soon enough it was discovered by Ernest Rutherford and his co-experimenters. It was found, that the *indivisible* atom is composed of electrons and an atomic nucleus. For more than 100 years the systematic experimental and theoretical efforts to uncover the most basic nature of things has now continued.

In the 1920s and 30s the laws governing the interactions of the electrically charged electrons and the nuclei were formulated and the final result is today known as the theory of Quantum Electrodynamics, QED. Only by probing deeper and increasing the energy it has been found to be incomplete. In the 1960s the Electroweak Theory was formulated, which contains the known electromagnetic interactions.

The multitude of atomic nuclei was explained in the 1930s by another simple principle: just two particles, the proton and the neutron are bound together in different quantities. This marked also the discovery of a new force, the so called *Strong Force*. After this discovery and the advent of particle physics with accelerators, a wealth of particles governed by the strong force, the so called *hadrons*, was found. The formulation of the underlying theory and the discovery of its elementary particles, the *quarks and gluons*, was especially difficult. The reason is, that these elements cannot be cleanly separated from one another, i.e. they cannot be observed as free particles. However since the 1970s we believe to have a good theory of the strong force known as Quantum Chromodynamics, QCD, which resembles QED in many aspects, yet is quite different in its phenomenology.

The work of this thesis deals mainly with improving our knowledge and testing

the predictions of QCD. Like Rutherford studied the structure of the atom in scattering experiments, the structure of the most abundant hadron, the proton, and its composition from quarks and gluons is studied. Using the world's first and only electron-proton collider HERA and the H1 apparatus, the structure of the proton is determined with unprecedented accuracy. For this the inclusive deep-inelastic scattering cross section of electrons on protons is measured as a function of the kinematic variables.

The basic principle and the theory behind Deep Inelastic Scattering (DIS) is described in chapter 2. Chapter 3 gives a short overview over the experimental devices used for the measurement. In chapter 4 the basics of the cross section measurement are explained. In chapter 5 the online and offline selection criteria as well as effects that influence the analysis sample as a whole are described. Chapter 6 gives a detailed account of the steps crucial for obtaining a measurement with small systematic uncertainties. In chapter 7 some further aspects of the event selection are discussed, before the cross section results are presented and compared to other published measurements. Finally in chapter 8 the consistency of the new measurement with the one previously published by the H1 collaboration is discussed in more detail.

Chapter 2

Deep-Inelastic Scattering

Deep-inelastic lepton-hadron scattering is the major tool for understanding the nucleon structure and the parton interaction dynamics. Since the discovery of the proton structure at the SLAC fixed target experiment in 1969, these measurements have played a decisive role in the development of the theory of strong interactions, Quantum Chromodynamics (QCD). Major progress in the exploration of strong interactions has been achieved at the electron-proton collider HERA, operating at the particle accelerator energy frontier. Throughout this thesis the discussion of deep-inelastic scattering will be specialised to the HERA case of electrons scattered off protons. The term *electron* in general also stands for its anti-particle, the positron unless explicitly stated.

Electrons are according to our current knowledge point-like elementary particles. They only interact via the well tested and understood electroweak forces and are therefore ideal probe particles.

2.1 Event Kinematics

Within the framework of the Standard Model neutral current electron-proton interactions $ep \rightarrow eX$ proceed via the exchange of a virtual photon, see figure 2.1.

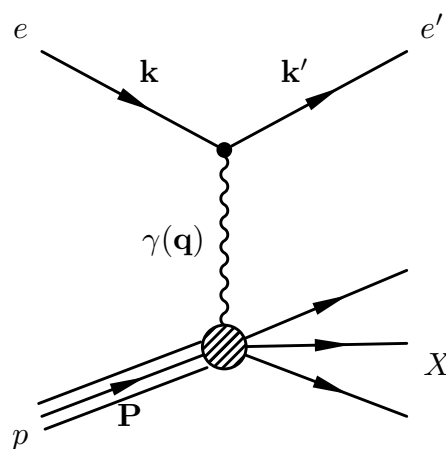


Figure 2.1: Lowest order Feynman diagram describing deep-inelastic electron-proton scattering and four-momenta assigned to the particles.

The incoming electron and proton are assigned the four-momenta \mathbf{k} and \mathbf{P} , while the scattered electron is described by \mathbf{k}' . The kinematics of the scattering process are most conveniently described by the following three Lorentz invariant variables:

$$\begin{aligned} Q^2 &= -\mathbf{q}^2 = -(\mathbf{k} - \mathbf{k}')^2 > 0 \\ x &= \frac{Q^2}{2\mathbf{P} \cdot \mathbf{q}} \\ y &= \frac{\mathbf{q} \cdot \mathbf{P}}{\mathbf{k} \cdot \mathbf{P}}. \end{aligned} \quad (2.1)$$

The hardness or resolution power of the interaction is determined by the Q^2 of the exchanged photon. The dimensionless variables x and y are both limited to values between 0 and 1. The Bjorken scaling variable x corresponds to the momentum fraction of the proton taking part in the reaction in the Quark Parton Model. The inelasticity of the reaction is characterised by y . The centre of mass energies of the electron-proton system \sqrt{s} and the intermediate boson-proton system W , respectively, are defined as:

$$\begin{aligned} s &= (\mathbf{k} + \mathbf{P})^2 \\ W^2 &= (\mathbf{q} + \mathbf{P})^2. \end{aligned} \quad (2.2)$$

The quantities defined in the equations 2.1 and 2.2 are not independent of each other. In the following the mass of the electron m_e is neglected and often the mass of the proton m_p is insignificant w.r.t the energy scale set by the HERA collider as $m_p \ll \sqrt{s}$:

$$Q^2 = (s - m_p^2) \cdot xy \approx sxy \quad (2.3)$$

$$W^2 = Q^2 \left(\frac{1}{x} - 1 \right) + m_p^2 \approx Q^2 \left(\frac{1}{x} - 1 \right) = sy - Q^2. \quad (2.4)$$

The regime of *Deep-Inelastic Scattering* is characterised by $Q^2 > 1 \text{ GeV}^2$ and $W > 2 \text{ GeV}$.

2.2 DIS Cross Section

Due to the ϕ symmetry, momentum conservation, and negligible particle masses, the DIS cross section depends on three variables, chosen as x , Q^2 , and y . At a fixed centre of mass energy \sqrt{s} and due to equation 2.3, only x and Q^2 are remaining.

The cross section can be calculated from the diagram in figure 2.1:

$$\sigma \sim L_{\alpha\beta} W^{\alpha\beta}, \quad (2.5)$$

where $L_{\alpha\beta}$ and $W^{\alpha\beta}$ are the leptonic and hadronic tensor respectively.

While $L_{\alpha\beta}$ is calculable in Quantum Electrodynamics (QED), the hadronic part has to be parametrised. Imposing Lorentz invariance and the known discrete symmetries of QED, two functions are required, which are related to the structure of the

proton. The *double differential DIS cross section* for the reaction $ep \rightarrow eX$ can then be expressed using the structure functions $F_2(x, Q^2)$ and $F_L(x, Q^2)$ in the form:

$$\frac{d^2\sigma}{dx dQ^2} = \frac{2\pi\alpha^2 Y_+}{xQ^4} \left(F_2(x, Q^2) - \frac{y^2}{Y_+} F_L(x, Q^2) \right), \quad (2.6)$$

where $Y_+ = 1 + (1 - y)^2$ is a simple function of y . F_L is also called *longitudinal structure function* for reasons that will be explained below. The electromagnetic nature of the interaction is obvious from the coupling given by the fine structure constant α and the photon propagator dependence $\propto 1/Q^4$. Contributions of electroweak Z^0 exchange are neglected for $Q^2 \ll M_Z^2$ and charged currents mediated by the exchange of W^\pm bosons are also not the topic of this thesis.

When performing the measurement, it is more convenient to define a *reduced cross section* σ_r omitting the kinematic factor $\kappa = (2\pi\alpha^2 Y_+)/xQ^4$:

$$\sigma_r = F_2(x, Q^2) - \frac{y^2}{Y_+} F_L(x, Q^2). \quad (2.7)$$

The ep scattering can also be viewed as a flux of virtual photons interacting with the proton. Due to $Q^2 \neq 0$ these photons can have longitudinal and transverse polarisation and using the convention of [Han63, AC99] the cross section can be decomposed as

$$\frac{d^2\sigma}{dx dQ^2} = \Gamma(y, Q^2) (\sigma_T(x, Q^2) - \epsilon(y)\sigma_L(x, Q^2)). \quad (2.8)$$

Here σ_T and σ_L denote the absorption cross sections for transversely and longitudinally polarised photons respectively, $\Gamma = (\alpha^2 Y_+)/ (2\pi x Q^2 (1 - x))$ is the photon flux, and $\epsilon = 2(1 - y)/Y_+$ is the photon polarisation.

Comparing the equations 2.6 and 2.8 one obtains the relations of the above introduced proton structure functions to the virtual photon absorption cross sections:

$$F_2(x, Q^2) = \frac{Q^2(1 - x)}{4\pi^2\alpha} \cdot (\sigma_T(x, Q^2) + \sigma_L(x, Q^2)) \quad (2.9)$$

$$F_L(x, Q^2) = \frac{Q^2(1 - x)}{4\pi^2\alpha} \cdot (\sigma_L(x, Q^2)) \quad (2.10)$$

Equation 2.10 explains the name of the longitudinal structure function F_L . Furthermore, as both σ_T and σ_L are required to be positive, it follows that

$$0 \leq F_L(x, Q^2) \leq F_2(x, Q^2). \quad (2.11)$$

Another possibility to express the relations between the introduced structure functions is the quantity $R(x, Q^2)$:

$$R(x, Q^2) = \frac{\sigma_L}{\sigma_T} = \frac{F_L(x, Q^2)}{F_2(x, Q^2) - F_L(x, Q^2)} \quad (2.12)$$

It is furthermore evident, that using a measurement of σ_r it is possible to determine both of the structure functions F_2 and F_L only if:

- the influence of F_L on the cross section is not too much suppressed by the kinematic dependence y^2/Y_+ , i.e. the inelasticity needs to be large $y \gtrsim 0.5$, and
- σ_r is measured as a function of all three variables x , y , and Q^2 , which requires a variation of \sqrt{s} .

The data set to perform this measurement with the H1 detector was taken in the years 2003-2007 and was not available for this thesis. The above argument may be reversed and the measurement will be restricted to the kinematic domain of *low* $y < 0.6$, where the cross section is a direct measurement of the structure function F_2 up to a small correction.

2.3 The Quark Parton Model

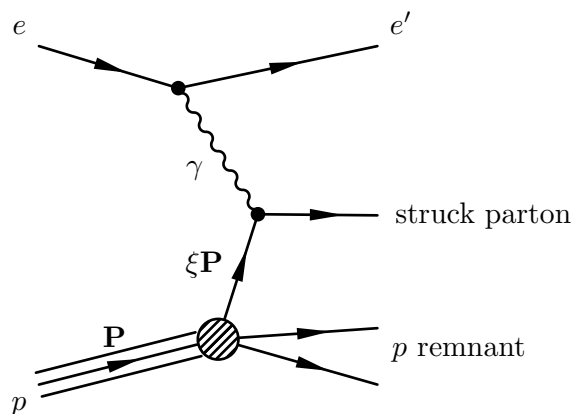


Figure 2.2: The Quark Parton Model interpretation of DIS: elastic electron scattering off a parton with momentum fraction ξ of the proton.

The Quark Parton Model (QPM) was introduced [Fey69] to explain the first DIS data taken and analysed at the SLAC in 1969 [B⁺69a, B⁺69b]. When viewed in the infinite momentum frame, the proton can be regarded as being composed of free constituents with negligible transverse momentum, the so-called partons. The interaction then takes place between the electron and a parton carrying a momentum fraction ξ of the proton, see figure 2.2. The ep cross section is an incoherent sum over all such processes:

$$\frac{d^2\sigma}{dx dQ^2} = \sum_i \int_0^1 d\xi q_i(\xi) \left(\frac{d^2\sigma}{dx dQ^2} \right)_{eq_i \rightarrow eq_i}. \quad (2.13)$$

Here *parton density functions* $q_i(\xi)$ are introduced, which describe the probability to find a parton i with momentum fraction ξ of the proton. Assuming, that the partons are quarks, as proposed before to explain the hadron structure [GM64], the cross section for elastic electron-quark scattering, calculated as:

$$\left(\frac{d^2\sigma}{dx dQ^2} \right)_{eq_i \rightarrow eq_i} = \frac{2\pi\alpha^2 Y_+}{Q^4} e_i^2 \delta(x - \xi) \quad (2.14)$$

can be inserted into equation 2.13. This implies, that the momentum fraction ξ of the struck quark is identical to the Bjorken x variable introduced in equation 2.1. Comparing the equation 2.13 to 2.6, one sees that the introduced structure functions are given by

$$F_2(x) = \sum_i e_i^2 x q_i(x) \quad (2.15)$$

$$F_L(x) = 0. \quad (2.16)$$

This explains two (approximate) features of the early experimental data:

- The structure functions are a function of only one *scaling variable* x as it was predicted by Bjorken [Bjo69].
- The helicity conservation does not allow absorption of longitudinally polarised photons on spin- $\frac{1}{2}$ partons, i.e. quarks. Therefore the longitudinal structure function is expected to vanish. This is also known as the *Callan-Gross relation* [CG69].

While these two features helped to establish our picture of the proton being made up of spin- $\frac{1}{2}$ quarks, both are actually not valid in general. Scaling violations were found rather soon [F⁺74]. Establishing $F_L \neq 0$ or equivalently $R \neq 0$ was difficult at the relatively large x values accessible at fixed target experiments and took longer to master [WRB⁺90].

2.4 Quantum Chromodynamics

On a first look it seems odd to treat quarks as non-interacting, as it is done in the Quark Parton Model. After all the quarks are bound to hadrons by a force, the so-called *strong force*.

The quantum field theory to describe the strong force is modelled in a similar manner as Quantum Electrodynamics and named *Quantum Chromodynamics*, QCD [FGML73, GW73, Wei73]. The key point is the new colour quantum number, which the quarks carry in addition to their electric charge. There are 3 colours red, green, and blue, and the interaction is required to be invariant under a local SU(3) transformation. Because of this symmetry group, eight massless gauge bosons enter the theory, the analog to the photon in the QED case. A general feature of Quantum Field Theories is the *running coupling constant*, i.e. the coupling evolves with the energy scale of the interaction. Due to the non-abelian nature of the gauge group SU(3), as opposed to the U(1) group of QED, the *strong coupling* α_s shows the opposite behaviour of the electromagnetic fine structure constant α . At large energy scales Q^2 the coupling decreases and quarks are *asymptotically free*, while at lower energies quarks are *confined* to *colourless* hadrons and cannot be observed as free particles. The running of α_s can be quantified using the renormalisation group equation in leading order as

$$\alpha_s(Q^2) = \frac{12\pi}{(33 - 2n_f) \ln \frac{Q^2}{\Lambda_{QCD}^2}}, \quad (2.17)$$

where n_f is the number of active quark flavours ($\max n_f = 6$). The parameter $\Lambda_{QCD} \sim 300$ MeV characterises the strength of the coupling. For $Q^2 < \Lambda_{QCD}^2$ the not well understood phenomenon of *confinement* sets in. On the other hand, for large enough momentum scales $Q^2 > 1 \text{ GeV}^2$ perturbative calculations using order-by-order expansions in α_s are possible.

The Quark Parton Model may be altered accordingly to take into account some features of QCD. Qualitatively fluctuations are expected due to emission and reabsorption of gluons by the quarks and splitting of gluons to $q\bar{q}$ pairs. A quark seen at a scale Q_0^2 carrying a momentum fraction x_0 can be resolved into more quarks and gluons at a higher $Q_1^2 > Q_0^2$ and lower $x_1 < x_0$, so the structure functions will acquire a Q^2 dependence violating the Bjorken scaling.

Formally this is expressed using the *factorisation theorem*, see e.g. [CSS88]. It states, that a cross section involving hadrons can be decomposed into a *short distance* part and a *long distance* part. The short distance or hard scattering part can be calculated perturbatively using the (ultraviolet) renormalisable theory of QCD. The long distance part involves the *parton density functions* (PDFs), into which the infrared divergences of QCD are absorbed. The PDFs need to be extracted from experiments. The structure function F_2 is expressed as a convolution of coefficient functions C_2^i and parton density functions f_i :

$$F_2(x, Q^2) = \sum_{i=q,g} \int_x^1 dz C_2^i \left(\frac{x}{z}, \frac{Q^2}{\mu_r^2}, \frac{\mu_f^2}{\mu_r^2}, \alpha_s(\mu_r^2) \right) f_i(z, \mu_r^2, \mu_f^2) \quad (2.18)$$

The coefficient function C_2^i is the hard scattering matrix element for an interaction of a photon with a parton i . It can be calculated using a perturbative expansion in α_s . The parton density function f_i gives the probability to find a parton with momentum fraction z in the proton. The hard scattering and the parton density functions are independent of each other and the whole process is a sum over all possible partons. The factorisation scale μ_f defines the border between the long and the short distance part. For example soft gluon emission is treated as being part of the (measured) proton structure below an energy scale of μ_f . The renormalisation scale μ_r on the other hand is needed to deal with the ultraviolet divergences of the higher orders in perturbation theory.

The physics has to be independent of the arbitrary choices for μ_r and μ_f , which leads to the scale dependent effects in $\alpha_s(Q^2)$ (running coupling constant) and f_i (scaling violations). Several useful *factorisation schemes* can be defined. In the DIS scheme¹ one chooses $\mu_r^2 = \mu_f^2 = Q^2$ and the coefficient functions to all orders like in the Quark Parton Model. Therefore one is left with a formula for F_2 very similar to 2.15:

$$F_2(x, Q^2) = \sum_i e_i^2 x f_i(x, Q^2), \quad (2.19)$$

where the functions simply acquire a Q^2 dependence. Also F_L is non-zero and its value can be calculated from F_2 and the gluon density $g(x, Q^2)$.

By exploiting the arbitrariness of the factorisation scale μ_f in the factorisation theorem 2.18, one can derive the DGLAP evolution equations, named after Dokshitzer, Gribov, Lipatov, Altarelli, and Parisi [GL72a, GL72b, Dok77, AP77]. These

¹Another commonly used scheme is the modified minimal subtraction scheme $\overline{\text{MS}}$ [Sir80].

describe how quark $q_i(x, Q^2)$ and gluon $g(x, Q^2)$ distribution functions evolve with the scale of the interactions Q^2

$$\frac{dq_i(x, Q^2)}{d \ln Q^2} = \frac{\alpha_s(Q^2)}{2\pi} \int_x^1 \frac{dz}{z} \left[\sum_j q_j(z, Q^2) P_{ij} \left(\frac{x}{z} \right) + g(z, Q^2) P_{ig} \left(\frac{x}{z} \right) \right] \quad (2.20)$$

$$\frac{dg(x, Q^2)}{d \ln Q^2} = \frac{\alpha_s(Q^2)}{2\pi} \int_x^1 \frac{dz}{z} \left[\sum_j q_j(z, Q^2) P_{gj} \left(\frac{x}{z} \right) + g(z, Q^2) P_{gg} \left(\frac{x}{z} \right) \right]. \quad (2.21)$$

The so-called *splitting functions* $P_{ij}(z)$ are calculable using pQCD as an expansion series in α_s :

$$P_{\alpha\beta}(z, \alpha_s) = \frac{\alpha_s}{2\pi} P_{\alpha\beta}^{(0)}(z) + \left(\frac{\alpha_s}{2\pi} \right)^2 P_{\alpha\beta}^{(1)}(z) + \dots \quad (2.22)$$

The leading order parts $P_{\alpha\beta}^{(0)}(x/z)$ can be interpreted as the probability for a parton β with a momentum fraction z of the proton to emit a parton α with momentum fraction x of the parent parton. The leading order graphs are displayed in figure 2.3.

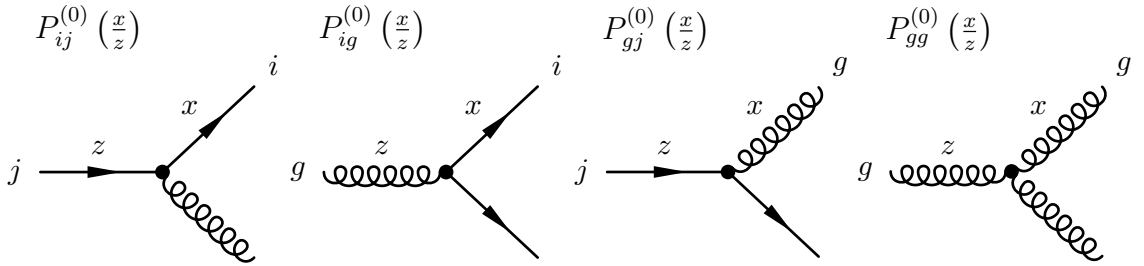


Figure 2.3: Diagrams for the lowest order splitting functions for the DGLAP equations.

The general approach to determine the parton density functions from experimental DIS cross sections measurements is as follows

- Parametrise the parton density functions at a low starting scale Q_0^2 by smooth analytical functions with few free parameters.
- Evolve these functions using the DGLAP equations 2.20, 2.21 to higher Q^2 values.
- Calculate the structure functions (equation 2.18) and the cross section (equation 2.6)
- Compare the calculation to experimental data and minimise the χ^2 adjusting the free parameters

Several constraints can be applied, like momentum sum rules, requiring the known quark flavour numbers of the proton and possibly a few more.

Presently most analyses of DIS data have used the coefficient and splitting functions at next-to-leading order (NLO). Examples for these analyses are the global analyses performed by the CTEQ collaboration [P⁺02] or the MRST group

[MRST02], or the more specialised analyses of the ZEUS [C⁺03, C⁺05] and H1 collaborations [A⁺01, A⁺03b] of mainly their own data. Since 2005 the splitting functions and coefficient functions are available at next-to-next-to-leading order (NNLO) [VMV04, MVV04, VVM05], which should finally lead to much better theory errors due to the reduced sensitivity to the renormalisation and factorisation scales.

A collection of F_2 measurements over several orders of magnitude in x and Q^2 together with a fit by the H1 collaboration is given in figure 2.4. The scaling behaviour of F_2 in the region $x \sim 0.2$ can be seen where it was originally discovered by the SLAC experiment, while especially at low x the scaling violations are obvious. Using the DGLAP equations it is possible to derive a measurement of the gluon density in the proton $xg(x, Q^2)$ and the strong coupling $\alpha_s(Q^2)$.

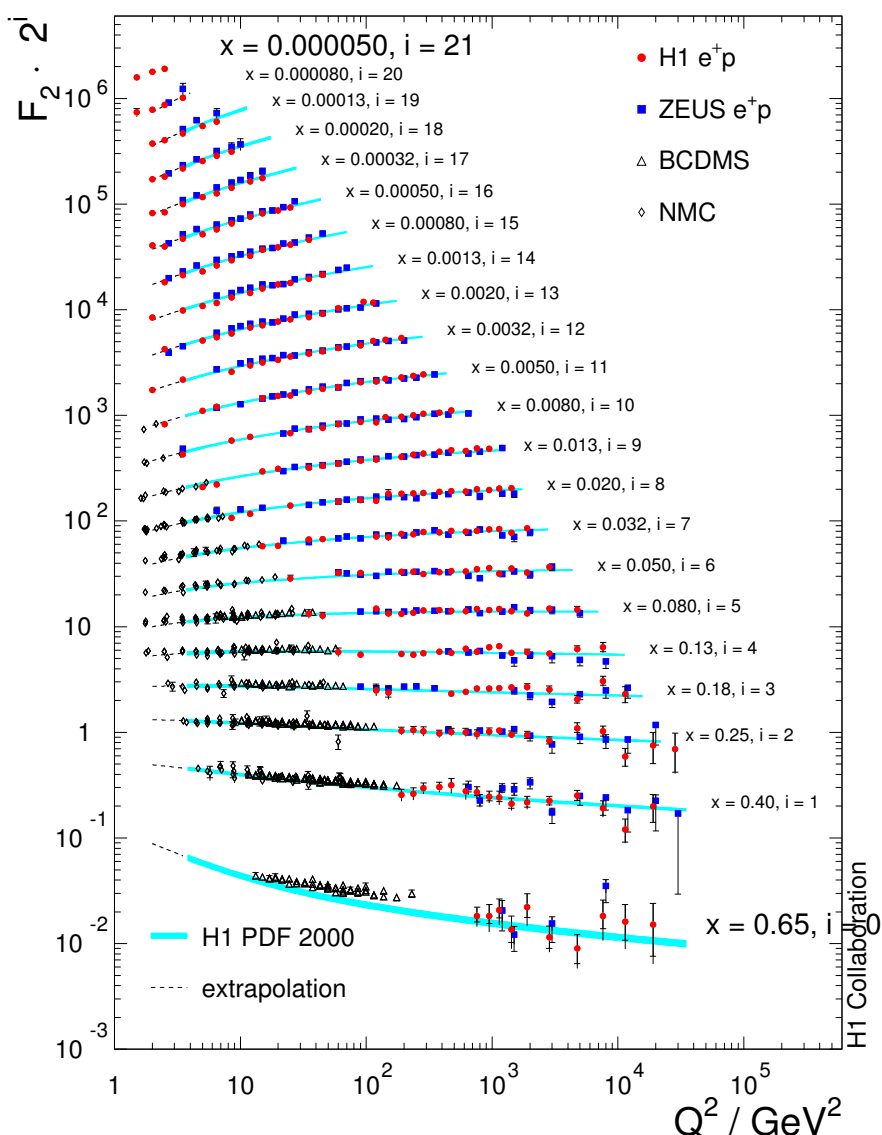


Figure 2.4: Data on F_2 from fixed target experiments and the HERA collider experiments together with a NLO QCD fit [A⁺03b]. The measurements at different x are displaced vertically by a factor 2^i .

2.5 The Rise of F_2 towards Low x

One of the first observations at the HERA collider was the strong rise of F_2 towards low x at fixed Q^2 [A⁺93a, D⁺93]. This can be attributed to a large density of low momentum gluons and sea-quarks in the proton. From experimental data reaching well below $x < 0.01$ it is seen, that F_2 rises approximately according to a power law in x :

$$F_2(x, Q^2) = c(Q^2) \cdot x^{-\lambda(Q^2)}. \quad (2.23)$$

At very low x a saturation of the growth of the parton densities is expected, as otherwise unitarity bounds would be violated. Unfortunately this point is beyond the kinematic reach of even the HERA collider. The behaviour of λ , which characterises the slope of the rise is displayed in figure 2.5.

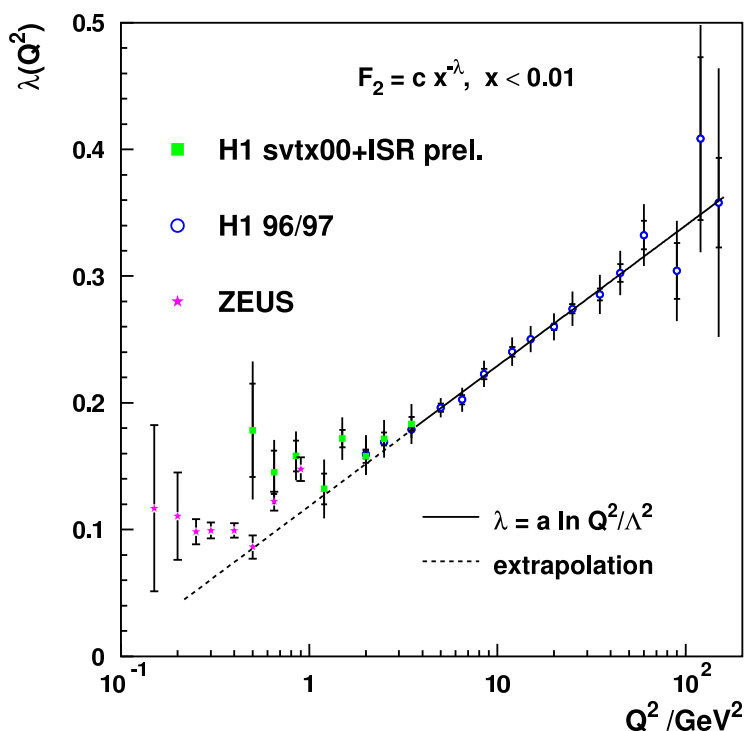


Figure 2.5: The exponent $\lambda(Q^2)$ describing the rise of $F_2 \propto x^{-\lambda}$ for low $x < 0.01$, taken from [New04]. In the regime of perturbative QCD, $Q^2 > 3 \text{ GeV}^2$, a linear fit is able to describe the data well, while at low $Q^2 < 1 \text{ GeV}^2$ a constant $\lambda \sim 0.08$ is approached, as expected from photoproduction.

The DGLAP equation, which sums effectively the leading terms in $\propto \alpha_s \ln Q^2$ may not be appropriate when the contributions $\propto \alpha_s \ln 1/x$ are large. Alternative approaches like the BFKL evolution equation [KLF76, KLF77, BL78] have been suggested, which predict a rise of the gluon as $xg(x, Q^2) \sim x^{-\lambda}$. However, the DGLAP evolution equations have up to now been able to describe the parton dynamics at low x of all available inclusive DIS data.

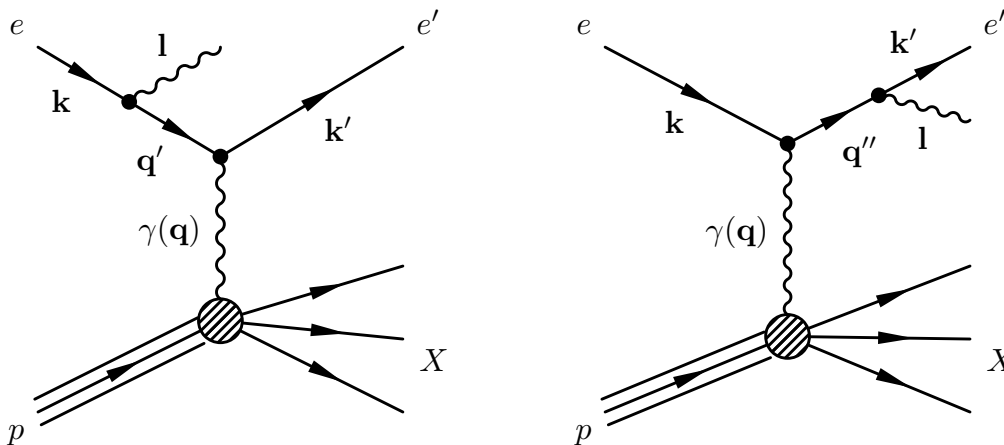


Figure 2.6: Lowest order diagrams for the process $ep \rightarrow eX\gamma$ with photon emission from the incoming and outgoing electron line, on the left and right respectively. The momenta assigned to the electron lines are labelled with \mathbf{k} , \mathbf{q}' , \mathbf{q}'' , and \mathbf{k}' respectively, the real photon has momentum \mathbf{l} , and the momentum assigned to the photon propagator is \mathbf{q} .

2.6 Radiative Corrections to ep Scattering

In addition to the lowest order contribution as shown in figure 2.1 and the QCD corrections discussed in section 2.4, there are also QED corrections to the DIS cross section. Especially important are here the processes which result in the emission of real photons, i.e. the processes contributing to $ep \rightarrow eX\gamma$, due to photon emission from the electron. The leading order graphs are shown in figure 2.6. For the cross section calculation all diagrams of the respective order have to be summed and squared, leading also to interference terms. However the propagator structure is rather simple, leading to amplitudes $\propto ((\mathbf{q}'^2 - m_e^2)\mathbf{q}^2)^{-1}$ and $\propto ((\mathbf{q}''^2 - m_e^2)\mathbf{q}^2)^{-1}$ respectively. Thus the cross section enhancements at low values of the squared four-momenta can be attributed to different experimental observations:

- Events with *Initial State Radiation* (ISR) or *Final State Radiation* (FSR) are characterised by finite \mathbf{q}^2 , but small $\mathbf{q}'^2 \simeq 0$ or $\mathbf{q}''^2 \simeq 0$ respectively. For ISR events this leads to the photon being emitted collinear with the incoming electron², which is often not detected. The effective centre of mass energy at the hadronic vertex is lowered and the apparent cross section is altered by a large amount despite the smallness of $\alpha \sim 1/137$ if the radiated photon is not taken into account in the reconstruction [S⁺]. On the other hand FSR events with a photon emitted collinear to the outgoing electron³ are most of the time experimentally not different from non-radiative DIS events, as the electron and the photon are not reconstructed separately.
- In events with small $\mathbf{q}^2 \simeq 0$, but finite \mathbf{q}'^2 and \mathbf{q}''^2 both the electron and

² This can be seen from the fact, that $(\mathbf{k} - \mathbf{l})^2 = \mathbf{q}'^2$ and the virtuality of all these momenta is small or zero due to on-shell conditions or by definition. Therefore the 4 momentum product $\mathbf{l} \cdot \mathbf{q}' = E_e E_\gamma (1 - \cos \angle(e, \gamma)) \approx 0$, hence $\angle(e, \gamma) \approx 0$.

³ See argument for the ISR photon.

photon have a sizable transverse momentum and are almost back-to-back in azimuth. These easily identifiable events are called *QED Compton* events. They can be used to measure the DIS cross section at very low Q^2 [A⁺04] or to determine the detector alignment.

- The last class of events is characterised by small $\mathbf{q}^2 \simeq 0$, $\mathbf{q}'^2 \simeq 0$, and $\mathbf{q}''^2 \simeq 0$. This means electron and photon are scattered at very small angles and cannot be detected in the main detector. The dominant elastic part of this process, so-called *Bethe-Heitler* events [BH34], is calculable with high precision in QED and independent of the proton structure. It is therefore used as the reference process for the luminosity measurement, see also section 3.2.4.

2.7 Experimental Status

Since the pioneering SLAC experiments many other experiments have measured DIS cross sections in lepton-nucleon scattering, for a review see e.g. [CSDdR98]. Not only are these measurements the best way to determine the structure of the hadrons, but they are also one of the most precise ways to test the validity of QCD in a well defined and accessible perturbative phase space. Also many of the parameters of the standard model, like the strong coupling constant α_s , the weak mixing angle, and CKM matrix elements can be extracted.

The kinematic plane covered by fixed target experiments and the HERA collider experiments H1 and ZEUS are shown in figure 2.7. Due to the high centre of mass energy of HERA with $\sqrt{s} = 320$ GeV the kinematic range was expanded by many orders of magnitude down to values of $x \sim 10^{-6}$ and up to values of $Q^2 \sim 30000$ GeV² compared to the previous fixed target experiments. The physics at the forthcoming Large Hadron Collider (LHC) will need the information on parton densities extracted from the HERA data as an important input.

To a large extent the phase space available for inclusive DIS cross section measurements at HERA has been covered by the two experiments H1 and ZEUS with rather good precision. Due to the strong $1/Q^4$ dependence of the cross section, the measurement becomes easily systematic dominated except for the highest $Q^2 \gtrsim 10000$ GeV². The region $10 \text{ GeV}^2 < Q^2 < 180 \text{ GeV}^2$ was covered by H1 [A⁺01] (see also [Gla98]) and ZEUS [C⁺01] using the data from the years 1996/97 with integrated luminosities of $\mathcal{L} \sim 20 - 30 \text{ pb}^{-1}$. A typical precision of 2 – 3% is reached in most of the analysis range, while the borders of the phase space (*low* $y < 0.05$ and *high* $y > 0.6$) are more influenced by systematic uncertainties of typically 5 – 10%. This data has to date a large impact on QCD fits and analyses.

The transition to the non-perturbative region of very low values of $0.05 \text{ GeV}^2 < Q^2 < 3 \text{ GeV}^2$ has to be accessed using specialised techniques. The most precise data at $Q^2 < 1 \text{ GeV}^2$ were published by ZEUS using a dedicated detector and a special running period in 1997 with $\mathcal{L} \sim 4 \text{ pb}^{-1}$ [B⁺00]. H1 has recently released preliminary results using three dedicated data sets recorded in 1997, 1999, and 2000, each with $\mathcal{L} \sim 0.5 - 2 \text{ pb}^{-1}$ [H1p07b], see also [Eck02, Laš04, Var06, Beh06]. The precision has reached similar level as for the higher Q^2 analyses.

The region of highest accessible $Q^2 > 100 \text{ GeV}^2$ was rather statistics limited until the 1999/2000 data set with a integrated luminosity of $\mathcal{L} \sim 65 \text{ pb}^{-1}$ brought

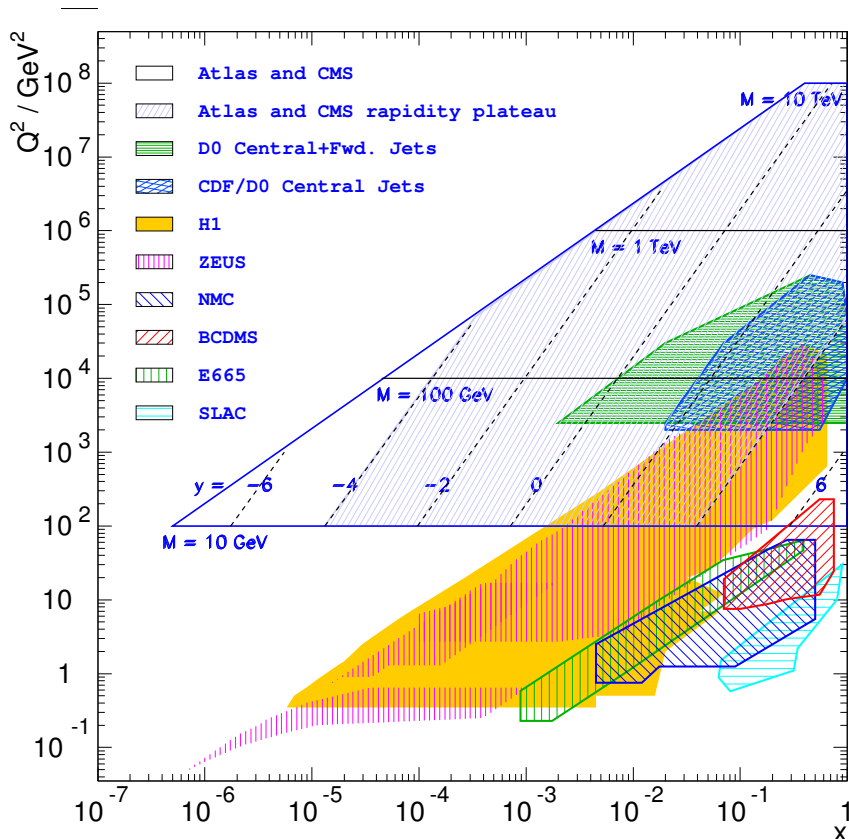


Figure 2.7: Kinematic (x, Q^2) plane covered by various fixed target experiments, the HERA collider experiments H1 and ZEUS, Drell-Yan measurements at the Tevatron, and the forthcoming LHC. Note that particle production in the central rapidity region of the LHC can be predicted using parton distribution functions measured at the same x at HERA.

the uncertainties to mostly below 5% [C⁺04, A⁺03b]. With the large amount of polarised e^+p and e^-p data taken after the HERA II upgrade in the years 2003-2007 ($\mathcal{L} \sim 400 \text{ pb}^{-1}$ in total), this region and the effects of the exchange of W^\pm and Z^0 bosons are being measured more precisely.

Another corner of the phase space, where the high luminosity of the HERA II phase is vital for precise measurements, is the high $0.6 < y < 0.9$ region. Here preliminary results with much improved errors have been presented recently by H1 [H1p07a, H1p07c].

Finally a separation of the two structure functions F_2 and F_L will be possible using the data taken at lowered proton beam energy in 2007, at $E_p = 460 \text{ GeV}$ ($\mathcal{L} \sim 13 \text{ pb}^{-1}$) and $E_p = 575 \text{ GeV}$ ($\mathcal{L} \sim 7 \text{ pb}^{-1}$).

2.8 Motivation of this Analysis

With the termination of the HERA program in June 2007 it is certainly worth to improve the precision of the measurements as far as possible. The aim of the work described in this thesis is to improve the measurement in the intermediate range

$10 \text{ GeV}^2 < Q^2 < 180 \text{ GeV}^2$ at low x using the H1 data from the year 2000. The analysis will be restricted to the medium and low $y < 0.6$ region, as the high y region will be covered with better precision using the data from the HERA II phase as explained above.

A reduction of the experimental uncertainties to the 1–2% level is feasible. This goal requires to understand and reduce all systematic error sources w.r.t previous measurements. The key points are

- The available luminosity is about a factor of 2 higher for calibration and study purposes. For the cross section measurement the effective luminosity is only about 20% higher, but anyhow the statistical uncertainties are small. In addition the H1 systems were running with better performance than ever before.
- Advances in computer technology and Monte Carlo models and simulation allow for higher statistics and more realistic Monte Carlo samples.
- The H1 reconstruction and analysis techniques have improved over time. The detector components critical for the measurement are understood better than before.

Chapter 3

The H1 Detector at HERA

This chapter introduces the HERA accelerator and the H1 detector. The main emphasis is given to the configuration used in the year 2000 and to the systems which will be referred to at a later stage.

3.1 The HERA Accelerator

The HERA machine was the world's first lepton-nucleon collider. It was located in Hamburg, Germany. The physics program started in summer 1992. In 2000 the HERA I phase was finished. In the following upgrade the H1 detector and HERA were prepared for higher luminosity operation phase HERA II. At the end of June 2007 the HERA program was terminated. Still the following sections are written in present tense.

The HERA accelerator consists of two separate accelerators each with a circumference of 6.3 km. The *electron machine* can be operated using positrons or electrons. For the *proton machine* other options of using deuterons or even heavier nuclei in a HERA III program [A⁺03c, A⁺03a, WH01] were not realised. The beams are made to collide at zero angle for the two experiments H1 and ZEUS. In addition there are two fixed target experiments, HERMES and HERA-B. Figure 3.1 gives an overview over the HERA accelerator facilities.

In the year 2000 the electron machine accelerated positrons to $E_e = 27.6$ GeV. Spin rotators for delivering a longitudinally polarised positron beam were only installed for the HERMES experiment. The proton achieved an energy of $E_p = 920$ GeV. This corresponds to a centre of mass energy $\sqrt{s} = 320$ GeV. The RF system of HERA can support up to 220 bunches in both machines, which collide with a rate of 10.4 MHz or every 96 ns. In the year 2000 about 175 of the bunches were filled with colliding positrons and protons. Some bunches are left unpaired for systematic studies. On average there were 14 of these *positron pilot bunches* and 6 *proton pilot bunches*. The typical maximum beam currents reached just after the injection of new beams were $I_p = 100$ mA for the protons and $I_e = 40$ mA for the positrons with a typical peak luminosity of $1.5 \cdot 10^{31} \text{ cm}^{-2}\text{s}^{-1}$.

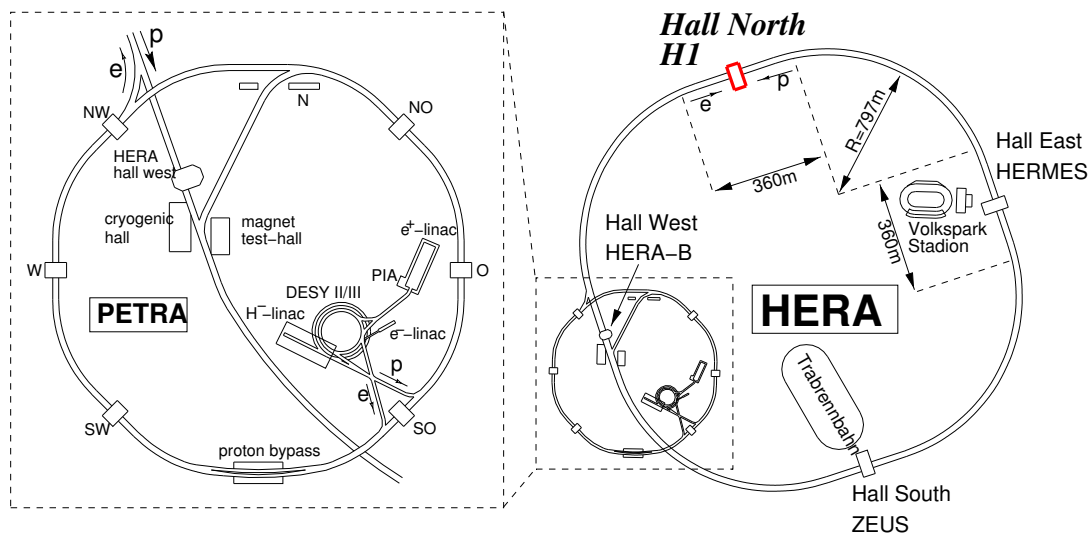


Figure 3.1: The HERA accelerator facility and its 4 experiments. On the left the pre-accelerator chain is shown in a zoomed version.

3.2 The H1 Detector

H1 is a general purpose magnetic detector with nearly hermetic calorimetric coverage. It was designed to study all aspects of electron-proton collisions. Special emphasis has been given to the identification and energy measurement of the scattered electron. An overview over the whole H1 detector is shown in figure 3.2. A complete description as of 1997 can be found in [A⁺97a, A⁺97b], where most of the numerical values are taken from unless mentioned otherwise.

The coordinate system of H1 is defined to have the positive z -axis in the direction of the incoming proton. The detector region at $z \gtrsim 120$ cm is called the *forward region*, while $z \lesssim -120$ cm defines the *backward region*. In between, just around the nominal interaction point at $z \sim 0$ we have the *central region*. The polar angle θ is measured with respect to this definition of the z -axis. As this work is mostly concerned with the scattered electron, this definition means, that electrons scattered just by a small angle w.r.t to their original direction have $\theta_e \lesssim 180^\circ$ and are detected in the backward direction. The different instrumentation of the H1 detector in the forward and backward direction is a consequence of the asymmetric beam energies of the HERA collider.

The main subsystems of the H1 detector are labelled with boxed numbers in figure 3.2. The main tracking systems are the *Central* [2] and *Forward Trackers* [3]. The calorimetry is provided by a *Liquid Argon Calorimeter (LAr)* with *electromagnetic* [4] and *hadronic* [5] sections in the central and forward region and a *Lead-Scintillating Fibre Calorimeter (SpaCal)* [12] in the backward direction. The calorimeter region is surrounded by a large superconducting coil [6], which provides a *uniform solenoidal magnetic field* of 1.15 T. The streamer tubes [9] in the iron return yoke [10] measure hadronic shower leakage and identify muons in the central region. In the forward direction there are dedicated muon systems [9] with a separate toroid [11].

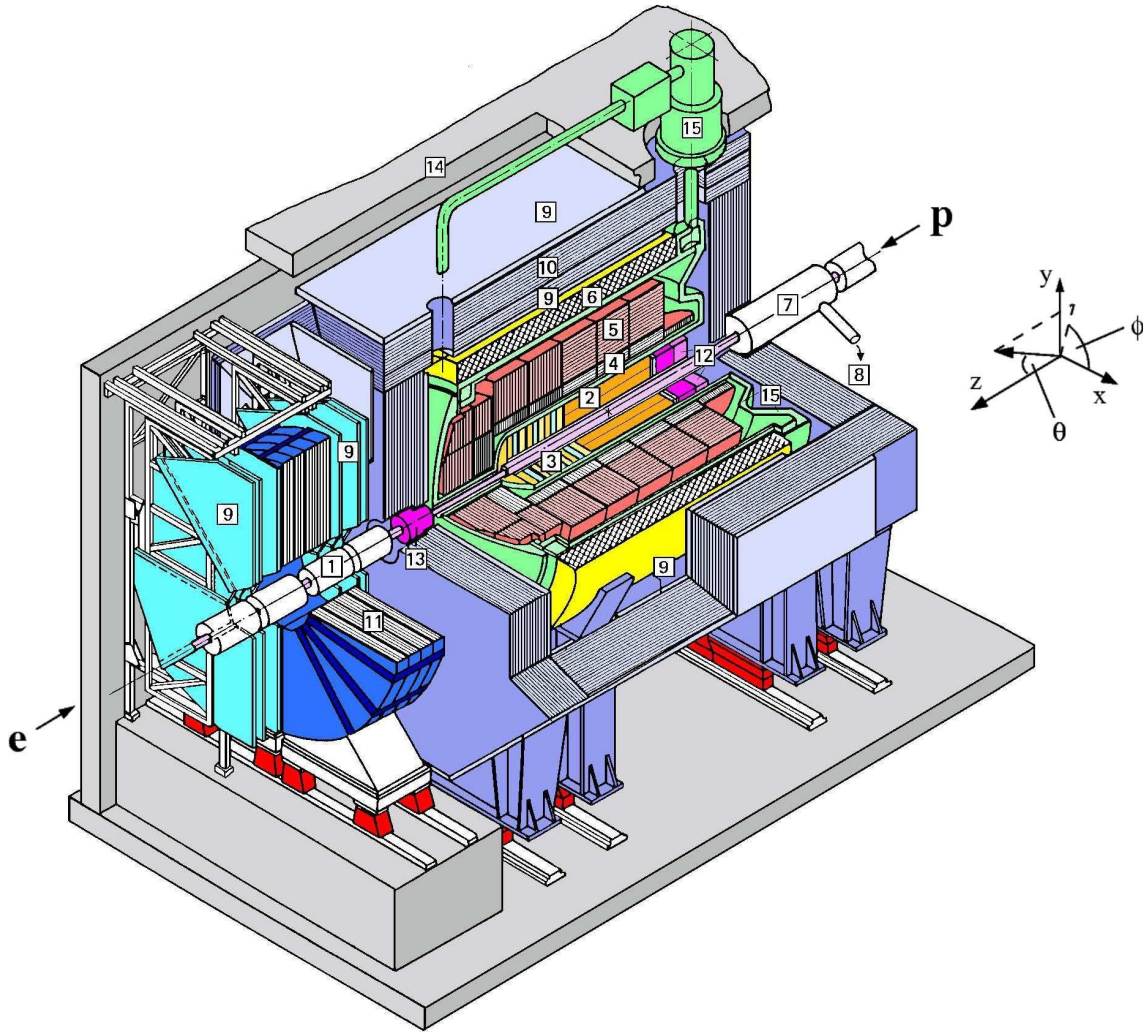


Figure 3.2: Schematic drawing of the H1 detector. Protons enter from the right, electrons from the left.

3.2.1 Central and Forward Tracking Systems

The main H1 track detectors, which measure charged particle tracks in the magnetic field, are divided into central and forward systems. The *Central Tracker* (CTD) covers approximately the polar angle range $15^\circ < \theta < 165^\circ$, while the *Forward Tracker* (FTD) covers $7^\circ < \theta < 25^\circ$.

The CTD is composed of a number of drift and proportional chambers for tracking and triggering. These chambers are complemented by a 2-layer central silicon vertex detector, as can be seen in figure 3.3. In the following the most important properties of the subcomponents are summarised.

Central Jet Chambers CJC1 and CJC2

The track reconstruction and pattern recognition in the central region is based on two concentric drift chambers with an active length in z of 220 cm and radial extensions of $20.3 \text{ cm} < r < 45.1 \text{ cm}$ for the inner chamber CJC1 and $53.0 \text{ cm} < r < 84.4 \text{ cm}$ for the outer chamber CJC2. The CJC1 is divided into 30 cells with 24 sense wires, while

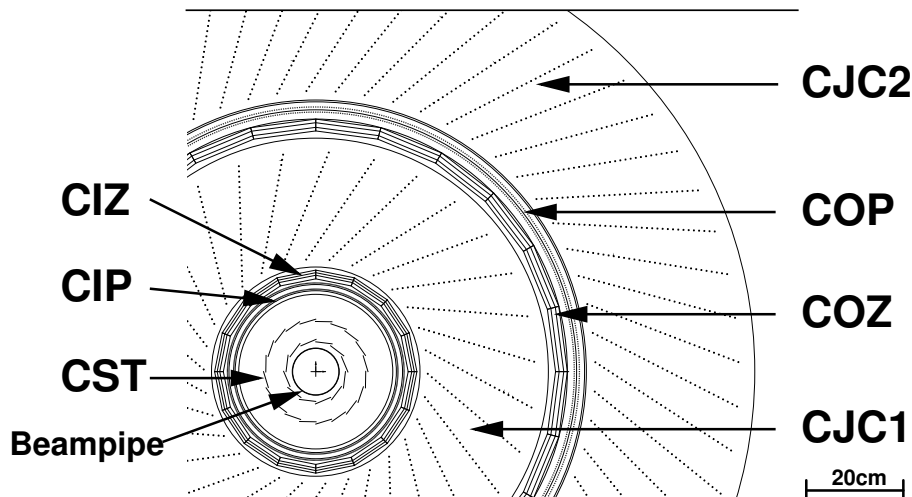


Figure 3.3: View of the central tracking detectors in the xy -plane

the CJC2 contains 60 cells with 32 sense wires each. The wires are oriented parallel to the beam axis, while the drift cells have an inclination of about 30° w.r.t the radial direction. This way the electrons created by the ionisation drift perpendicular to the wires and an optimal resolution of $\sigma_{r\phi} \sim 170 \mu\text{m}$ in the $r\phi$ -plane is reached.

In addition the z -coordinate of the hits can be determined using the charge division, where a resolution of $\sigma_z \sim 4 \text{ cm}$ is reached. Also a measurement of the specific energy loss of charged particles dE/dx can be determined.

Central z -Chambers CIZ and COZ

Two thin drift chambers, the *Central Inner z -Chamber* (CIZ) and the *Central Outer z -Chamber* (COZ), complete the precise track measurement in the central region by providing accurate information on the z -coordinate. They are located inside the CJC1 and in between CJC1 and CJC2 respectively. The CIZ is divided in 15 rings of 12 cm length in z -direction, the COZ has a finer division in 24 rings of 9 cm length. The wires are strung in radial direction around the beam axis. The optimal resolution in z -direction reached is about $\sigma_z = 200 - 260 \mu\text{m}$, while the $r\phi$ coordinate can be determined with about 2% resolution using charge division.

In the track reconstruction the information of the z -chambers is combined with the CJC information using a neural network deformable template approach [Gla98]. This yields a much improved precision on the z -position of the event vertex of 2 mm, which is about a factor of 10 better compared to using CJC information only. This translates into an improved resolution on the electron scattering angle θ_e . The resolution on the measurement of the charged particle momenta is $\sigma_p/p^2 < 0.01 \text{ GeV}^{-1}$.

Central Proportional Chambers CIP and COP

Mainly for triggering purposes the CTD contains two proportional chambers, the *Central Inner Proportional Chamber* (CIP) and the *Central Outer Proportional Chamber* (COP). Both are segmented into two radial layers. The CIP is further

subdivided into 8 ϕ sectors and 60 segments along z with a length of 3.6 cm. It is the chamber placed closest to the beam pipe and has an angular coverage of about $9^\circ < \theta < 171^\circ$. The COP contains 16 ϕ sectors and 18 segments along the z -axis.

For triggering the fast signals are combined to *ray*-signatures, which are coincidences of CIP hits with either COP hits or hits from the FTD compatible with charged tracks from the main interaction region.

In addition to triggering the CIP can also be used to measure the interaction vertex of an ep event using the scattered electron only and independent of the hadronic final state. Due to the large angular acceptance in θ and the simple pad-structure, the CIP is especially well suited for this task. This is explored in section 6.3.2.

Central Silicon Tracker CST

Since 1997 the central tracking is complemented by the *Central Silicon Tracker* CST [P⁺00]. It consists of two concentric layers surrounding the beam pipe at radii $r = 5.75$ cm and $r = 9.75$ cm. The active length is about 36 cm with an angular coverage of $30^\circ < \theta < 150^\circ$. The layers are made up of identical ladders, where one ladder is made of 6 silicon sensors grouped in two half-ladders. The inner layer consists of 12, the outer of 20 ladders. Each silicon module has readout strips on both the p - and the n -side. The strips on the p -side measure the $r\phi$ -coordinate with a resolution of $\sigma_{r\phi} \sim 12 \mu\text{m}$, while the ones on the n -side measure the z -coordinate with $\sigma_z \sim 22 \mu\text{m}$.

The track reconstruction is done using CTD tracks reconstructed as described above. These tracks are extrapolated to the CST hits and a linking is performed. In this analysis the special feature provided by the CST, the good resolution of the *impact parameter* of tracks for tagging of heavy quark production is not needed, but it still benefits from a more precise track measurement. Many technical details are similar to the *Backward Silicon Tracker* (BST), which is of greater importance to this analysis and described below in section 3.2.3.

Forward Track Detector FTD

In the forward region the tracking is complemented by the *Forward Track Detector*. It consists of three identical super modules. Each super module contains planar wire drift chambers with three different orientations for accurate θ measurement, a multi wire proportional chamber for triggering, a passive transition radiator, and a radial wire drift chamber for precise measurements in the $r\phi$ -plane.

3.2.2 Liquid Argon Calorimeter

The calorimetric measurements in most of the angular range, namely $4^\circ < \theta < 153^\circ$, are provided by the *Liquid Argon Calorimeter* (LAr) [A⁺93c, A⁺93b]. It is placed inside the superconducting coil of H1 and therefore provides energy measurements without the need for large dead material corrections. The calorimeter is divided into electromagnetic and hadronic sections, as can be seen in figure 3.4. In both sections the ionisation loss of the shower particles in the liquid argon is used to measure the energy, but the passive material for the shower development is different: lead

in the electromagnetic and stainless steel in the hadronic sections. Mechanically the calorimeter consists of eight *wheels*. The six barrel wheels are segmented in ϕ into eight octants. The whole calorimeter is placed in a large cryostat to keep the temperature of the liquid argon stable at about 90 K.

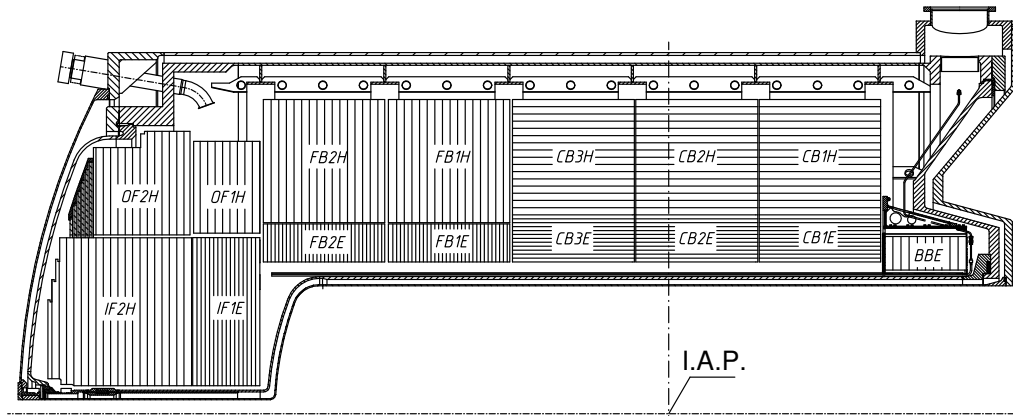


Figure 3.4: View of the LAr calorimeter in the rz -plane. The different sections are labelled according to their position as inner/outer forward (IF/OF) or forward/central/backward barrel (FB, CB, BB). The last letter denotes an electromagnetic (E) or hadronic section (H).

The depth of the electromagnetic section varies between 20–30 radiation lengths (X_0), the whole calorimeter is equivalent to 5–8 nuclear interaction lengths (λ). For electromagnetic particles a good energy resolution of $\sigma_E/E = 10\%/\sqrt{E/\text{GeV}} \oplus 1\%$ is reached¹. As the calorimeter is not compensating, the response to hadrons is lower than for electrons and photons. The correction is done using software reweighting, exploiting the fine segmentation with about 45,000 channels. This results in a resolution of $\sigma_E/E = 50\%/\sqrt{E/\text{GeV}} \oplus 2\%$ for hadrons.

3.2.3 Backward Detectors

As will be explained in more detail in section 4.1, the scattered electron for low $Q^2 < 120 \text{ GeV}^2$ is scattered most of the time into the backward region of the H1 detector. Therefore the subdetectors in the backward part of H1 experiment, see figure 3.5, are of a critical importance for this analysis since they are used to select the events and reconstruct the kinematics. The energy of the scattered electron is measured in the *scintillating fibre Spaghetti Calorimeter* SpaCal. The polar angle of the scattered electron is measured with the help of the *Backward Drift Chamber* BDC, mounted in front of the SpaCal. The *Backward Silicon Tracker* BST is used to measure the polar angle and the event vertex for independent cross checks.

Spaghetti Calorimeter SpaCal

The SpaCal [N⁺96, A⁺96] not just completes the calorimetric measurement in the backward region of H1, it is the *backbone of the inclusive DIS analysis* at low Q^2 .

¹ The symbol \oplus is used to denote quadratic addition: $A \oplus B \equiv \sqrt{A^2 + B^2}$.

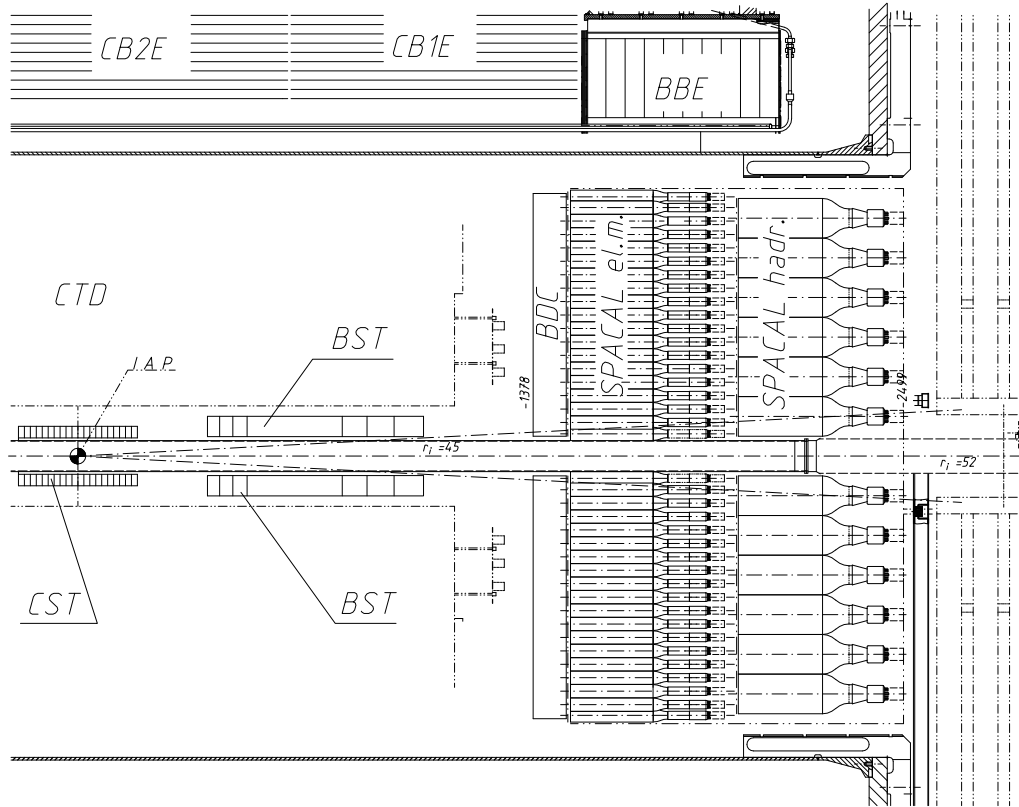


Figure 3.5: Cut in the rz -plane of the H1 backward region. The main components discussed here are the SpaCal, BDC, and BST.

It provides a precise measurement of the energy and impact position of scattered electrons and the *Inclusive Electron Trigger* (IET) for the online event selection. The trigger capabilities will be explored in more detail in section 5.3.

The SpaCal covers the polar angle range of $153^\circ < \theta < 177.5^\circ$ as measured from the nominal z vertex position. It consists of an electromagnetic section with 1192 cells of size $4.05 \times 4.05 \times 25 \text{ cm}^3$ in front of a hadronic section with 136 cells of size $11.9 \times 11.9 \times 25 \text{ cm}^3$. Individual cells in the electromagnetic section are combined to 4×4 super modules. The super module around the beam pipe, the so-called *insert*, has a special construction with a *veto layer*. The overall construction and the insert section are shown in figure 3.6, the numbering of the individual cells as used in the software is shown in the appendix A.

The SpaCal cells are made of lead sheets with embedded scintillating fibres. In the electromagnetic section the fibres have a diameter of 0.5 mm and the lead-to-fibre ratio is 2.3 : 1 by volume, while the hadronic section has larger fibres with a diameter of 1.0 mm and a higher lead-to-fibre ratio of 3.4 : 1. The fibres from each cell are bundled together and attached via light mixers to photomultiplier tubes (PMT). The stability of the PMT gain can be checked using a dedicated LED system. Another important feature is the good timing resolution of the PMTs of better than 1 ns, which allows to reject non- ep background during data collection.

The electromagnetic section comprises 27.5 radiation lengths, equivalent to about 1 hadronic interaction length. The hadronic section adds about one more interaction length to the calorimeter. Due to the fine sampling in the electromagnetic section an

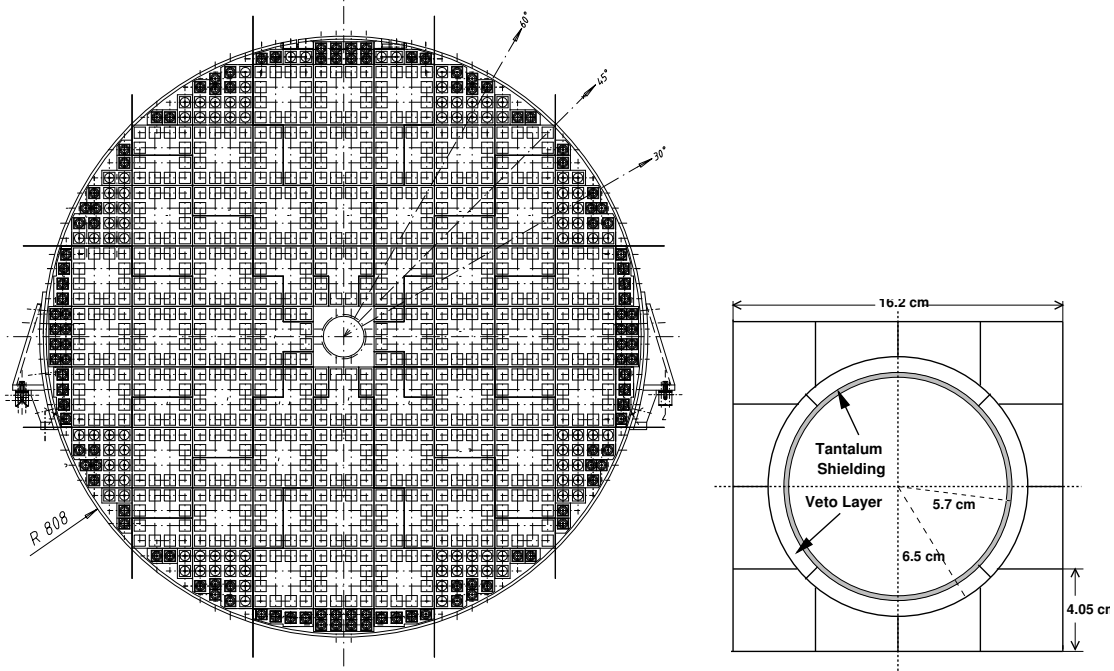


Figure 3.6: Technical drawing of the whole SpaCal on the left: the small boxes indicate individual cells, which are combined to 4×4 super modules. On the right the special insert super module is shown.

energy resolution of $\sigma_E/E = 7\%/\sqrt{E/\text{GeV}} \oplus 1\%$ is reached for electrons. The impact point is reconstructed with a resolution of about $\sigma_{xy} = 4.4 \text{ mm}/\sqrt{E/\text{GeV}} \oplus 1.0 \text{ mm}$ in the xy -plane.

The hadronic section is used for a coarse hadronic energy measurement and to distinguish hadronic from electromagnetic showers. The combined energy resolution for hadrons increases linearly with the energy and was determined to be $\sigma_E/E \approx 30\%$ [A⁺96]. Due to space constraints it is not deep enough to contain all hadronic showers.

Backward Drift Chamber BDC

The BDC [Sch96b] is a thin drift chamber mounted in front of the SpaCal with the same angular acceptance. It consists of 4 double layers, each of them divided into 8 sectors. The sense wires are strung perpendicularly to the beam axis and are fixed at the sector edges leading to an octagonal geometry with almost radial drift directions. The double layers are rotated by 11.25° with respect to each other to allow for an estimate of the azimuthal coordinate. In addition, this reduces the efficiency losses at the sector edges. The overall structure is displayed in figure 3.7 on the left.

The drift cells are 1 cm wide in the inner region and 3 cm wide in the outer one. At the transition from the inner to the outer region a special cell is introduced with 0.5 cm drift distance at the inner side and 1.5 cm drift distance at the outer one. The cells within one double layer are shifted by half a drift cell in radial direction to solve the inner-outer hit assignment ambiguity. The cell structure is illustrated

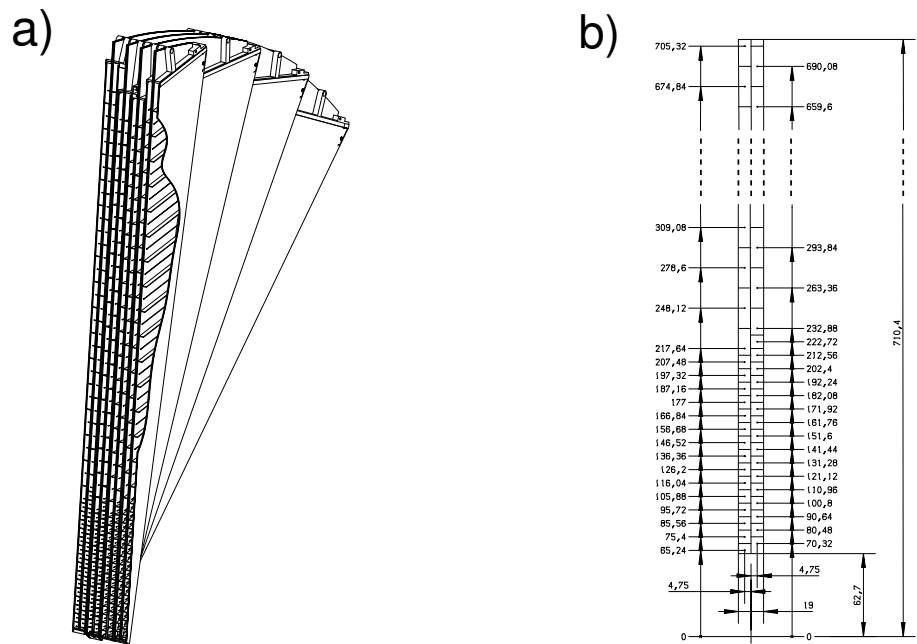


Figure 3.7: Three-dimensional view of a section of the BDC illustrating the layer structure and the drift cell geometry. The chamber has a radial extension from 6 cm to 71 cm. At a radius of about $r = 22$ cm the segmentation is changed and a transition drift cell is introduced.

in figure 3.7 on the right. The radial resolution for minimum ionising particles is $400 \mu\text{m}$, the azimuthal resolution is about 2 mm.

Backward silicon Tracker BST

The BST in the configuration installed in the years 1998-2000 is shown in figure 3.8. It consists of eight planes mounted perpendicularly to the beam axis with a 16-fold azimuthal subdivision.

The z positions of the planes are arranged to allow for a uniform polar angle acceptance. This is achieved by arranging the z positions in a geometric series:

$$z_{i+1} = z_i \cdot \sqrt[N]{\frac{r_{\max}}{r_{\min}}}. \quad (3.1)$$

Here $r_{\min} = 5.9$ cm and $r_{\max} = 12.0$ cm denote the inner and outer radius of the sensitive detector region, $N = 8$ is the number of installed planes. The module BST2 located closer to the nominal interaction point occupies the z_i positions with $i = 1, 2, 3, 4$ starting at $z_1 = -35.8$ cm, while BST1 planes are at z_i for $i = 9, 10, 11, 12$. The last plane is therefore located at $z_{12} = -95.7$ cm. This results in a maximum of 4 hits per track in the plateau region $164^\circ < \theta < 176^\circ$.

Each BST plane is equipped with 16 modules, whose active area is a wedge shaped, single sided, double metal silicon strip sensor shown in figure 3.9a. One of these sensors contains 640 readout strips concentric around the beam axis at a pitch of $96 \mu\text{m}$. The signals are amplified and temporarily stored by 5 custom on-sensor front-end chips, called APCs (Analogue Pipeline Chips). The APCs contain

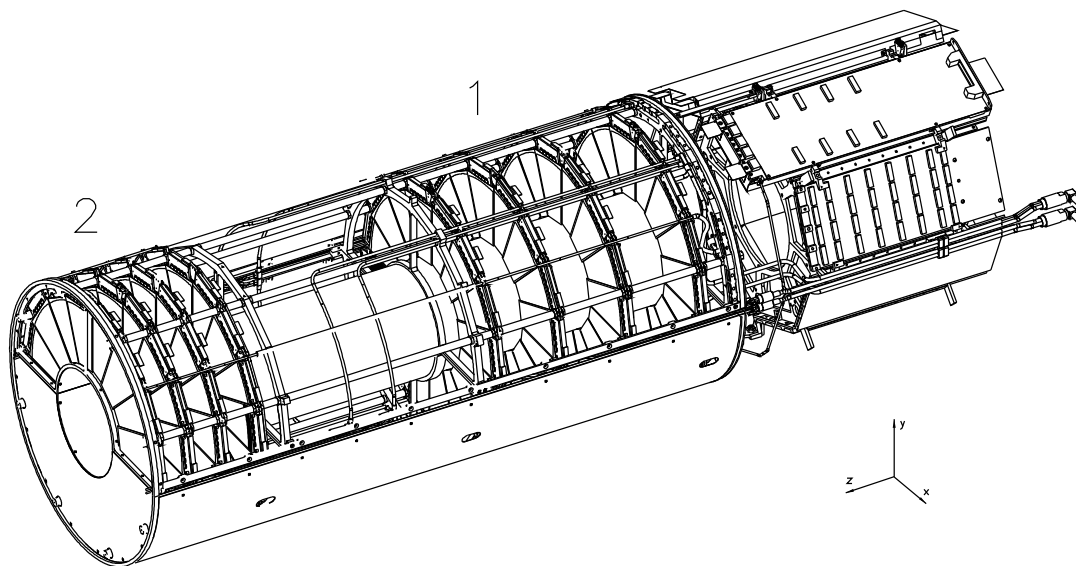


Figure 3.8: Schematic layout of the H1 Backward Silicon Tracker (BST). The active area is composed of 8 planes subdivided into two modules, BST1 and BST2 (labelled here with the numbers “1” and “2”). Each plane is made of 16 r -sensors and one u -sensor (mounted on the back side, not shown here). In the rear section electronic readout boards are placed. Also indicated are the electric shielding and the water cooling pipes. The upper and lower halves of the detector are separate structures to ease installation around the beam pipe.

a capacitance storage pipeline with a length of 32 bunch crossings. Using the r -sensors the polar angle of a track and the event vertex can be determined from a one-coordinate measurement only in the solenoidal magnetic field.

In addition, each plane contains a prototype installation, a single sided, single metal silicon strip sensor. It is placed in the azimuthal sector $45^\circ < \phi < 67.5^\circ$. This u -sensor type, shown in figure 3.9b, has its 640 readout strips parallel to the reference edge of the sensor at a pitch of $75 \mu\text{m}$. It thus measures hits in u -coordinate space defined by $u = r \sin \phi_u$, where ϕ_u is the azimuthal angle with respect to the reference edge of the sensor. Combining the information from r - and u -sensors it is possible to measure the transverse momentum and determine the charge of a track in the BST.

The readout procedure is described in [H⁺98] and summarised here. During data taking nearly 100,000 strips are read out, where the information of two neighbouring modules, i.e. 1280 strips, are transmitted serially. An online hit finding is performed, taking into account individual *pedestals* of each channel, which are dynamically updated. Readout induced coherent shifts in the amplitude of groups of strips, so called *common mode*, are also corrected for. For reconstructed tracks, the most probable signal-to-noise values for the hits is about 15 for the r -sensors and 30 for the u -sensors, which reflects the different layout of the two wafer types. The single hit resolution is about $20 \mu\text{m}$ for the r -sensors and $15 \mu\text{m}$ for the u -sensors. A first version of a 4-plane BST based on r -sensors is described in [E⁺97b].

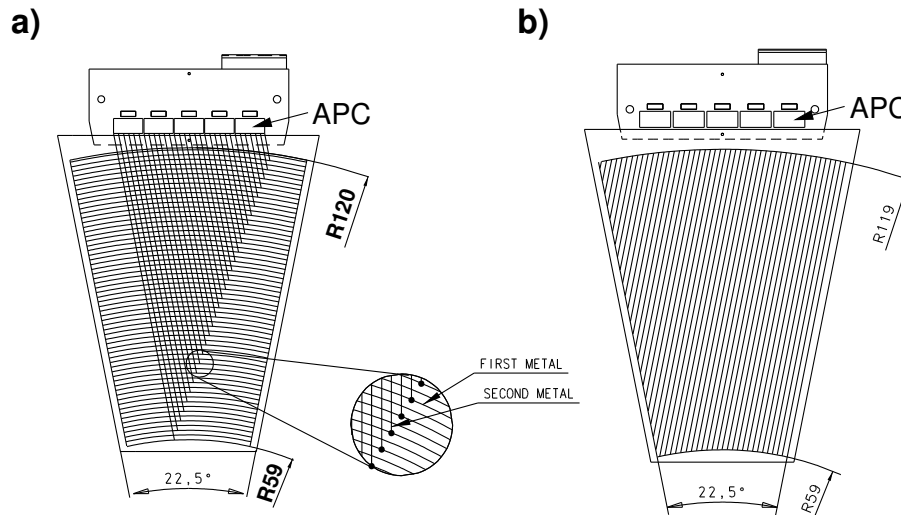


Figure 3.9: Two types of silicon sensors used in the BST: a) *r*-sensor, b) *u*-sensor. Both contain 640 readout strips, which are $96\ \mu\text{m}$ and $75\ \mu\text{m}$ apart from each other respectively. The signals are routed to the hybrid, where they are amplified and stored in the custom APC chips.

3.2.4 Luminosity System

The proportionality factor between the number of detected *signal events* N , corrected for acceptance, efficiencies, etc., for a given process and its measured *cross section* σ is called *luminosity* \mathcal{L} :

$$N = \mathcal{L}\sigma. \quad (3.2)$$

H1 uses the Bethe-Heitler events $ep \rightarrow e\gamma p$ introduced in section 2.6 as a *reference process* to measure \mathcal{L} , as its cross section is large and precisely calculable to about 1% uncertainty. In turn this value is used by all other physics analyses to convert their measurements to an absolute cross section which can be compared to theory and other experiments.

The *H1 Luminosity System* [A⁺97a] was designed to measure the Bethe-Heitler process. Since the angular distributions of the electrons and photons are strongly peaked in the direction of the electron beam, the detectors are placed close to the beam line and far away from the nominal interaction region. The system consists of two electromagnetic calorimeters, a *Photon Detector* (PD) and an *Electron Tagger* (ET), located at $z = -102.9\ \text{m}$ and $z = -33.4\ \text{m}$, respectively. A schematic overview of the system is given in figure 3.10. For the online measurement the ET and PD are used in coincidence, while the offline corrections are derived from a detailed analysis of the PD only.

The electrons scattered under a small angle but with reduced energy are bent by the HERA magnets so they reach an exit-window in the beam pipe at $z = -27.3\ \text{m}$ and then hit the ET. The ET consists of 7×7 cells covering an area of $154 \times 154\ \text{mm}^2$. Apart from the luminosity measurement it can also be used to tag *photoproduction* events, as will be explained in more detail in section 4.3.2.

The photons reach the PD through an exit-window at $z = -92.3\ \text{m}$ where the electron beam pipe bends upwards. It has to be shielded from a high flux of

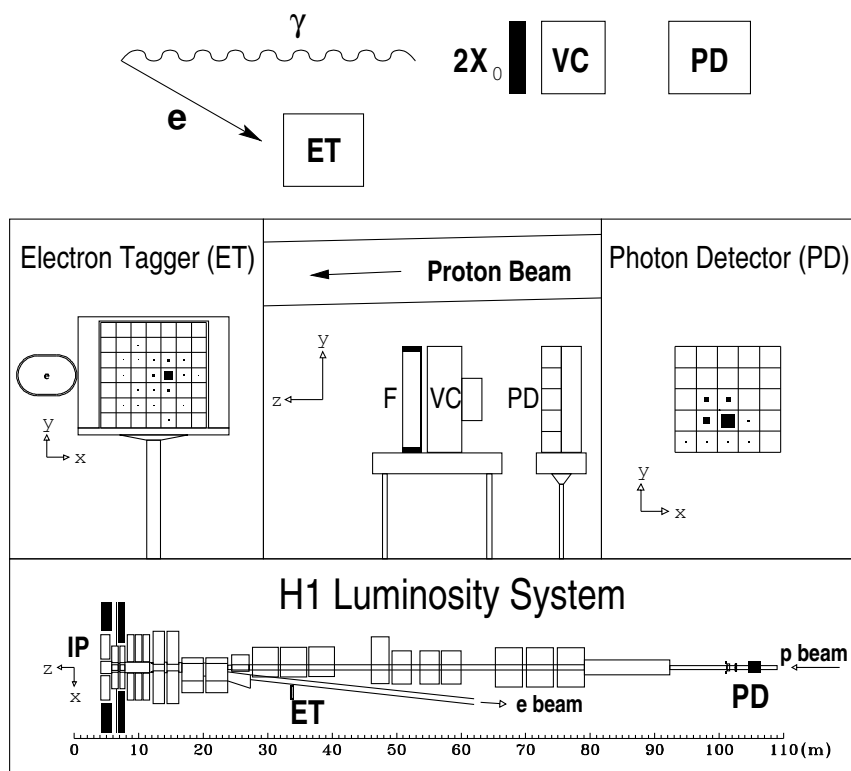


Figure 3.10: A schematic overview of the H1 Luminosity System. On top the detection principle is shown. The middle panels show a typical event with both the electron and the photon detected. The lower panel puts the positions of the ET and the PD into perspective with the main H1 detector.

synchrotron radiation by a $2X_0$ lead filter. A Water Cherenkov Veto Counter is used to assess and reject events where the photon has showered in the filter. The PD itself consists of 5×5 cells covering an area of 100×100 mm².

The total systematic uncertainty of the H1 luminosity measurement is about 1.5%. This value can only be reached taking into account many systematic effects. Two of these effects will be discussed in more detail in section 5.6: background from rest gas in the beam pipe $eA \rightarrow e\gamma A$, which is analysed using electron pilot bunches, and tails in the proton bunch structure. Other important effects are the energy calibration of the PD and the acceptance for Bethe-Heitler photons, which is mostly limited by beam line elements and the beam optics.

3.2.5 Trigger System

The high bunch crossing frequency of 10.4 MHz delivered by HERA, interesting physics processes with rates that differ by orders of magnitude, and large background rates made a sophisticated trigger and readout system a necessity for H1. The background rates are typically given by the hadronic interactions of the protons, while the physics rate is governed by the much weaker electromagnetic and weak interactions.

H1 uses a *four level trigger system* to reduce the amount of data written to tape while keeping the interesting physics. More abundant processes have to be *prescaled*,

effectively lowering the luminosity for these reactions. This way the limited bandwidth can be used optimally. Figure 3.11 gives an overview over the H1 trigger system and associated input rates and decision times. The rate is reduced gradually by a factor 10^6 until the events are written to tape for offline analysis.

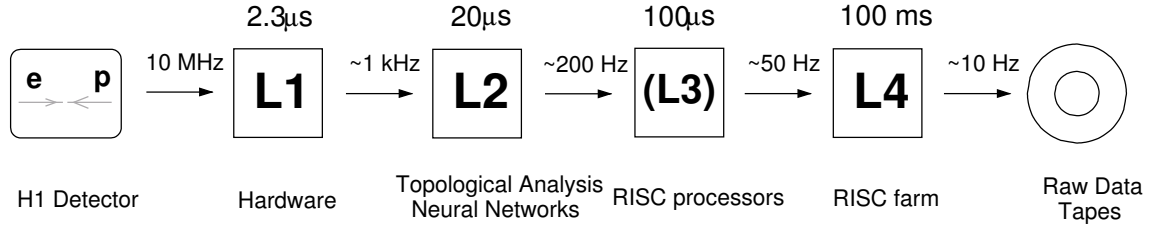


Figure 3.11: The four trigger levels of H1 with respective input rates and processing times.

The *first level trigger* L1 works dead time free. Various subdetectors provide L1 information, which must not be delayed by more than $2.3 \mu\text{s}$ with respect to the bunch crossing time. This information is provided to the *Central Trigger* in the form of so called *Trigger Elements* (TE). Up to 256 of these TEs, which are simply Boolean values, can be processed by the central trigger. The trigger elements are combined by logical operations to *Subtriggers*, that should in the ideal case reflect a certain type of physical event. Up to 128 of these subtrigger conditions can be processed. If any of the active subtriggers signals a positive decision, the central trigger system decides to keep this event (L1Keep). The *dead time* starts and all H1 detectors prepare their data from $2.3 \mu\text{s}$ ago for readout. In case a subtrigger is prescaled by a *prescale factor* i , only every i -th event triggers the L1keep signal. This means there is a difference between the *raw subtrigger* based only on the information delivered by the TEs and the *actual subtrigger* taking the prescale into account. Typically prescale factors are applied to subtriggers which aim to record physics events with large cross sections and have therefore high rates. The collected luminosity is effectively reduced by the prescale factor for these subtriggers, but should still be sufficient for analysis or monitoring purposes.

At the *second trigger level* L2 refined information from all trigger detectors are used to perform *neural network* (L2NN) or *topological* (L2TT) analyses within $20 \mu\text{s}$. Both systems can deliver up to 16 L2 trigger elements, which are combined with the L1 subtriggers. If any actual L1 trigger is validated by L2 or without L2 condition, the whole detector readout procedure starts, which takes approximately 1 ms.

The third trigger level L3 was not activated until 2006 and is therefore not discussed here.

The *fourth trigger level* L4 is based on a full event reconstruction in a RISC processor farm. Its purpose is not online event selection, but rather a reduction of offline storage space needed. It verifies the trigger decision based on the full detector information and determines if the event is part of a set of *event classes*. Events not classified or classified as *soft scale* (e.g. photoproduction, low Q^2) are then downscaled, i.e. another sort of *prescaling factor* is applied. This factor is typically of the order 2 – 10 for soft physics and 100 for events which are believed to be pure background. This allows the monitoring of losses at L4.

Chapter 4

Basics of the Cross Section Measurement

The basic idea of a cross section measurement is simple: the events have to be selected and the kinematic variables have to be reconstructed from the detector measurements. Then the signal events have to be binned and corrected for background, efficiency, acceptance, and radiative effects. In this chapter these steps are discussed in a general way. A major point is the usage of events generated by *Monte Carlo Event Generators* and simulated H1 detector response. These *Monte Carlo events*, often just called *MC*, simplify the cross section measurement and are discussed here as well.

4.1 Reconstruction of DIS Events

As discussed already in the sections 2.1 and 2.2, the DIS cross section is described as a function of the kinematic variables x , y , and Q^2 . For a given centre of mass energy $\sqrt{s} = \sqrt{4E_e E_p}$, where E_e and E_p are the energies of the incoming electrons and protons respectively, only two of these variables are independent due to equation 2.3: $Q^2 = sxy$, which is usually employed to calculate x .

The H1 detector can reconstruct the *scattered electron* as well as the *hadronic final state* (HFS). From an inclusive point of view, the final state of the scattering always consists of just the scattered electron e' and the hadronic final state X . The abbreviation *HFS* is used throughout this thesis to refer to the measurement of all final state particles excluding the identified scattered electron. As four independent measurements are available for the reconstruction of two kinematic variables, a multitude of *different reconstruction methods* are possible. Advantages and drawbacks of the respective methods are discussed later and are only shortly summarised here.

Using only the *scattered electron energy* E'_e and its *polar angle* θ_e , the kinematic quantities can be reconstructed using the *Electron Method*. From the definitions in the equations 2.1 one derives:

$$y_e = 1 - \frac{E'_e}{2E_e} (1 - \cos \theta_e) = 1 - \frac{E'_e}{E_e} \sin^2 \frac{\theta_e}{2} \quad (4.1)$$

$$Q_e^2 = 2E'_e E_e (1 + \cos \theta_e) = \frac{E_e'^2 \sin^2 \theta_e}{1 - y_e}. \quad (4.2)$$

The electron method allows a reconstruction independent of the HFS with very good resolution at high $y > 0.1$, where it is used by default in this analysis. On the other hand it depends on the precise knowledge of radiative corrections, as ISR events are wrongly reconstructed, see section 2.6, and the resolution degrades for lower inelasticities $y < 0.1$.

From these formulae it can also be seen, that low Q^2 corresponds to high electron scattering angles $\theta_e \rightarrow 180^\circ$ in the H1 coordinate system (which in fact are small angles w.r.t the incident electron beam). Figure 4.1 shows, that most of the kinematic range $Q^2 < 120 \text{ GeV}^2$ corresponds to electrons scattered into the backward region of H1. The inelasticity there is approximately equal to the fractional energy loss of the electron $y_e \approx 1 - E'_e/E_e$ for high y . At low y the region of the *kinematic peak* with $E'_e \sim E_e$ is dominating the (x, Q^2) plane.

For the reconstruction of the HFS one has to consider, that losses in the direction of the incident proton, i.e. the forward beam pipe, are inevitable. Viewed in the QPM-picture, see figure 2.2, it is impossible to fully reconstruct the *proton remnant*, but the hadrons created by the *scattered parton* have sufficient transverse momentum to be mostly reconstructed in the central detector¹.

The first HFS quantity mostly independent of forward beam pipe losses is its *transverse momentum* $p_{t,HFS}$, which is equal to the transverse momentum of the electron $p_{t,e}$ due to momentum conservation

$$p_{t,HFS} = p_{t,e} = |E'_e \sin \theta_e| \quad (4.3)$$

$$p_{t,HFS} = \left| \sum_{i \in HFS} \mathbf{p}_{\perp,i} \right|, \quad (4.4)$$

where $\sum_{i \in HFS}$ sums the transverse momentum vectors $\mathbf{p}_{\perp,i}$ of all particles in the HFS.

The second quantity derived from the longitudinal momentum conservation and mostly insensitive to forward beam pipe losses is $(E - p_z)_{tot}$. All particle masses are neglected. Due to momentum conservation this is always $(E - p_z)_{tot} = 2E_e$, unless there are (undetected) losses in the backward direction and receives contributions from the electron and the HFS $(E - p_z)_{HFS}$:

$$(E - p_z)_{tot} = (E - p_z)_{HFS} + E'_e(1 - \cos \theta_e) = 2E_e \quad (4.5)$$

$$(E - p_z)_{HFS} = \sum_{i \in HFS} E_i(1 - \cos \theta_i). \quad (4.6)$$

One can also define a *hadronic angle* γ_h , which in the QPM is equivalent to the polar angle of the struck parton:

$$\tan \frac{\gamma_h}{2} = \frac{(E - p_z)_{HFS}}{p_{t,HFS}} \quad (4.7)$$

Using these hadronic quantities in equations 4.1 and 4.2 it is simple to derive the kinematic quantities measurements from the HFS only and define the *Hadron*

¹For non-diffractive events the proton remnant and the struck parton are colour-connected and therefore the *gap* between the proton remnant and the struck parton is filled with hadrons.

Method [JB79]:

$$y_h = \frac{(E - p_z)_{HFS}}{2E_e} \quad (4.8)$$

$$Q_h^2 = \frac{p_{t,HFS}^2}{1 - y_h}. \quad (4.9)$$

This method has worse resolution than the electron method and depends on a good reconstruction of the HFS, but on the other hand it is still usable at lower $y < 0.1$. Its main application is the reconstruction of *charged current* events, which is beyond the scope of this thesis, and systematic studies of the HFS.

A more balanced way to reconstruct the kinematics using electron and HFS information is used in the Σ *Method* (Sigma Method)². It reconstructs y similar to the hadron method, and Q^2 similar to the electron method. It completely avoids the usage of the incoming electron energy E_e , which is replaced by $(E - p_z)_{tot}/2$. This way it is less sensitive to radiative corrections and energy calibration uncertainties:

$$y_\Sigma = \frac{(E - p_z)_{HFS}}{(E - p_z)_{tot}} \quad (4.10)$$

$$Q_\Sigma^2 = \frac{E_e'^2 \sin^2 \theta_e}{1 - y_\Sigma} \quad (4.11)$$

$$x_\Sigma = \frac{Q_\Sigma^2}{2(E - p_z)_{tot} E_p y_\Sigma} = \frac{Q_\Sigma^2}{2(E - p_z)_{HFS} E_p}. \quad (4.12)$$

The Σ method provides a good resolution in a wider kinematic range, but it is inferior to the electron method at high y . Therefore it is used by default in this analysis for lower $y < 0.1$. Furthermore cross checks between the electron and Σ method are possible.

Equation 4.10 gives another illustrative explanation for the inelasticity variable y : it is the fraction of $(E - p_z)_{tot}$ carried by the HFS. This is indicated in figure 4.1. The general direction of the HFS particles as quantified by γ_h is also seen to point in the forward direction at low y and more in the backward direction for high y .

Another reconstruction method using only the polar angle information θ_e and γ_h and therefore mostly independent of the calorimeter energy scales is the *Double Angle Method*. It will be introduced in section 6.1 where it is used for the SpaCal calibration.

Instead of combining two methods, the Electron Method at higher y and the Σ method at lower y , as it was done in previous H1 publications [A⁺01], one may look for a single method, which covers the whole measurement range. In [BB99] several options are explored to derive a combined method with good resolution and low reconstruction bias over a larger kinematic range. One option employed for high $Q^2 > 100 \text{ GeV}^2$ analysis by H1 [A⁺03b] is the *e Σ Method*, which combines the measurements by the electron and Σ methods according to

$$x_{e\Sigma} = x_\Sigma, \quad Q_{e\Sigma}^2 = Q_e^2, \quad y_{e\Sigma} = \frac{Q_{e\Sigma}^2}{4E_e E_p x_{e\Sigma}}. \quad (4.13)$$

² The name comes from the fact, that some authors define $(E - p_z)_{HFS} \equiv \Sigma$ [BB95b].

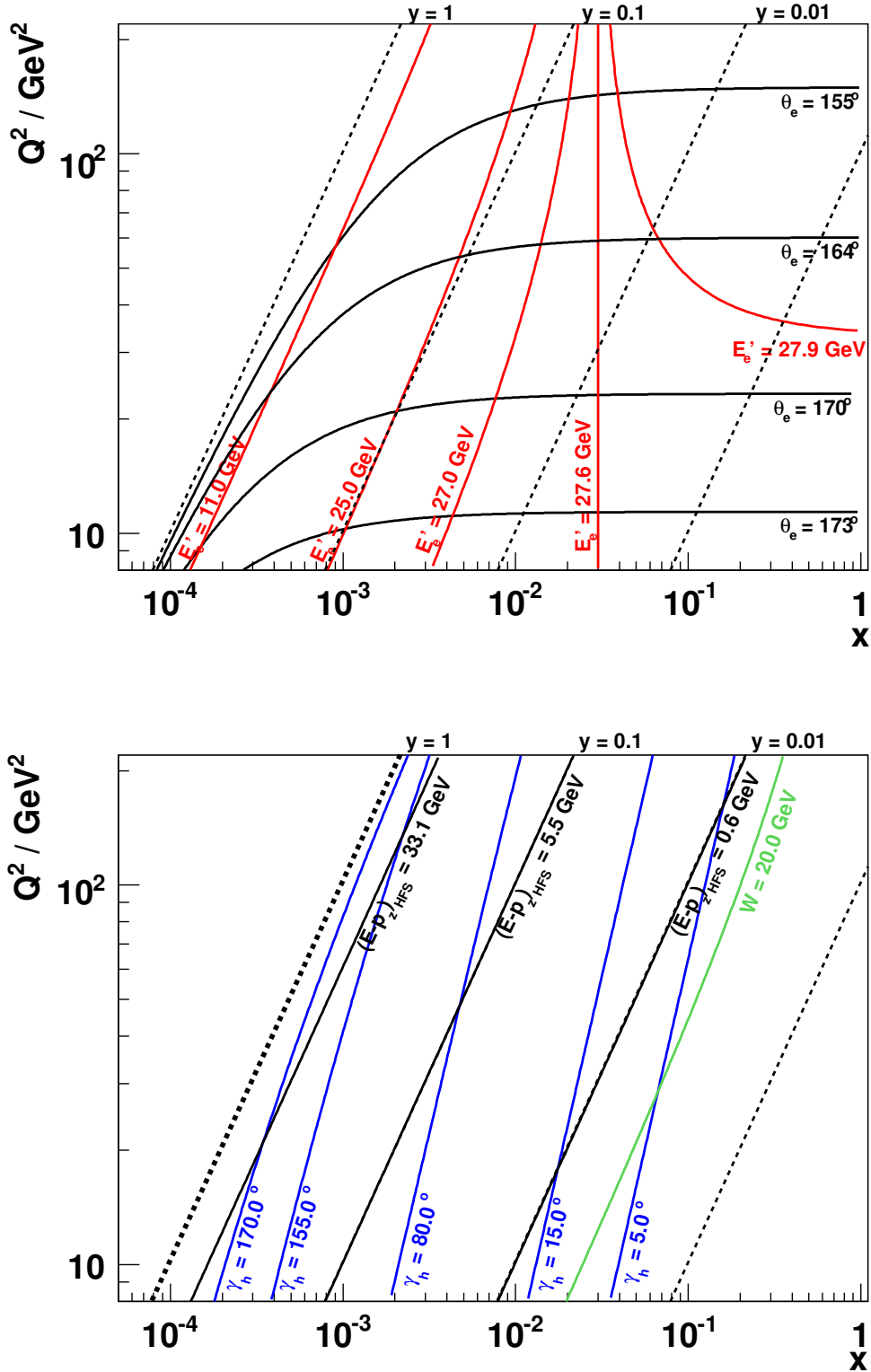


Figure 4.1: The kinematic (x, Q^2) plane for the DIS process $ep \rightarrow eX$ at the Born level in the Q^2 range of this analysis for $\sqrt{s} = 320$ GeV. Top: Dependencies on the scattered electron variables E_e' and θ_e . Bottom: Dependencies on the HFS variables $(E - p_z)_{\text{HFS}} \propto y$, γ_h , and W .

Another option is the *PT Method* used by the ZEUS collaboration [C⁺01] to measure in a wide kinematic range $2.7 \text{ GeV}^2 < Q^2 < 30000 \text{ GeV}^2$. This method represents a combination of the Σ and Double Angle Methods.

Details concerning these two alternative methods follow, while other options are not considered further. The $e\Sigma$ and *PT* Methods indeed manage to provide a precise reconstruction of the kinematics over the whole kinematic range. However they have the large drawback, that they are influenced by the correlated systematic error sources of the HFS measurement and therefore fail to achieve the low total uncertainty of the electron method at higher y , see section 7.5.

4.2 Monte Carlo Models

Monte Carlo programs are necessary for the measurement of DIS cross sections. The corrections for limited detector efficiency and acceptance, smearing of reconstructed kinematic variables due to detector resolution, and radiative effects, which are highly correlated, can be determined using a Monte Carlo simulation. The main task is then to prove that these items are correctly described by the simulation. Furthermore Monte Carlo events are used to estimate the effects of systematic uncertainties on the cross section measurement.

The production of MC events is done in several steps. First certain *Monte Carlo generators* are used to generate events according to a specific physics model. In this analysis two generators are used, *DJANGO* and *PHOJET*. This phase also involves the *hadronisation* of final state quarks and gluons. The result of this step are a set of four-momenta and the identities of the final state particles. Next is the detailed and realistic simulation of the H1 detector response to these generated events. The result of this step are events similar to real data, which are treated mostly analogue for the reconstruction and analysis. In addition to the *reconstructed detector quantities* the corresponding *generated quantities* are available for analysis.

4.2.1 DJANGO

The *DJANGO* generator program [SS91] is used to generate complete ep DIS events including leading order QED radiative corrections as implemented in the program HERACLES [KSM92]. For this analysis the version DJANGOH 1.4 is used. As input structure functions leading order parton distributions with $F_L = 0$ from the PDFLIB [PB00] with the code *GRV5004* are used. During analysis the cross section is reweighted to a NLO QCD fit to the measurement using the H1 data of the years 1996/97 H1 [Leh98]. A small additional modification is discussed in section 7.4.

The hadronic final state is simulated using various programs which include first order QCD matrix elements, and models for parton cascades and the hadronisation. The parton cascades are performed according to the Colour Dipole Model [GP88, AGLP89] as implemented in ARIADNE [Lön92]. The hadronisation is performed by the JETSET package [Sjö94] implementing the Lund string model [AGIS83, AGS83].

Especially challenging is a realistic simulation of the HFS at low values of W . In former versions of DJANGO the simulation was restricted to $W > 5 \text{ GeV}$, where JETSET can be used reliably. This may lead to differences in the MC at low $p_{t,HFS}$ compared to the data. To improve this situation, the SOPHIA model [MER⁺00]

has been included in DJANGO to simulate the low $W < 5$ GeV region down to the proton resonances. SOPHIA was developed for astrophysical applications and provides a good description of a large variety of experimental data.

For this analysis 50 million events were generated with DJANGO 1.4, corresponding to an integrated luminosity of $\mathcal{L}_{MC} \approx 104 \text{ pb}^{-1}$ and therefore about five times more than the data. The phase space was restricted to $Q^2 > 2 \text{ GeV}^2$. To avoid a large statistics at very low and eventually unused Q^2 values, the actual number of events below $Q^2 < 5 \text{ GeV}^2$ are reduced by a Q^2 *weighting scheme*.

4.2.2 PHOJET

The only appreciable background from other ep physics processes to this analysis is *photoproduction*, i.e. ep scattering at very low $Q^2 \approx 0$. To model this process the generator PHOJET in version 1.10 [ER96] is used. It aims for a complete description of the total photoproduction cross section based on the two-component Dual Parton Model including soft and hard hadronic processes. The hadronisation is done using the Lund String Model implemented by JETSET as for DJANGO. The phase space is restricted to $y > 0.1$ and $Q^2 < 1 \text{ GeV}^2$, so there is no overlap with the DJANGO simulation. In total 10 million events are used for this analysis, which have to be normalised to identified photoproduction in the data, see section 4.3.2.

4.2.3 Detector Simulation

After generation the Monte Carlo events are processed by a software package designed to simulate in detail the response of the H1 detector. The H1SIM program (version 33800), which is based on GEANT3 [B⁺87], simulates the effects of the final state particles passing through the detector, including multiple scattering, showering, and decays of longer lived particles. For the shower development in the calorimeters a fast parametrisation H1FAST [GRP90] is chosen to save computing time. The energy depositions are digitised according to the expected response of each subdetector. Finally the reconstruction of the *simulated detector response* is done in a way analogue to data.

A major point in the simulation is the realistic implementation of the material distribution, as otherwise smearing and resolution effects cannot be properly described. As previous analyses [Len01] have shown, the amount of dead material in the backward region is typically of the order $0.5 - 1.6 X_0$, see figure 4.2. This means a large percentage of the scattered electrons shower and loose energy before they reach the BDC and the SpaCal. Furthermore detector noise and efficiencies are implemented in the simulation. Dedicated studies using special reference samples are used to test, that the MC description of these effects is realistic, otherwise corrections are applied.

The detailed simulation of events is a computing intensive task and the generation and simulation of samples as large as used in this analysis has only become feasible in the last years due to the availability of fast and comparatively cheap microprocessors. Still, an Intel Xeon CPU running at 3 GHz needs about 5 s for one single event. The MC samples used in this analysis were produced in a PC farm at DESY Hamburg.

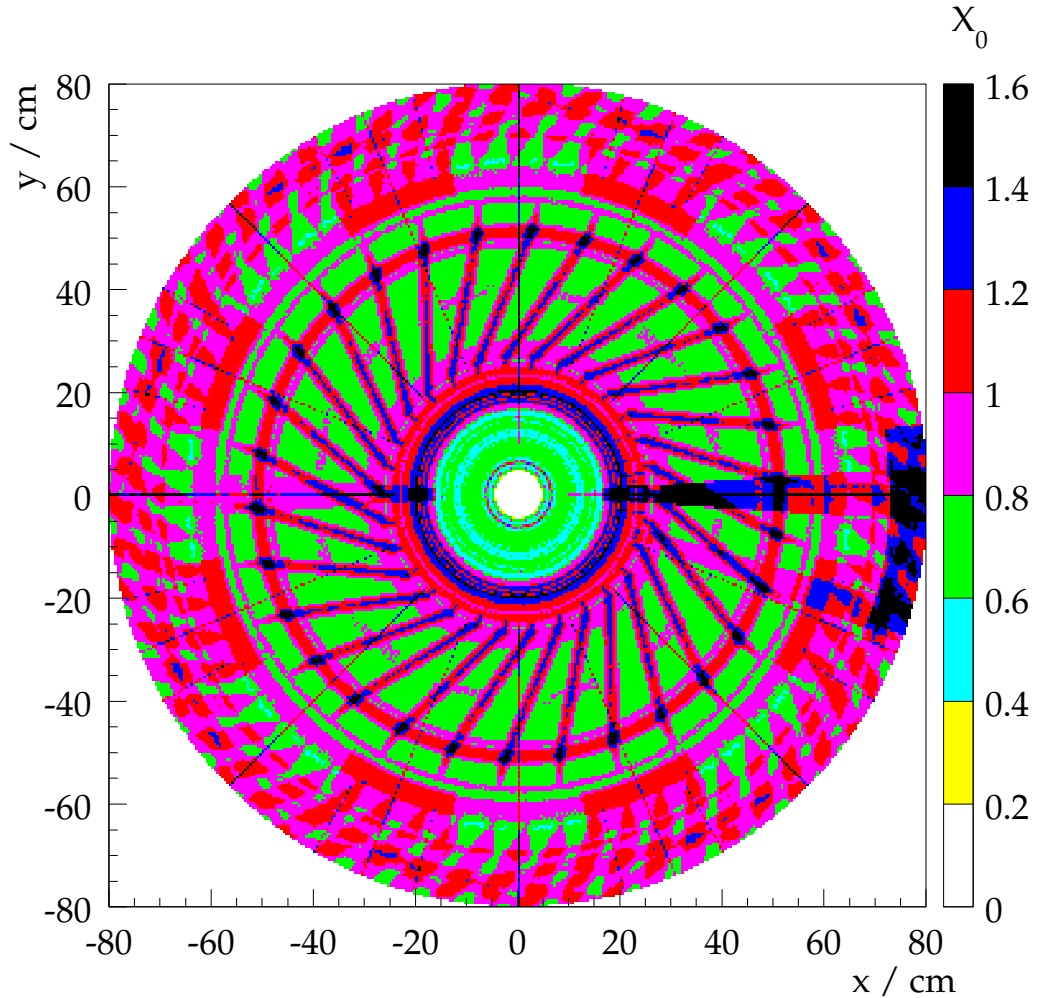


Figure 4.2: The material distribution implemented in the H1 detector simulation which is passed by a particle travelling from the nominal interaction point as a function of its impact point on the SpaCal surface. Figure taken from [Len01].

4.2.4 Radiative Corrections

The structure functions F_2 and F_L are defined with respect to the Born cross section, i.e. they describe the ep interaction using the single photon exchange approximation. In reality there are of course higher order QED corrections, which are suppressed by the smallness of $\alpha \approx 1/137$. A detailed theoretical summary can be found in [Spi92], while [Gla98] contains a short overview of the effects on the cross section measurement.

The major sources of corrections to the inclusive cross section measurement comes from the topologies with emission of real photons from the lepton line, as discussed already in section 2.6. Here the main effects are ISR events wrongly reconstructed by the electron method due to the undetected ISR photon. Radiation from quarks is expected to be small at low x and is not simulated.

As shown in [Gla98], the measured cross section is influenced by as much as 50% for high y at $Q^2 = 35 \text{ GeV}^2$. While these effects can be reduced by requiring *large enough* $(E - p_z)_{tot} > 35 \text{ GeV}$, it is important to test, that the radiative corrections

are correctly implemented in DJANGO. This is done comparing the total generated DIS cross section as a function of the kinematic variables (x, Q^2) calculated at the leptonic vertex to the analytic prediction of the HECTOR package [ABB⁺96].

In previous analyses of special runs in 1999 and 2000 it was already discovered [Beh06], that using the Q^2 weighting feature of DJANGO introduces an inconsistency in the event generation: the fractions of the *subprocesses* Born, ISR, FSR, and Compton do not agree between the initial calculation and the final amount of generated events. The investigation showed, that a simple reweighting of the single subprocesses by typically less than 1% improves the agreement to the HECTOR prediction, while the effect on the measured cross section is small compared to other uncertainties. This *subprocess reweighting* is by default applied to the MC sample.

The cross check of the DJANGO 1.4 sample used in this analysis with the HECTOR calculation is shown in figure 4.3. Besides the statistical fluctuations at the highest Q^2 values and edge effects for the lowest and highest x values within each Q^2 bin, an agreement to better than 0.5% is observed, which is finally added as uncorrelated uncertainty of the cross section measurement. The influence of the subprocess reweighting is found to be small but typically beneficial for the agreement.

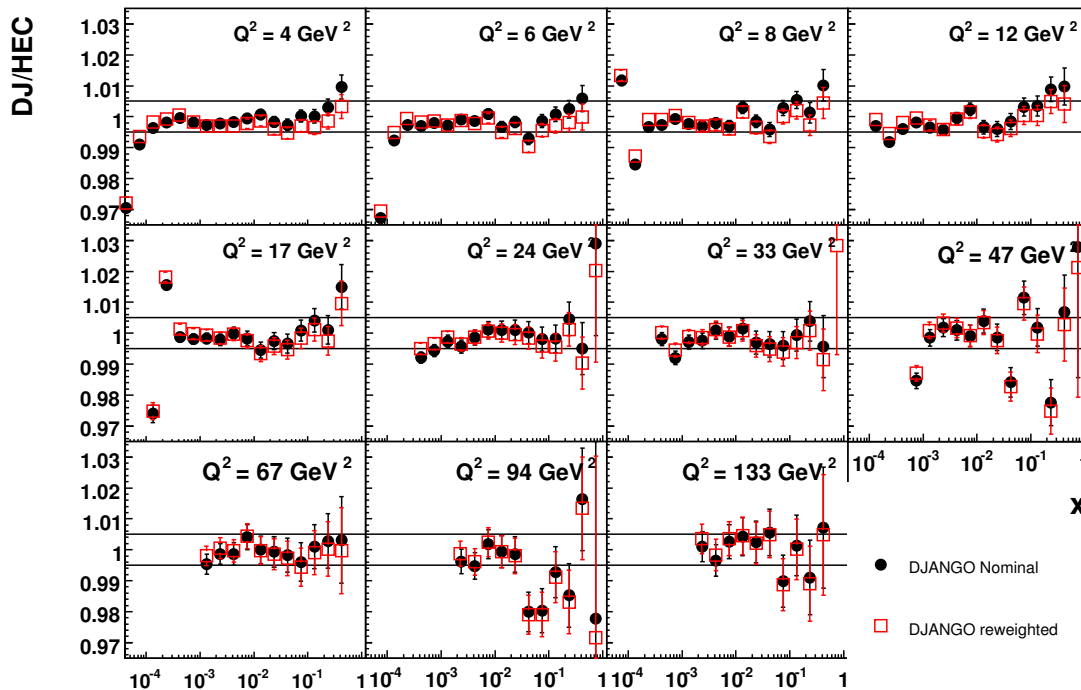


Figure 4.3: Comparison of the total DIS cross section including all radiative corrections as calculated by the HECTOR package and generated by the DJANGO program. The ratio of the two is shown for standard DJANGO event weights and including the subprocess reweighting, which is found to have only a small influence. An agreement to typically better than 0.5% is observed and indicated by the two lines in each Q^2 bin.

4.3 Electron Identification and Background Processes

It is obvious, that before one can reconstruct a DIS event, the scattered electron has to be identified. Furthermore background events have to be rejected or eventually be corrected for.

4.3.1 Electron Identification

As mentioned in the introduction, this work is concerned with the kinematic range $10 \text{ GeV}^2 < Q^2 < 180 \text{ GeV}^2$ at medium and low y . As shown in figure 4.1, the scattered electron is detected in the SpaCal calorimeter at $155^\circ \lesssim \theta_e \lesssim 173^\circ$, so the analysis efforts are concentrated there.

In addition the restriction to medium and low y means that the energy of the scattered electron is relatively large, $y < 0.6$ corresponds to about $E'_e > 11 \text{ GeV}$. As shown in figure 4.1, the HFS is then mostly detected in the central and forward part of the LAr calorimeter at $\gamma_h < 155^\circ$. The electron identification is straight forward: the cluster in the SpaCal with the highest energy is chosen. Suitable selection cuts on the cluster properties exclude most hadronic clusters.

Detailed studies [Gla98] have shown, that for $E'_e > 11 \text{ GeV}$ this criterion for the electron identification approaches 100% efficiency and is independent of the HFS simulation. As a cross check an ordering in transverse momentum p_t of the SpaCal clusters can be chosen. This criterion should be applicable for all values of y , as the HFS transverse momentum is carried by typically many particles but should be balanced by the single electron cluster. The differences in the results are found to be completely negligible.

4.3.2 Photoproduction Background

The only appreciable background from other ep physics processes is *photoproduction* (γp). Here the exchanged photon is quasi-real $Q^2 \approx 0$ and the scattered electron escapes undetected through the backward beam pipe. If the generated hadronic particles, which are typically pions, are scattered into the backward region of H1, they may produce energy depositions in the SpaCal that are misidentified as electrons. The charged pions π^\pm typically leave little energy in the electromagnetic section of the SpaCal. The neutral pions π^0 decay to 2γ and leave their full energy in the calorimeter. Also a track can be produced, if at least one of the photons showers in the dead material before the trackers.

A large fraction of this background is removed by the general electron selection requirements explained in more detail in section 5.2. This includes mostly requirements on SpaCal cluster properties and a matching track segment in the BDC. The requirement of $(E - p_z)_{tot} > 35 \text{ GeV}$ rejects the events where a high energy electron with $E'_e > 10 \text{ GeV}$ has escaped the central detector. The remaining fake electrons have a steep energy spectrum which does not extend far beyond 10 GeV. Therefore they are a sizable background only to high $y > 0.6$ measurements.

The remaining background is quantified using the PHOJET simulation. One complication is that the total cross section and kinematic dependencies are not fully

described by this MC model. This has been observed for analyses covering lower $Q^2 < 10 \text{ GeV}^2$ [Beh06, Gla07] as well as the phase space of this analysis [Rai04]. This is the main reason to restrict the analysis to the lower y domain, where the γp background is small³.

To adjust the normalisation of the PHOJET MC to the data, a special sample is selected, which in addition to the standard selection criteria, guarantees pure photoproduction events. Such a sample can be defined by different means

- A track measured in the CJC or the BST can be linked to the cluster. Up to a small fraction it should have the correct charge, i.e. be positive for DIS positrons. The tracks with *wrong charge* are then mostly background.
- The scattered electron in photoproduction events can be detected in the electron tagger ET as described in section 3.2.4.

These approaches have been shown to give consistent results with an uncertainty of 15% [Beh06]. In this analysis the PHOJET sample is normalised using *tagged γp events* with the electron detected in the ET. The additional selection criteria are listed in table 4.1. The ET is not simulated in the MC, but its acceptance has been determined as a function of y averaged over the data taking period using Bethe-Heitler events. As shown in figure 4.4 it is sizable only for $0.3 < y < 0.6$, corresponding to energies in the ET of about $8 \text{ GeV} < E_{ET} < 17 \text{ GeV}$. This weight is applied to the events simulated by PHOJET to be compared to the tagged data events.

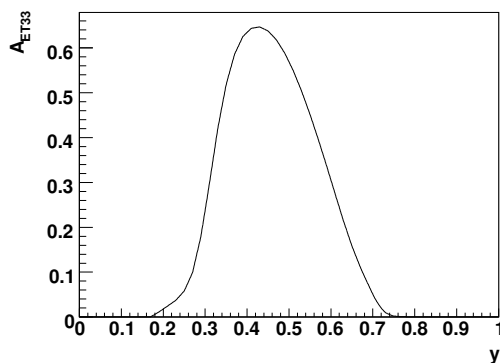


Figure 4.4: Acceptance of the Electron Tagger at $z = -33 \text{ m}$ for photoproduction events as a function of the inelasticity y .

The limited acceptance in y means that studies with the ET and the usual requirement of $(E - p_z)_{tot} > 35 \text{ GeV}$ suffer from much reduced statistics. Also the total hadronic energy in the central detector is limited to typically 15 GeV, which is rather unlikely to produce a fake electron cluster of more than 11 GeV. A

³The most appropriate way to measure in the high y region without any uncertainty from the γp MC model is to use the *wrong charge track background* directly determined from data, which however needs large statistics, good tracking detectors (i.e. the upgraded BST from the HERA II phase), and detailed studies of tracking efficiencies. As mentioned in the introduction first preliminary results are available already [H1p07a, H1p07c].

Selection criterion	Explanation
$E_{ET} > 7$ GeV	ET acceptance and trigger efficiency
L1 Trigger Element 115 active	
$ x_{ET} < 6.5$ cm	
$Q_{gen}^2 < 0.01$ GeV ²	ET acceptance for MC
$((E - p_z)_{tot} + 2E_{ET} + 2E_{\gamma,PD}) < 70$ GeV	Reduction of overlap with Bethe-Heitler events
$E_{\gamma,PD} < 2$ GeV	

Table 4.1: Summary of the additional selection criteria for tagged γp events. Cuts are imposed on the properties of the scattered electron in the ET and the photon in the PD.

good description of the energy spectra of tagged electrons E_{ET} without $(E - p_z)_{tot}$ requirement and the fake electrons selected in the backward region of the central H1 detector E'_e with $(E - p_z)_{tot}$ requirement is achieved as shown in figure 4.5. The equivalent luminosity assigned to the sample of 10 million PHOJET events from this study is $\mathcal{L} = 2.315 \text{ pb}^{-1}$ with an uncertainty of $\pm 15\%$. This number is consistent with a comparable analysis in the lower $1.5 \text{ GeV}^2 < Q^2 < 12 \text{ GeV}^2$ domain using the same detector setup [H1p07b], where a value of $\mathcal{L} = 2.35 \text{ pb}^{-1}$ was determined for an equivalent event sample [Pet07].

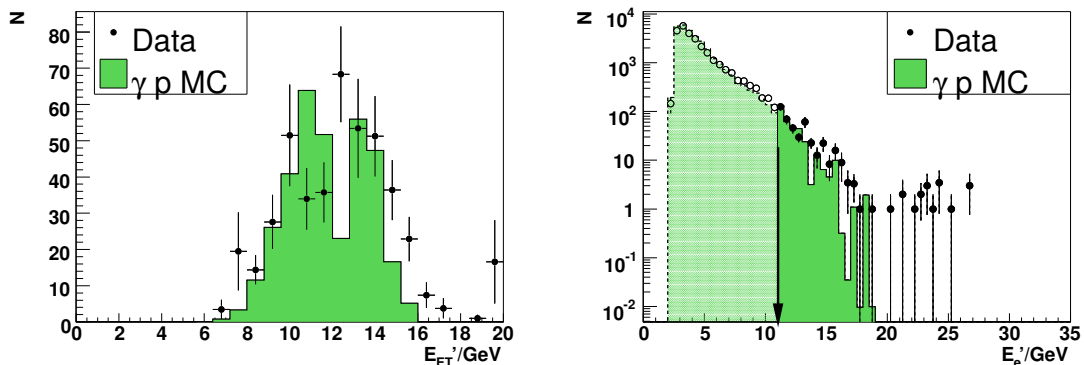


Figure 4.5: Energy spectra in tagged γp events of the scattered electrons in the ET (left) and the falsely identified electron in the SpaCal (right). The left plot is shown for no $(E - p_z)_{tot}$ requirement, while the right one employs the usual selection of $(E - p_z)_{tot} > 35$ GeV. The range relevant for the main analysis is $E'_e > 11$ GeV, indicated by the arrow.

4.3.3 Non- ep Background

Another source of background are particles not produced by ep interactions of the colliding bunches, the so called *non- ep related background*. Possible sources are particles produced by cosmic rays or by interactions of the HERA beams with beam line elements (*beam - wall interactions*) or residual gas in the beam pipe (*beam - gas interactions*).

The rate of these backgrounds is much larger than the one of DIS events. However they have a different timing, different topologies of energy deposition, and a different distribution of the reconstructed vertices along the z -axis. For this analysis a localised electromagnetic energy deposition above a certain threshold in the SpaCal is required on the first trigger level, which in addition has a timing compatible with an ep interaction. This suppresses most background already at this stage. Further suppression is reached during the analysis, when a reconstructed event vertex is required.

The remaining background can be studied using additional information about the HERA beam bunch structure. Some of the bunches are filled only with one of the two particle species, the e -pilot and p -pilot bunches. Furthermore there are also some completely empty bunches. Any events selected for these special bunches are supposed to be pure background. The total amount of background events in the whole sample is then estimated by scaling the number of selected events for e.g. the p pilot bunches N_{ppil} by the run period averaged ratio of all colliding bunches to all p pilot bunches $\langle n_{coll} \rangle / \langle n_{ppil} \rangle$.

The number of events found in empty and p -pilot bunches was very low, see table 4.2. After reconstruction they did not accumulate in any region of the phase space. A correction would therefore be global and on the level of 0.1%. The effect on the further analysis is therefore negligible.

Bunch Type	$\langle n \rangle$	N	Effect
colliding	175	$1.708 \cdot 10^6$	DIS signal + ep background
empty	25	5.0	global $2.6 \cdot 10^{-5}$, negligible
p -pilot	6	7.3	global $1.2 \cdot 10^{-4}$, negligible
e -pilot	14	454.0	0.3% correction of \mathcal{L} , see section 5.6

Table 4.2: Summary of the average number of different bunch types $\langle n \rangle$ for the 2000 data taking period, the number of DIS events selected N (corrected for trigger prescale), and the effect on the analysis results.

The situation is slightly different for the e -pilot bunches. Here a significant number of events with a total weight of about 450 pass the selection. Figure 4.6 compares a few key distributions of these events to the data events from colliding bunches. It is obvious, that these events behave just like normal DIS ep events and cannot be pure e -gas interactions. This effect was observed before [Beh06] and is explained by non vanishing proton current in the e -pilot bunches. This may happen already at the stage of the beam preparation, if kicker magnets do not efficiently remove single proton bunches.

It is therefore assumed, that these events are not a measure of background, but they are rather treated as normal DIS events. The only sizable effect is a small correction of the total integrated luminosity, which is explained together with other global corrections on section 5.6.

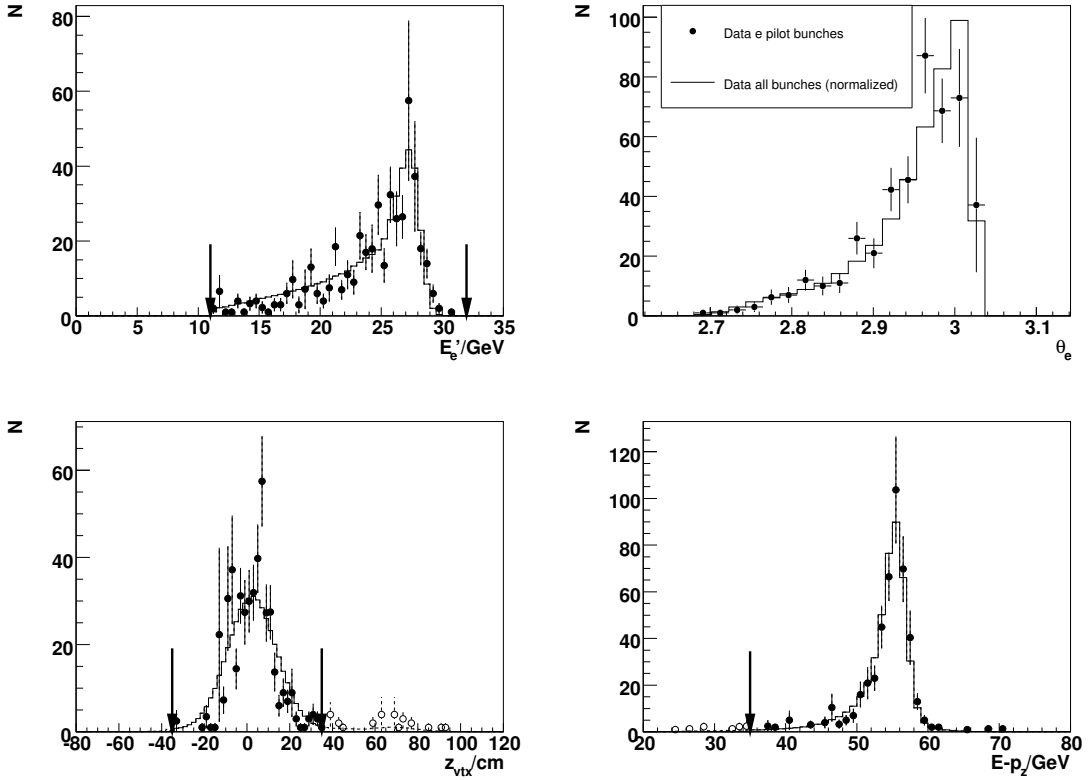


Figure 4.6: Some key distributions of events selected for e -pilot bunches compared to the whole set of selected data events: Energy of the scattered electron E'_e , reconstructed vertex position z_{vtx} , and $(E - p_z)_{tot}$. The latter sample is normalised to the same number of events as the former.

4.4 Covered Phase Space and Resolutions

After introducing the different possible reconstruction methods in section 4.1 and the Monte Carlo tools in section 4.2, this section will discuss the accessible phase space and the precision of different reconstruction methods. The MC events are reconstructed as for the final results, including all adjustments to model the data behaviour which are presented in the coming chapters. Thus the simulated events can be used to realistically evaluate the performance of the kinematics reconstruction. This is done analysing the relative differences of the generated to the reconstructed values, e.g.

$$\Delta x \equiv \frac{x_{rec} - x_{gen}}{x_{gen}}, \quad \Delta y \equiv \frac{y_{rec} - y_{gen}}{y_{gen}}, \quad \Delta Q^2 \equiv \frac{Q_{rec}^2 - Q_{gen}^2}{Q_{gen}^2} \quad (4.14)$$

as a function of the generated values, i.e. here x_{gen} etc. Partially this is also possible using the error propagation on the formulae of section 4.1 directly. The important properties are the *reconstruction bias* and the *reconstruction resolution*. These are defined here as the mean value $\langle \Delta x \rangle_{reco}$ and the 1σ width of a Gaussian fit $\sigma_{reco}(\Delta x)$ to the Δx distribution respectively and analogue for the other kinematic variables y and Q^2 .

In addition to considerations about detector acceptance, available event statistics, and comparability to published results, the properties of reconstruction bias and resolution are the main deciding factors, how the kinematic plane is *divided into bins*. H1 has traditionally chosen an equidistant binning in $\log_{10} Q^2$ and $\log_{10} x$ with a special treatment of the high $y > 0.6$ region [A⁺01, Gla98]. In Q^2 eight bins per decade were chosen, while the x binning has five bins per decade and larger bins at higher x . This will not be altered fundamentally here.

A sensible binning will require that at least the $\pm 1\sigma$ core of the Δ distributions of events generated at the central bin values is contained within this bin. For n equidistant bins per decade in e.g. $\log_{10} x$ the bin with the central value x_c contains the interval $[x_c/w, x_c \cdot w]$ with $w = \sqrt[n]{10}$. Therefore n should be adjusted in a way, that the following requirement is approximately fulfilled:

$$|\langle \Delta x \rangle_{reco}| + \sigma_{reco}(\Delta x) \lesssim \frac{100\%}{2} \left(\sqrt[n]{10} - 1 \right). \quad (4.15)$$

For this study *precision* is thought of as *resolution* on an event-by-event basis. Effects of the residual systematic errors, i.e. uncontrolled shifts of the mean values for the total sample are considered much later in section 7.5.

4.4.1 Electron Method

Analytically the error propagation from the formulae 4.1 and 4.2 gives

$$\frac{\delta y_e}{y_e} = \frac{1 - y_e}{y_e} \left(\frac{\delta E'_e}{E'_e} \oplus \frac{\delta \theta_e}{\tan \theta_e / 2} \right) \quad (4.16)$$

$$\frac{\delta Q_e^2}{Q_e^2} = \frac{\delta E'_e}{E'_e} \oplus \tan \theta_e / 2 \cdot \delta \theta_e. \quad (4.17)$$

The uncertainties depend of course on the deviations of the measured input values E'_e and θ_e which are given here by $\delta E'_e$ and $\delta \theta_e$, respectively.

Most Q^2 reconstruction schemes tend to deteriorate in their relative precisions as $\theta_e \rightarrow 180^\circ$. But at least for this analysis the prefactor is typically not that large, $\tan \theta_e / 2 < 20$, and the angular measurement is rather precise, $\delta \theta_e \sim 10^{-3}$, so this part is not critical.

The uncertainty of the electron energy measurement is usually small, $\delta E'_e / E'_e \sim 2\%$, but still give the only sizable effect in Q_e^2 , which is well measured to a corresponding $\sim 2\%$ throughout the kinematic plane. The y_e and therefore as well the x_e measurement suffers $\propto 1/y$ at low y , while it actually improves $\propto (1 - y)$ at high y . The reason can be qualitatively understood from figure 4.1: for the kinematic peak region, which constitutes a large part of the accessible phase space, differences in y or x are determined by tiny differences in E'_e .

The results in figure 4.7 show the basically bias free measurement of Q_e^2 with a resolution of typically $\sim 4\%$. The choice of eight bins per decade in Q^2 is conservative, as this requires according to equation 4.15 corresponding values below 17%.

The reconstruction performance in x_e (and y_e) depends as expected strongly on y . For $y > 0.1$ the reconstruction is nearly bias free, while below $y < 0.05$ the reconstruction bias is so large, that the method is virtually unusable. The resolution

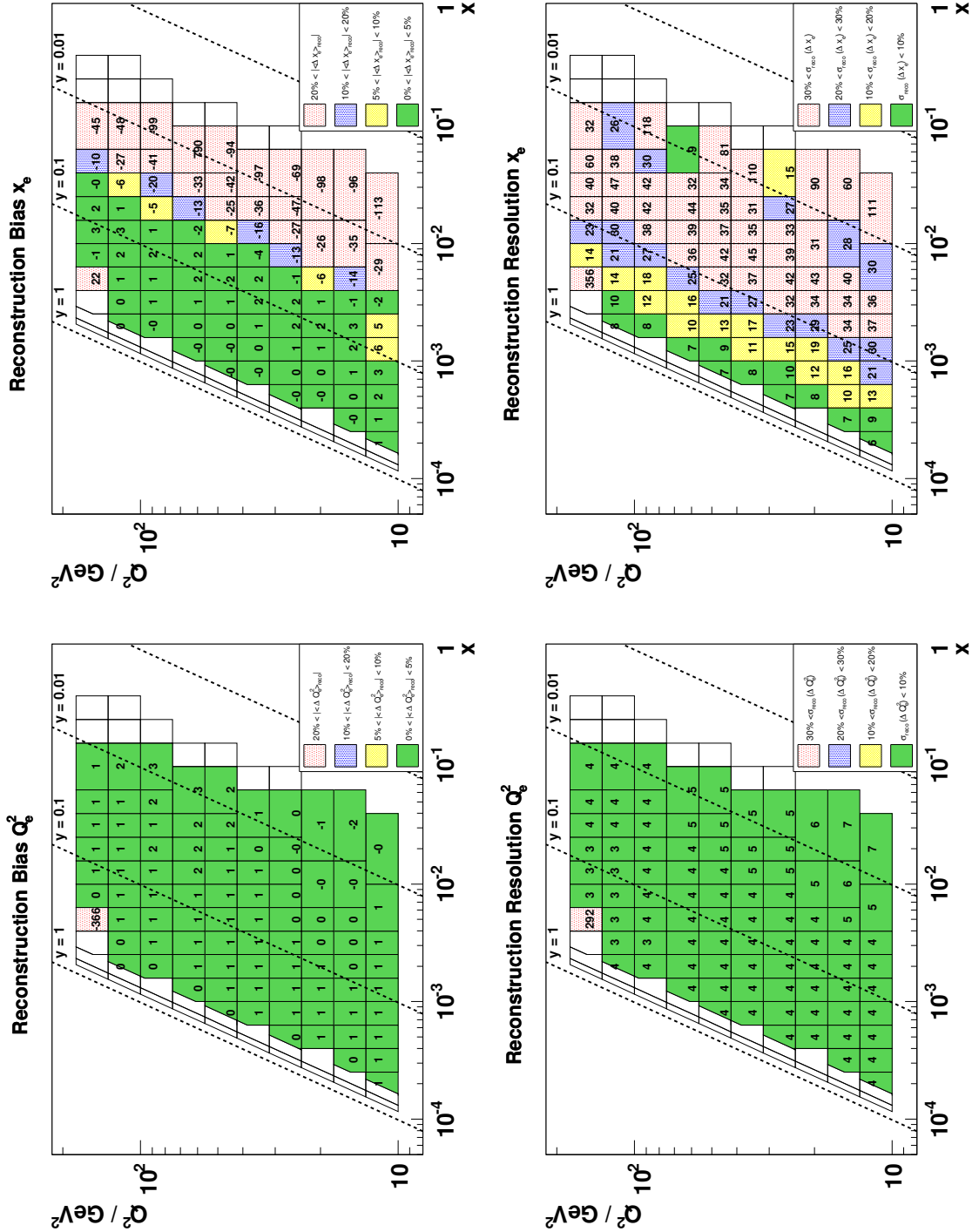


Figure 4.7: Results for reconstruction bias and resolution of the Electron Method derived from MC Δx_e and ΔQ_e^2 distributions by Gaussian fits as a function of the generated point $(x, Q^2)_{\text{gen}}$ on the kinematic plane.

in x_e is as well excellent with about 10% at $y \sim 0.5$ and degrades to 25% at $y \sim 0.1$. This then also defines the border, where the electron method is usable: for 5 bins per decade in x equation 4.15 demands resolution and bias values below 29%.

4.4.2 Σ Method

Analytically the error propagation from the formulae 4.10 and 4.11 gives

$$\frac{\delta y_\Sigma}{y_\Sigma} = (1 - y_\Sigma) \left(\frac{\delta(E - p_z)_{tot}}{(E - p_z)_{tot}} \oplus \frac{\delta E'_e}{E'_e} \oplus \frac{\delta \theta_e}{\tan \theta_e/2} \right) \quad (4.18)$$

$$\frac{\delta Q_\Sigma^2}{Q_\Sigma^2} = y_\Sigma \cdot \frac{\delta(E - p_z)_{tot}}{(E - p_z)_{tot}} \oplus (1 - y_\Sigma) \cdot \frac{\delta E'_e}{E'_e} \oplus \tan \theta_e/2 \cdot \delta \theta_e. \quad (4.19)$$

Here in addition to the error sources present for the Electron Method, the uncertainty of $(E - p_z)_{tot}$ given by $\delta(E - p_z)_{tot}$ has to be considered. Typically its relative precision is worse than for E'_e and θ_e . The results are shown in figure 4.8.

The Q_Σ^2 reconstruction is slightly worse than for Q_e^2 because of the $(E - p_z)_{tot}$ influence. This statement holds especially for higher $y > 0.2$. At medium and low $y < 0.2$ the reconstruction is comparable to Q_e^2 , rather bias free and with a reasonable resolution of $\sim 6\%$.

The x_Σ reconstruction is biased with the current treatment of the HFS in the higher $y > 0.1$ region to about 10%. The resolution is very even across the kinematic plane and typically $\sim 15\text{--}25\%$ in the range $0.01 < y < 0.6$ and then rapidly degrades below $y < 0.01$. For the determination of the accessible kinematic range and the bin width it is therefore the main point to consider. While resolution and bias values of the order 30% are well matched with five x bins per decade according to equation 4.15, this value is exceeded at low y . The binning therefore combines two or three of the basic bins at lower $y \sim 0.01$ to provide a reasonable measurement.

4.4.3 Alternative Reconstruction Schemes

The alternative $e\Sigma$ and PT reconstruction schemes mentioned before provide a reasonable reconstruction throughout the kinematic range considered here, as expected. The PT Method reconstructs x_{PT} with similar properties as x_Σ , while Q_{PT}^2 is especially well reconstructed at low y and higher Q^2 . The properties of the $e\Sigma$ -method are by construction similar to the electron method for $Q_{e\Sigma}^2$ and similar to the Σ method for $x_{e\Sigma}$ as shown in the figures 4.7 and 4.8. Therefore the reconstruction properties at high y are not optimal.

4.4.4 Acceptance and Phase Space

The kinematic phase space for this measurement is limited by several factors, which are illustrated in figure 4.9:

- The selection on the minimum scattered electron energy $E'_e > 11$ GeV, which is chosen to fully cover the range $y < 0.6$, but exclude the region of high photoproduction and difficult electron identification.

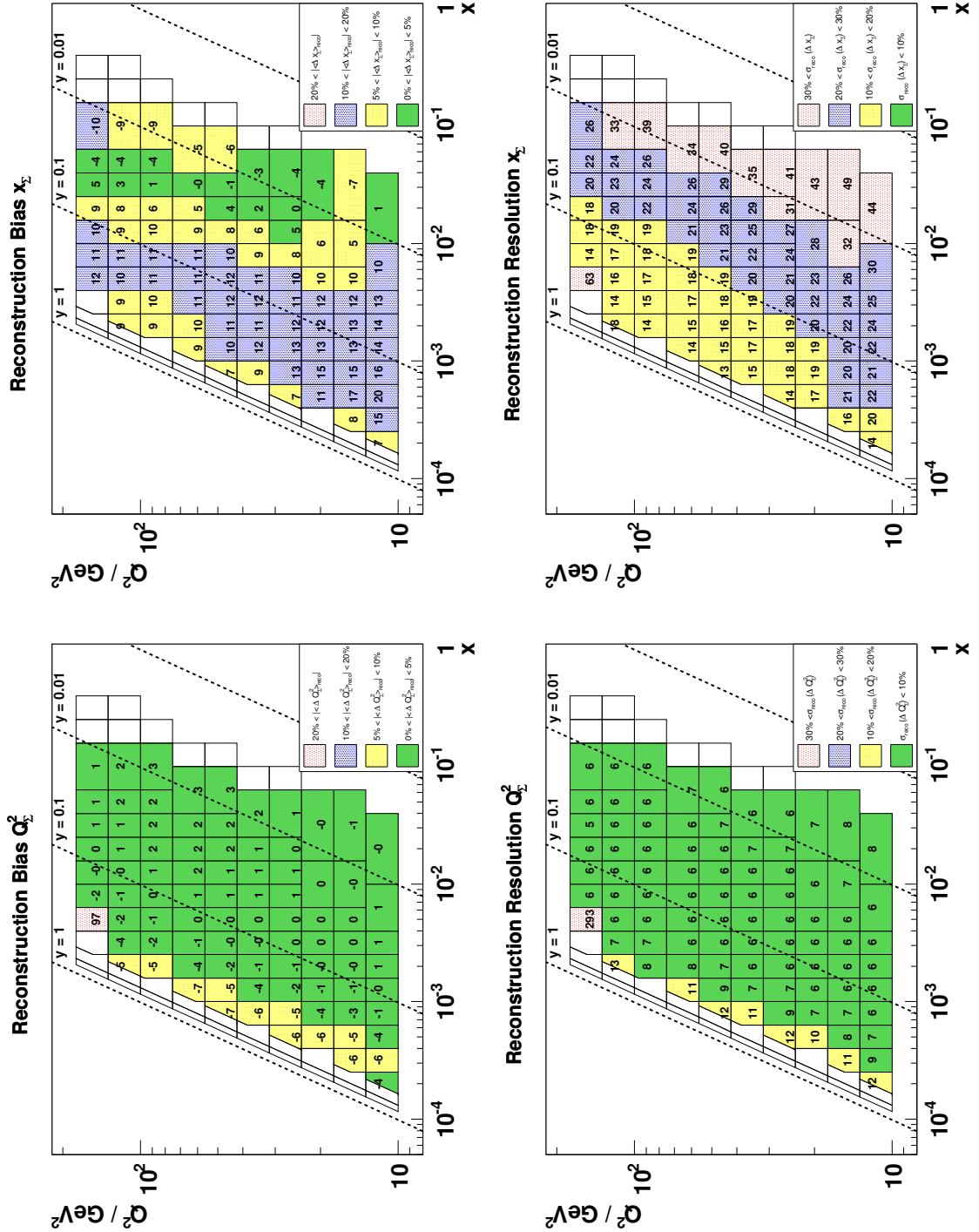


Figure 4.8: Results for reconstruction bias and resolution of the Σ Method derived from MC Δx_e and ΔQ^2 distributions by Gaussian fits as a function of the generated point $(x, Q^2)_{\text{gen}}$ on the kinematic plane.

- The requirement to detect the scattered electron in the SpaCal, which limits the polar angle to approximately $\theta_e > 155^\circ$ and therefore the measurement to $Q^2 < 120 \text{ GeV}^2$ ⁴.
- At high θ_e the acceptance limit of the SpaCal is not exploited fully. The limitation here stems more from the possibility to reconstruct the event vertex and the trigger setup. The region up to $\theta_e < 173^\circ$ is used, which corresponds roughly to $Q^2 > 10 \text{ GeV}^2$.
- At low y the acceptance is limited by a reasonable containment of the HFS, quantified by $\gamma_h > 5^\circ$ and, mostly equivalent, by a minimal amount of hadronic activity which is guaranteed by $W > 20 \text{ GeV}$.

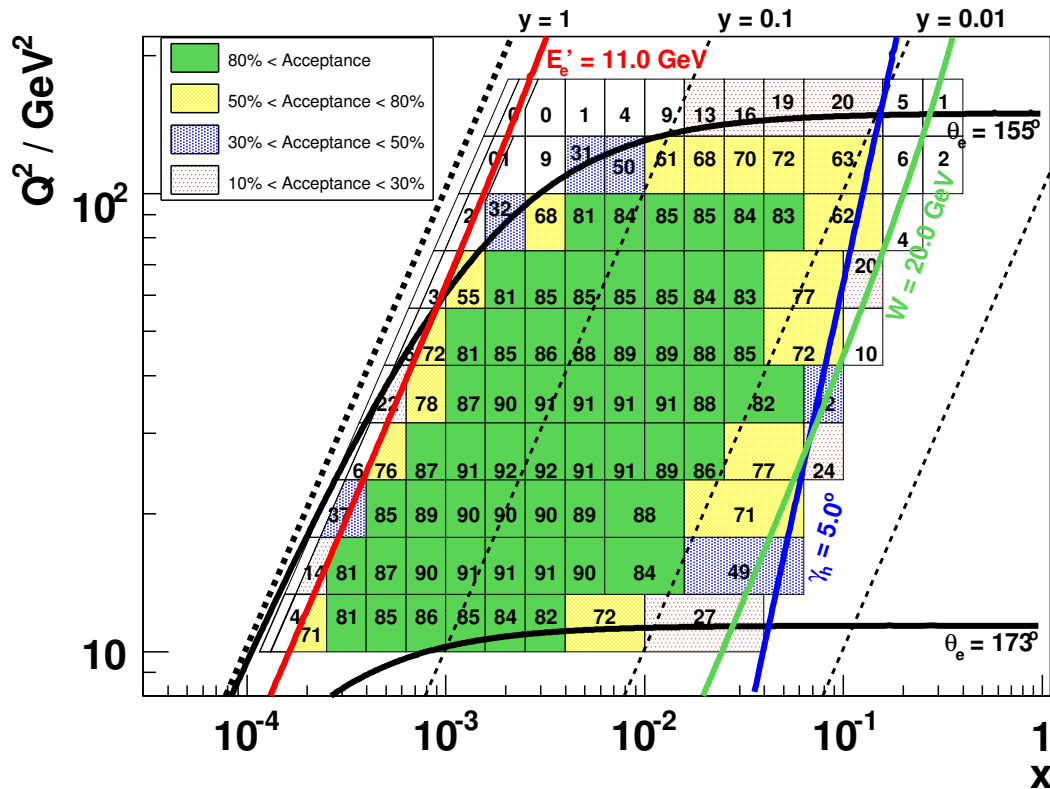


Figure 4.9: Acceptance of this analysis in the (x, Q^2) plane due to selection criteria imposed on the data on the scattered electron energy $E_e' > 11 \text{ GeV}$, detection of the electron in the backward region defined by its scattering angle θ_e , and HFS detection in the central detector quantified by γ_h and W .

⁴ The discussion in the following is slightly simplified here with respect to the θ_e acceptance limits: the numerical values quoted correspond to events from the nominal interaction point $z_{vtx} = 0$, while in reality events from the range $|z_{vtx}| < 35 \text{ cm}$ are accepted. This z_{vtx} distribution is correctly implemented in the MC, see section 5.5, and therefore the calculated acceptance takes it into account.

In figure 4.9 the acceptance A binned according to the generated kinematic is shown. It is defined here as

$$A = \frac{N_{\text{rec cuts}}^{\text{gen}}}{N_{\text{no cuts}}^{\text{gen}}}, \quad (4.20)$$

where $N_{\text{no cuts}}^{\text{gen}}$ is the number of events generated in a bin by the DJANGO generator without any cuts imposed and $N_{\text{rec cuts}}^{\text{gen}}$ are the number of events passing the reconstruction level cuts. This definition does not consider wrong reconstruction and smearing effects, which are later quantified by the *Purity* and *Stability* in section 7.3. It is obvious, that in the bulk of the measurement the acceptance is very high at $A \sim 80 - 90\%$, while it starts dropping rapidly below the limits discussed above.

Another point for the acceptance is the ability to reconstruct the event vertex for a precise determination of θ_e and the rejection of background. Conceptually it would be best to measure the event vertex from the scattered electron only, as this way the measurement is truly inclusive and independent of the simulation of the HFS. Three methods are in principle available for this, using the Central tracker, BST or the CIP, respectively.

Using the Central Tracker the vertex can only be reconstructed from electrons with $\theta_e < 165^\circ$, corresponding to $Q^2 > 50 \text{ GeV}^2$. Explicitly requiring a reconstructed electron track needs efficiency corrections of $\sim 5\%$ [Gla07], as the MC simulation is not setup to properly describe tracks at the edge of the CJC with a short length. Therefore by default the determination of the event vertex uses all available tracks, i.e. also the HFS. Most DIS events with $\gamma_h > 15^\circ$ have several charged particle tracks from the HFS in the central region and for such events this is the most precise measurement available.

The BST provides a very precise measurement independent of the HFS. It is most effective at high $\theta_e > 164^\circ$ and therefore at lower $Q^2 < 50 \text{ GeV}^2$. It has been shown, that a precise description of the BST efficiency to better than 2% is challenging [Lař04]. Furthermore the performance during the long data taking period in 2000 was rather variable. That is why the BST will only be used as a tool to control other detector and reconstruction efficiencies in this analysis.

The CIP is effective for approximately $\theta_e < 171^\circ$, so it covers most of the measurement range starting from $Q^2 > 20 \text{ GeV}^2$. It provides only a coarse measurement without much redundancy due to its two layer structure, but still can be used to increase the vertex reconstruction efficiency in the low y region significantly.

An illustration of two typical DIS events in the kinematic range of this measurement is given in figure 4.10.

4.5 Cross Section and Structure Functions

The measurement of the cross section is performed in bins of x and Q^2 , which are the appropriate variables, as the structure function F_2 is usually quoted in terms of these. The relative resolutions were seen to be rather constant over most of the accessible kinematic range, if an appropriate reconstruction method is chosen. This justifies the chosen equidistant binning in $\log_{10} x$ and $\log_{10} Q^2$ with five and eight bins per decade respectively. The numerical values are summarised in table 4.3 and correspond to the previous H1 publication covering this kinematic range [A⁺01].

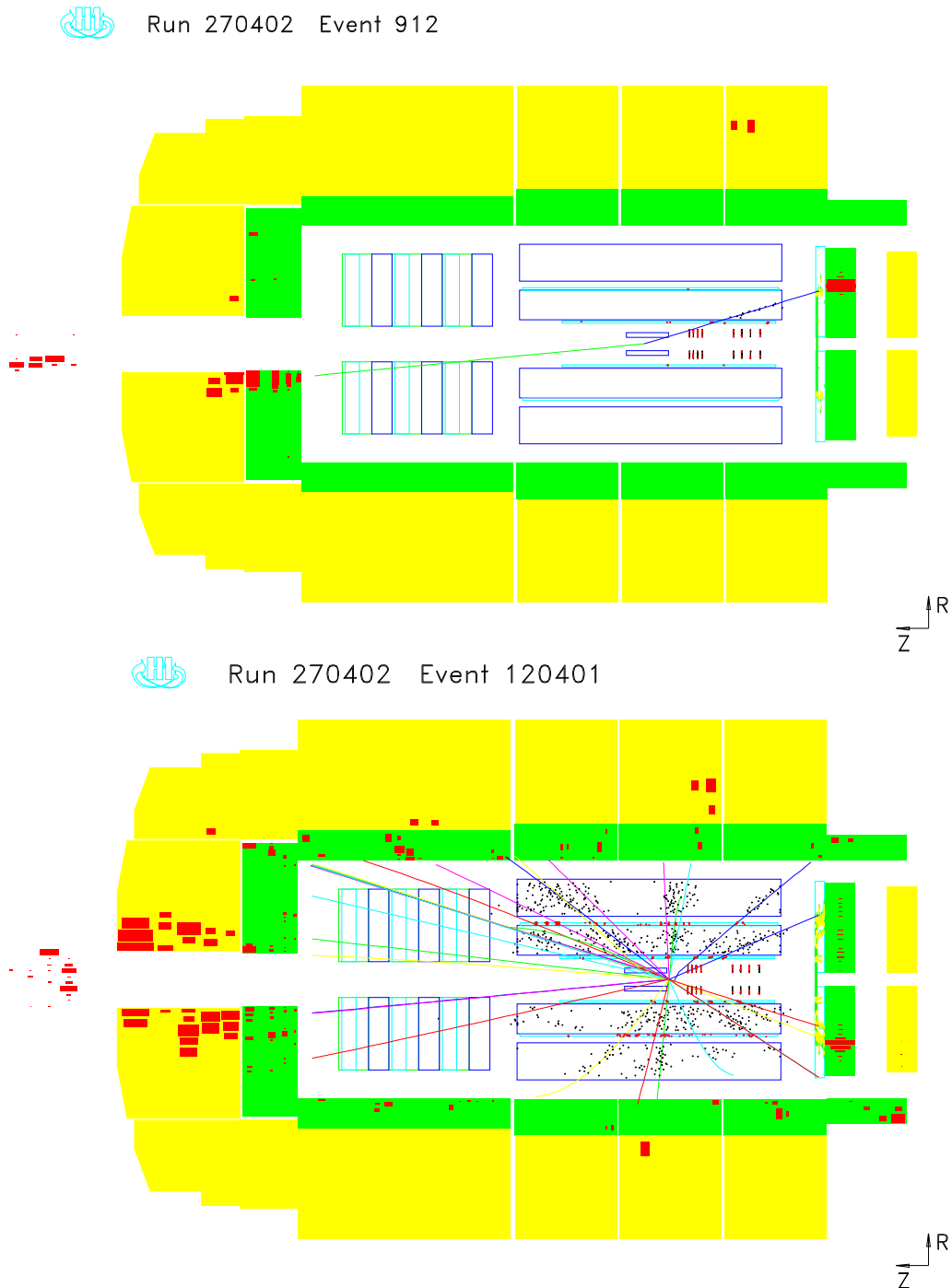


Figure 4.10: Displays of two DIS events as seen by the H1 detector, both with a clear scattered electron in the SpaCal. The top panel shows a typical low y event, which is reconstructed using the Σ Method ($y_{\Sigma} = 0.0050$, $Q_{\Sigma}^2 = 63 \text{ GeV}^2$, $x_{\Sigma} = 0.13$). Here the HFS is detected just on the forward inner edge of the H1 calorimeter and the event vertex is reconstructed by the electron track in the Central Tracker. The lower panel shows a typical high y event, which is reconstructed using the Electron Method ($y_e = 0.52$, $Q_e^2 = 51 \text{ GeV}^2$, $x_e = 0.00097$). Tracks and clusters from the HFS fill the whole polar angle range.

Bin Boundaries Q^2/GeV^2							
10.00	13.34	17.78	23.71	31.62	42.17	56.23	74.99
100.0	133.4	177.8					
Bin Centres Q_c^2/GeV^2							
12.	15.	20.	25.	35.	45.	60.	90.
120.	150.						
Bin Boundaries x							
	0.000158	0.000251	0.000398	0.000631			
0.00100	0.00158	0.00251	0.00398	0.00631			
0.0100	0.0158	0.0251	0.0398	0.0631			
0.100	0.158						
Bin Centres x_c							
	0.00020	0.00032	0.0005	0.0008			
0.0013	0.0020	0.0032	0.005	0.008			
0.013	0.020	0.032	0.05	0.08			
0.13							

Table 4.3: Standard bin boundaries and central values in Q^2 and x . At low $y \sim 0.01$ several bins are combined, while the high $y > 0.6$ region is fully excluded. See text and graphical representation in e.g. figure 4.8.

The region at high $y > 0.6$ is completely excluded from this analysis. The treatment of the (x, Q^2) bins at the border of the two binnings is shown in the kinematic plane plots as e.g. figure 4.8.

As shown in the last section the resolution degrades significantly at the acceptance edge near $y \sim 0.01$. Therefore the last two bins with good acceptance are combined and the former bin boundary between the two bins is taken as new central value. In the three lowest Q^2 bins the situation is slightly worse and therefore two larger bins are built from two or three basic bins respectively. The treatment is slightly modified compared to the one used in [A⁺01], which used the larger y bins for all values of Q^2 .

The cross section measurement is in principle performed using the integrated luminosity \mathcal{L}_{Data} and the number of events collected in a bin N_{Data} according to the relation $\sigma = N_{Data}/\mathcal{L}_{Data}$. However various corrections have to be applied and one ends up with

$$\frac{d^2\sigma(x, Q^2)}{dx dQ^2} = \frac{N_{Data} - N_{\gamma p} - N_{BG}}{A \cdot \mathcal{L}_{Data}} \cdot \frac{1}{\epsilon} \cdot \frac{1}{1 + \delta_{RC}} \cdot c_{BC}. \quad (4.21)$$

The single items here are

- $N_{\gamma p}$ the number of photoproduction events in the bin taken from the PHOJET MC simulation,
- N_{BG} the number of events due to other (non- ep) background,
- A the detector acceptance, which is quantified using the DJANGO MC simulation as $A = N_{rec}^{MC}/N_{gen}^{MC}$, see section 4.4.4,

- ϵ extra efficiency corrections not included in the MC
- δ_{RC} the effect of radiative corrections on the Born level cross section $\delta = \sigma_{rad}^{MC} / \sigma_{Born}^{MC} - 1$, where σ_{rad}^{MC} and σ_{Born}^{MC} are bin integrated full and Born level cross sections respectively taken from MC simulation or analytical programs as used in section 4.2.4,
- c_{BC} the so called *bin centre correction*, which transforms the *bin integrated* value to the double differential value at the chosen bin centre (x_c, Q_c^2) . It can be derived from MC as $c_{BC} = \frac{d^2\sigma^{MC}(x_c, Q_c^2)}{dx dQ^2} / \sigma_{Born}^{MC}$.

It is possible to perform the acceptance, bin centre, and radiative corrections using the Monte Carlo directly, as DJANGO contains all radiative effects. Exploiting

$$N_{gen}^{MC} = \mathcal{L}^{MC} \sigma_{rad}^{MC}, \quad (4.22)$$

one obtains the formula to determine the cross section via the *Monte Carlo Method*

$$\frac{d^2\sigma(x, Q^2)}{dx dQ^2} = \frac{N_{Data} - N_{\gamma p} - N_{BG}}{N_{rec}^{MC}} \cdot \frac{\mathcal{L}^{MC}}{\mathcal{L}_{Data}} \cdot \frac{1}{\epsilon} \frac{d^2\sigma^{MC}(x, Q^2)}{dx dQ^2}. \quad (4.23)$$

The main work of this thesis is to compare and adjust in detail the individual components of equation 4.21. Eventually the Monte Carlo method 4.23 is used to calculate the cross sections.

The Monte Carlo input cross section $\frac{d^2\sigma^{MC}(x, Q^2)}{dx dQ^2}$ should be as close as possible to the measured one in order not to influence the result. The reliability is checked by iterating the procedure at least once, reweighting the input MC events to the measured cross section from the iteration before. Effects are found to be well below 1%, so one iteration is enough to ensure convergence.

Typically instead of calculating σ , the *reduced cross section* σ_r will be used as defined in equation 2.7. At low enough y , σ_r is mostly equivalent to the structure function F_2 . In the range considered here it is justified to perform a small correction using a theoretical calculation of the longitudinal structure function F_L to obtain

$$F_2(x, Q^2) = \sigma_r(x, Q^2) + \frac{y^2}{Y_+} F_L(x, Q^2). \quad (4.24)$$

Here F_L will typically be a prediction by a QCD fit, as no direct F_L measurement in the kinematic domain considered is available yet.

Chapter 5

Data Selection and Treatment

In this chapter the basic selection criteria for the data will be explained and motivated. This covers both online and offline criteria. As both H1 and HERA are complex systems, technical problems occur from time to time. With the goal of a final precision of the order 1%, the data with bad performance of either H1 or HERA have to be excluded. Finally some studies of effects that influence the measured cross section as a single normalisation constant are presented.

5.1 Data Sample and Run Selection

The work described in this thesis is concentrated on the data taken with the H1 detector in the year 2000, only chapter 8 deals with the data taken in the years 1996/97. Throughout the year 2000 the general data taking conditions have been stable, so no subdivision into different periods is necessary.

The operation cycle of the HERA accelerator divides the H1 data set into *luminosity fills*. These are characterised by using the same electron and proton beams and therefore similar beam related properties. The *life time* of the electron beam limits the duration of a luminosity fill to about 12 hours. The H1 data acquisition system splits the data further into *runs*, which have a duration of few minutes to about one hour and contain typically 10,000 – 100,000 events. For a single run the detector setup and online event selection conditions are stable, while e.g. between the runs often the prescales of subtriggers are adjusted. The *Luminosity Fill Number* and the *H1 Run Number* are used to specify the time at which an event was recorded. If technical problems are found, some runs or even whole fills can be excluded from the analysis.

Before the detailed analysis starts, a run and event selection is performed on the basis of the following standard criteria:

- **Trigger Phase.** When HERA brings the beams into collision, but has not yet finished the beam steering, H1 already starts data taking. This data is classified as trigger phase 0 and excluded from the analysis. Furthermore all except a few phase 1 runs, which are taken just after the start of the luminosity fill, are rejected by the requirement on the trigger prescales.
- **Run Quality.** If a major system of H1, like the CJC, SpaCal, or LAr Calorimeter were not in operation or the data quality was found to be bad

in offline checks, a run may be declared as *poor*. Such runs are excluded from the analysis. Furthermore short runs with a total luminosity of less than 0.1 nb^{-1} are excluded.

- **High Voltage and Readout Status.** The subcomponents of H1 can be operated independently of each other. However it is obvious, that the information provided by each component, which should be used in the analysis has to be read out, otherwise runs are not considered. The systems which are checked for this analysis are the CJC1+2, LAr, SpaCal, BDC, CIP, COP, CIZ, TOF, and Luminosity system. In addition the high voltage of all these subdetectors should be on the nominal value. This is monitored permanently and saved for each recorded event, which can later be individually rejected from the analysis. A typical situation is e.g. a sudden increase of background, which triggers the safety mechanism of a gas amplification track detector like the CJC. In turn the high voltage is lowered quickly and raised only after some minutes back to the nominal value. The luminosity is corrected and an additional rejection of runs is performed, in which this correction exceeds $1/3$ of the luminosity in this run.
- **Trigger Prescale.** This analysis uses events collected by three subtriggers (S0, S3, and S9), which are typically prescaled. The properties of these subtriggers and the method used for correcting for the prescales are discussed in detail in section 5.3. In order to reduce statistical fluctuations the maximum allowed prescales of the triggers are limited to 20 for S3 or S9, and 40 for S0. This selection reduces the available luminosity by nearly 40%. This can also be seen in figure 5.1. The reason is, that in the year 2000 highest priority was not given to the inclusive triggers and other subtriggers were allowed to take more of the limited bandwidth. Some analysis steps, for example the SpaCal calibration in section 6.1, can be performed without requiring events to be triggered by an inclusive trigger and therefore this part of the run selection is not performed there.

The run range considered was 262144 - 279215 and some short periods excluded in addition to the above criteria are summarised in table 5.1. The data selected for analysis according to the listed criteria corresponds to an integrated luminosity of 27.52 pb^{-1} before prescale correction.

5.2 Event Reconstruction and Selection

For most of the results presented in this thesis data or MC events are required to pass a set of *selection cuts* on reconstructed quantities. Often these cuts are varied to study more specific details, but they are typically similar to the *standard event selection* summarised in table 5.2. Overall the selection is kept rather simple to avoid uncontrolled losses not described in the simulation. In the following the reconstruction steps are explained in more detail, if they are specific to this analysis and not included into the standard H1 reconstruction software.

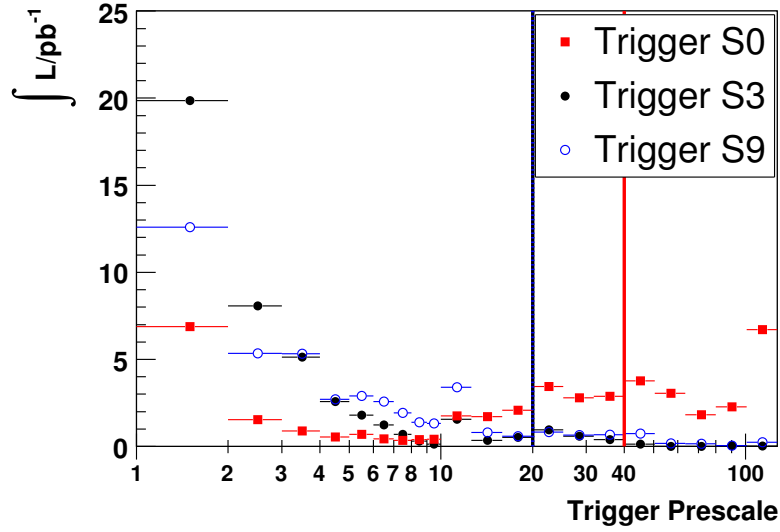


Figure 5.1: Integrated luminosity \mathcal{L} recorded by H1 differentiated by the applied prescale on the trigger conditions S0, S3, S9. The selection of runs with prescales of less than 20 for S3 or S9, and less than 40 for S0 is indicated.

5.2.1 SpaCal

The scattered electron is identified by an electromagnetic cluster in the SpaCal as explained in section 4.3.1. The *cluster energy*, calculated as a sum of all its cells as found by the clustering algorithm [Sch96a], is usually required to be in the range $11 \text{ GeV} < E'_e < 32 \text{ GeV}$. Another important property of the cluster is its *centre of gravity*, i.e. its position, in the xy -plane. This is calculated as a weighted sum over the positions of all contained cells i

$$\vec{r} = \frac{\sum_i w_i \vec{r}_i}{\sum_i w_i}, \quad (5.1)$$

where the weights w_i of the individual cell centres \vec{r}_i are determined using their energies E_i according to a logarithmic scheme [A⁺92]

$$w_i = \max \left(0, w_0 + \ln \frac{E_i}{\sum_i E_i} \right). \quad (5.2)$$

The *cutoff parameter* $w_0 = 4.8$ excludes cells below a certain energy threshold from the calculation. This weighting scheme has been shown to give the best results for the position reconstruction [Pös96].

As the SpaCal has no longitudinal segmentation, no information on the lateral shower shape is available. The z -position of the shower centre is calculated using a parametrisation depending mostly on the energy of the cluster [SZ96]

$$z_{\perp} / \text{cm} = 0.001956 \cdot E'_e / \text{GeV} + 0.8529 \cdot \ln(2479 \cdot E'_e / \text{GeV}) \quad (5.3)$$

The quantity z_{\perp} is the penetration depth of a particle with normal incidence on the SpaCal surface and is translated to the z -coordinate of the cluster using an approximation of the incidence angle and the surface location.

Run Numbers	Reason for exclusion
278687 - 278978	Special runs with <i>shifted vertex</i>
265660 - 265709 267315 - 267325 269384 - 269519	low BDC efficiency
269310, 274836, 276911, 279162	other BDC readout problem
277448 - 277456	Fill 2553: many events in <i>p</i> -pilot bunches
264235, 264236, 264237, 264415 270638 - 270660 271207 - 271222 271672, 272683 - 272776 272852 - 272867	L2TT Trigger problems, see sec. 5.3.2

Table 5.1: Summary of the H1 runs excluded from the analysis of the year 2000 data in addition to the general selection criteria given.

In addition the cluster must satisfy a set of properties to reduce background from hadrons. Firstly, if the cluster is close to the beam pipe hole in the calorimeter, the energy collected in the adjacent veto cells is required to be $E_{veto} < 1$ GeV. This condition however is never an issue for the kinematic range considered here. Next, the energy collected behind the cluster in the hadronic section of the SpaCal is required to be less than 15% of the total cluster energy, i.e. $E_{had}/E'_e < 0.15$. Finally, the transverse shower size should be sufficiently small to reject hadrons whose showers are usually broader. Therefore a *cluster radius* is calculated using the same logarithmic weighting scheme as in equation 5.2

$$r_{log} = \sqrt{\frac{\sum_i w_i (\vec{r}_i - \vec{r})^2}{\sum_i w_i}}. \quad (5.4)$$

In [Gla98] it was shown that this definition is mostly independent of the impact point on the SpaCal surface. However, the fast shower parametrisation [GRP90] used in the MC simulation is known to describe the transverse shower shape not optimally. Therefore different cutoff parameters w_0 are used, $w_0^{DATA} = 4.85$ and $w_0^{MC} = 5.05$, to obtain more similar r_{log} distributions for signal DIS electrons. A selection criterion of $r_{log} < 4$ cm is imposed for the electron cluster.

The relevant distributions of E_{had}/E'_e and r_{log} are shown in figure 5.2.

5.2.2 Electron Tracking in the Backward Detectors

As mentioned before, no explicit track reconstruction for the electron is required in the Central Tracker, as this does not cover the whole kinematic range, lowers the efficiency, and the efficiency loss needs an additional correction in the MC.

However by default a track segment in the BDC is required. The reconstruction is performed using the *BDC LEpton Validator* algorithm (BDCLEV) [GW98]. It starts from the line connecting the SpaCal cluster and the central vertex as an initial approximation. The scattered electron azimuthal angle ϕ_e is taken from the SpaCal cluster centre of gravity and is used to transform the BDC measurements from the

Reconstructed Quantity	Subdetector	Short Explanation
$11 \text{ GeV} < E'_e < 32 \text{ GeV}$	SpaCal	DIS $y < 0.6$, $Q^2 < 150 \text{ GeV}^2$
$E_{veto} < 1 \text{ GeV}$	SpaCal	Avoid leakage
$E_{had}/E'_e < 0.15$	SpaCal	γp background reduction
$r_{log} < 4 \text{ cm}$	SpaCal	γp background reduction
$N_{BDC}^{Hit} \geq 4$	BDC	precise θ_e , γp backgr. reduction
$\Delta r_{SpaBDC} < 2.5 \text{ cm}$	SpaCal/BDC	
Fiducial Cut x_{BDC} / y_{BDC}	BDC	
$ z_{vtx} < 35 \text{ cm}$	CT or CIP	precise θ_e , non- ep backgr. reduct.
$\Delta z_{vtx} < 8 \text{ cm}$ or $N_{CIP}^{Hit} \geq 1$	CT/CIP	
$(E - p_z)_{tot} > 35 \text{ GeV}$	comb. HFS	γp background and ISR reduction
$p_{t,HFS}/p_{t,e} < 0.3$	comb. HFS	Well reconstructed HFS
$Q_e^2 > 10 \text{ GeV}^2$	combined	Analysis phase space
elastic QED Compton	SpaCal	Not in MC model

Table 5.2: Summary of the cuts on reconstructed quantities applied to select DIS events in the phase space of interest. Details about the origin of the quantities are explained in the following subsections.

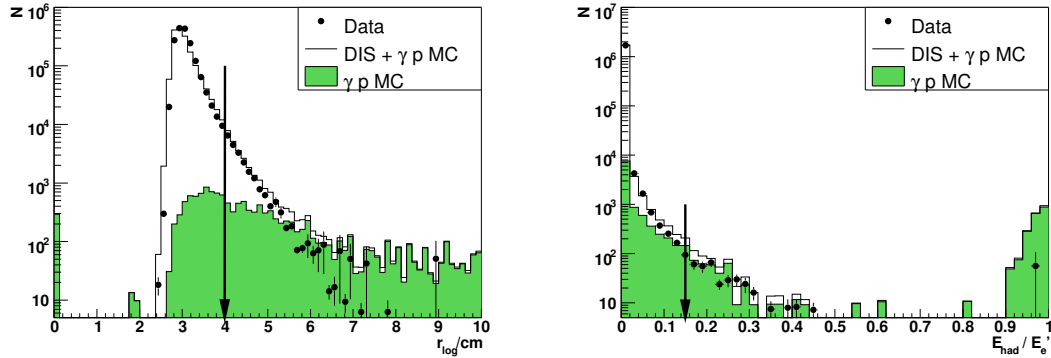


Figure 5.2: Basic SpaCal cluster properties and selection cuts imposed for background rejection denoted by an arrow.

component along the wire to the H1 coordinate system. Only the BDC hits in the octants containing ϕ_e are used for the reconstruction.

The electron scattering angle θ_e is determined in a minimisation procedure. A least squares track fit combines the central vertex, the SpaCal cluster coordinates, and all BDC measurements (with a two-fold drift direction ambiguity) in a corridor of variable size Δr around the current best estimate of the track direction. Initially, the corridor has 5 cm size. It is gradually reduced with improved track parameters to ~ 5 times the BDC resolution of about $300 \mu\text{m}$. The SpaCal cluster is considered to be linked to the BDC track segment if there are at least $N_{BDC}^{Hit} \geq 4$ hits from the 8 layers remaining at the final iteration. Furthermore the distance of the reconstructed BDC track extrapolated to the z position of the SpaCal cluster should be $\Delta r_{SpaBDC} < 2.5 \text{ cm}$. Fiducial cuts are performed on this position in (x_{BDC}, y_{BDC}) after performing a small correction for beam tilt and offset. Together with the Cen-

tral Tracker vertex the electron scattering angle θ_e is measured precisely using the BDC information.

As an alternative the track reconstruction is possible in the BST, which is in this work used to perform cross checks and efficiency studies. Here only the information from the r -strip detectors is used. The reconstruction starts with the SpaCal cluster. The hits in three ϕ sectors corresponding to the azimuthal location of the cluster ϕ_e are considered, which are converted into the H1 beam system. The r coordinate of each BST hit in the selected sector is projected along the line connecting the hit and the SpaCal cluster to the outermost BST plane. A clustering of the projected hits in this plane is then used as an initial approximation for the track finding. Using an iterative minimisation technique with robust rejection of outliers, similar to the BDC reconstruction, all selected hits are included into a least squares minimisation. The contribution of each hit is weighted with an exponential suppression factor, which depends on the distance from the hit to the track, and on an additional parameter, which defines the width of an effective corridor around the track. For the first iteration, the width of the corridor is equal to the SpaCal spatial resolution. It is gradually reduced until it reaches $250\ \mu\text{m}$. A successfully reconstructed track has to have at least hits in $N_{BST}^{Hit} \geq 3$ out of usually 4 planes in the acceptance. Furthermore the distance of the reconstructed BST track extrapolated to the z position of the SpaCal cluster should be smaller than $\Delta r_{SpaBST} < 1.0\ \text{cm}$. In addition to the electron scattering angle θ_e also the location of the event vertex z_{vtx} is measured. The advantage of this procedure is, that these measurements are completely independent of the determination using the Central Tracker vertex and the BDC.

5.2.3 Event Vertex

The length of the proton bunches in z determines the luminous region in the H1 interaction region. It is approximately a Gaussian with a width of $\sigma_z \sim 10\ \text{cm}$ with a maximum close to zero. Therefore a reconstructed event vertex in the region $|z_{vtx}| < 35\ \text{cm}$ is required. By default the *primary vertex* reconstructed by the Central Tracker (CT) is used, if the estimated precision is better than $\Delta z_{vtx} < 8\ \text{cm}$. This requirements rejects badly (and most probably wrongly) reconstructed events. Secondary vertices and Forward Tracker vertices, which are also provided by the H1 software are not considered.

If no *central vertex* is available, typically due to the lack of tracks from the HFS for low y events, the CIP is used to reconstruct the event vertex. The algorithm used here is derived from the one used for the BST reconstruction. The initial approximation is defined using the *default vertex*, i.e. the average event vertex of the current run or the simulation in the MC respectively, and the SpaCal cluster. The CIP information is provided in *pad hits*, which are organised in two layers and therefore are located at two radii. Only CIP hits from the 2 ϕ octants closest to the azimuthal location of the cluster ϕ_e are considered, which are converted into the H1 beam system. The further algorithm is equivalent to the one used for the BST. If at least a hit in $N_{CIP}^{Hit} \geq 1$ out of the two possible layers is associated to the electron, the event has a *reconstructed CIP vertex*, which is used in the same way as the *central vertex*. It is also used in the BDC reconstruction.

5.2.4 Hadronic Final State

The standard selection requires $(E - p_z)_{tot} > 35$ GeV to reduce radiative effects and the contribution from photoproduction. To ensure a well reconstructed HFS, the transverse momentum should be reasonably balanced with the one from the electron, thus $p_{t,HFS}/p_{t,e} > 0.3$ is required. While the contribution of the electron to $(E - p_z)_{tot}$ is rather simple to calculate, the hadronic contribution $(E - p_z)_{HFS}$ is more involved. The HFS consists of typically many particles, so the reconstruction is much more ambiguous. In the following some details are given.

The inclusive hadronic final state is reconstructed using a combination of the LAr calorimeter, Central Tracker, and SpaCal information. The cluster in the SpaCal, which is selected as the scattered electron is excluded. The calculation is always done w.r.t the reconstructed event vertex used for the event selection. While in the most forward and backward parts of the H1 detector only the calorimeters are used, in the barrel region of the LAr calorimeter the calorimetric measurements are combined with tracks using a special algorithm FSCOMB [BB95a, A⁺97c]. The measurement from the tracks should be superior at lower particle energies, while eventually at higher energies the calorimetric measurement will be more precise. Therefore tracks are required to have a total momentum of $p^{Track} < 10$ GeV, otherwise they are discarded. On the other hand tracks with very low transverse momentum $p_t^{Track} < 0.3$ GeV are always used, as they do not reach the calorimeter in the solenoidal magnetic field.

To avoid double counting of energies, the remaining tracks are extrapolated to the LAr calorimeter and the energies inside a cylinder of 20 cm in the electromagnetic and 40 cm in the hadronic section are added. If the total energy exceeds the track momentum, the calorimetric measurement is used and the track is discarded. Otherwise the track is used and the calorimeter energy is masked.

The determination of $(E - p_z)_{HFS}$ is affected by the presence of extra activity, so called *noise*, in the calorimeters. The bias is particularly strong for small $(E - p_z)_{HFS}$ and thus small y_Σ . The correction for the SpaCal is discussed in section 6.2.1. Noise regions in the LAr are identified using a dedicated topological algorithm. In the central region LAr cells with energy below 0.4 GeV and separated from other energy depositions by more than 40 cm are classified as noise and subtracted from the inclusive HFS. In the forward region the requirements for signals are tightened: there LAr cells with an energy of less than 0.8 GeV and separated from other energy depositions by more than 20 cm are rejected. The further treatment of this basic *combined HFS* measurement is presented in section 6.2.

5.2.5 Phase Space Selection

For the comparison between data and the MC simulation the reconstructed data events have to be restricted to the phase space of interest, therefore $Q_e^2 > 10$ GeV² is required. This avoids deviations caused by events at lower Q^2 , as the MC only covers the phase space above $Q_{gen}^2 > 2$ GeV².

While the MC generator also produces QED Compton events, the elastic contribution may not be adequately included. Therefore a rejection of QED Compton events is tested. This builds on the simple properties discussed in section 2.6: two electromagnetic clusters in the SpaCal approximately back-to-back in azimuth

($\cos(\phi_1 - \phi_2) > -0.95$) and a combined energy close to the nominal electron beam energy ($E_1 + E_2 > 18$ GeV, $E_1 > 4$ GeV, $E_2 > 4$ GeV).

For the final cross check the analysed phase space can be further reduced to the bins, in which the cross section determination is eventually performed.

5.3 Online Event Selection

As explained in section 3.2.5, H1 uses a multi-level *trigger system* for the online event selection. This means, that during data taking not all events are recorded. For the cross section calculation the following procedure has to be used:

- One or a few useful subtriggers have to be specified and only events which have the *actual trigger bit* of at least one of these subtriggers set can be used for the cross section calculation. In this analysis events taken by three subtriggers are used.
- Either the offline selection has to be chosen to guarantee no loss in efficiency or an appropriate correction has to be performed. The subtriggers used in this analysis are highly efficient, so the former way is chosen.
- In case the subtriggers are *prescaled*, special care has to be taken to correctly calculate the proper event weights. Several methods can be used for this.

An independent study with equivalent results is documented in [Urb05].

5.3.1 Subtrigger Definition

This analysis uses three subtriggers, S0, S3, and S9. These all rely mostly on the *Inclusive Electron Trigger* (IET) provided by the SpaCal calorimeter. It compares *local energy depositions* in the calorimeter to a set of predefined *energy thresholds*. Furthermore *radial cuts* on the SpaCal plane can be applied. As the local energy depositions are typically given by the scattered electron, a rough online selection on the electron kinematics, i.e. E'_e and θ_e can be applied.

The energy thresholds of the SpaCal IET are controlled on the first trigger level L1 by different trigger elements SPCLe_IET>1, SPCLe_IET>2, and SPCLe_ToF_E_2. The L2TT system provides elements, which validate only the energy depositions above a certain radius r_{Spac} on the SpaCal xy -plane. Here only one element SPCL_R30 is relevant, which is effective for about $r_{Spac} > 30$ cm.

In addition to the trigger elements based on SpaCal information, a Ray_T0 element based on the central proportional trigger chambers CIP/COP and the FTD proportional chambers, is used. This element is typically not triggered by the electron, but rather by charged particles from the HFS. The operation principle is illustrated in figure 5.3, but not further discussed here.

Table 5.3 summarises the setup of the used subtriggers. In addition all triggers contain so called *global (veto) options* (GO), which are typically based on various *Time-of-Flight* measurements. They are used to additionally reject events which are supposed to originate from non- ep interactions already on L1. A detailed analysis of the GO performance is given below in section 5.6.1.

The three subtriggers used for this work have slightly complementary properties:

from the efficiency measurement.

The first step is to study the efficiency of the SpaCal based L1 and L2TT elements, i.e. the `Ray_T0` element is neglected first of all. A large set of SpaCal independent subtriggers was used to check for problems and inefficiencies of the SpaCal elements given in table 5.3. The trigger efficiency as a function of E'_e and r_{Spac} is shown in figure 5.4. The different energy thresholds of the individual triggers can be seen as well as the radial cut applied on L2 for S3 and S9. The `SPCL_R30` element actually corresponds to a rectangular shape in xy , which covers all $r_{Spac} > 30$ cm, but also some $25 \text{ cm} < r_{Spac} < 30$ cm.

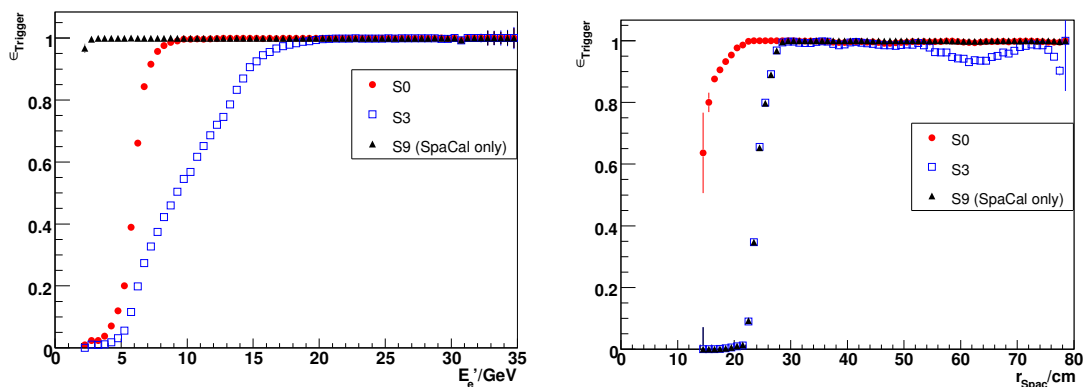


Figure 5.4: Efficiency of the SpaCal L1 and L2 elements of the used subtriggers S0, S3, and S9 as a function of the selected electron energy E'_e and its radius on the SpaCal plane r_{Spac} . For the left plot inefficient regions are masked, while the right plot only considers energies above the threshold of the triggers. The threshold behaviour and the lower efficiency of S3 at higher radii was traced to its `SPCLe_ToF_E_2` condition.

While both S0 and S9 have a sharp threshold behaviour, the subtrigger S3 shows a slightly different characteristics with a slow rise. Another technical problem is visible for S3 at $r_{Spac} \sim 60$ cm, where the efficiency drops significantly. In the xy plane this corresponds to a few well localised areas of about 70 cells total, where the efficiency drops to 0. Both of these features are related to the `SPCLe_ToF_E_2` condition. In contrast to the IET elements, which require local depositions, this element is activated, if the total energy detected in the electromagnetic SpaCal in a time window of about 20 ns around the value expected for ep interactions is above a threshold of about 12 GeV. As both S0 and S9 cover the inefficient regions, there is no loss in the overall efficiency, as will be shown later.

The L2TT trigger system was malfunctioning during a few short periods in 2000. This is easily visible if figure 5.5, which shows the efficiency of the S9 SpaCal only elements for a selection in E'_e and r_{Spac} , which should have close to 100% efficiency. This is found to be true except for a few runs, which are hence excluded from the run selection further on. The subtrigger S3 is similarly influenced, as both contain the `SPCL_R30` element provided by the L2TT. The exclusion of these few runs is performed to obtain a trigger setup with constant efficiency throughout the whole data taking period.

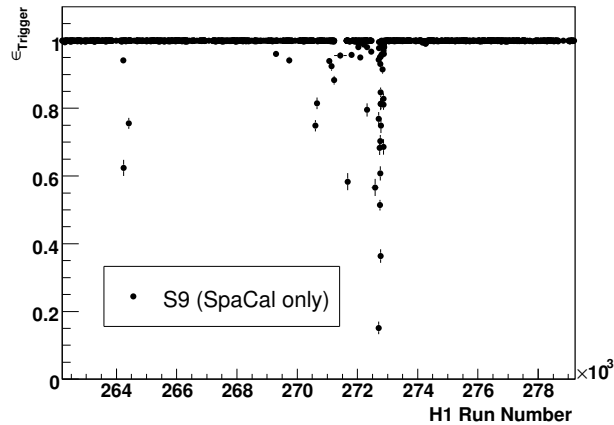


Figure 5.5: Efficiency of the SpaCal elements of the S9 subtrigger as a function of the H1 Run Number. Inefficiencies well located in time are found and the corresponding runs are excluded from further analysis.

From this study a part of the *fiducial cut* was derived based on the S0 performance. The inner region of the SpaCal is excluded from the element `SPCLe_IET>2` used for S0. Furthermore the trigger efficiency was checked for each SpaCal cell. Here some dead cells and cells with lower trigger efficiency were identified, which are further on excluded from the analysis by a fiducial cut. The summary of excluded cells and SpaCal regions is given in table 5.4.

Excluded SpaCal Cells/Regions	Reason for exclusion
Central box ($-16.5 \text{ cm} < x < 10.5 \text{ cm}$) && ($-10.5 \text{ cm} < y < 16.5 \text{ cm}$)	Not included in IET trigger (S0)
Cell #225, 250, 253, 289, 290, #763, 886, 924, 1090	Lower S0 efficiency
Cell #466, 542, 602, 1149, 1153	Dead cells (no signals)
Cell #467, 558, 557, 656, 657, 763	Adjacent to dead cells [Pet07]
Cell #22, 23, 29, 30	Technical problems, background [Pet07]
$r_{Spac} > 73 \text{ cm}$	Containment of SpaCal

Table 5.4: Summary of the fiducial cuts applied in the analysis, performed on the basis of (x_{BDC}, y_{BDC}) projected on the SpaCal plane. Single cells or clusters of cells are rejected with an additional margin of 0.5 cm around the borders. The first three items are derived from the trigger studies, while the last three are taken from the SpaCal calibration procedure and isolated discrepancies between data and MC in the further analysis. An overview over the cell numbers is given in the appendix, figure A.1.

The second step is to determine the efficiency of the remaining S9 element `Ray_T0`. There were no subtriggers in the H1 setup without a SpaCal and a CIP condition at the same time, therefore here events with the S9 SpaCal only condition

SPCL $_e$ _IET>1&&SPCL_R30 are chosen as reference¹. The Ray_T0 is defined as the logical OR of the ray condition provided by central or forward proportional chambers, $zVtx_T0 \mid \mid FwdRay_T0$. Furthermore some veto conditions for high track multiplicities are present. Figure 5.6 clearly shows the dependence on the number of Central Tracker tracks $N_{CentTracks}$ reconstructed and fitted to a common vertex. Only for $N_{CentTracks} \geq 2$ the efficiency is high $\epsilon \sim 99\%$ and for high $N_{CentTracks} > 20$ the efficiency drops slightly again because of the high multiplicity veto elements. The trigger S9 is the main trigger for the high y analysis with $E'_e < 10$ GeV. Nevertheless it is used in this analysis to improve the statistical precision in phase space regions not covered by S3.

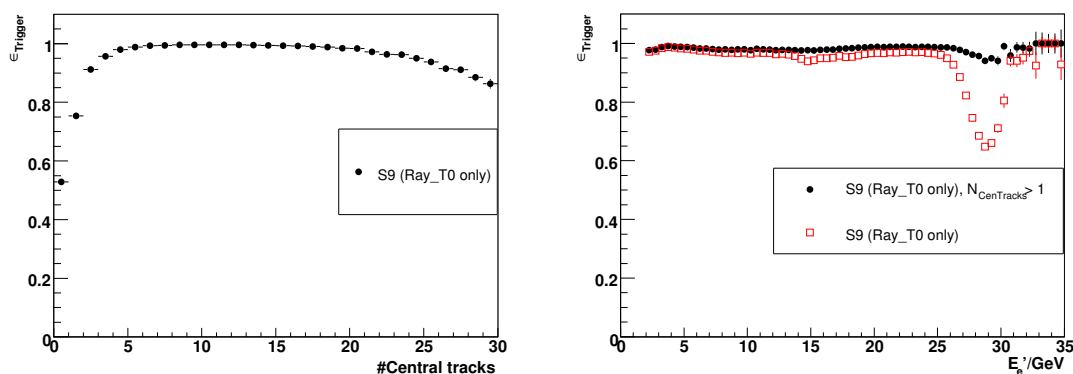


Figure 5.6: Efficiency of the Ray_T0 condition provided by the proportional chambers. For more than $N_{CentTracks} \geq 2$ the efficiency reaches a high level of $\sim 99\%$. Without this selection mainly events from the kinematic peak region with little hadronic activity in the central region contribute to the inefficiency.

The last step is to test, whether the combination of requiring any of the triggers S0, S3, or S9 will cover the phase space as defined by the offline selection criteria with full efficiency. The reference sample is again provided by an actual subtrigger on the SpaCal independent sample with the full offline event selection as in the first step. The probabilities for events to have a positive S9 decision given its SpaCal only elements and a positive or negative decision of S0 and S3 are calculated separately. The sample is divided into subsets triggered by either none, one, two, or all three of the considered subtriggers. This procedure is illustrated in figure 5.7.

The results are shown in figure 5.8. The main emphasis has to be put on the fact, that the total trigger efficiency does not depend on any of the technical or kinematic variables investigated. It is very high after performing the fiducial cut mentioned before and reaches $\epsilon_{Trigger} > 99.95\%$ everywhere. Therefore no efficiency corrections are needed.

The individual contributions of the three subtriggers change depending on the phase space, but S0 in principle covers the whole phase space. The other triggers are

¹ As SPCL $_e$ _IET>1&&SPCL_R30 is not actually a subtrigger, the reference sample is not strictly bias free. However, the tight conditions on the event selection should eliminate most of the bias. Furthermore a cross check using the S0 actual trigger as reference was performed and yielded equivalent results.

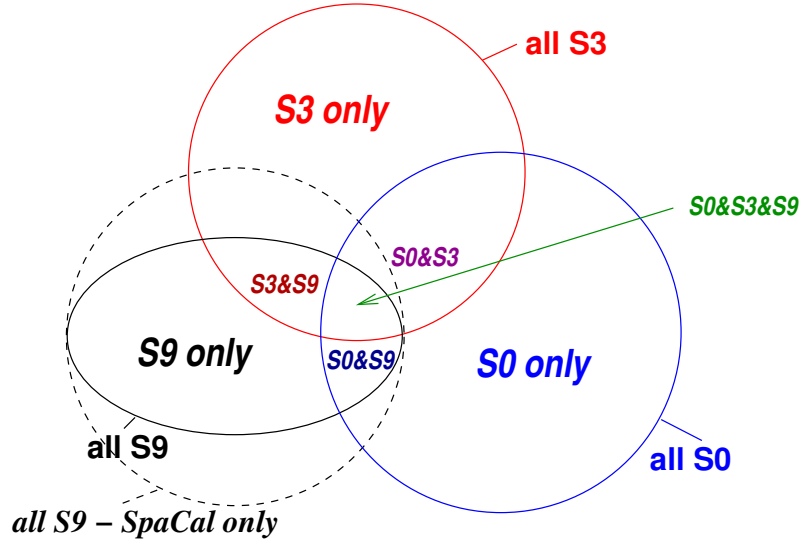


Figure 5.7: Subdivision of the event sample into subsets corresponding to events triggered by one, two, or all three subtriggers. The test of the SpaCal based Trigger Elements are done using an independently triggered sample. The efficiency of the track based element of the S9 trigger is calculated separately and indicated by the two sets all S9 - SpaCal only (dashed line) and all S9 (full line). The final sample triggered by any of S0, S3, or S9 is bounded by the outer full lines.

used only to improve the statistical uncertainties of the measurement. The region $r_{Spac} \lesssim 25$ cm and correspondingly the lower $Q_e^2 \lesssim 15 \text{ GeV}^2$ is mostly triggered by S0 only due to the applied online selection on S3 and S9. As the measurement is not statistics limited at lower Q^2 this poses no problem. Finally, S9 helps to cover the higher $y \sim 0.5$ region and the small localised areas, where S3 is not fully efficient.

5.3.3 Combining Prescaled Triggers

Given highly efficient triggers, as shown above, the further analysis only has to correct for the *artificial efficiency loss* introduced by prescaling during the online selection. The three triggers employed for this analysis cover slightly different, but largely overlapping phase spaces. All of the triggers are typically prescaled by different amounts, where the prescale of a trigger t is constant for all the events i of a run j and denoted by p_j^t .

The correction in parts of the phase space covered by a single prescaled trigger, or if just one trigger was used, would be simple: depending on the value of the actual subtrigger bit $a_{ij}^t = 0$ or 1, the total event weight N is simply given by the number of events with actual subtrigger weighted by the prescale p_j^t :

$$N^t = \sum_{i,j} a_{ij}^t p_j^t. \quad (5.5)$$

The statistical error of N^t , denoted by $\sigma(N^t)$, is of course increased with respect to the case of no prescaling ($p_j^t = 1 \forall j$) and is especially influenced by large event

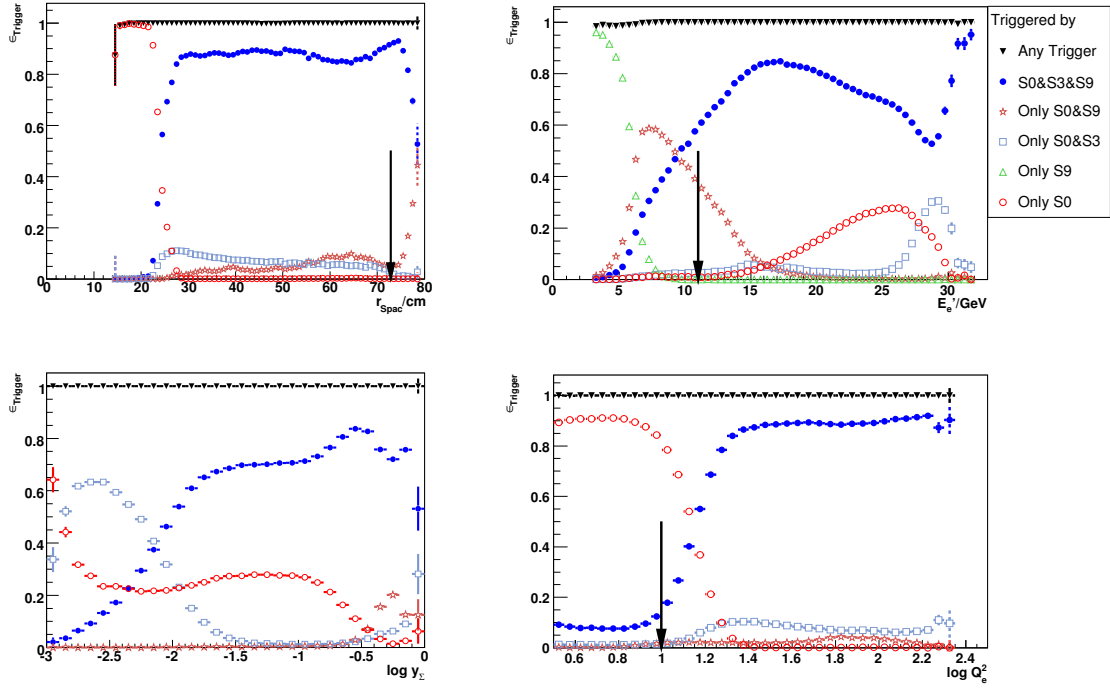


Figure 5.8: Final results for the trigger efficiency measured with the reference sample defined by the offline analysis cuts and non-SpaCal reference triggers as a function of technical variables r_{SpaCal} and E'_e and the reconstructed kinematics y_Σ and Q_e^2 . Offline analysis selections as $r_{\text{SpaCal}} < 73 \text{ cm}$, $E'_e > 11 \text{ GeV}$, and $Q_e^2 > 10 \text{ GeV}^2$ are indicated by arrows. The total trigger efficiency is given by the black triangles, while the other symbols show, how the sample is split into the disjoint subsets introduced in figure 5.7.

weights

$$\sigma(N^t) = \sqrt{\sum_{i,j} a_{ij}^t (p_j^t)^2}. \quad (5.6)$$

If the trigger definition and performance is stable for all runs, which is the case for the data considered, it is therefore beneficial to use an *average trigger prescale* $\overline{p^t}$ calculated with the luminosities for each run \mathcal{L}_j

$$\overline{p^t} = \frac{\sum_j \mathcal{L}_j}{\sum_j \mathcal{L}_j / p_j^t}. \quad (5.7)$$

The raw number of reconstructed events $N_{\text{raw}}^t = \sum_{i,j} a_{ij}^t$ is then corrected by this number

$$N^t = N_{\text{raw}}^t \overline{p^t}. \quad (5.8)$$

The only disadvantage of using *average prescales* is, that they are not adequate for a subset of the data, but only the whole sample. Hence to assess the stability of the data taking in section 5.4, each event is weighted with the prescale of the run it was taken in, referred to as *event wise prescales*.

In case of overlapping phase spaces a scheme for the treatment of the overlaps has to be chosen. In [Urb05] two possible choices are discussed in more detail: the method usually employed by the H1 Inclusive Working Group nELAN, called the *nELAN method*, and the method presented in [E⁺97a], called the *Rick method*.

For the nELAN method the triggers are ordered by their prescales. The trigger $t = 1$ with the lowest prescale is given the highest priority and all events with an actual subtrigger bit $a_{ij}^{t=1} = 1$ are weighted by the corresponding prescale $p_j^{t=1}$. All the remaining events are required to be outside the phase space of this trigger, which is satisfied by requiring that the *raw subtrigger bit* $r_{ij}^{t=1} = 0$. Thus random inefficiency and the remaining phase space can be covered by the trigger $t = 2$ with the second lowest prescale. All remaining events with an actual subtrigger bit $a_{ij}^{t=2} = 1$ are accordingly weighted by its prescale $p_j^{t=2}$. This procedure is repeated until the trigger with the lowest priority is reached. The procedure eventually divides the phase space into disjoint subsets with the maximal size for triggers of the lowest prescale to minimise the statistical errors. However it also discards a part of the events in the overlap areas, which have an actual subtrigger of lower priority, and a raw subtrigger without actual subtrigger of higher priority, e.g. $a_{ij}^{t=2} = 1$ and $r_{ij}^{t=1} = 1$, but $a_{ij}^{t=1} = 0$. The nELAN method is also valid if average prescales are used and is the default method in this work.

The Rick method has the advantage to use all events with a positive actual subtrigger bit for any of the considered subtriggers. The approach corrects for the prescale by calculating the probability for the event to have been triggered. For one trigger this probability is simply r_{ij}^t/p_j^t and correspondingly the probability for at least one of the N_{SubTr} subtriggers to trigger the event is calculated as

$$P_{ij} = 1 - \prod_{t=1}^{N_{SubTr}} \left(1 - \frac{r_{ij}^t}{p_j^t} \right). \quad (5.9)$$

The event weight is then simply $w_{ij} = 1/P_{ij}$. For practical purposes the *averaged event trigger probability* is calculated from P_{ij} as the luminosity weighted average as it was done for the trigger prescale in equation 5.7.

In [Urb05] it is shown, that both methods are equivalent from a mathematical point of view. The statistical uncertainties are smaller or at least equal for the Rick method compared to the nELAN method. In this work the Rick method is used as a cross check. The corrected total event weights in all bins agree to typically better than 1/5 of the corresponding statistical uncertainty, i.e. differences are insignificant. Indeed the statistical uncertainties provided by the Rick method are smaller. However the improvements are limited to about $\sim 5\%$, e.g. instead of 1.00% statistical uncertainty using the nELAN method, the Rick method provides 0.95%, which is of no practical concern.

5.3.4 Event Selection on L4

A further online selection is done after a full reconstruction on the fourth trigger level L4. It may downscale soft physics, e.g. low Q^2 in this analysis, in addition to the L1 prescales by another factor which is typically in the range 2 - 10. This partially increases the statistical uncertainty, however the effect is small.

A potential problem is posed by events, which are wrongly classified as background and downscaled by a large factor 100. For the lower $Q^2 < 3.5 \text{ GeV}^2$ analysis described in [Beh06], this rejection was significant with about 1% of all events. For this analysis however only 11 events with an L4 weight of 100 were found². Therefore the L4 rejection is below 0.1% of all events and no global correction is done. However the events with large weights are not fully rejected but kept in the analysis and increase the statistical uncertainty locally. The total uncertainty in these bins is still not dominated by these L4 rejected events.

5.4 Stability Studies

The total rate of DIS events in the considered phase space is large, so the stability of the detector performance can easily be assessed using the total *event count per luminosity*, the so called *event yield*, as a function of the fill or run number.

In addition to the standard event selection, an equal SpaCal acceptance for DIS events is required regardless of the position of the vertex $|z_{vtx}| < 35 \text{ cm}$. This is satisfied by a restriction of the electron polar angle to the range $160^\circ \lesssim \theta_e \lesssim 172^\circ$ ³. Thus differences in the mean or the width of the luminous region, which may change from fill to fill, do not influence the yield. Also event wise prescales were used in contrast to the standard treatment. Figure 5.9 shows the result after the full run selection. No significant deviations from the mean value are observed and no further problems except the ones listed in table 5.1 are found.

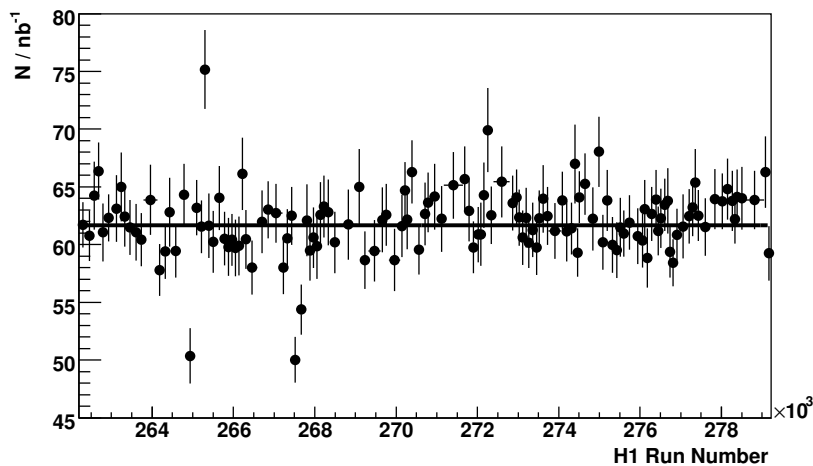


Figure 5.9: Total event yield per luminosity with the final run selection as a function of the H1 Run Number. Each shown bin contains a luminosity of about 300 nb^{-1} . The line shows the average value of $61.7 \text{ events per nb}^{-1}$.

²Events rejected by L4 are present after using only the L1&L2 actual trigger bits and ignoring the *L4 verified* bit provided on H1 *Data Summary Tapes*, which is irrelevant for the online selection and ignored.

³Specifically the applied selection guarantees, that a scattered electron with θ_e and ϕ_e measured in the beam system would be within the SpaCal fiducial cut for any hypothetical vertex position $|z_{vtx}| < 35 \text{ cm}$, which introduces a ϕ_e asymmetry and the given range in θ_e is only approximate.

5.5 Vertex Analysis and Reweighting

For the accurate acceptance calculation it is important that the geometrical beam parameters are correctly modelled in the MC. The effects of small beam offsets of ~ 1 mm in the x and the y coordinate and a tilt of the beam in the H1 coordinate system are approximately introduced in the MC simulation. In the data these values are reconstructed in the standard H1 software with good precision by performing linear fits of the distributions $x_{vtx}(z_{vtx})$ and $y_{vtx}(z_{vtx})$ using a large number of events. All selections and kinematics calculations use values corrected for tilt and offset and are therefore independent of fill-to-fill variations in the data.

Special care is taken to correctly model the distribution of events along the z -coordinate in the MC, as this influences directly the distribution of accepted θ_e and therefore the kinematics. To obtain the *true* z_{vtx} distributions unbiased by acceptance and detector efficiencies, a specially tightened selection was chosen as proposed in [Gla98]:

- An acceptance cut on θ_e was performed like in the previous section 5.4 to equalise the acceptance in the range $|z_{vtx}| < 40$ cm.
- The selection in electron energy was restricted to $15 \text{ GeV} < E'_e < 25 \text{ GeV}$. This avoids any γp background and the low y region, where the vertex reconstruction efficiency of the Central Tracker is low.
- No CIP vertices are used as they may be biased for event vertices far away from the nominal one. For the central vertices at least $N_{CenTracks} \geq 2$ was required to guarantee at least one track from the HFS and therefore avoid any dependence on the electron kinematics.

Figure 5.10 shows the variations of the mean $\langle z_{vtx} \rangle$ and the width $\sigma(z_{vtx})$ of the luminous region as a function of the luminosity fill determined in Gaussian fits. The width is typically similar $\sigma(z_{vtx}) \approx 11$ cm and determined by the proton machine. On the other hand the beam timing and therefore the mean may be different for each fill, variations of ± 5 cm are not uncommon.

The whole MC sample was generated with $\langle z_{vtx} \rangle_{gen}^{MC} = 0.9$ cm and $\sigma(z_{vtx})_{gen}^{MC} = 11$ cm. The corresponding distribution has to be reweighted to match the data distribution. For this purpose the mostly unbiased z_{vtx} distributions are determined for data and MC according to the above procedure and fitted with a smooth function. For data the final run selection and trigger treatment was used. The function chosen is a Gaussian plus a polynomial of the degree 10 to properly fit the tails at least in the range $|z_{vtx}| < 40$ cm. For data the Gaussian core of the distribution has the parameters $\langle z_{vtx} \rangle_{fit}^{Data} = 2.0$ cm and $\sigma(z_{vtx})_{fit}^{Data} = 11.7$ cm. For the MC the values used for the generation are reproduced quite well by the Gaussian core with $\langle z_{vtx} \rangle_{fit}^{MC} = 0.83$ cm and $\sigma(z_{vtx})_{fit}^{MC} = 11.1$ cm.

These functions are normalised to contain the same number of events in the interval $|z_{vtx}| < 40$ cm and the ratio $(z_{vtx}^{Data}/z_{vtx}^{MC})_{fit}$ is used as additional event weight in the MC depending on the generated position of the vertex $z_{vtx,gen}^{MC}$, as long as its value is in the considered interval. The reweight function is shown in figure 5.11 together with the comparison of the z_{vtx} distributions in data and MC after applying the reweighting. It is obvious, that due to the choice of $\sigma(z_{vtx})_{gen}^{MC} < \sigma(z_{vtx})_{fit}^{Data}$ large

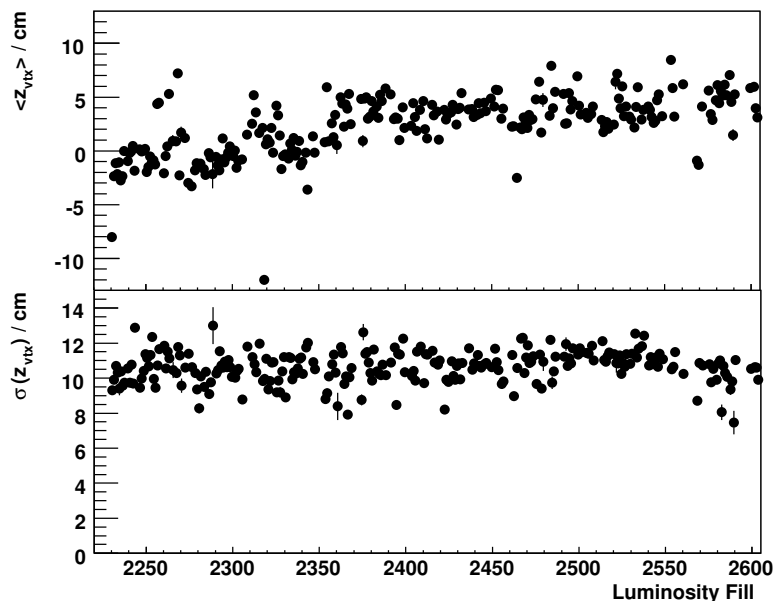


Figure 5.10: Mean $\langle z_{vtx} \rangle$ and spread $\sigma(z_{vtx})$ of the vertex distributions determined by Gaussian fits for each luminosity fill.

weights are needed in the tails and therefore the statistical precision for these events suffers. However the MC statistics is large and the effect therefore not critical.

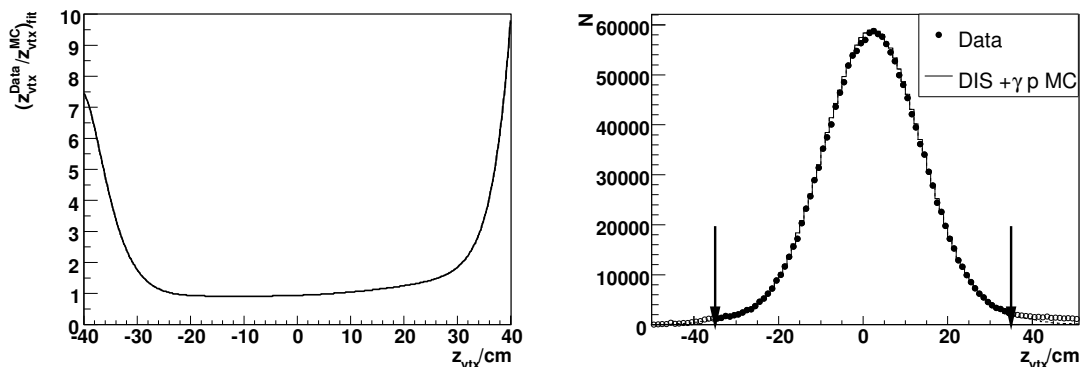


Figure 5.11: The function used to reweight the MC z_{vtx} distribution to the one observed in data (left panel). Comparison of the analysis z_{vtx} distributions in data and the reweighted MC. The analysis selection cuts at $|z_{vtx}| < 35 \text{ cm}$ are indicated by arrows (right panel).

5.6 Global Normalisation Effects

Before turning to the details of the data analysis, this section discusses a few effects, which finally influence the cross section measurement as a global normalisation. The most important are related to the luminosity measurement. Some aspects can be cross checked using low Q^2 DIS events. In addition the efficiency of the *global*

options of the triggers are discussed, which are also found to have an phase space independent influence. Table 5.5 summarises the size of all effects discussed below.

Effective \mathcal{L} Correction	Change w.r.t Standard Value
Global Trigger Options Inefficiency	$(-0.5 \pm 0.3) \%$
Photon Detector Reanalysis	-1.2%
Correction for e -gas background	$(+0.35 \pm 0.0) \%$
Satellite Correction	$(0.0 \pm 1.5) \%$
Total	-1.35%

Table 5.5: Summary of the corrections applied to the luminosity value as calculated by standard H1 Luminosity tools.

5.6.1 Global Trigger Options

In section 5.3 most of the aspects of the online event selection done via the SpaCal triggers was discussed. The discussion was only neglecting the so called *global options* (GO), mostly based on various *Time of Flight* (ToF) measurements. These are used to reject non- ep background already on the first trigger level. Only the trigger S0 is discussed, as it has the simplest GO setup and it is at the same time the only trigger to cover the full phase space of the analysis.

The GO setup of S0 consists of two sets of conditions. The first part requires the absence of signals compatible with p -beam induced background: `!VETO_inner_BG && !VETO_Outer_BG && !VLQToF_BG`. The relevant detectors are the *veto wall* (VETO elements) and the *Very Low Q^2 spectrometer* (VLQ element). Both are located in the vicinity of the SpaCal in the backward region of H1. The second part of the GO options requires signals from various detectors in the forward region of H1, which have a timing compatible with an ep interaction or at least not compatible with background: `FToF_IA || FIT_IA || (!FToF_BG&&!FIT_BG)`. Due to the location in the forward region of H1 these elements should be sensitive only to e -beam induced background.

A problem in determining the GO inefficiency is, that there are no *independent subtriggers* available, which do not contain the used global options and at the same time trigger DIS events at low Q^2 efficiently enough. A study at higher Q^2 with the electron detected in the LAr showed, that the inefficiency is not negligible and caused typically by *noise* or *pile up* of signal events with background [Hab06].

Therefore a different approach is used, which assumes that any inefficiency of the GOs is independent of the physics process studied. As reference the Bethe-Heitler process as used for the luminosity measurement is chosen. The trigger S91 employed for the offline correction determination does not contain any veto elements and is therefore well suited [Gla06]. It is found, that the inefficiency of the first set of conditions sensitive to p -beam related background is appreciable at about 0.5%, see figure 5.12 [Gla07]. The influence of the second set is negligible. The total luminosity is corrected by -0.5% and the systematic uncertainty is estimated to be 0.3% in line with previous results. Most of the inefficiency is given by the VLQ element. The spectrum for the sum of electron and photon energy $E'_e + E_\gamma$ detected in the

ET and PD should peak close to the nominal beam energy for signal events. The fact, that rejected and triggered events have the same shape within the statistical uncertainty confirms the hypothesis, that the inefficiency is caused by pileup with background or noise and therefore is phase space independent.

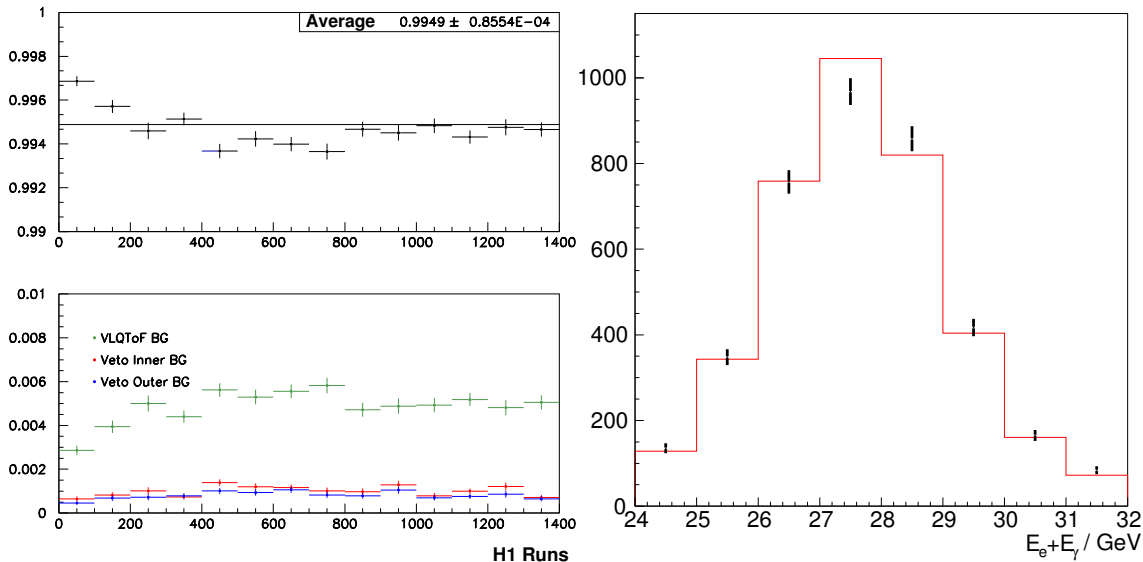


Figure 5.12: Determination of the $S0$ global option efficiency in the year 2000 done with the help of Bethe-Heitler events and $S91$ trigger, from [Gla07]. On the left panel the total efficiency and the elements contributing to the inefficiency are shown. The final efficiency is 99.5% and mostly independent of the run number. On the right panel the distributions for $E'_e + E_\gamma$ detected in the ET and PD are shown for triggered (full red line) and rejected events (small dots).

5.6.2 Photon Detector Reanalysis

The major task for reaching the highest possible precision for the luminosity measurement is an analysis of the Bethe-Heitler events in the Photon Detector PD triggered by the subtrigger $S91$. The main systematic errors in this analysis used to be the energy scale calibration of the PD and the determination of its acceptance. In the last years a new method was introduced, which reduced the influence of the PD energy scale significantly [Lev07]. The luminosity analysis was repeated and also the special run selection of this analysis was taken into account to derive a customised acceptance correction, which is sensitive to short time scale beam steering and therefore to the run selection. In comparison to the luminosity value obtained by standard H1 tools, a value smaller by -1.2% was found [Lev06]. The estimated systematic uncertainty of that value is 1.5% , so the change due to the reanalysis is within that uncertainty.

5.6.3 Correction for e -gas Background

In section 4.3.3 the e -pilot bunches were studied separately to determine non- ep background. Instead of background a significant DIS signal was found, which can

be explained with residual proton current in the corresponding bunches.

For the luminosity determination the e -pilot bunches are used for the determination of the contribution of Bethe-Heitler events from rest gas in the beam pipe $eA \rightarrow e\gamma A$, so called e -gas events. This contribution is subtracted from the luminosity measured using the PD, for the year 2000 this correction is about 1.5% [Lev06]. Knowing that some of the events are actually caused by standard ep interactions, this correction is too large, as the leaked p current is not considered. In the following the influence of the *fake* e -gas events on the luminosity is evaluated.

The original e -gas background correction performed on the luminosity value obtained by standard H1 tools is done as [A⁺97a]

$$\mathcal{L}^0 = \frac{N_{BH}^{tot} - R_{Ie} N_{BH}^{epil}}{\sigma_{BH}}. \quad (5.10)$$

Here N_{BH}^{tot} and N_{BH}^{epil} are the number of Bethe-Heitler events detected for all and the e -pilot bunches, respectively, and σ_{BH} the visual part of the Bethe-Heitler cross section. The average ratio of the total electron current to the one stored in the pilot bunches was $R_{Ie} = I^{etot}/I^{epil} = 13.11$. It now has to be assumed, that the number used for the e -gas events has a component of *fake* events caused by the residual proton current, i.e. $N_{BH}^{e,pil} = N_{BH,eA}^{epil} + N_{BH,ep}^{epil}$. Therefore instead of using \mathcal{L}^0 , rather the *true* luminosity \mathcal{L} should be used

$$\mathcal{L}^0 = \mathcal{L} \cdot \left(1 - R_{Ie} \frac{N_{BH,ep}^{epil}}{N_{BH}^{tot}} \right). \quad (5.11)$$

The ratio $N_{BH,ep}^{epil}/N_{BH}^{tot}$ cannot be determined by the luminosity system, but it can be approximated using the DIS selection. It was found to be $N_{DIS}^{epil}/N_{DIS}^{tot} = 2.66 \cdot 10^{-4}$, the correspondingly normalised figures were shown in section 4.3.3. Therefore the true luminosity \mathcal{L} is 0.35% larger than \mathcal{L}^0 determined according to equation 5.10 with standard H1 tools. A corresponding shift of the mean value is performed, while keeping the uncertainty constant.

5.6.4 Analysis of the Proton Beam Satellite Bunches

The proton beam of HERA has a complicated longitudinal structure, which consists of the main bunches, but also additional *satellite bunches*. These additional local maxima are caused by deficiencies of the *radio frequency systems* (RF) used to accelerate the protons. Two RF systems are used: the 52 MHz system matches the bunch length after the transfer from the PETRA pre-accelerator and the 208 MHz system is used eventually for the accelerated beam. During the compression of the bunches some proton current typically leaks from the main bunch and forms satellite bunches shifted in z by $\Delta z = \pm c/(2 \cdot 208 \text{ MHz}) = \pm 72 \text{ cm}$. In addition a small fraction of the protons may become unbunched and form so called *coasting beam*.

The satellite bunch at $z_{vtx} \approx +70 \text{ cm}$ is well visible also in the DIS selection, as the acceptance of the SpaCal is enhanced for lower Q^2 events originating from this region. Figure 5.13 shows the structure with a selection similar to the one

used in section 5.4, but modified to guarantee equal acceptance for DIS events from the range $-35 \text{ cm} < z_{vtx} < 105 \text{ cm}$. The satellite bunch at $z_{vtx} \approx -70 \text{ cm}$ is difficult to study with DIS events. To have equal SpaCal acceptance for the region $-105 \text{ cm} < z_{vtx} < 35 \text{ cm}$, would require to restrict the analysis to a Q^2 range of about $60 \text{ GeV}^2 \leq Q^2 \leq 90 \text{ GeV}^2$. Due to the strong $1/Q^4$ dependence of the cross section the statistical precision would be very limited.

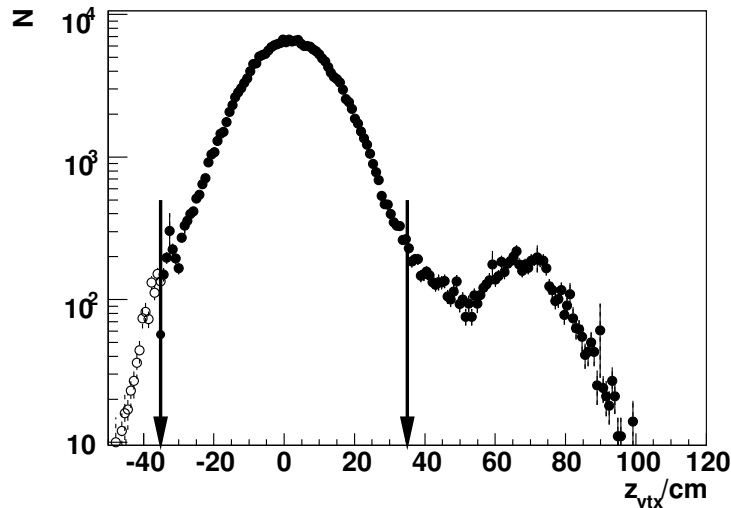


Figure 5.13: Distribution of reconstructed z_{vtx} values of DIS events. A special selection is made to assure an acceptance independent of z_{vtx} and the electron kinematics. The arrows indicate the nominal analysis range $|z_{vtx}| < 35 \text{ cm}$, while the fraction of events detected at $z_{vtx} > 35 \text{ cm}$ corresponds to the luminosity correction for the +70 cm satellite.

For the analysis the luminosity of the satellite bunches as well as tails from the main bunch are not considered due to the selection $|z_{vtx}| < 35 \text{ cm}$. However the luminosity system on its own cannot measure the z -position of the Bethe-Heitler events. It integrates over a wide range of $\sim 6 \text{ m}$ around the nominal interaction point. Due to the beam optics the contributions from further than $\sim 1 \text{ m}$ away can be neglected. Using other timing sensitive detectors, the amount of luminosity *lost* due to the selection on z_{vtx} is estimated and corrected for [LP95, GL96]. For the run range considered here and the selection $|z_{vtx}| < 35 \text{ cm}$ the size of this *satellite correction* is determined to be 4.9% using the standard H1 tools for luminosity calculation. The contribution from the region $z_{vtx} < -35 \text{ cm}$ is estimated to be 1.3%, the corresponding value for the region $z_{vtx} > 35 \text{ cm}$ is 3.6%. The precision of this determination should be on the order of 15 – 30% [Lev06], so the final contribution to the luminosity uncertainty is $\sim 1\%$ and therefore a significant contribution.

From figure 5.13 the fraction of events detected with $z_{vtx} > 35 \text{ cm}$ can be obtained, which is a direct measure of the needed satellite correction. It is determined to be 5.1%, which has to be compared to the value 3.6% given by the standard H1 analysis tools. This discrepancy is just about within the quoted measurement uncertainty, but should be improved in the future.

Chapter 6

Detector Performance and Calibration

In order to achieve a high precision of the measured DIS cross section special care must be taken to optimise the detector performance and improve the description of detector related effects in the Monte Carlo simulation.

This chapter documents the steps performed to reconstruct the properties of the scattered electron and the hadronic final state (HFS) precisely and with as little systematic uncertainties as possible. One important step is the calibration of the calorimeters, which can be done using a subset of the data itself due to the over-constrained kinematics. The subdetectors of H1 are not perfectly aligned with respect to each other. Small shifts in the relative positions of detectors lead to uncertainties in the reconstruction of the kinematics and can usually be corrected for up to some extent. Furthermore the detection efficiency of the BDC is discussed shortly.

6.1 SpaCal Double Angle Calibration

One main source of systematic uncertainty is related to the energy of the scattered electron E'_e measured in the SpaCal. Any deviation in the measurement $\delta E'_e$ is amplified $\propto 1/y$ for the kinematics reconstruction by the Electron Method. It is therefore important to calibrate the energy measurement in the SpaCal to the level of a few permille, so its uncertainty does not dominate the measurement error. As the cross section measurement uses MC events for the acceptance correction, the main importance is not the calibration to the absolute scale, but a good description of scale variations in the simulation.

The calibration of the electromagnetic part of the SpaCal has first of all to equalise the performance of the 1192 individual photo multipliers used to collect the scintillation light from the individual cells. The time dependent variations are controlled with the help of a dedicated LED system, which allows to control and correct fluctuations in the response [Mey96]. During data taking the calibration is adjusted using the *kinematic peak method* [J⁺95], which however is only possible for the inner region. The outer region can be calibrated using the signals from minimum ionising muons, which either originate from cosmic rays [Dir96] or proton beam induced background, so-called *beam halo muons* [Arn95].

As a final calibration step in this analysis, the *Double Angle Method* is used. It was introduced in [Hoe92, BEK92] and has subsequently become the standard method to perform the electron calibration in inclusive analyses [Gla98]. The Double Angle calibration makes use of the fact, that the kinematics of the ep scattering is over-constrained. Given measurements of the electron scattering angle θ_e and the hadronic angle γ_h , see equation 4.7, the inelasticity y can be reconstructed as

$$y_{DA} = \frac{\tan(\gamma_h/2)}{\tan(\gamma_h/2) + \tan(\theta_e/2)}. \quad (6.1)$$

With y_{DA} it is now possible to express the energy of the scattered electron as in the electron method 4.1 and one obtains

$$E_{DA} = E_e \frac{1 - y_{DA}}{\sin^2(\theta_e/2)}. \quad (6.2)$$

The measurement of this *Double Angle Energy* E_{DA} is to first order independent from other possibly uncalibrated energy measurements.

To be useful as reference for the SpaCal calibration, a special subset of the standard DIS event selection is used. Well reconstructed events from the kinematic peak region at low $y \sim 0.03$ are selected with cuts on the hadronic angle $15^\circ < \gamma_h < 80^\circ$. Wrongly reconstructed events are rejected by requiring the inelasticities reconstructed by the Double Angle and Hadron Methods to match $|y_{DA} - y_h| / (y_{DA} + y_h) < 0.2$. In addition the energy of the scattered electron is required to be in the range $20 \text{ GeV} < E'_e < 32 \text{ GeV}$, which again mostly rejects wrongly reconstructed events, as the selection on γ_h provides typically events with $E'_e \sim 27 \text{ GeV}$.

Using the Monte Carlo simulation, one can compare the measurements provided by the Double Angle method E_{DA} and the SpaCal E'_e to the energy set by the Monte Carlo event generator $E_{e,gen}$ for this selection. In figure 6.1 it is shown, that the resolution of E_{DA} is much better than E'_e . The absolute energy scale $E_{e,gen}$ is reproduced up to a small offset of typically 0.4%. The bias is slightly larger at smaller radii, where both the central tracker and the CIP cannot always determine the event vertex due to limited acceptance. This bias however is expected to be reproduced in the data, as the vertex reconstruction efficiency is well described by the MC, see section 7.1. Therefore the relative calibration Data-MC will not be affected beyond the later discussed systematic limitations. Furthermore a large and growing bias in the outer region for $r_{Spac} > 74 \text{ cm}$ is seen, which is due to the acceptance edge of the SpaCal and typically excluded from the analysis by a safe fiducial cut at $r_{Spac} < 73 \text{ cm}$.

In the following several corrections to the SpaCal energy measurements are applied to achieve a ratio $\langle E_{DA}/E'_e \rangle = 1$ for the calibration sample. For this purpose the distributions of the pulls $\delta = E_{DA}/E'_e$ (or equivalently its inverse) are measured as a function of suitable variables like the SpaCal cell number or r_{Spac} and a robust estimator of the mean is formed, denoted by $\langle \cdot \rangle$ [YYG90]. The following steps are performed

- For each cell an individual gain is determined.
- A correction for time-dependent effects is applied.

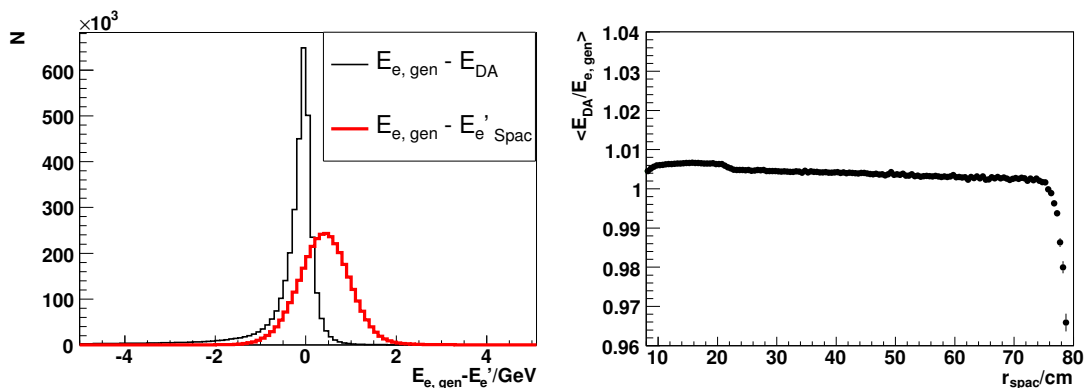


Figure 6.1: Comparison of the absolute energy scale given by the MC generator $E_{e,gen}$ and measurements by the Double Angle Method and the SpaCal (left). The superior resolution and nearly bias free measurement of the DA method is obvious. The bias of the DA method to the absolute energy scale is small and mostly constant as a function of r_{Spac} (right).

- Several corrections for geometry dependent dead material effects are applied.

The H1 reconstruction software provides reconstructed SpaCal energies on several levels: the *raw electromagnetic* scale, the scale for *electromagnetic particles corrected for energy losses*, and the scale at the *final level* including corrections for hadronic particles. In order to fully control the energy scale in both Data and MC, the correction for dead material is redone starting from the *raw electromagnetic* scale, which however already includes the online kinematic peak and cosmic muon calibrations [Fer01]. The same procedure is applied to Data and MC, only time dependent effects are not simulated.

6.1.1 Cell Gain Correction

The energy of a cluster in the SpaCal is typically shared between several cells i with cell energies E_i

$$E_{Spac} = \sum_{i \in Cluster} E_i. \quad (6.3)$$

For each cell a gain g_i is introduced, so the *cell calibrated (cc)* SpaCal energy E_{Spac}^{cc} is given as

$$E_{Spac}^{cc,\alpha} = \sum_{i \in Cluster} E_i(1 + g_i^\alpha). \quad (6.4)$$

The *cell gains* are determined in an iterative procedure, with $g_i^0 = 0$ for the first iteration. This is achieved by constructing the pull distributions for iteration α

$$\delta_i^\alpha = \frac{E_{Spac}^{cc,\alpha}}{E_{DA}}, \quad (6.5)$$

weighted by the relative contribution of the cell i to the current event

$$w_i = \frac{E_i(1 + g_i^\alpha)}{E_{DA}}. \quad (6.6)$$

The update to the iteration $\alpha + 1$ is performed as

$$g_i^{\alpha+1} = g_i^\alpha - (\langle \delta_i^\alpha \rangle_{w_i} - 1), \quad (6.7)$$

where $\langle \delta_i^\alpha \rangle_{w_i}$ denotes the robust mean of the pull distribution over all calibration events weighted by w_i in iteration α .

At this stage of the calibration the goal is to determine mostly the calibration of the *hottest cell*, i.e. the cell i with the highest energy in the cluster $E_{imax} = \max_j E_j$ and to limit the energy losses between cells, which is treated below. This is achieved by requiring $E_{imax}/E_{Spac}^{cc} > 0.6$ ¹. In contrast to the standard event selection no trigger requirements are imposed on the selected data events to maximise the statistics. The fiducial cuts are also relaxed and remove only events in the central region $-12.5 \text{ cm} < x_{Spac} < 10.5 \text{ cm}$ and $-10.5 \text{ cm} < y_{Spac} < 12.5 \text{ cm}$, close to the dead cells, and the high radii. This is done to maximise the available statistics while avoiding an effective correction for energy leakage. To equalise the treatment of Data and MC events, the gains of the known dead cells are fixed to $g = -1$ during the calibration.

The *effective number of calibration events* for cell i is given by summing over all calibration events as $N_i^{eff} = \sum_{events} w_i$. It is displayed in figure 6.2 for the full Data and MC sample used. The statistics available for the calibration drops rapidly towards the outer region. Nevertheless the minimally required 10 effective events per cell are reached for all cells except the ones avoided by the reduced fiducial cut.

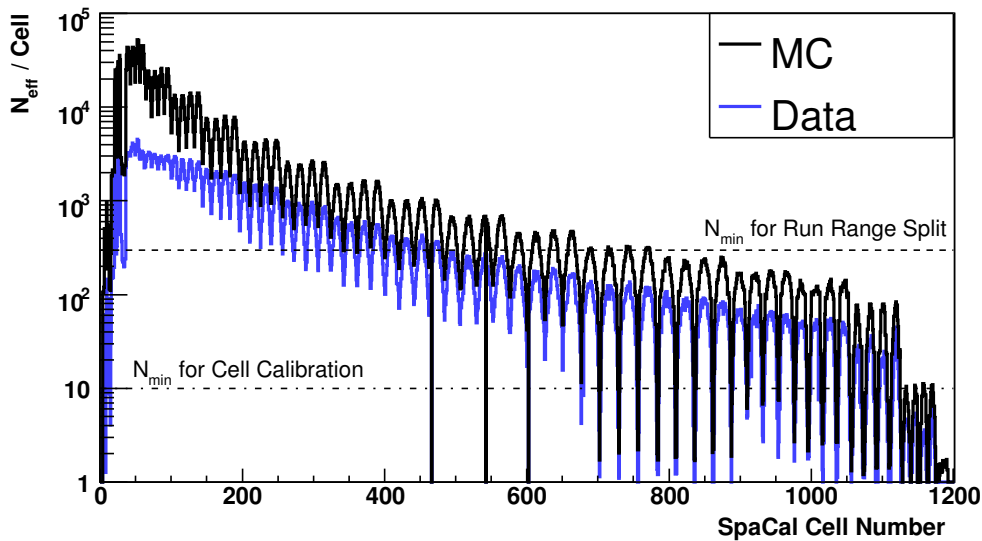


Figure 6.2: Number of effective calibration events available for the determination of the cell calibration constants as a function of the cell number (for the numbering scheme see A.1). Indicated are the requirements of at least 10 events to determine a calibration constant and at least 300 events in data to split the calibration in time periods.

¹This requirement is only imposed for the actual cell calibration step and not employed afterwards at any time.

While the MC simulation does not contain any operational changes or instabilities in time, these are present in data. Three times in 2000 an updated *kinematic peak calibration* was implemented [Fer01], which is well visible as $\sim 1\%$ effects, see below. To account for this change in the precalibration, the data sample is split into the same four run ranges see table 6.1. If the hottest cell of a calibration event has more than 300 effective calibration events, this event is used only for the calibration period it was taken in. However, if the available statistics of the hottest cell of the event was lower, all these events are collected and no split is performed. This way the calibration of the inner cells up to $r_{Spac} \lesssim 50$ cm is performed in periods, while the outer cells are calibrated globally. This is consistent with the procedure used for the precalibration, which was subject to the same statistical limitations and therefore a similar split in inner and outer range.

SpaCal Calibration Period	Run Range
1	262144 - 264528
2	264529 - 269500
3	269501 - 274500
4	274501 - 279306

Table 6.1: Split of the data sample into four periods for cell wise calibration

Performing the iterative determination of the gains g_i it was noted, that the above procedure converges rapidly for cells located far away from fiducial cuts, so the calibration procedure could be stopped after about three iterations. However the iteration for cells very close to the fiducial cuts tends not to converge and unreasonably large calibration factors occur. Therefore the main criterion for stopping the calibration procedure was, that the change for the current iteration $\langle \delta_i^\alpha \rangle$ averaged over all cells with sufficiently large statistics was below $3 \cdot 10^{-4}$, which is reached after typically 5 to 9 iterations. The obtained calibration constants for the MC are typically $g_i^{MC} \sim 0.02$. For data the inner region is calibrated already reasonably well and the corrections there are typically smaller with $g_i^{Data} \sim 0.01$. In the outer region however larger corrections of $g_i^{Data} \sim \pm 0.05$ occur. Some cells are recalibrated by up to 20% in data.

The dependence of the deviation $\langle E_{Spac}/E_{DA} \rangle$ before and after the application of the cell gains is shown for Data and MC in figure 6.3 as function of r_{Spac} . The correction of typically $\sim 2\%$ brings both scale deviations much closer to unity and residual fluctuations are typically less than 1%. These fluctuations will be corrected with the following refinements.

6.1.2 Correction for Finite Cell Size

The cells of the SpaCal have a transverse size of 4.05×4.05 cm². A significant dependence on the impact position of the electron relative to the centre of its hottest cell is observed. The impact position is reconstructed from the SpaCal measurement only, see equation 5.1. In figure 6.4 the residual miscalibration $\langle E_{Spac}/E_{DA} \rangle$ is shown for all available calibration events. Especially in data the energy of electrons with an impact position close to the cell borders or even the corners is on average too low by 1 - 2%. This loss of energy in the additional inactive material between the cells

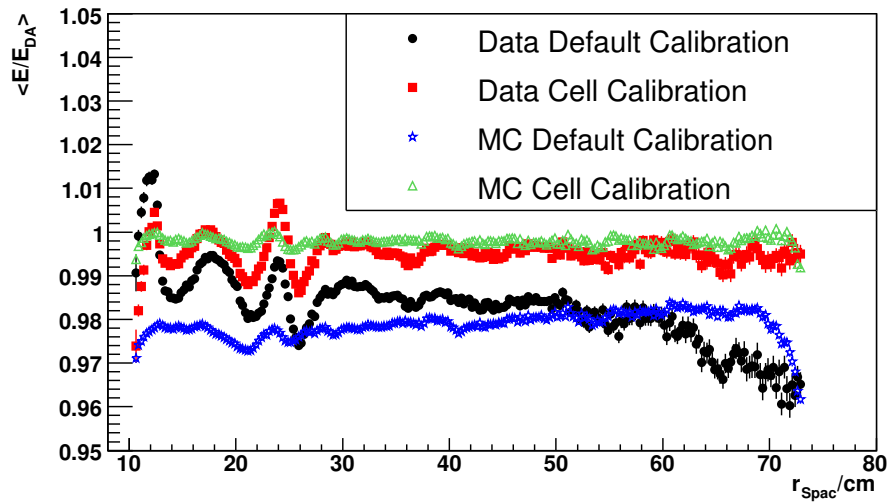


Figure 6.3: Deviation of the SpaCal energy measurement from the calibration scale E_{DA} before and after the application of the cell calibration constants. The energy is in both cases corrected by $\sim 2\%$ and residual deviations are typically less than 1% , see text.

is not well described in the MC, where the effect is much less obvious. The value $\langle E_{Spac}/E_{DA} \rangle$ is further on applied as additional correction to the measured SpaCal energy². Due to the large available statistics a fine binning of 20×20 for one cell in $\Delta(x, y)$ could be chosen.

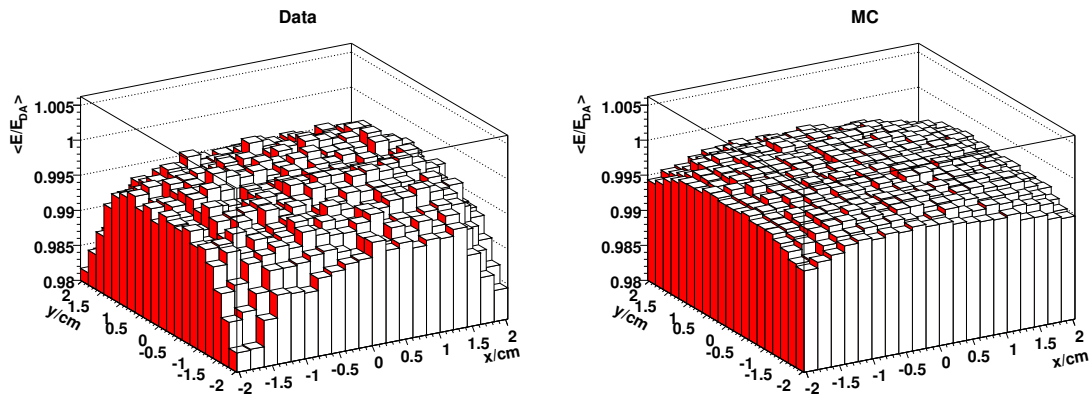


Figure 6.4: Deviation of the SpaCal energy measurement from the calibration scale E_{DA} as a function of the cluster barycentre relative to the centre of the hottest cell.

²In [Laš04, Var06] this correction was called *Inbox correction*.

6.1.3 Time Dependent Correction

When the residual pull $\langle E/E_{DA} \rangle$ after applying all corrections discussed so far is investigated with respect to the time stability, it is found that the mean for the whole calibration sample drifts by approximately $\pm 1\%$ over the course of the data taking period. While the mean for the whole sample can be adjusted, the resolution will therefore suffer.

As unit for time dependant effects the *total H1 integrated luminosity* \mathcal{L}_{tot} is chosen, as this is closely related to the actual data taking conditions. Ageing and radiation damage effects are expected to be roughly proportional to \mathcal{L}_{tot} .

In order to apply a single factor for the whole SpaCal, it must be assured, that not the instability of a few high statistics cells influences the result for the whole SpaCal. In figure 6.5 the time dependence of $\langle E/E_{DA} \rangle$ is shown for several regions in the SpaCal at different radii r_{Spac} . It is obvious that the time dependent developments are the same for the subsamples as the whole sample. The sample was also subdivided into four different regions in ϕ_{Spac} with similar results. Also no correlation to the mean of the z_{vtx} distribution was found, which could in principle bias the E_{DA} determination.

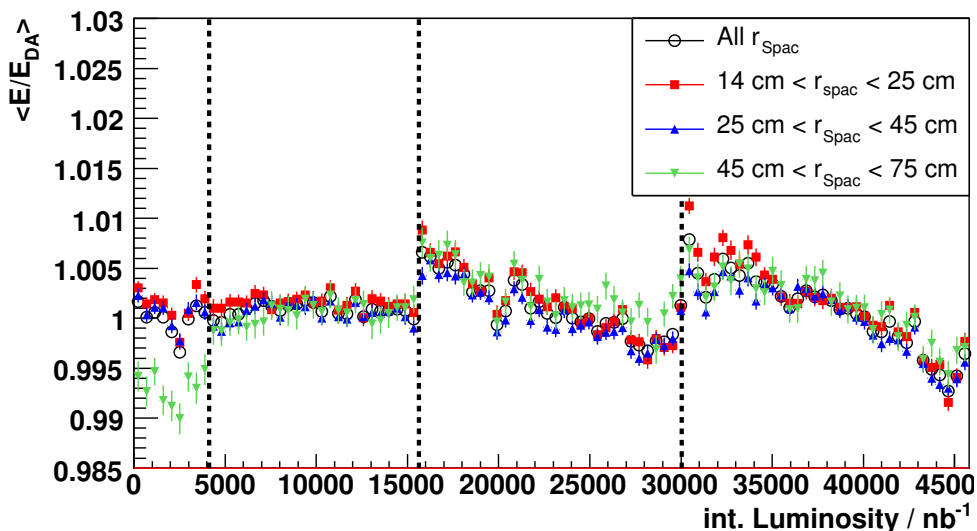


Figure 6.5: Deviation of the SpaCal energy measurement from the calibration scale E_{DA} as a function of the total integrated H1 luminosity. The division into the calibration periods from table 6.1 is indicated by the three vertical lines. The full calibration sample as well as subsamples at different r_{Spac} are shown, which behave very similar w.r.t their relative time evolution.

Therefore the observed calibration deviation is fitted with a polynomial of degree 6 separately for each of the four SpaCal calibration periods and the corresponding correction is applied for all events. The origin of this time dependence is not fully understood. The slow reduction in the SpaCal response over time may be caused by drifts of the photomultiplier voltage due to ageing of electronics modules. The faster fluctuations could be caused by short periods of different cooling water temperature and are eventually not corrected for.

6.1.4 Correction for Losses in Dead Material

As the last step in the calibration procedure a further correction for energy lost in passive material in front of and inside the SpaCal is performed. In figure 6.3 systematic variations of up to $\pm 1\%$ were visible as a function of r_{Spac} , which are not fully reproduced in the MC, despite the efforts to improve the material distribution, see figure 4.2. A further source of energy losses are the cracks between the SpaCal super modules, which contain 4×4 cells, see figure 3.6. While material in front of the SpaCal is distributed mostly radially symmetrically, the SpaCal internal structures are oriented mostly horizontally or vertically.

Therefore the correction was chosen to be done in the variables x_{Spac} , y_{Spac} , and r_{Spac} . An iterative approach was used to disentangle the small correlation between the correction in these variables. The final correction factor is a product of the three pulls $\delta_r \cdot \delta_x \cdot \delta_y$, which are determined using a fine spacing of 0.25 cm in the variables x_{Spac} , y_{Spac} , and r_{Spac} . The three corrections are shown in figure 6.6. While most of the structures are similar for data and MC, the corrections for data are typically larger by a factor of two and can reach locally up to 2%.

A further small improvement could be reached by refining the correction depending on r_{Spac} . This factor should compensate losses in the material in front of the SpaCal and should not only depend on the cluster position, but also on the path the electron took through the detector. Therefore a further correction depending on r_{Spac} , but determined in slices of the measured event vertex position z_{vtx} was determined. Seven ranges in z_{vtx} were defined with the width varying between 4 cm and 15 cm according to the available statistics. This correction eventually has only the effect to slightly improve the resolution of the energy measurement.

6.1.5 Final Corrections and Assessment

After applying all the aforementioned corrections to the data and the MC the same way, the final quality of the calibration must be judged. In all the variables used for the correction the pull distributions $\delta = \langle E_{Spac}/E_{DA} \rangle$ are flat and show no miscalibrations. A cross check of the pull distribution is shown as a function of the independent variable *box radius* defined as $r_{box} = \max(|x_{Spac}|, |y_{Spac}|)$ ³. In figure 6.7 the deviation is shown before and after the dead material corrections. While the corrections work flawlessly on the MC, in the data small residual effects remain. These however do not exceed 0.2%.

The calibration is applied to the standard DIS selection and the quality of the data-MC agreement is evaluated in figure 6.8. It can be seen, that the calibration dramatically improves the quality of the description of the E'_e spectrum.

The width of the kinematic peak is slightly smaller in MC than for the data. This reflects the fact, that the applied calibrations can correct the average, but cannot compensate for fluctuations caused by showering effects not fully described in the simulation. In [Sie99] this energy loss was investigated in detail and a correction using the BDC as preshower detector was developed. These detailed investigations essentially showed, that a correction of the preshower effects leads to a good agree-

³Former calibrations were carried out using r_{box} instead of x_{Spac} and y_{Spac} directly [Gla98], as many SpaCal internal structures are located at constant r_{Box} .

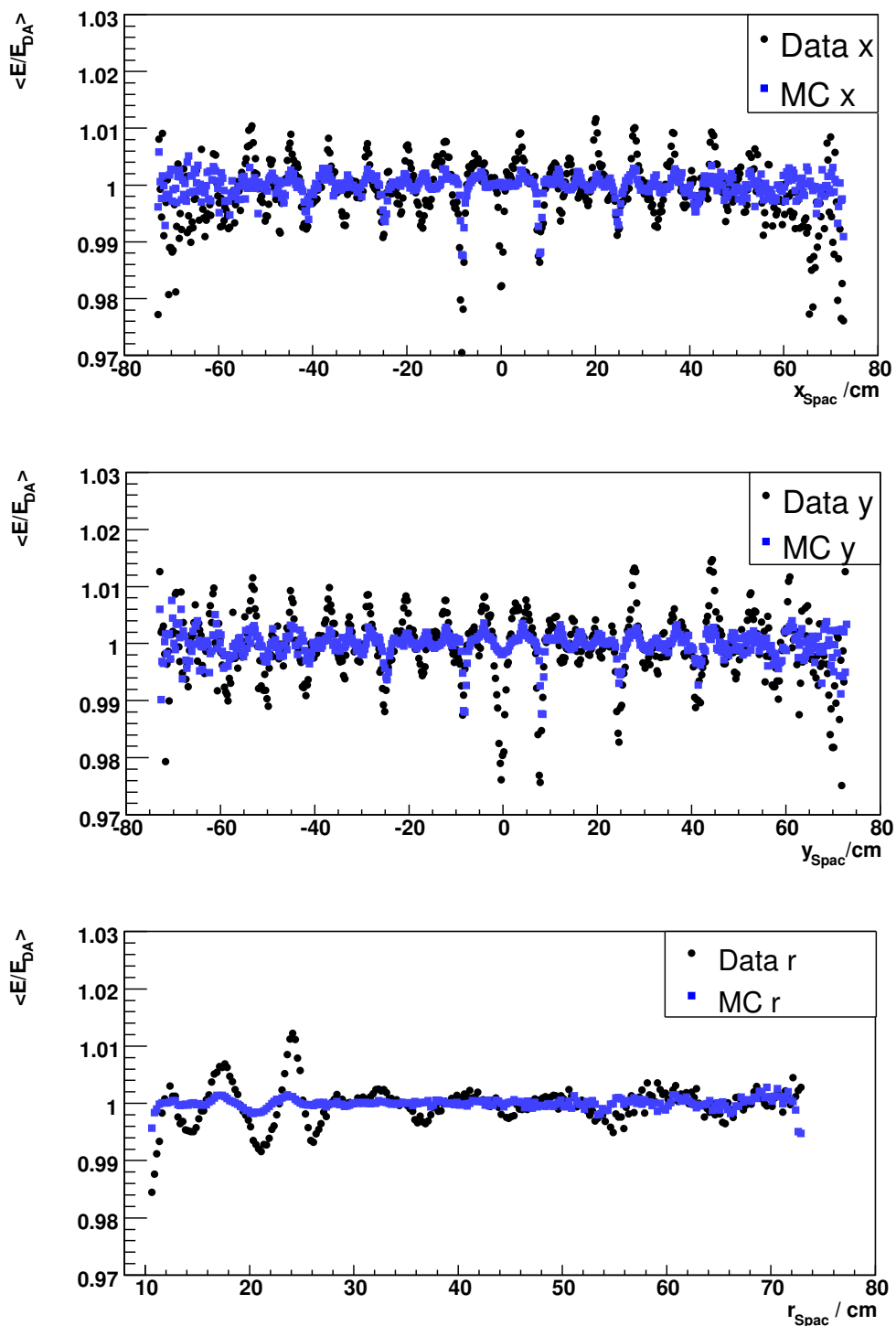


Figure 6.6: *SpaCal calibration correction for energy loss in dead material as a function of the impact position on the SpaCal plane given in x_{Spac} , y_{Spac} , and r_{Spac} . The pulls in the former two variables show clearly effects with the periodicity of the SpaCal cell and super module size, while the radial distribution shows effects of the dead material distribution in front of the SpaCal, see figure 4.2.*

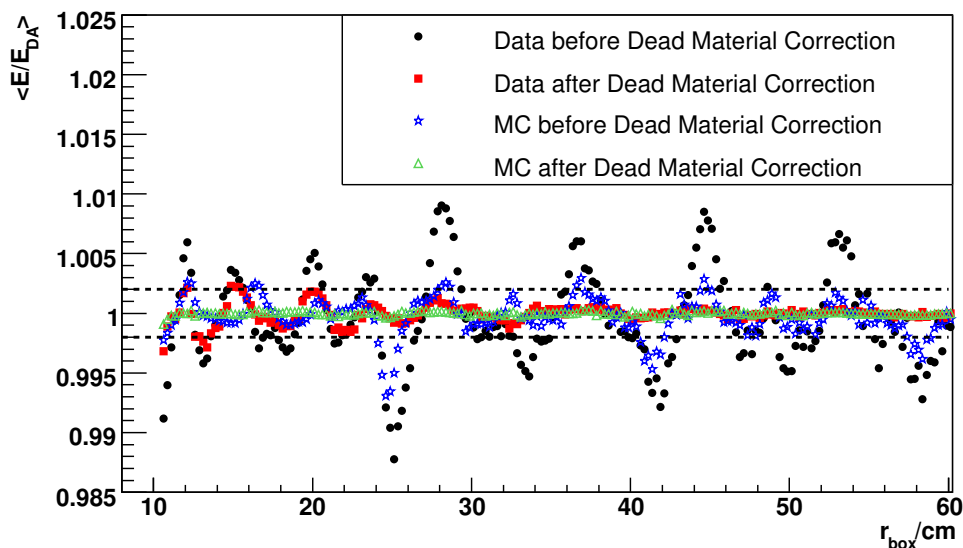


Figure 6.7: Deviation of the SpaCal energy scale from E_{DA} before and after the dead material corrections as a function of r_{box} . The horizontal dashed lines indicate a $\pm 0.2\%$ deviation from unity, which is not exceeded after the correction.

ment between data and MC resolutions. Here the resolution in the MC is adjusted to the one observed in the data by applying additional Gaussian smearing. The functional form of the amount of the smearing σ_E was chosen to depend on E'_e as

$$\frac{\sigma_E}{E'_e} = \begin{cases} p_0 & \text{for } E'_e < p_1 \\ p_0 - p_2 \cdot \frac{(E'_e - p_1)^2}{E'_e} & \text{for } E'_e \geq p_1 \end{cases} \quad (6.8)$$

The optimal parameters were determined in a fit as $p_0 = 0.0087$, $p_1 = 25.6$ GeV, and $p_2 = 6.2 \cdot 10^{-3}$. This leads to an additional smearing of constant 0.9% for low energies and a reduction above 25.6 GeV. The functional form is shown in figure 6.9. The reason for this apparent improvement of the resolution at highest energies is taken from [Sie99] as well: electrons contributing to the entries at the peak position $E'_e \sim 27$ GeV have typically not lost a significant fraction of their energy and are therefore measured better than the ones at slightly lower energies. One should compare the introduced smearing to the expected intrinsic SpaCal resolution according to [N⁺96], as shown in figure 6.9. The applied additional smearing is of the order of the constant term. It should only in the kinematic peak region have an impact compared to the intrinsic resolution which is dominated by the sampling term $\propto 7\%/\sqrt{E/\text{GeV}}$.

In addition to the detailed calibration carried out at energies at the kinematic peak $E'_e \sim 27.6$ GeV, the calibration has to be investigated at lower energies. The main tool is the use of neutral pions decaying to two photons, $\pi^0 \rightarrow 2\gamma$. The invariant mass of the pion can be reconstructed from the two decay clusters. This is not executed here, but well documented in [Var06, H1p07b] for two special data sets taken just before and in the middle of the investigated data set. A consistent correction of +3% for the data energy scale compared to the MC at low $E'_e = 2$ GeV

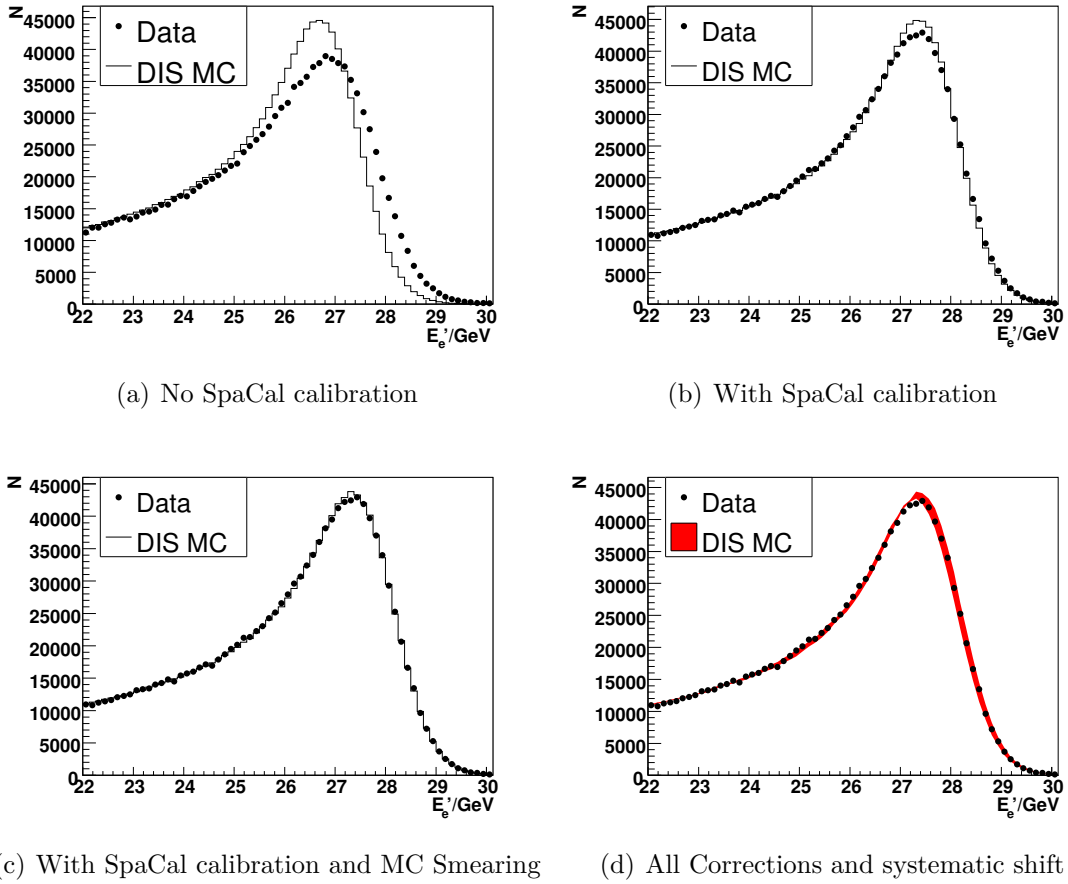


Figure 6.8: Comparison of the scattered electron energy in the kinematic peak region for Data and MC with different corrections applied as indicated. In plot (d) the effect of a shift of the MC energy scale by 0.2% is shown.

was determined. This correction is linearly extrapolated to high energies and confirmed by further checks using $J/\psi \rightarrow e^+e^-$ and QED Compton events. The used correction together with the residual systematic scale uncertainty is shown in figure 6.9.

6.2 HFS Calibration and Tuning

The correct reconstruction of the hadronic final state is important for the extension of the cross section measurement to lower values of y , or equivalently higher x , using the Σ Method. However it is also much more involved than the reconstruction of the electron. The used general algorithm was presented already in section 5.2.4. This section shortly discusses the calibration procedure and further corrections applied to optimise the description. The treatment follows the scheme used for previous inclusive H1 analyses [A⁺01, H1p07b] as described in more detail in [Ark00, Var06].

The goal is to reconstruct an inclusive *hadronic vector* \vec{p}_{HFS} , which can be used to derive the interesting quantities $(E - p_z)_{HFS}$ and $p_{t,HFS}$. The contributions of the different subdetectors, LAr and SpaCal calorimeter, and tracks reconstructed

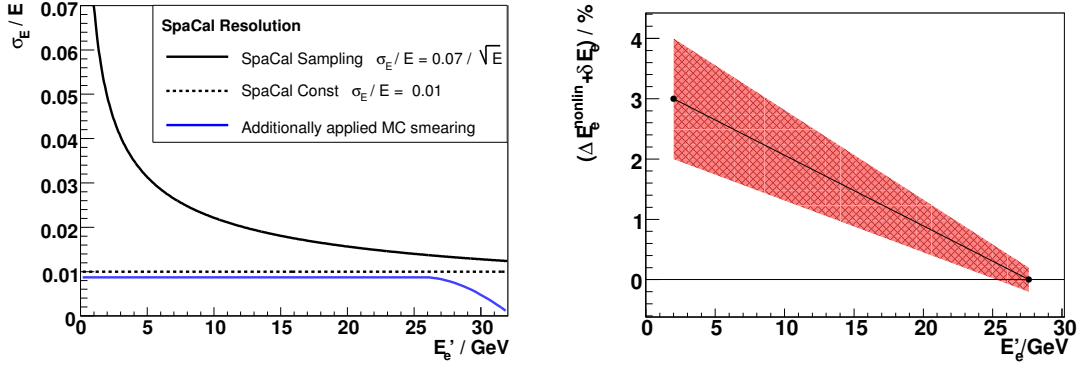


Figure 6.9: Left: SpaCal intrinsic resolution compared to the additionally applied smearing in the MC. Right: Correction of the data energy scale for nonlinear effects at low energies by ΔE_e^{nonlin} and the assigned residual systematic uncertainty $\delta E_e'$ of 1% at low and 0.2% at high electron energy.

by the Central Tracker, can be distinguished

$$\vec{p}_{HFS} = \vec{p}_{HFS}^{LAr} + \vec{p}_{HFS}^{Tracks} + \vec{p}_{HFS}^{SpaCal}. \quad (6.9)$$

The tracks are reconstructed by the standard H1 software with good quality, but the calorimeters need to be calibrated and corrected for noise influence and possible differences between the simulation and the data.

Starting from equation 6.9, the contributions to $(E - p_z)_{HFS}$ follow an additive relation as well, which translates to the reconstruction of $y_h \propto (E - p_z)_{HFS}$. The contributions of different detectors are reconstructed with different properties and therefore a good description of the HFS energy flow should be reached and can be investigated using the fractions f_{HFS}^i

$$f_{HFS}^i = \frac{(E - p_z)_{HFS}^i}{(E - p_z)_{HFS}}. \quad (6.10)$$

As the reconstruction of y_Σ is similar, results are also applicable there.

6.2.1 Hadronic SpaCal

Due to the limited length of the SpaCal of a total of $\sim 2\lambda$ hadronic interaction lengths and the non-compensating nature, its response to hadrons needs special optimisation. Starting from the equation describing the Double Angle reconstruction 6.1, it follows that the polar angle of the electron θ_e and the hadronic angle defined in equation 4.7 are related via the inelasticity y in the following way:

$$\left(\frac{1}{y} - 1\right) \tan \frac{\gamma_h}{2} = \tan \frac{\theta_e}{2}. \quad (6.11)$$

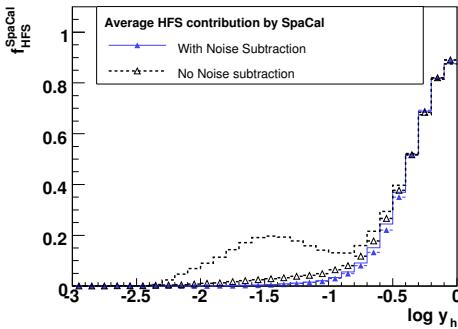
For $y > 0.5$ it is therefore $\gamma_h > \theta_e$ and one should expect a significant fraction of the HFS to be measured in the SpaCal. As the presented measurement is limited to lower $y < 0.6$, the response of the SpaCal to the HFS is not of prime importance.

The starting point for the measurement of \bar{p}_{HFS}^{SpaCal} is the sum of all cells not belonging to the scattered electron reconstructed by the H1 software at the *final energy scale*. As investigated in [Gla98], this measurement has to be multiplied by ~ 1.5 . For this analysis the total correction factor of 1.45 was found [Pet07], which is applied to both data and MC.

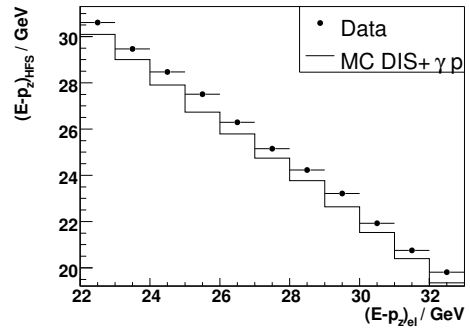
Without further corrections, the $(E-p_z)_{HFS}$ fractions contributed by the SpaCal are seen to be large $f_{HFS}^{SpaCal} \sim 0.8$ at high y as expected, see figure 6.10 (a). However even at low $y < 0.1$ significant contributions are visible. These cannot be due to HFS particles, as the general direction γ_h is pointing in the forward direction. This extra activity may be induced by the scattered electron: energy may leak outside the electromagnetic cluster due to showering or radiative photons emitted at large angles. The influence of these sources is expected to be proportional to E'_e and the *noise* is reduced as

$$E_{HFS}^{SpaCal} = \max\left(0, E_{HFS}^{SpaCal} - \beta E'_e\right). \quad (6.12)$$

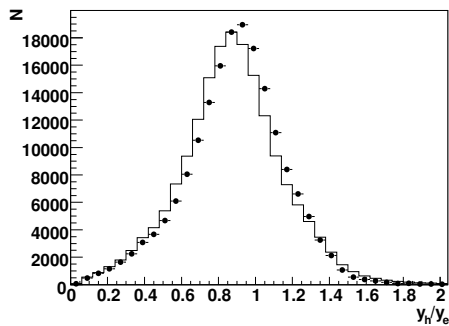
For the data taken in 1996 this method and the coefficient $\beta = 0.03$ was originally proposed in [Gla98]. In [Var06] a value of $\beta = 0.10$ was chosen for the analysis of data with a shifted vertex distribution and therefore enhanced showering effects. Balancing the requirements for a good reconstruction by the Σ Method at high and low y , an optimised value of $\beta = 0.075$ is used here.



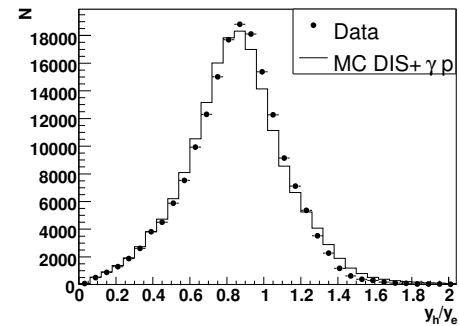
(a) Effect of the SpaCal noise suppression on y_h fraction f_{HFS}^{SpaCal} in data (points) and MC (lines)



(b) Mean of $(E-p_z)_{HFS}$ in slices of $(E-p_z)_{el}$: SpaCal HFS energy scale shifted in data by ~ 600 MeV w.r.t MC



(c) Comparison y_h/y_e for $0.4 < y_e < 0.6$ shows clear shift data - MC



(d) Comparison y_h/y_e for $0.4 < y_e < 0.6$ after data adjustment

Figure 6.10: Illustration of the two adjustments of the HFS contribution given by the SpaCal

A possibility to investigate the response of the SpaCal to the HFS in more detail at high $y \sim 0.5$ is to compare it to the response to the electron. Due to the conservation of $(E - p_z)_{tot} \sim 55$ GeV, the contributions by the electron and the one of the HFS $(E - p_z)_{HFS}$ should be directly correlated. This is displayed in figure 6.10 (b) for the relevant range of $0.4 \lesssim y \lesssim 0.6$. A shift of the data energy scale of 600 MeV is observed. This is further subtracted from the SpaCal HFS contribution in data and a systematic uncertainty of half this shift, i.e. 300 MeV, is associated with it.

Similarly one can compare the measurement of the inelasticity by the electron to the hadron method, y_h/y_e , for the phase space $0.4 < y_e < 0.6$, where the measurement of y_e is very precise and y_h is mostly influenced by the SpaCal contribution. In figures 6.10 (c, d) the distributions are shown before and after the application of the correction in data. The agreement of the data to the MC distribution is improved, the residual disagreement is covered by the assigned systematic uncertainty.

6.2.2 LAr Calibration

The electron in the SpaCal is detected as a single compact cluster. In contrast to this, there are typically many particles created in the HFS, which are then detected as several smaller energy depositions or tracks. Here the depositions in the LAr calorimeter are investigated in more detail. Two typical event configurations at lower and higher y were shown in figure 4.10.

The reconstruction of the HFS in the LAr is done using the sum of all cell energies at the *final energy scale* of the H1 software. As the LAr calorimeter has a fine granularity with 45,000 cells, the software can perform corrections for losses in dead material and reweight the electromagnetic and hadronic shower contributions to compensate for their different response [A⁺97b]. During the readout and the reconstruction already several *online noise cuts* are applied. The signal loss due to these cuts cannot be recovered, however it should be simulated in the MC as well as possible. The FSCOMB algorithm explained in section 5.2.4 rejects further isolated energy depositions below certain thresholds on the analysis level. The result is a split of the LAr HFS vector as

$$\vec{p}_{HFS}^{LAr All} = \vec{p}_{HFS}^{LAr} + \vec{p}_{HFS}^{LAr Noise}, \quad (6.13)$$

where typically only the *LAr signal* \vec{p}_{HFS}^{LAr} is considered for the event reconstruction. A part of the identified noise may be caused by signal clusters. It is therefore important to determine, if the noise simulation and subtraction is well described in the simulation. This will be mostly done by investigating the y_h -fractions f_{HFS}^i and especially $f_{HFS}^{LAr Noise}$. The calibration procedure should eventually make up for the signal loss due to online noise suppression and the subtracted FSCOMB noise.

The HFS is calibrated using the transverse momentum balance between the scattered electron $p_{t,e}$ and the reconstructed HFS $p_{t,HFS}$. As calibration procedure a *Lagrangian method* introduced in [Ark00] is used, which minimises the functional of the form

$$L = \sum_{i=1}^N \left\{ \left(p_{t,e} - p_t^{SpaCal} - p_t^{Track} \right)_i - \sum_{j=1}^M \alpha_j (p_t^{LAr})_{ij} \right\}^2. \quad (6.14)$$

The summation $i = 1 \dots N$ runs over all specially selected calibration events. The contributions of the LAr are split into $j = 1 \dots M$ regions. Due to the LAr structure the regions are the 8 wheels, subdivided into 8 octants and 2 sections, i.e. electromagnetic and hadronic section, which are calibrated with the constants α_j respectively. The set of M linear equations obtained from the minimisation $\partial L/\partial \alpha_j = 0$ is solved using matrix techniques. The results for the procedure are taken from [Pet07] and are displayed in figure 6.11. The calibration constants for the electromagnetic sections are rather similar for data and MC, while they differ for most of the hadronic sections and especially in the very forward region. In the following the impact of this calibration on the reconstruction of DIS events is discussed shortly.

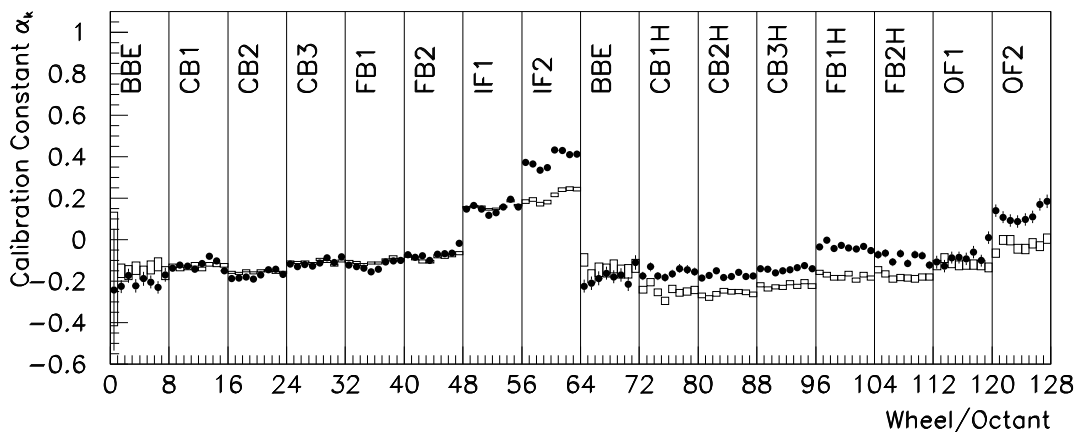
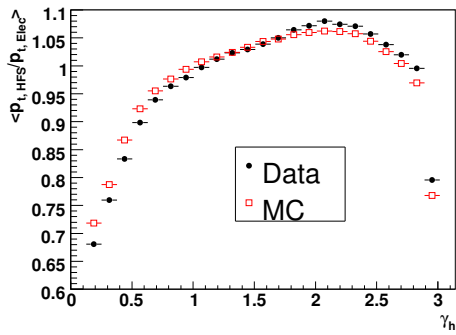


Figure 6.11: LAr calibration constants determined with the Lagrangian Method, taken from [Pet07]. Points are the data constants, the open symbols are the corresponding MC values. The location and the naming scheme for the sections are explained and shown in figure 3.4, the 8 points within one section correspond to the eightfold azimuthal division of the LAr calorimeter.

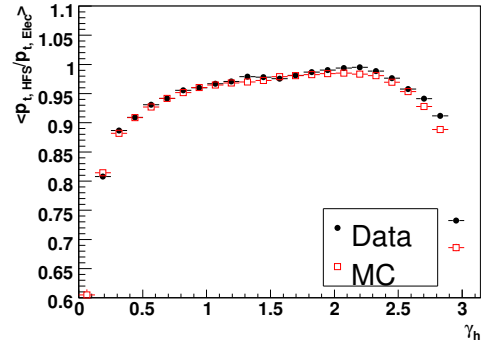
6.2.3 HFS Description in the DIS Analysis Sample

The energy and the polar angle of the scattered electron can be determined with good precision. Therefore also the transverse momentum $p_{t,e}$ is well defined. Due to the momentum conservation, one could naively expect a p_t balance ratio near unity $p_{t,HFS}/p_{t,e} \sim 1$ for all events. However losses in the detection of the HFS are unavoidable and therefore the mean of the distribution $\langle p_{t,HFS}/p_{t,e} \rangle$ depends on the event kinematics. For the measurement of the cross section it is again important to reproduce the behaviour of the data as well as possible in the MC simulation. In the following the mean and the width of the $p_{t,HFS}/p_{t,e}$ distributions are investigated as a function of variables sensitive to the direction of the hadronic energy flow like γ_h , y_Σ , or $p_{t,e}$. These two parameters are extracted in Gaussian fits limited to the range $0.5 < p_{t,HFS}/p_{t,e} < 1.5$.

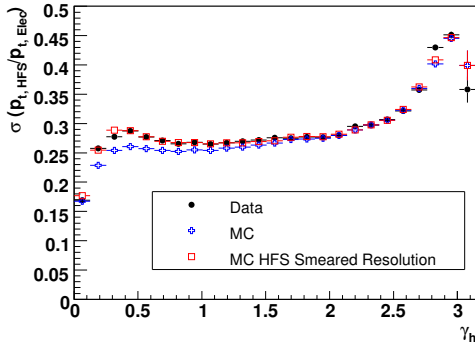
In the figures 6.12 (a, b) the dependence of $\langle p_{t,HFS}/p_{t,e} \rangle$ on the hadronic angle γ_h is displayed before and after the calibration. A reasonable agreement is observed already before the calibration, however the discrepancy increases in the forward



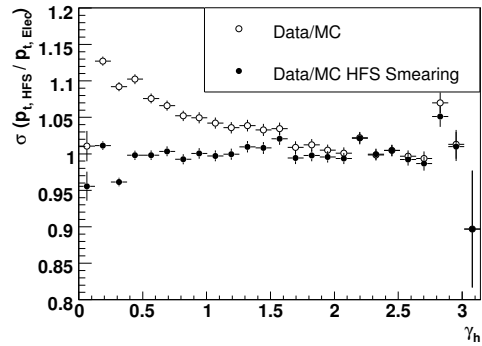
(a) p_t balance without LAr calibration



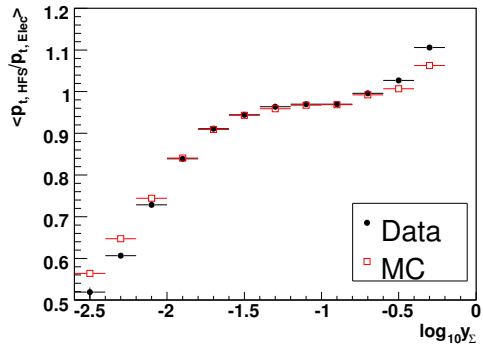
(b) p_t balance with LAr calibration



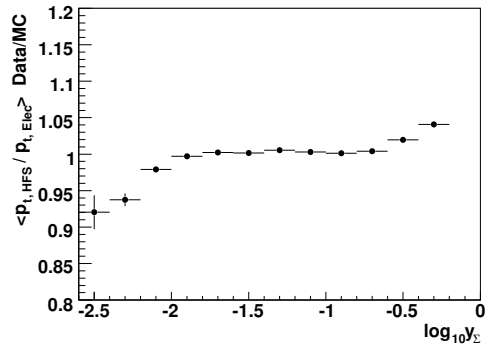
(c) Absolute HFS resolution in data and MC before and after additional smearing



(d) Relative data/MC HFS resolution before and after additional smearing



(e) Cross check of the HFS Energy Scale as fct. of y_Σ in data and MC



(f) Cross check of the HFS Energy Scale as fct. of y_Σ , relative data/MC

Figure 6.12: Tests of the HFS Energy scale and resolution in data and MC simulation using the mean and width of the $p_{t, HFS}/p_{t, e}$ distributions as function of γ_h and y_Σ .

region $\gamma_h < 40^\circ$. Also the mean $\langle p_{t,HFS}/p_{t,e} \rangle$ deviates from unity by typically 5–10%. After the calibration the agreement is improved a lot in the forward region and the mean of the distribution is closer to 1 regardless of the phase space.

In the figures 6.12 (c, d) the width of the Gaussian fits $\sigma(p_{t,HFS}/p_{t,e})$ is shown as a function of γ_h , which is equivalent to the achieved resolution in the HFS measurement. At high γ_h it deteriorates significantly due to the worse measurement of the SpaCal. While the resolution is well described for central and backward pointing γ_h , the discrepancy is growing for low γ_h and reaches up to 10%. The reason may be an unsatisfactory simulation of the noise or the dead material. To adjust the behaviour of the simulated events an additional smearing of the HFS energy scale in the MC was introduced. For this the resolutions $\sigma(p_{t,HFS}/p_{t,e})_{Data}$ and $\sigma(p_{t,HFS}/p_{t,e})_{MC}$ are fitted with a polynomial of degree 8 as a function of γ_h and all HFS measurements are smeared by a Gaussian of the width

$$\sigma_{Smear}(\gamma_h) = \sqrt{\sigma_{Data}^2(\gamma_h) - \sigma_{MC}^2(\gamma_h)}. \quad (6.15)$$

As can be seen in the figures 6.12 (c, d) the resolutions of the data and the simulation are well matched after the adjustment. The behaviour is also improved if investigated as a function of $p_{t,e}$ or y_Σ .

In [Var06] it was found, that the momentum balance is usually well described for $y_\Sigma > 0.01$, but worse for smaller inelasticities. A similar behaviour is found in the phase space analysed here, as can be seen in the figures 6.12 (e, f). The data-MC agreement is better than 2% in the range $0.01 < y_\Sigma < 0.3$. For lower $y_\Sigma < 0.01$ there is an approximately linear rise in the deviation with $\log_{10} y_\Sigma$. The cause for the deviation is thought to lie mostly in the imperfect description of the noise in the LAr calorimeter. The additional deviation at high $y_\Sigma > 0.3$ is covered by the assigned systematic uncertainty on the SpaCal HFS contribution, which is equivalent to about 3%, while for the low y region the assigned systematic uncertainty is increased beyond the 2% used for the rest of the phase space to reach 10% for $y = 0.001$. Figure 6.13 shows the dependence derived from figure 6.12 (f).

Finally, the description of the hadronic energy flow is investigated using f_{HFS}^i , the average contributions to y_h , as a function of y_h , see figure 6.14. As expected the SpaCal contributes mostly at highest y , while the LAr calorimeter covers the medium and lower y domain. In the medium y domain tracks contribute roughly 30% to the y_h measurement. For the MC simulation the ranges allowed by the systematic uncertainties are indicated. Considering these variations a reasonable agreement is observed in most of the y_h range. The large noise influence below $y_h < 0.01$ is visible, which on average constitutes an effect of 20 – 80% on the measured y_h . The assigned systematic uncertainty of 15% of the subtracted FSCOMB noise is mostly adequate, but fails to cover the full discrepancy at very low $y < 0.006$, which is just the edge of the analysis range and believed not to have a severe impact on the DIS cross section measurement ⁴. The uncertainties on the noise subtraction procedure

⁴This discrepancy in the noise simulation of the LAr calorimeter is a long standing problem, which was also investigated in detail in [Var06, Beh06]. The reason is thought to lie in the imperfect simulation. For the MC events special data taken without online noise suppression is used to add random energy depositions. While this procedure works reasonably in general, the available special noise data is statistically limited and may not perfectly reflect the actual data taking conditions.

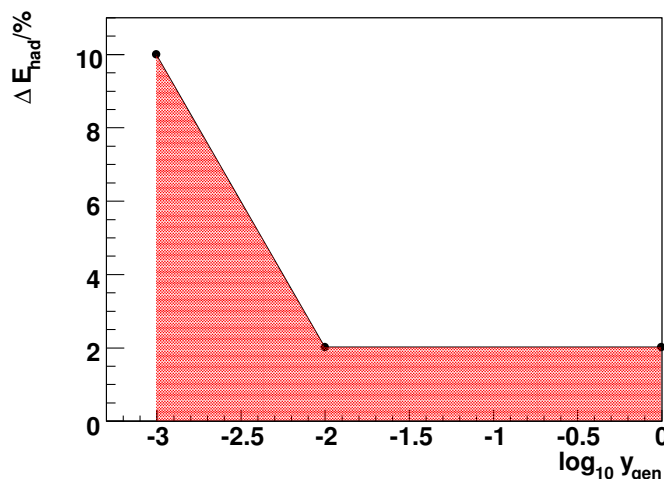


Figure 6.13: Assigned uncertainty on the hadronic energy scale for the LAr and Track contribution. The uncertainty of the SpaCal contribution is not shown and is equivalent to 3%, which is the dominant error source for $\log_{10} y > -0.3$.

and the LAr energy scale is causing the largest uncertainties of this analysis for the measurement with the Σ method at lower y .

6.3 Alignment

The polar angle of the scattered electron θ_e is measured using different subdetectors of H1. In this analysis it is usually determined using the Central Tracker and the BDC. Alternatively the CIP and the BDC are employed if the Central Tracker could not reconstruct the event vertex. Considering their weight and size, the nominal positions of the subdetectors must be corrected by small amounts to the real positions. The Central Tracker of H1 defines the reference coordinate system to which the position of the other subdetectors should be measured.

In this work this section will be kept short, as it has been performed mostly by other people with the exception of the CIP vertex reconstruction and alignment.

6.3.1 Backward Detectors

The alignment of the backward detectors BDC and SpaCal can be determined using QED Compton events or electrons with a track measured in the Central Tracker. The measurement in the central tracker can be compared in azimuthal angle ϕ and polar angle θ to the detector to be aligned. From the behaviour of the difference as a function of ϕ or θ of the reference measurement, the alignment constants can

Most of the noise is actually beam related and an improved simulation mechanism is tested at the moment [Gla07]. This will add noise depositions to the LAr calorimeter using events taken by the random trigger, which are constantly recorded at a rate of 0.2 Hz. First results have shown, that the amount of noise identified in the simulated data indeed increases [Pet07] and the small discrepancy visible in figure 6.14 is expected to be reduced.

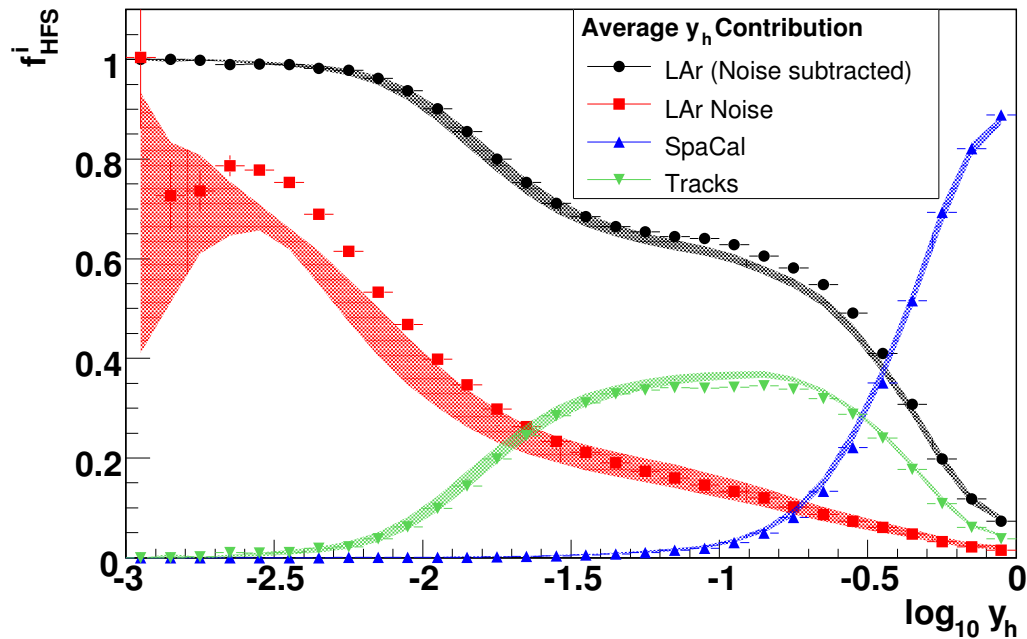


Figure 6.14: Contributions to y_h from different detector components, points are data and the shaded areas represent the range of the MC simulation considering the assigned systematic uncertainties.

be extracted. The QED Compton events can be exploited due to their property to have two clusters in the SpaCal back-to-back in azimuth. It is found, that simple shifts in the x , y , and z -direction are sufficient to remove the misalignment.

These studies have been performed in great detail in [Mer05] and the results were confirmed by an independent measurement [Pet07]. The different analyses and methods typically show some small systematic differences. For the systematic error on the θ_e measurement the alignment of the BDC is most critical. In this analysis the shifts relative to the nominal position of $\Delta x_{BDC} = 0$, $\Delta y_{BDC} = 0.18$ cm, and $\Delta z_{BDC} = -0.52$ cm are used. These values taken from [Pet07] agree with [Mer05] to ~ 0.05 cm in the $x - y$ plane and 0.2 cm in the z -direction. The effect on the θ_e measurement is therefore estimated to be about 0.2 mrad.

The BST alignment is performed with good precision using electron tracks to determine shifts and rotations of all its individual wafers. This is done using the global minimisation package Millipede [Blo]. The results are again taken from [Pet07] and the typical precision achieved is here on the same level of 0.2 mrad in θ_e .

6.3.2 CIP

The reconstruction of the event vertex using the CIP was shortly described in section 5.2.3. The used algorithm has been written specifically for this analysis. Therefore the alignment of the CIP is investigated here with respect to the Central Tracker measurement. As reference a basically background free sample with an electron energy of $20 \text{ GeV} < E'_e < 32 \text{ GeV}$ and a well reconstructed central vertex with a

precision of $\Delta z_{vtx} < 2$ cm with at least two vertex fitted tracks is used. Only events with a CIP vertex reconstructed by hits in both layers, $N_{CIP}^{HIT} = 2$, are considered.

In figure 6.15 the differences of the polar angle measurement achieved by the CIP and the Central Tracker vertex $\Delta\theta = \theta_{CT} - \theta_{CIP}$ is shown as a function of ϕ_{Spac} . A sinusoidal dependence as well as an offset is visible, corresponding to shifts in the $x - y$ plane and the z direction respectively. For data and MC the alignment constants were determined from the fit values as in [Gla98] and are collected in table 6.2. In figure 6.15 it is shown, that for both data and MC the average $\Delta\theta$ is reduced considerably after the application of the constants.

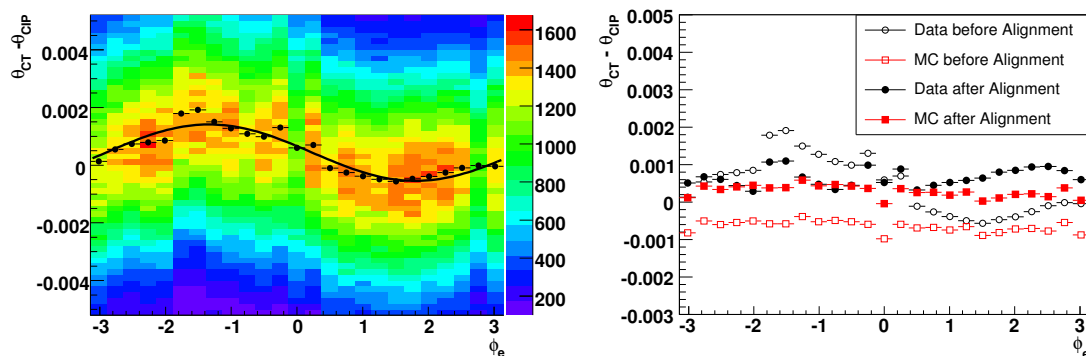


Figure 6.15: Dependence of the relative CIP misalignment $\Delta\theta = \theta_{e,CT} - \theta_{e,CIP}$ on ϕ_{Spac} . Left: Full distribution, fit in slices of ϕ_e and sin function for unaligned data; Right: Mean of Gaussian fits in slices of ϕ_e for data and MC before and after the application of the alignment constants.

	CIP Alignment Constants		
	Δx / cm	Δy / cm	Δz / cm
Data	0.028	-0.092	-0.1
MC	0.0	0.0	-0.4

Table 6.2: CIP alignment constants in data and MC

The z -shift in MC is used to remove a small θ bias compared to the determination using the Central Tracker vertex. As the determination of the CIP vertex is based on the rather coarse pad structure of the CIP and only two layers are provided, these biases are difficult to avoid or correct for. Therefore the systematic uncertainty on θ_e determination with the CIP is taken to be 0.5 mrad.

6.4 BDC Efficiency

The electron identification and polar angle measurement is completed by the BDC. The selection requires a matching BDC track segment with a minimum number of hits least $N_{BDC}^{Hit} \geq 4$ and matching the SpaCal cluster better than $\Delta r_{SpacBDC} < 2.5$ cm. These criteria have a certain efficiency ϵ_{BDC} , which must be well reproduced

in the simulation. Otherwise the difference in the efficiencies will directly influence the measured cross section.

The dependence of ϵ_{BDC} on r_{Spac} is shown in figure 6.16 for data and MC. It is here simply defined as the fraction of events passing this selection criteria of the number of events passing all except this one. It is apparent, that the data has a localised problem around $r_{Spac} \sim 25$ cm, where the efficiency drops by $\sim 10\%$. This effect has been observed in all previous H1 analyses in this region, see e.g. [Kat97, Beh06]. It is most probably related to deficits in the construction of the BDC in the region of the transition cells at $r_{BDC} \sim 22$ cm, see figure 3.7. There the field configuration or the drift-time algorithm are not optimised for the geometry and hits are lost. In addition the MC simulation for the outer BDC region shows a slightly lower efficiency than observed in data, which has to be corrected as well.

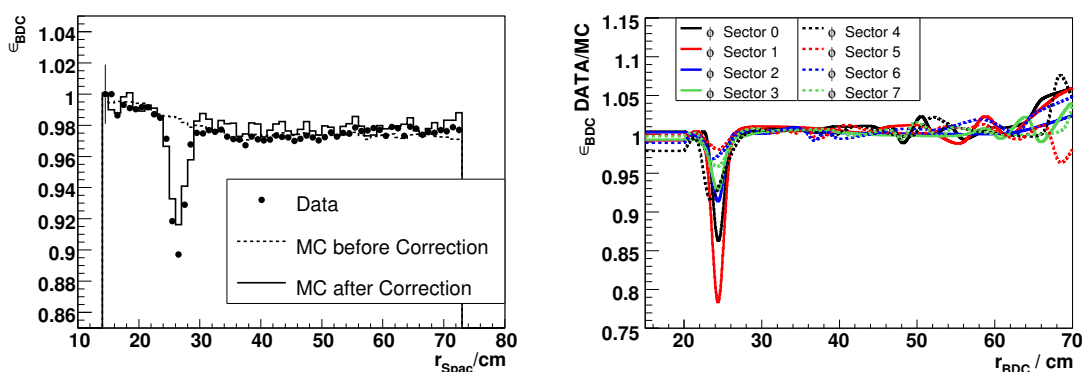


Figure 6.16: Left: BDC efficiency in data and MC before and after applying the efficiency correction, right: BDC efficiency correction functions measured with a sample reconstructed by the BST, results from [Pet07].

In this analysis the efficiency of the BDC is measured in data and MC using a clean reference sample reconstructed with the help of the BST. This is the first time this correction has been performed based on a well measured and fully independent sample. The correction functions are determined in eight ϕ sectors according to the BDC geometry. The results are taken from [Pet07] and shown in figure 6.16.

After applying the correction in the MC, the BDC efficiency description is much improved as shown. The sharp efficiency drop at $r_{Spac} \sim 25$ cm is mostly, but not perfectly reproduced. The reason is a small, but consistent bias in the BDC measurement in the low efficiency region, which is not corrected for in this analysis. Measured as a function of reconstructed Q_e^2 , the correction is about 3% for $10 \text{ GeV}^2 < Q_e^2 < 20 \text{ GeV}^2$ and less than 1% everywhere else. Therefore an uncorrelated systematic uncertainty of 1% for the bins up to $Q^2 \leq 20 \text{ GeV}^2$ and 0.5% at all higher Q^2 is assigned.

Chapter 7

DIS Cross Section Results

In this chapter the ingredients for the cross section measurement from the previous three chapters are collected and the main result of this work, the measurement of the inclusive deep-inelastic scattering cross section, is presented. Chapter 6 described in detail the work carried out to measure as precisely as possible the basic event properties: the energy and polar angle of the scattered electron, and the inclusive hadronic final state vector. These measurements are used in the DIS event selection, which was presented in chapter 5. Further on the measurements are used to reconstruct the event kinematics and eventually measure the cross section as explained in chapter 4.

To correctly measure the cross section using the Monte Carlo method from equation 4.23, it is important that the simulation properly describes the behaviour of the data. For many of the properties this was shown in the previous chapters, for the remaining selection criteria this will be done in the following three sections.

After these studies, the effect of systematic uncertainties is discussed and the measurement is presented and put into the context of previous publications.

7.1 Vertex Reconstruction Efficiency

One of the main criteria for the event selection is the requirement of a reconstructed event vertex. As discussed already in section 4.4.4 this eventually also limits the accessible phase space. The reconstruction can be done using tracks measured in the Central Tracker from either HFS particles or the scattered electron itself. For this analysis this is complemented by the use of the CIP, which can reconstruct the vertex from the scattered electron at higher θ_e up to 170° . The use of particles from the HFS is conceptually not well suited for an *inclusive* measurement, where any HFS configuration should be taken into account. It however considerably improves the reconstruction quality. One then has to demand, that the simulation describes the reconstruction efficiency well. The hadronisation model used in the DJANGO generator is known to reproduce the HFS topologies well in general. Yet it has been shown in [Beh06], that *diffractive final states* are only approximately described.

The possibility to use an independently reconstructed *reference sample* is important, as this allows the selection for nearly pure signal events from the main bunch region. The vertex reconstruction efficiency can then be determined for data and MC in the same way. The efficiency to reconstruct either a Central Tracker (CT)

or a CIP vertex is defined as

$$\epsilon_{Vtx, CT||CIP} = \frac{N_{Ref\&\&(CT||CIP)}}{N_{Ref}}. \quad (7.1)$$

The number of events in the reference sample N_{Ref} is determined applying the standard selection criteria from table 5.2, except that all measurements based on the CT, CIP, or BDC are replaced by BST measurements. The number of events with a reconstructed CT or CIP vertex $N_{Ref\&\&(CT||CIP)}$ is then determined requiring in addition the CT or CIP selections. The kinematics of the events is calculated using the quantities used for the reference selection.

The selection criteria for the BST are a minimum of $N_{BST}^{Hit} \geq 3$ BST hits and the distance of the reconstructed BST track extrapolated to the z position of the SpaCal cluster should be $\Delta r_{SpacBST} < 1.0$ cm. In figure 7.1 the distributions of these quantities are shown. The observed agreement is reasonable. However, as no adjustments on the MC simulation have been performed, the overall efficiency of the BST in the simulation is somewhat higher than in data. For the use as a reference this is irrelevant. As shown in figure 7.2, the reconstructed position of the event vertex z_{vtx} typically agrees well between the reference value and the value reconstructed by the CT or CIP.

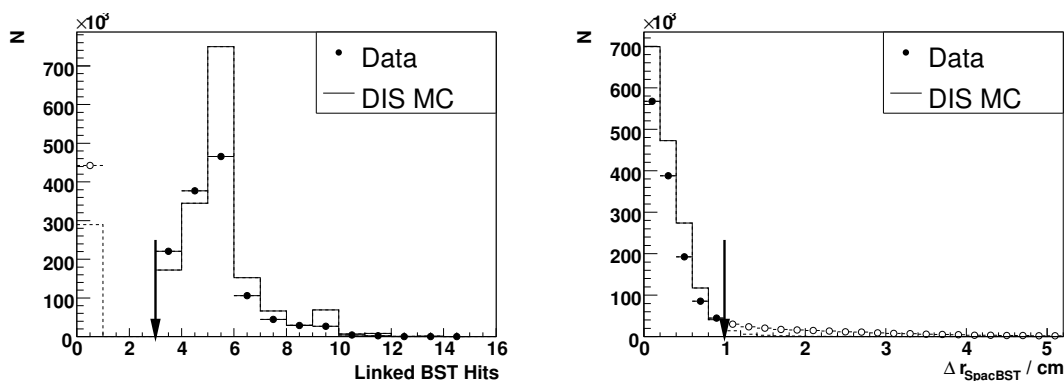


Figure 7.1: Distributions for the basic selection criteria for the BST reference sample: number of linked BST hits N_{BST}^{Hit} (left) and matching to the SpaCal cluster $\Delta r_{SpacBST}$ (right). Arrows indicate the selection performed. Distributions are normalised to luminosity.

The total efficiency ϵ_{Vtx} to reconstruct either a CT or a CIP vertex, is in the following also studied in more detail. For this purpose the sample $N_{Ref\&\&(CT||CIP)}$ is decomposed into additive contributions of events with both or only one type of vertex reconstructed

$$N_{Ref\&\&(CT||CIP)} = N_{Ref\&\&CTonly} + N_{Ref\&\&CIPonly} + N_{Ref\&\&CT\&\&CIP}. \quad (7.2)$$

The division is performed such, that all events reconstructed by the Central Tracker are given by the sum $N_{Ref\&\&CTonly} + N_{Ref\&\&CT\&\&CIP}$ and similar for the CIP. Ideally all the components should be well described in the simulation and the total efficiency should be close to 100% in the analysis range. Eventually it is sufficient, if the total efficiency is the same in data and the simulation.

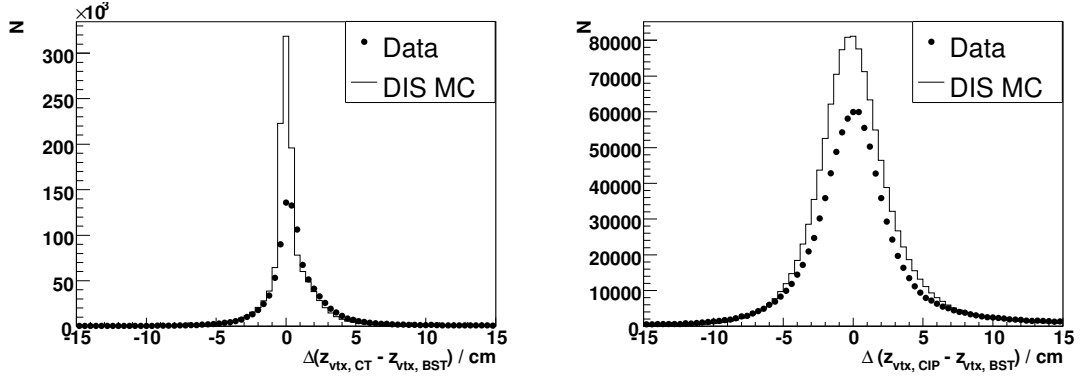


Figure 7.2: Difference of the event vertex position z_{vtx} reconstructed by the BST and the CT (left) or CIP (right). Distributions are normalised to luminosity.

The general behaviour is shown in figure 7.3 as a function of y_Σ , which is closely related to the hadronic energy and particle flow. The overall efficiency is close to 100% for $\log_{10} y_\Sigma > -1.5$, as particles from the HFS typically fill the central region. Below this point the efficiency of the CT drops rapidly. The efficiency of the CIP on the other hand is reasonably high even below $y_\Sigma < 0.01$, because it does not depend on the HFS. The agreement between data and MC simulation is good.

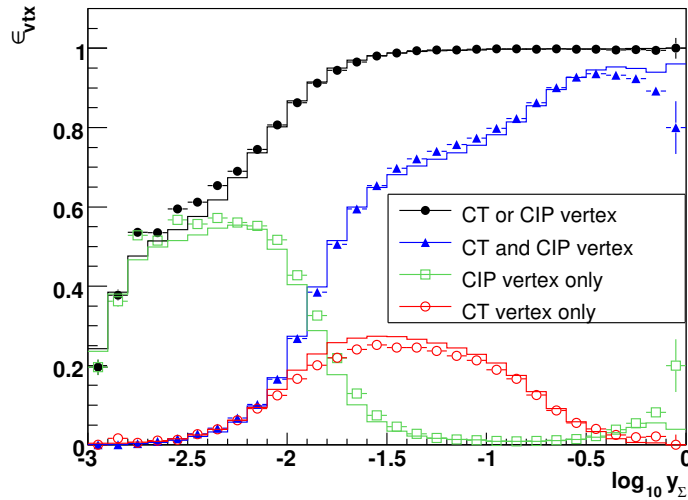


Figure 7.3: Vertex reconstruction efficiency by the CT or CIP as a function of y_Σ for data (symbols) and MC (lines). Shown is the total efficiency by combining CT and CIP (black full dots) and the individual contributions by the CT and CIP according to equation 7.2. The total efficiency of the CT is given by the sum of the contributions CT and CIP and CT only and similar for the CIP.

The final comparison is made in the bins used for the cross section extraction, see figure 7.4. The x and Q^2 of the events are reconstructed using the electron or Σ Method according to the same prescription as used for the final measurement. In all bins the efficiencies of the individual detectors CT and CIP agree well between

the data and the simulation. The events at highest x or equivalently lowest y are dominantly reconstructed by the CIP only, as both the electron and the HFS are typically not within the acceptance of the Central Tracker. On the other hand in the lowest two Q^2 bins the efficiency of the CIP is low, as the electron scattering angle is mostly $\theta_e > 170^\circ$ and therefore out of the CIP acceptance. Overall the total vertex reconstruction efficiency is exceptionally well described to the level of 0.5% and no additional correction is performed. Only in 3 bins at lowest Q^2 and highest x significant deviations of the order 2% are seen. These bins also suffer from a low overall acceptance, as shown in figure 4.9.

7.2 Other DIS Event Selection Cuts

The description of the further selection cuts from table 5.2 is tested on the final analysis sample itself. The efficiency of a certain *cut* is calculated applying all but the cut in question as

$$\epsilon_{Cut} = \frac{N_{all}}{N_{all-Cut}}. \quad (7.3)$$

This efficiency should be well described in the simulation for the signal events. The data also contain background events, which the selection is supposed to reduce. Therefore for data the number of selected events N_{all} and $N_{all-Cut}$ is subtracted for the background taken from the PHOJET normalisation. Typically the selection efficiency is studied as a function of the scattered electron energy E'_e . The electron identification efficiency usually drops towards lower E'_e and the background contamination by γp events increases.

7.2.1 Cluster Based Selection Cuts

The basic electron cluster selection was discussed already in section 5.2.1, all three cuts on r_{log} , E_{had}/E'_e , and E_{veto} are tested as one single requirement. Figure 7.5 shows the efficiency of the imposed selection. It can be seen, that the selection is well described except for the region $E'_e < 15$ GeV. A similar behaviour was observed already in [Var06]. It was traced to the bad description of the logarithmic cluster radius r_{log} in the PHOJET simulation, which is also apparent from figure 5.2. If the procedure to determine the PHOJET normalisation from section 4.3.2 is repeated without applying the cluster based selection, the equivalent γp luminosity is increased from $\mathcal{L}_{\gamma p} = 2.315 \text{ pb}^{-1}$ to $\mathcal{L}_{\gamma p}^{noClus} \sim 4.6 \text{ pb}^{-1}$. Adjusting the normalisation of the γp MC separately for the determination of N_{all} and $N_{all-Cut}$, the cut efficiency is well described within the normalisation and statistical uncertainties. In [Var06] it was further shown, that the selection efficiency for a special background free sample is well described.

7.2.2 BDC Linking Efficiency

The BDC efficiency was discussed already in section 6.4, as it requires a large correction. Determining the BDC linking efficiency as a function of E'_e , a similar problem as in the previous section appears: the BDC selection implies a large change in

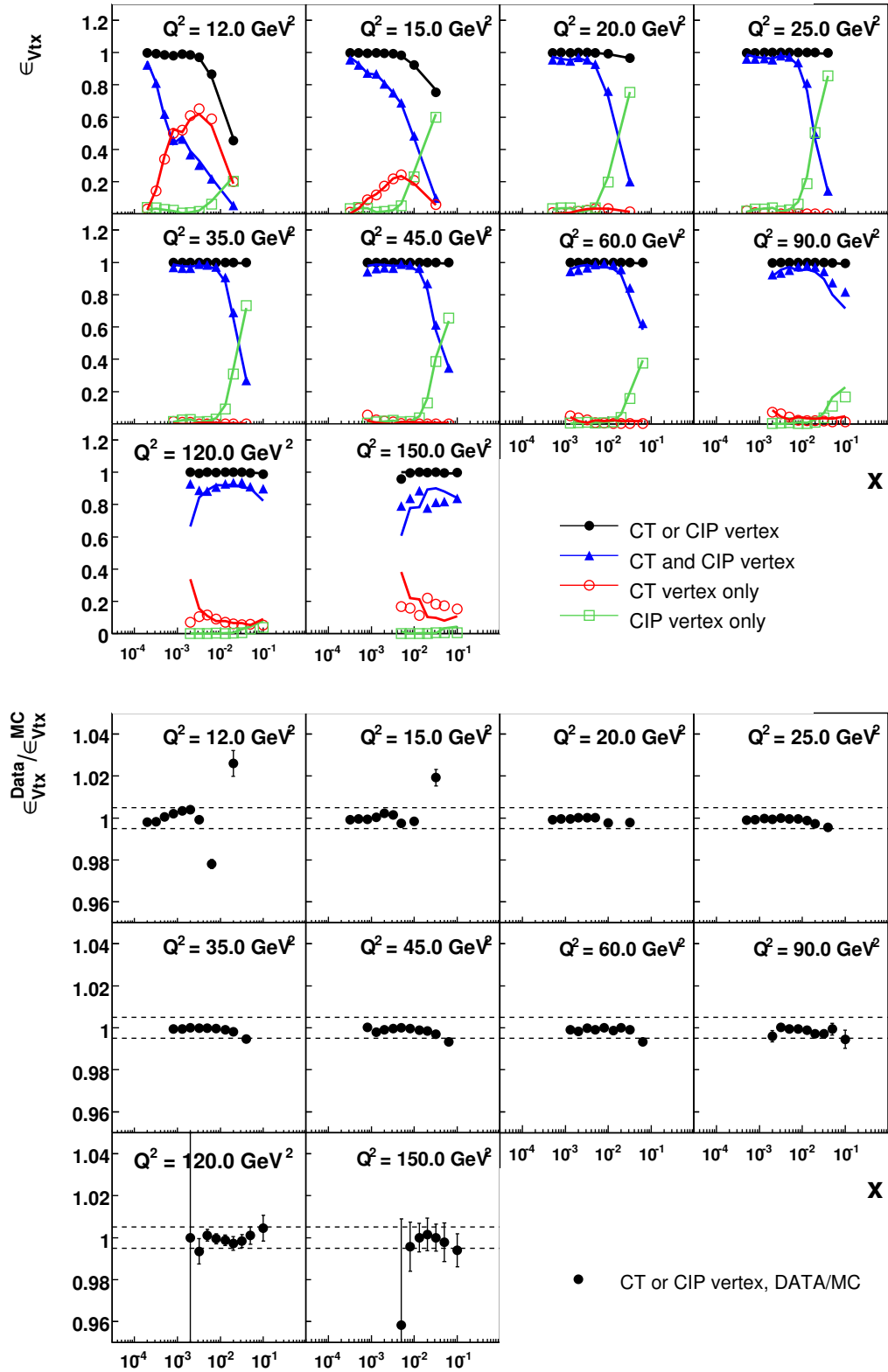


Figure 7.4: Vertex reconstruction efficiency in the selected analysis bins. Top: Total and partial efficiencies in data (symbols) and MC (lines). Bottom: Ratio of the total vertex efficiency in data and MC, the dashed lines indicate a deviation of 0.5%, which is the assigned systematic uncertainty.

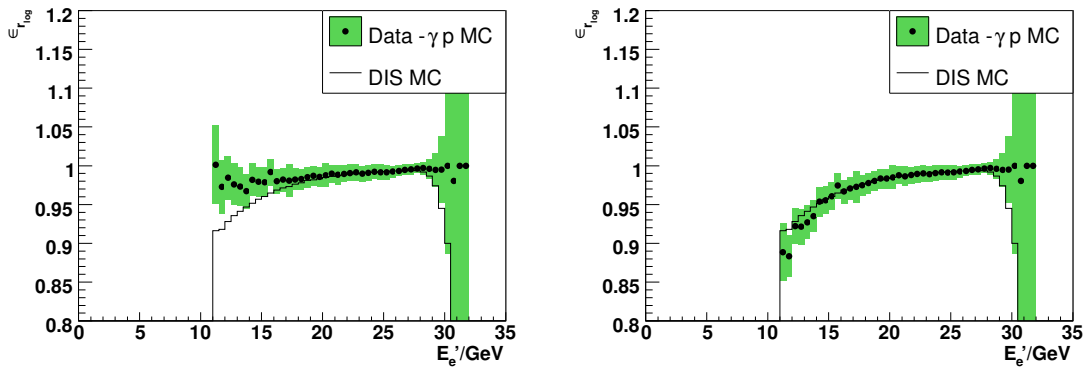


Figure 7.5: Efficiency of the cluster based DIS event selection with the standard PHOJET normalisation (left) and with specially adjusted PHOJET normalisation before and after the selection (right). The shaded band indicates the effect of a systematic 15% variation of the PHOJET normalisation and the statistical uncertainty.

the equivalent γp luminosity from $\mathcal{L}_{\gamma p} = 2.315 \text{ pb}^{-1}$ to $\mathcal{L}_{\gamma p}^{\text{noBDC}} \sim 4.2 \text{ pb}^{-1}$. Taking this and the systematic variation of $\mathcal{L}_{\gamma p}$ by 15% into account, the BDC selection is reasonably well described also for lower E_e' , see figure 7.6.

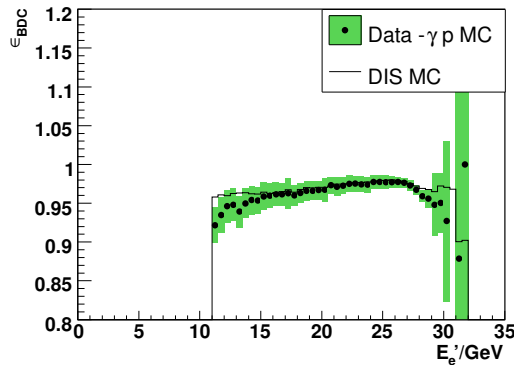


Figure 7.6: Efficiency of the BDC based DIS event selection with the with specially adjusted PHOJET normalisation before and after the selection. The shaded band indicates the effect of a systematic 15% variation of the PHOJET normalisation and the statistical uncertainty.

7.2.3 QED Compton Rejection Efficiency

Elastic QED Compton events are a special subclass of the inclusive DIS sample. They can be rejected by a simple cut introduced in section 5.2 from the analysis to test for possible systematic effects. In figure 7.7 it is seen, that the Compton rejection reduces the electron selection efficiency at lower E_e' . The cut is found to be very well described in the MC sample and no statistically significant effect is observed in the measured cross section. Therefore it is decided, that the QED Compton rejection is not necessary and will not be performed.

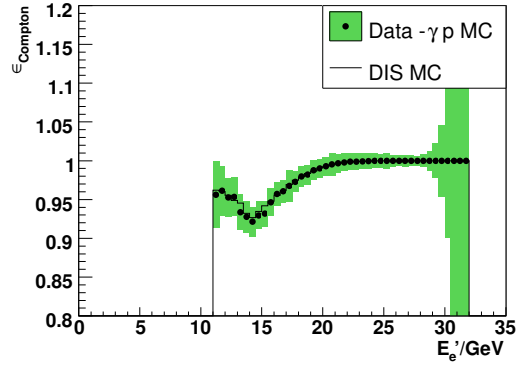


Figure 7.7: Efficiency of the QED Compton rejection cut. The shaded band indicates the effect of a systematic 15% variation of the PHOJET normalisation and the statistical uncertainty.

7.2.4 Momentum Balance Selection Efficiency

In the analysis cuts on the transverse as well as the longitudinal momentum balance are imposed. The selection $p_{t,HFS}/p_{t,e} > 0.3$ demands a reasonable containment of the HFS also at low y . The properties of this p_t balance criterion was studied already in great detail in connection with the LAr calibration in section 6.2.3. A disagreement at low y_Σ was observed. This shows up also in the efficiency study as a small 2% discrepancy at high $E'_e \sim 27$ GeV, see figure 7.8 on the left. Therefore an additional uncorrelated systematic uncertainty of 2% for the low y domain is introduced.

The selection on the longitudinal momentum balance $(E - p_z)_{tot} > 35$ GeV rejects mainly γp background and radiative events with undetected photons. The efficiency of this selection is well described as shown in figure 7.8 on the right. For $E'_e \gtrsim 17.5$ GeV this selection poses no efficiency loss at all, as the electron contribution alone satisfies the cut.

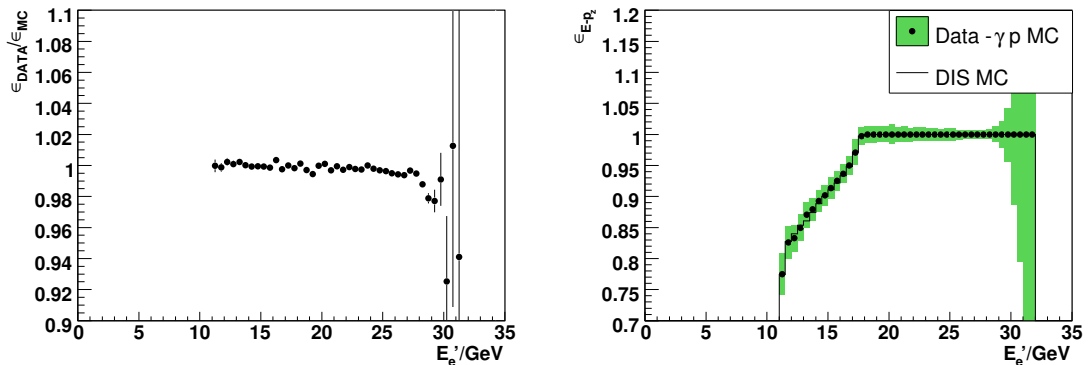


Figure 7.8: Left: Ratio of efficiency of the p_t balance cut in data and MC, which is well described except for a small 2% discrepancy at the kinematic peak. Right: The efficiency of the $(E - p_z)_{tot}$ selection is well described.

7.3 Bin Selection

The binning used for the measurement was already presented and discussed in the sections 4.4 and 4.5. The optimisation of the binning was performed there mainly on the reconstruction properties of the Electron and Σ Methods as well as the detector acceptance. Before extracting the cross section, a final control on event migrations is performed. For this the *purity* and *stability*

$$\text{Purity} = \frac{N_{Rec\&\&Gen}}{N_{Rec}} \quad \text{and} \quad \text{Stability} = \frac{N_{Rec\&\&Gen}}{N_{Gen}}, \quad (7.4)$$

are calculated for each bin from the MC simulation. Here N_{Gen} is the number of events generated and N_{Rec} the number of events reconstructed by a certain method in a given bin. Only events generated and reconstructed in the same bin contribute to $N_{Rec\&\&Gen}$ ¹. A high purity guarantees, that the reconstruction process does not lead to large event migrations into a given bin. If the stability is high, there is no large migration of events out of a given bin.

The results for the Electron and Σ Methods are shown in figure 7.9. They reflect mainly the reconstruction properties of both methods discussed before. The Electron Method achieves a large purity and stability of typically more than 60% at high $y > 0.1$, but much less at lower y . The Σ Method on the other hand achieves values of $\sim 50\%$ down to $y \sim 0.01$ with the chosen binning. The cross section is only calculated in bins, where both purity and stability are above 25%, to keep event migrations to a reasonable level.

The decision, which method to use for the final result is based on the total measurement uncertainty. This effectively limits the use of the Electron Method to $y > 0.1$ and the remaining bins are covered by the Σ Method. With this choice, the purity is always at least 38% and the minimal stability is 42%.

7.4 Control Distributions for the DIS Sample

In this section the description of the data by the simulation is demonstrated by showing various control distributions with all applied corrections and calibrations. For this it is beneficial, if the input structure functions used for the MC cross section calculation are adapted to the measured cross section. This can be achieved by reweighting the simulated events according to the generated kinematics by

$$w_\sigma = \frac{\sigma_{new}(x_{gen}, Q_{gen}^2, y_{gen})}{\sigma_{old}(x_{gen}, Q_{gen}^2, y_{gen})}. \quad (7.5)$$

In order to simplify the calculation of the full cross section, the event kinematics at the hadronic vertex was used, as proposed in [Gla98]. The cross section σ_{old} used for the event generation was calculated using leading order parton distributions with $F_L = 0$ from the PDFLIB [PB00] with the code *GRV5004*. For the initial reweighting the results of a QCD fit to older H1 data was taken from [Leh98] to calculate σ_{new} .

¹The detector acceptance given by the selection criteria on the reconstructed quantities and shown in section 4.4 does not contribute to the purity and stability.

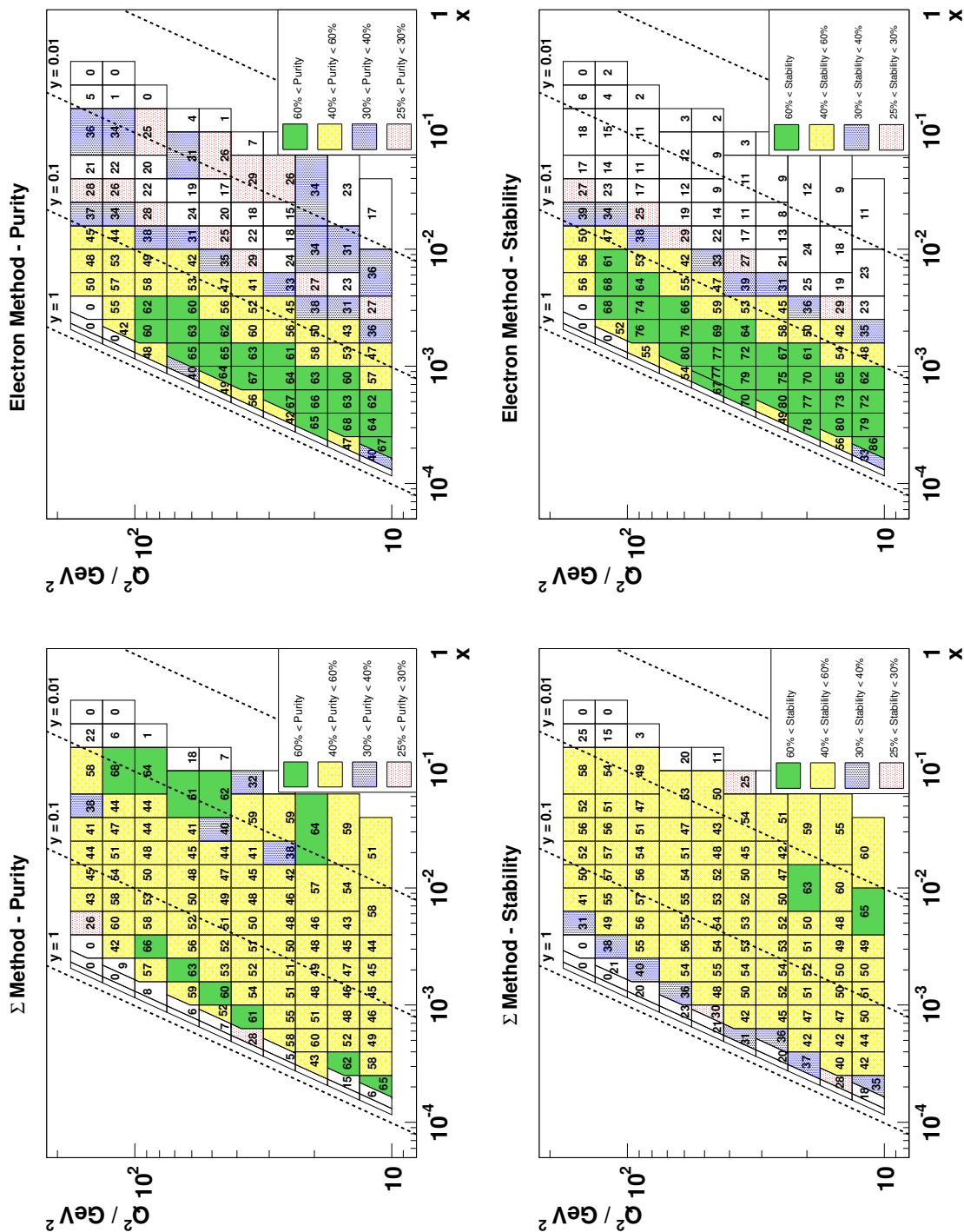


Figure 7.9: Purity and Stability for the chosen analysis binning for both the Electron and the Σ Methods.

To adjust this fit to the new measurement, the structure function F_2 was modified by a simple polynomial as

$$F_2^{new} = F_2^{old} \cdot \left(1 + p_0 + p_1 \log_{10} \frac{y}{y_0} + p_2 \log_{10} \frac{x}{x_0} + p_3 \log_{10} \frac{Q^2}{Q_0^2} \right), \quad (7.6)$$

where y_0 , x_0 , and Q_0^2 are arbitrary constants and p_i parameters adjusted in a χ^2 fit. The structure function F_L was not modified, as this analysis has no sensitivity at high y .

Eventually it was sufficient to fix $p_2 = p_3 = 0$ and with $y_0 = 0.12$ the fit parameters $p_0 = 0.058$ and $p_1 = -0.013$ were obtained. This corresponds to a smooth adjustment of the cross section of typically 5 – 7% in the analysis range and improves the agreement between the input cross section and the measured cross section from $\chi^2/\text{n.d.f}$ of about 5.7 to 0.95. The measured cross section does not change significantly as a result of this reweighting procedure, but the agreement in the control distribution does.

In figure 7.10 a collection of control plots related to properties of the scattered electron is shown. A very good agreement between data and the simulation is observed. Small discrepancies are visible on the distribution of r_{Spac} and ϕ_e , the radial and azimuthal coordinates of the electron cluster in the SpaCal. The reason is the correction needed for the BDC efficiency. It may not be able to fully describe the real efficiency locally. However, one bin for the cross section measurement averages over a wider range in r_{Spac} and the full available ϕ , so the observed local deviations do not influence the result.

Figure 7.11 presents a collection of control plots related to properties of the hadronic final state or combined measurements. Again a very good agreement is observed. Both momentum balance distributions, $(E - p_z)_{tot}$ and $p_{t,HFS}/p_{t,e}$, show small deviations. The $(E - p_z)_{tot}$ distributions peak close to $2E_e = 55.2$ GeV, as expected. The small shift is due to the residual uncertainties of the calibration procedures. For the transverse momentum balance the small disagreement near $p_{t,HFS}/p_{t,e} = 0.3$ is located in the very low y region, as shown before. These discrepancies are covered by the systematic uncertainties. The small deviations on the y_Σ distribution near $\log_{10} y_\Sigma \sim -1$ is due to the noise in the LAr calorimeter and is covered by the assigned systematic uncertainty on the subtraction procedure.

7.5 Systematic Uncertainties

The statistical uncertainties of the measurement are small and typically less than 1% except for the acceptance limited bins at the highest Q^2 values. Therefore the systematic uncertainties and their better control is the main task of this work and has been discussed in detail in the previous chapters. A summary with references to the detailed discussion is shown in table 7.1.

The choice of the *sources of systematic errors* is done very similar to the previous H1 publication [A⁺01] and more recent work in the lower Q^2 domain, see [Beh06, Var06]. The sources can be split into three categories:

- **Uncorrelated uncertainties** influence the measurement independently in each bin. A typical example is the available MC statistics. But also errors

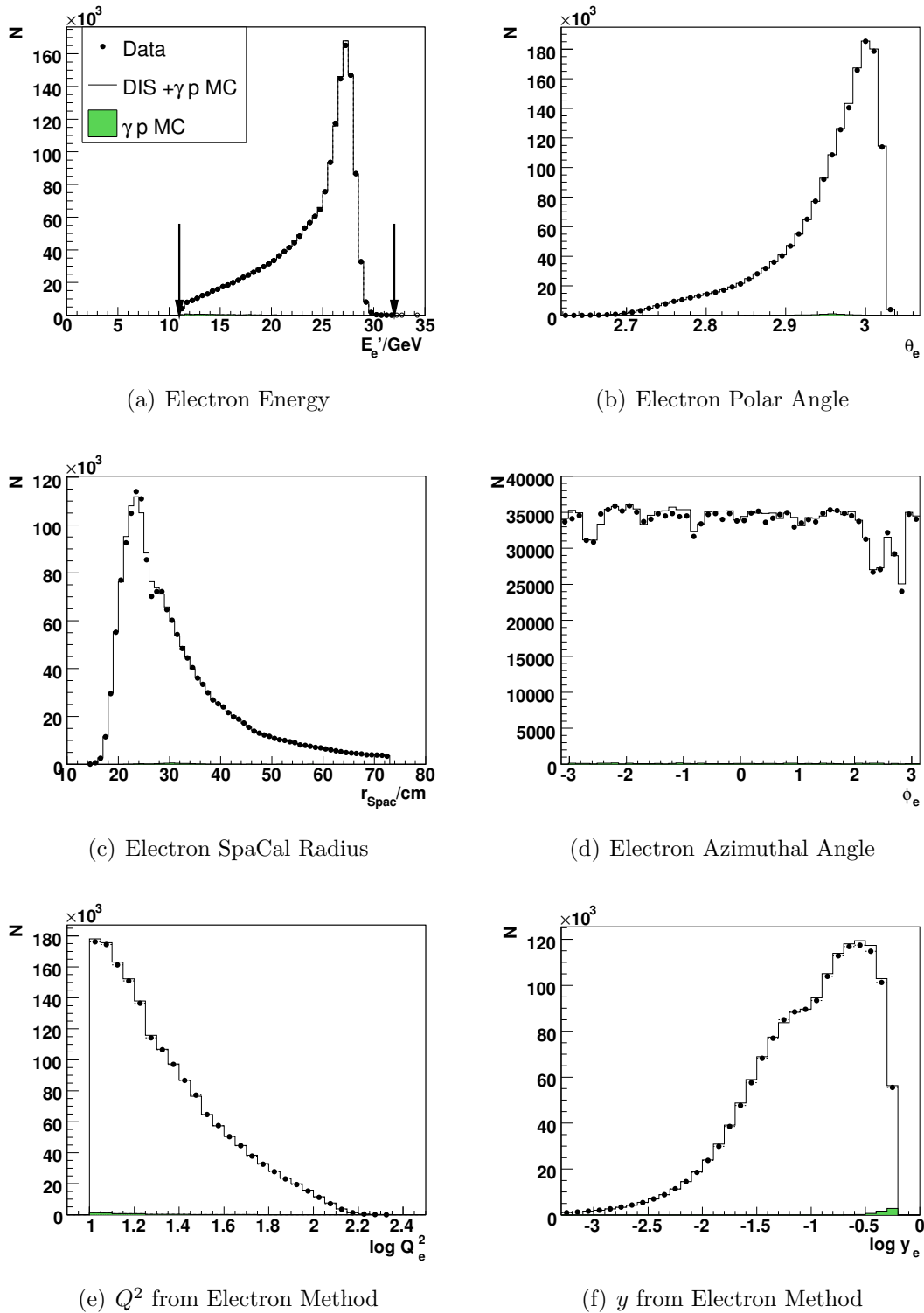
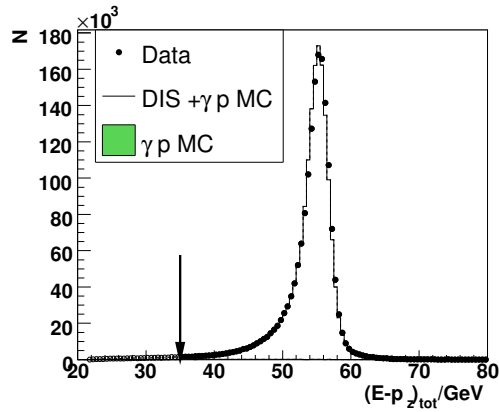
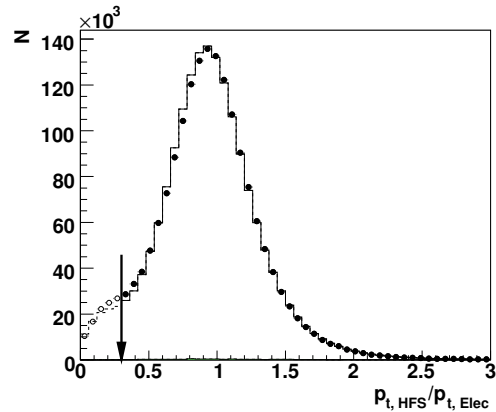


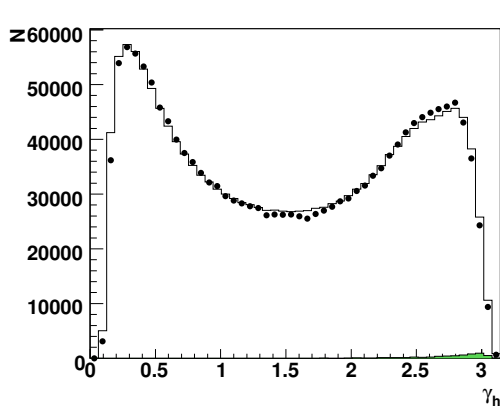
Figure 7.10: Control plots related to the scattered electron. Dots are the data, the full histograms show the prediction of the simulation. Arrows indicate the analysis selection on E'_e . The normalisation is adjusted to the luminosity and only events within the final bin selection contribute to the plots.



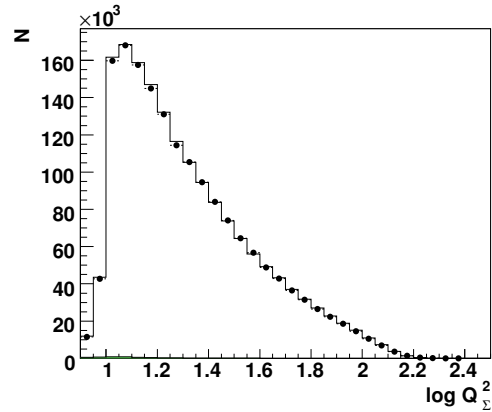
(a) Longitudinal Momentum Balance



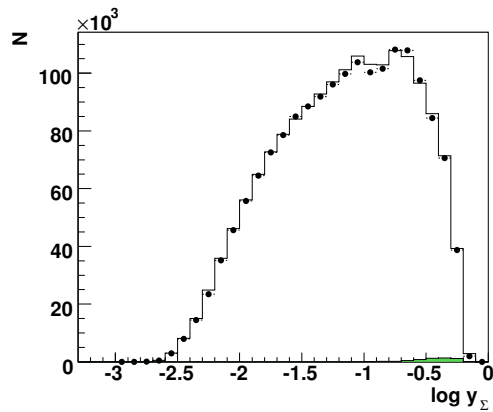
(b) Transverse Momentum Balance



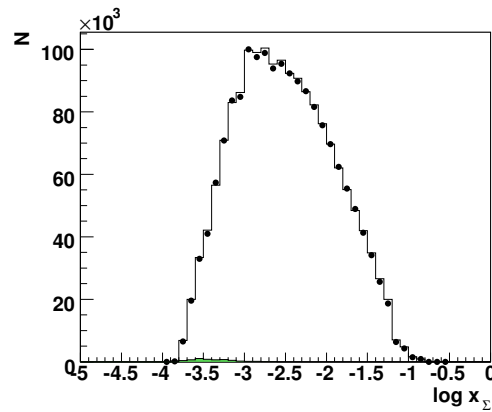
(c) Hadronic Angle



(d) Q^2 from Σ Method



(e) y from Σ Method



(f) x from Σ Method

Figure 7.11: Control plots related to HFS or combined quantities. Dots are the data, the full histograms show the prediction of the simulation. Arrows indicate the analysis selection on $(E - p_z)_{tot}$ and $p_{t,HFS}/p_{t,e}$. The normalisation is adjusted to the luminosity and only events within the final bin selection contribute to the plots.

Correlated Uncertainties		
Source	Variation	Reference
E'_e scale uncert.	0.2% at 27.6 GeV, 1% at 2 GeV, interpolated linearly	6.1
θ_e uncert.	CT 0.2 mrad, CIP 0.5 mrad	6.3
HFS energy scale uncert. (CT and LAr)	2% for $y \geq 0.01$, 10% at $y = 0.001$, interpolated linearly in $\log_{10} y$	6.2.3
LAr noise subtraction	15% of the identified noise	6.2.3
HFS energy scale uncert. (SpaCal)	0.3 GeV	6.2.1
γp MC normalisation	15%	4.3.2

Uncorrelated Uncertainties		
Source	Size	Reference
Radiative corrections	0.5%	4.2.4
Vertex reconstruction eff.	0.5%	7.1
BDC efficiency	1% for $Q^2 \leq 20 \text{ GeV}^2$ otherwise 0.5%	6.4
$p_{t,HFS}/p_{t,e}$ cut	2% only for $y \leq 0.01$	7.2.4
DJANGO MC statistics	typically $< 0.6\%$	

Normalisation Uncertainties		
Source	Size	Reference
Luminosity	1.5%	[Lev07]
Global trigger options	0.3%	5.6

Table 7.1: Table of sources of systematic uncertainties considered for the cross section measurement with size of the resulting error or size of the variation respectively. The reference column indicates the section of this work, where the applied size is discussed, except for the luminosity uncertainty.

introduced by the imperfect description of the BDC or vertex reconstruction efficiency are treated as uncorrelated.

- **Correlated uncertainties**, as for example used for the electron energy measurement, influence all measurements at the same time, though the effect depends on the kinematic domain. Here the assumption is made, that residual errors in calibration or correction procedures can be quantified by correlated shifts for the whole analysis range. The size of the resulting error in a certain bin and for a certain reconstruction method is evaluated with the help of the MC simulation. The reduced cross section σ_r^0 from the nominal analysis is compared to its variations, when calculated with a systematic shift of the source i in positive and negative direction, σ_r^{i+} and σ_r^{i-} . The relative uncertainty is

evaluated as

$$\delta_i = \frac{\sigma_r^{i+} - \sigma_r^{i-}}{2\sigma_r^0}, \quad (7.7)$$

which may be positive or negative depending on the kinematic domain the error source, and the reconstruction method.

- **Normalisation uncertainties** influence all measurements at the same time and by the same amount. Most important is the luminosity uncertainty.

The table in the appendix B contains the full information about the measurement. All uncertainties are quoted as relative values. The statistical uncertainty δ_{sta} and the quadratic sum of all uncorrelated uncorrelated sources δ_{unc} are listed separately as well as the effect of the correlated uncertainties. An estimate of the total uncertainty δ_{tot} of a measurement is given by the quadratic sum

$$\delta_{tot} = \sqrt{\sum_i (\delta_{cor}^i)^2 + \delta_{unc}^2 + \delta_{sta}^2}. \quad (7.8)$$

The typical size of the uncertainties and comparison between the different methods and previous measurements are presented in the following section.

7.6 Results and Internal Consistency

In this section the final results of the measurement as well as internal cross checks are presented, which were carried out to ensure a precise cross section measurement. The final results with full information about all measurement uncertainties is collected in a table in the appendix B.

7.6.1 The Measurement and Discussion of its Uncertainties

The reduced cross calculated according to equation 4.23 is shown in figure 7.12 for both the Electron and the Σ Methods. In total the double differential cross section is measured at 89 points in the kinematic variables x and Q^2 . The central bin values cover the range of $12 \text{ GeV}^2 \leq Q^2 \leq 150 \text{ GeV}^2$ and $2 \cdot 10^{-4} \leq x \leq 1 \cdot 10^{-1}$. For many of these points measurements using both methods are available, whose agreement is reasonable and will be looked at in more detail below.

The total uncertainties of the measurement are typically small and reach the level of 1.3 – 2.0%. Only at the highest Q^2 values of $Q^2 \geq 120 \text{ GeV}^2$ the measurement accuracy drops because of the acceptance limitation of the SpaCal calorimeter for the scattered electron.

For three typical bins at $Q^2 = 15 \text{ GeV}^2$, $Q^2 = 35 \text{ GeV}^2$, and $Q^2 = 90 \text{ GeV}^2$ the figure 7.12 also contains a detailed account of the associated measurement uncertainties. It is obvious, that the statistical uncertainty is not the limiting factor for the measurement, as it is typically below or close to 1%. The uncorrelated uncertainties contribute roughly 1% to the total uncertainty. The Electron Method is far superior to the Σ Method at low x , which however extends the measurement range with good accuracy to higher x . The reason is the different response of these

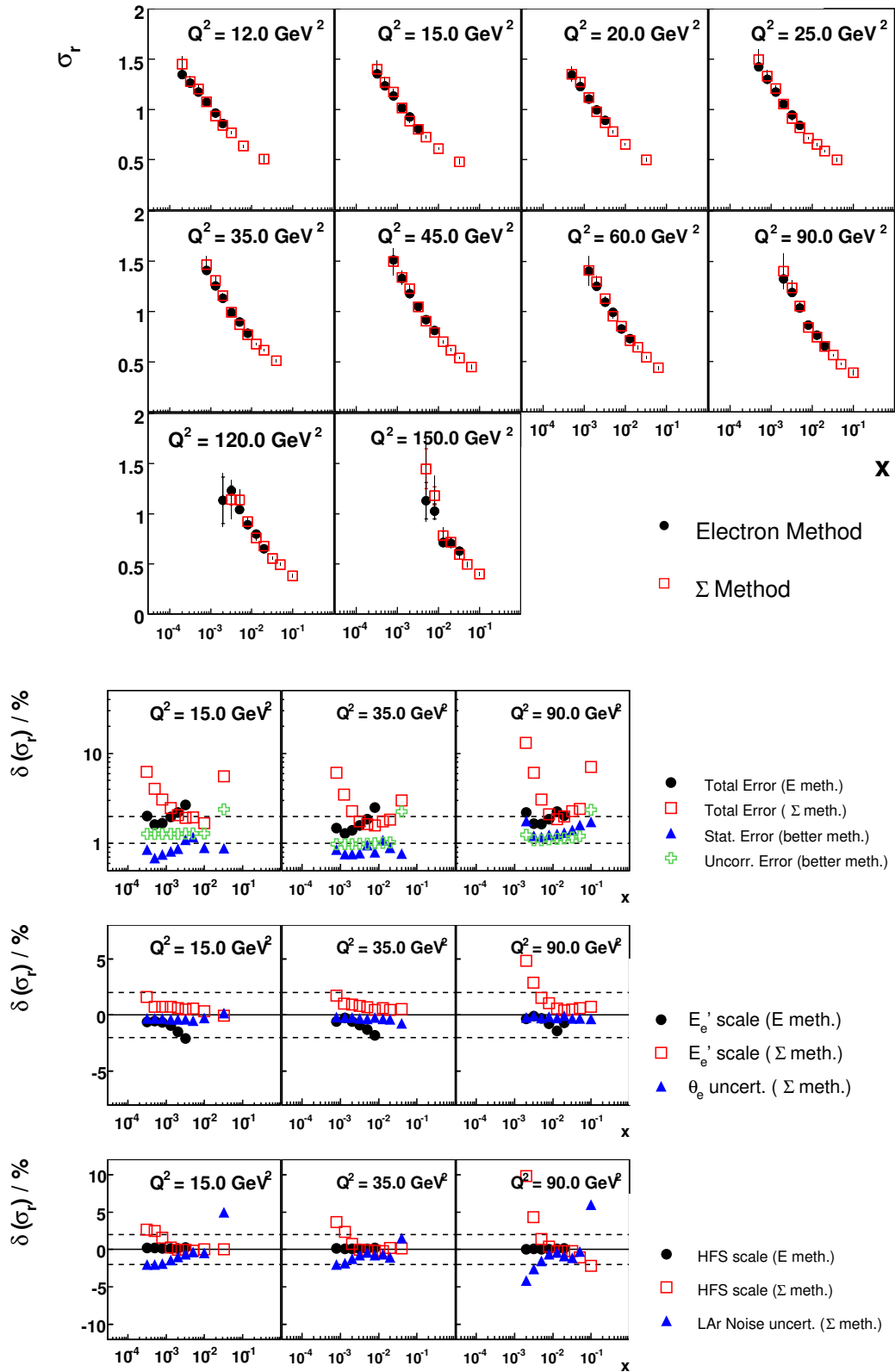


Figure 7.12: Top: Reduced cross section measured with the Electron and the Σ Method in bins with both purity and stability of more than 25%. Below the most important measurement uncertainties for the bins $Q^2 = 15, 35, 90 \text{ GeV}^2$ are presented.

reconstruction schemes to the assigned systematic uncertainties, of which the most important are shown as well:

- The reconstruction by the Electron Method is rather insensitive to the electron energy scale at low x , but increasingly sensitive at higher x . The measurements by the Σ Method do not only respond with a different sign of the shift, but also the behaviour depending on low or high x is different.
- The uncertainty on the electron scattering angle θ_e is small and similar for both methods.
- While the Electron Method is nearly independent of the systematic effects assigned to the measurement of the HFS quantities, the precision of the Σ Method is influenced strongly by the HFS energy scale and the LAr noise both at low and high x .
- The uncertainty on the γp background has only a small influence on the lowest x bins for low Q^2 and the influence of the HFS measurement in the SpaCal is typically low as well.

In the highest x domain the systematic uncertainties due to the HFS measurement limit the accuracy of the measurement. With an improved simulation of the noise in the LAr calorimeter the uncertainties may be reduced there as well.

7.6.2 Consistency of the Electron and Σ Methods

On a first look the agreement between electron and Σ Method is reasonable. There is a tendency for the Σ measurements to be higher than the corresponding measurement using the Electron Method at low x and vice versa at higher x . This can be qualitatively explained by the different sensitivities to the correlated error sources, as shown in figure 7.12. Forming a standard χ^2 using the total measurement errors yields $\chi^2 = 37.8$ for 57 points.

However, as shown above, the uncertainties are to a large part correlated between both measurements. Therefore one should go beyond a simple χ^2 definition. In [LMGL05] it was already discussed, that an extended test represents a powerful possibility to cross check the systematics. Here the treatment is slightly varied with respect to the discussion there.

Consider the bin i with the two reduced cross sections $\sigma_{r,e}^i$ and $\sigma_{r,\Sigma}^i$. The measurements are influenced by the systematic variations, such that their values for a certain set of shifts α_j can be determined with the sensitivities δ_{cor}^j as

$$\sigma_r^i \rightarrow \sigma_r^i(\alpha_j) = \sigma_r^i \cdot \left(1 + \sum_j \delta_{cor}^j \alpha_j \right). \quad (7.9)$$

In our case the summation runs over $j = 1..6$ sources of systematic uncertainties. The χ^2 is measured as

$$\chi^2(\alpha_j) = \sum_i \frac{(\sigma_{r,e}^i(\alpha_j) - \sigma_{r,\Sigma}^i(\alpha_j))^2}{(\Delta_{e,\Sigma}^i)^2} + \sum_j \alpha_j^2, \quad (7.10)$$

where $\Delta_{e,\Sigma}^i$ should be an estimator for the uncertainty of the difference of Electron and Σ measurements in bin i excluding the effect of the correlated sources. This definition is essentially the same as used e.g. in global QCD analyses [P⁺02], except that no theory is involved.

The determination of $\Delta_{e,\Sigma}^i$ requires some thought, as both measurements may make use of largely the same events. This was checked by splitting the available MC sample into 75 subsamples of a luminosity $\mathcal{L} \sim 2 \text{ pb}^{-1}$ and calculating the ratio $\sigma_{r,e}^i/\sigma_{r,\Sigma}^i$ for all bins. The RMS of the distribution, scaled to the available data luminosity, should be a good representative of the statistical uncertainty. Surprisingly it is found, that the statistical uncertainty calculated this way is mostly equivalent to the simple quadratic sum of the individual statistical errors δ_{sta}^i . Also the ratio $\sigma_{r,e}^i/\sigma_{r,\Sigma}^i$ typically deviates significantly from unity, being about 1.5 at lowest x and 0.5 at highest x . Therefore it is concluded, that the measurements are statistically mostly uncorrelated and $\Delta_{e,\Sigma}^i$ is formed using a simple quadratic addition of the individual statistical and uncorrelated uncertainties

$$\Delta_{e,\Sigma}^i = \{(\delta_{sta,e}^i \oplus \delta_{unc,e}^i) \sigma_{r,e}^i(\alpha_j)\} \oplus \{(\delta_{sta,\Sigma}^i \oplus \delta_{unc,\Sigma}^i) \sigma_{r,\Sigma}^i(\alpha_j)\}. \quad (7.11)$$

The minimisation of $\chi^2(\alpha_j)$ is performed with the help of the fit program MINUIT. The determined systematic shifts are shown in table 7.2. It is observed, that the energy measurements in the calorimeters can be well constrained with this procedure. The distribution of shifts indicates, that the systematic uncertainties were estimated reasonably. Only the uncertainty related to the LAr noise may be slightly underestimated, the systematic shift exceeds one standard deviation with $\alpha_{Noise} = 1.3$. It is also obvious, that despite the efforts spent on the calibration of the scattered electron energy, the assigned uncertainty is at the limit, as the fit gives $\alpha_{E'_e} = 1.0$, a shift of exactly one standard deviation. The most important correlations are present for the shift in the LAr noise, which has a correlation coefficient of +0.72 to the electron energy scale and +0.64 to the HFS energy scale in the LAr calorimeter. Also the HFS measurements in the LAr and SpaCal calorimeters are correlated with a coefficient of +0.60.

Systematic Source α_j	Shift	Error
Electron Energy Scale $\alpha_{E'_e}$	1.01	0.28
Electron Polar Angle α_{θ_e}	-0.08	0.98
HFS Energy Scale (LAr+CT) α_{LAr}	-0.66	0.30
LAr Noise Subtraction α_{Noise}	1.28	0.52
HFS Energy Scale SpaCal α_{HSpa}	-0.55	0.25
γp MC normalisation $\alpha_{\gamma p}$	-0.63	0.93

Table 7.2: Systematic shifts in units of standard deviations of the assigned uncertainty fitted to improve the agreement of the cross section measured by the Electron and the Σ Methods.

The agreement between the electron and Σ points is good with a χ^2 of 54.7 for the 57 points and 6 fit parameters after shifting the systematics. It is concluded, that the measurements by the Electron and the Σ Methods agree within the assigned measurement uncertainties. Also the magnitude of the systematic variations was

estimated reasonably, as far as this test can tell, with only one out of six variations slightly exceeding the level of one standard deviation.

7.6.3 Splitting the Measurement Samples

Further tests to assure a good measurement can be carried out by splitting the event samples into two parts and compare the measurements. This way possible local efficiency or calibration deficits can be discovered. Here the measured cross section was tested with respect to variations, if the sample is split according to

- the reconstructed position of the scattered electron in the lower or upper half of the SpaCal, $y_{Spac} < 0$ and $y_{Spac} > 0$; the same test can be performed using the left and right part of the SpaCal, $x_{Spac} < 0$ and $x_{Spac} > 0$,
- the reconstructed position of the vertex position, i.e. $z_{vtx} < 0$ and $z_{vtx} > 0$,
- the data taking period, using the data for the H1 run numbers before and after 270353, which leads to two samples with luminosities of $\mathcal{L}_1 = 9.8 \text{ pb}^{-1}$ and $\mathcal{L}_2 = 12.5 \text{ pb}^{-1}$.

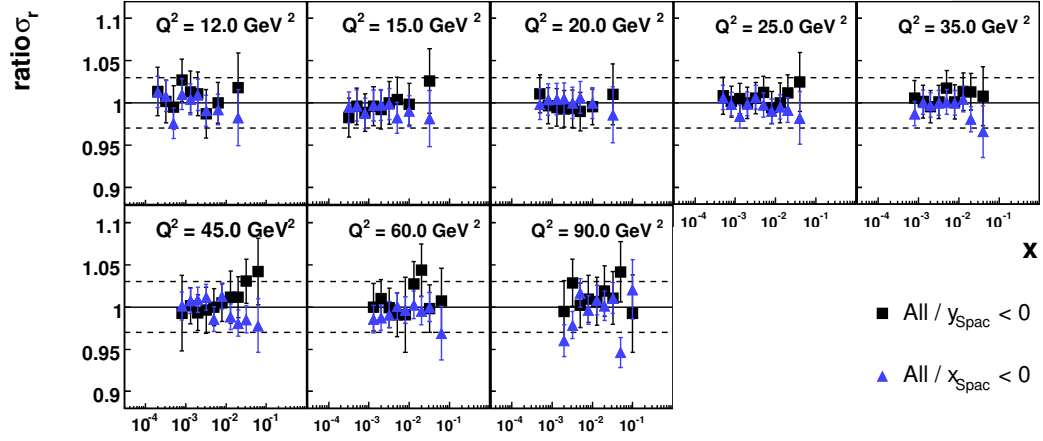
While for the first two options a simple additional selection on the standard analysis is performed, for the third option also the vertex reweighting (section 5.5) and the calculation of the average prescales (section 5.3.3) are adapted separately. One should note, that some of the corrections and calibrations are not specifically optimised for these selections, but rather the analysis sample as a whole. Some important examples are the BDC efficiency and the HFS calibration. Therefore one should not expect an agreement within only the statistical uncertainty, yet including the uncorrelated systematic uncertainty should cover the differences.

Figure 7.13 presents the ratio of the reduced cross section measured with the partial event or data samples compared to the standard analysis using all events. Overall the agreement is typically very good and mostly covered by statistical uncertainties.

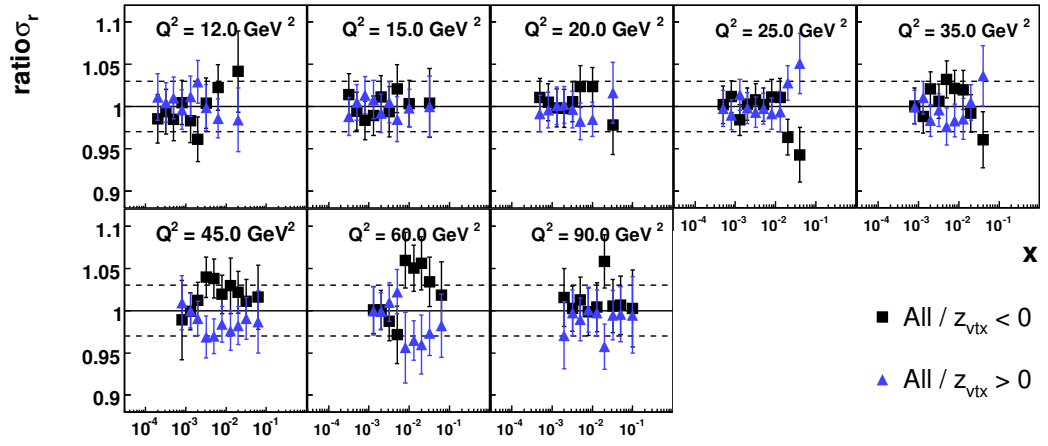
The only significant deviation was found in the test using the separation according to the z_{vtx} position. Here the medium $Q^2 = 45$ and 60 GeV^2 bins show a rather large 3 – 5% variation at medium $x \sim 10^{-2}$, which is only covered on the level of two standard deviations, as the added statistical and uncorrelated uncertainties are of the order of 2 – 3%. No specific reason could be identified.

7.6.4 Alternative Reconstruction Methods

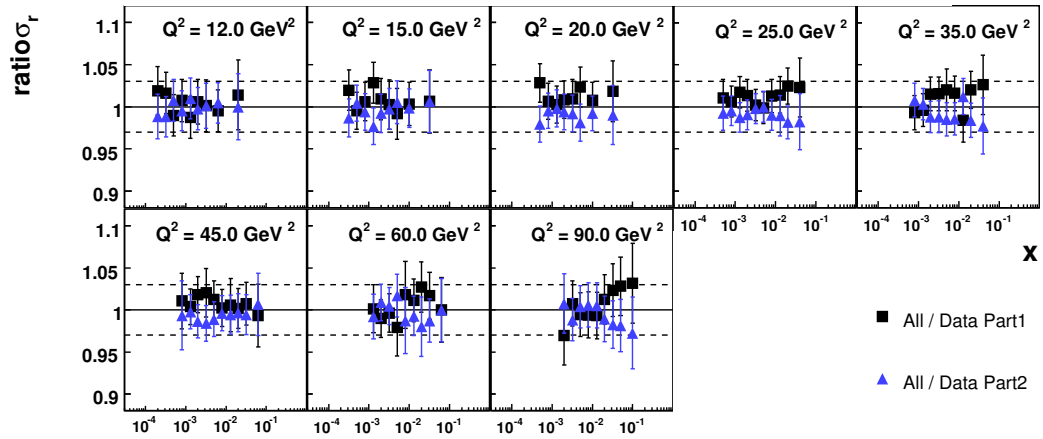
In the chapters 4.1 and 4.4 alternative methods for the reconstruction of the DIS events, the $e\Sigma$ and the PT Method, were mentioned. These methods were used by H1 for the data at higher Q^2 [A⁺03b] and by the ZEUS collaboration for the full Q^2 range [C⁺01], respectively. They can cover the whole kinematic region with good reconstruction resolution and also good purity and stability. The deviation of the cross section measurement from the combined Electron and Σ Methods is typically smaller than 1%. Mostly their measurements are very similar to the *pure* Σ Method except for the lowest x , where they agree better with the Electron Method.



(a) Event sample split into different SpaCal regions $y_{\text{Spac}} < 0$ and $x_{\text{Spac}} < 0$. The complementary samples $y_{\text{Spac}} > 0$ and $x_{\text{Spac}} > 0$ are not shown, as they show exactly the opposite behaviour.



(b) Event sample split according to the reconstructed z position of the vertex.



(c) Data sample split into an early and late half, the full MC sample is used in each case.

Figure 7.13: Cross checks of the reduced cross section measured with partial event or data samples compared to the nominal analysis. Uncertainties shown correspond to the quadratic sum of statistical and uncorrelated errors. The dashed lines are a guide to the eye and placed at $\pm 3\%$.

There are some reasons, which prevent the use of these extended reconstruction schemes. First, a cross check like the one in section 7.6.2 cannot be performed, as they do not provide a clearly different dependence on the correlated uncertainties. Most important however is their response to systematic variations of the detector measurements. Figure 7.14 shows a comparison of the total measurement uncertainties with different reconstruction methods for three Q^2 bins.

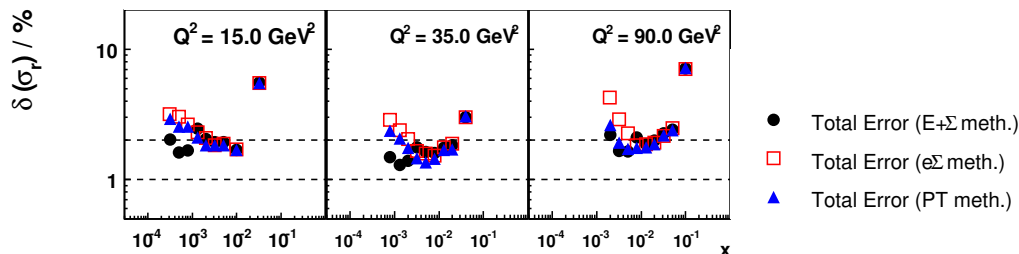


Figure 7.14: Total measurement uncertainties for the three bins with $Q^2 = 15, 35, 90 \text{ GeV}^2$. The standard combination of the Electron and the Σ Methods is compared to the $e\Sigma$ and the PT Methods. The uncertainties of the alternative methods are mostly inferior, especially at lowest x the Electron Method provides the best accuracy.

While the $e\Sigma$ and PT Method provide virtually identical uncertainties at high x , they are significantly worse at low x . This is due to their dependence on the HFS measurement, i.e. the HFS energy scale uncertainty and the influence of the LAr noise. The PT Method is overall the better of the two and actually manages to provide a small benefit over all other considered reconstruction schemes at single points for medium x . It is concluded, that a measurement with maximum precision requires the use of the *pure* Electron Method at low x , while at higher x all other schemes need to use the HFS measurement and are mostly equivalent. The combination of two methods cannot be avoided.

7.7 Context of the New Measurement

The measurement of the inclusive DIS cross section has been one of the main goals of the HERA collider experiments. Precise measurements have been published before, which a new measurement has to be compared to. The detailed comparison follows in section 8.1, while here the measurement of this analysis is put into the context of other measurements in the adjacent phase space.

Figure 7.15 shows the final measurement together with other measurements at the same Q^2 using the H1 detector. As has been explained in the introduction and motivated in more detail at various points in this thesis, the kinematic range of this measurement is limited. At lowest x , i.e. highest y , the measurement is performed in special analyses. At high $Q^2 \gtrsim 120 \text{ GeV}^2$ the scattered electron is mostly detected in the LAr calorimeter, which constitutes a separate analysis. It covers the phase space, where the uncertainties of the SpaCal analysis are large due to acceptance limitations. Furthermore a comparison to the prediction of the QCD analysis result

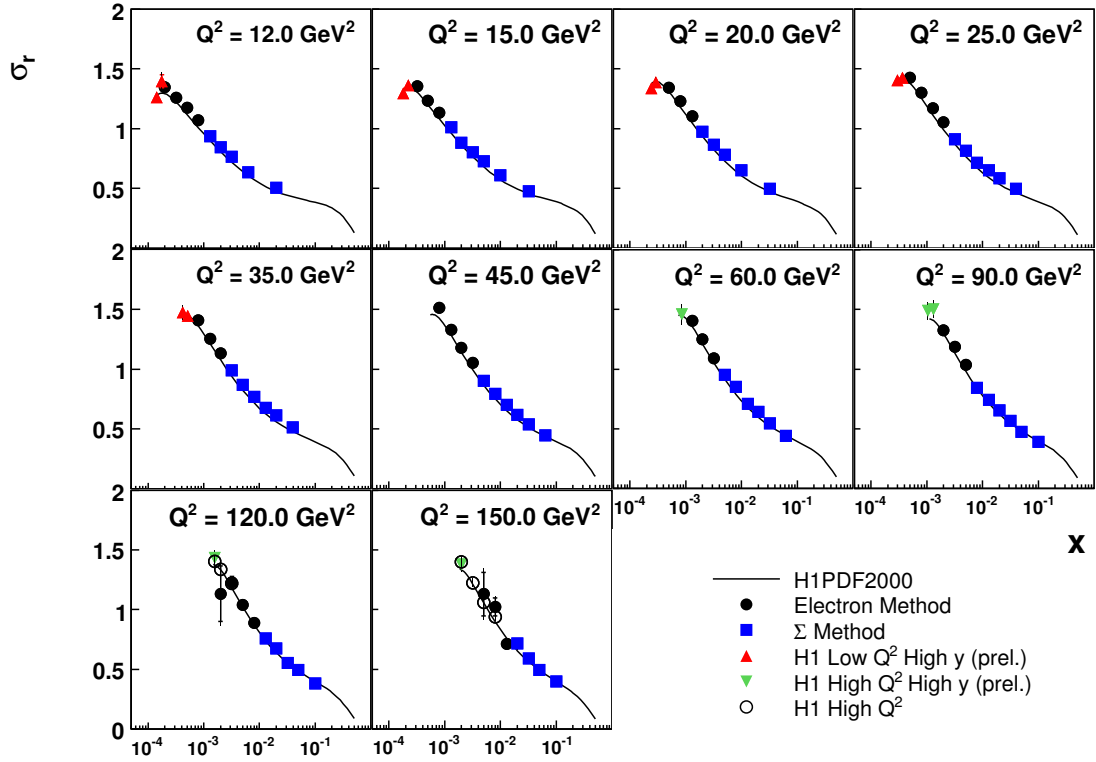


Figure 7.15: Final measurement points together with other, partially new preliminary measurements by H1. The additional data sets are taken from “H1 Low Q^2 High y (prel.)” [H1p07a], “H1 High Q^2 High y (prel.)” [H1p07c], and “H1 High Q^2 ” [A⁺03b]. Data at different values of Q^2 are shifted to the grid of this measurement using the ratio of the H1PDF2000 prediction at the old and the x, Q^2 values.

H1PDF2000 [A⁺03b] is shown. Except for a small offset the new measurement follows this expectation.

The total point wise measurement uncertainties of the published and the new data sets are shown for three Q^2 bins in figure 7.16 and compared to the published results of the ZEUS [C⁺01] and H1 [A⁺01] collaborations. The older results had a total uncertainty on the level of 2 – 3%. These uncertainties are now reduced to the typical level of 1.3 – 2.0%. The results for the measured cross section are confirmed by an independent analysis [Pet07]. Therefore one major goal of this work, to obtain a measurement of the inclusive deep-inelastic scattering cross section with improved uncertainties, is accomplished. There are several reasons for this improvement:

- The efficiencies of the BDC and the vertex reconstruction could for the first time be studied in detail using the independent reconstruction by the BST, allowing to control the corresponding efficiencies to a very good precision.
- The SpaCal triggers are fully efficient for the analysis selection, therefore no additional uncertainty is introduced.
- The correlated uncertainties could be mostly reduced by 50% w.r.t to the old measurement, except for the HFS energy scale, which controlled on a similar level as before.

- Due to the much larger available MC statistics, the corresponding uncertainty is now negligible. For the older measurement it was of the same order as the statistical data uncertainty.

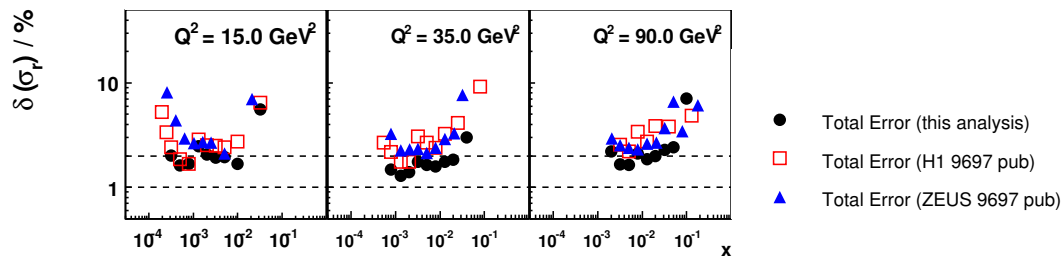


Figure 7.16: Total measurement uncertainties for the bins $Q^2 = 15, 35, 90 \text{ GeV}^2$ excluding the overall normalisation for this analysis and the measurements covering the same kinematic domain previously published by H1 and ZEUS.

Chapter 8

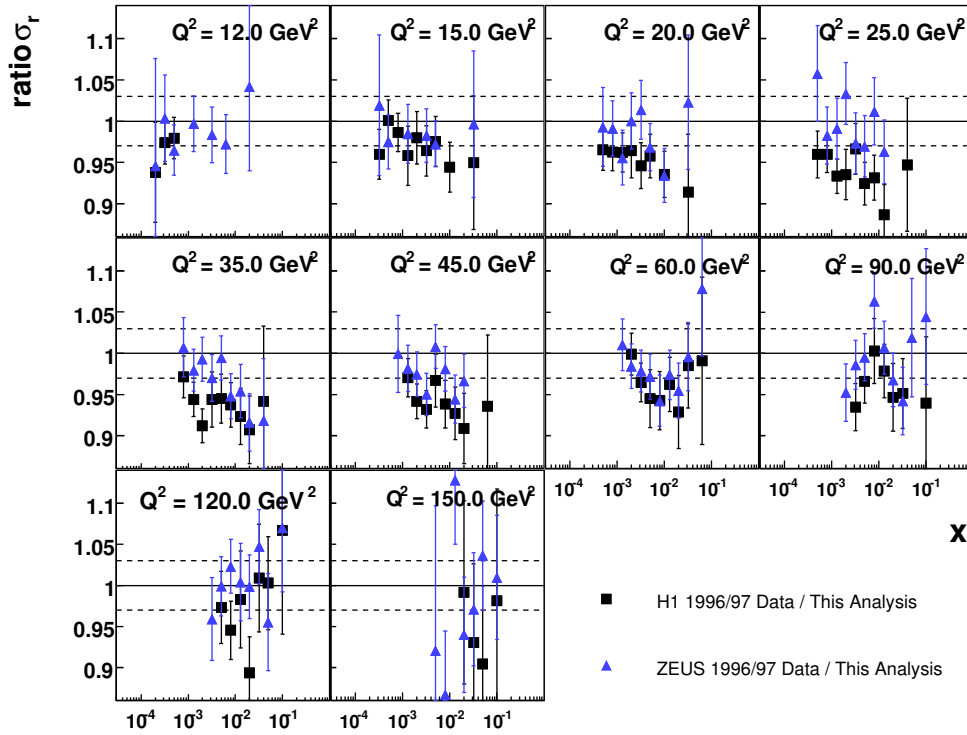
Analysis of the Published H1 Measurement

With the new measurement presented in detail in the previous chapter, the accuracy for the inclusive DIS cross section has been raised significantly compared to the available results. The detailed checks of the new measurement and the confirmation by an independent analysis give confidence in the new measurement. In this section the new results are compared in detail to the previously published measurements in the same kinematic domain. As a significant discrepancy is found, the published H1 measurement is analysed for possible reasons.

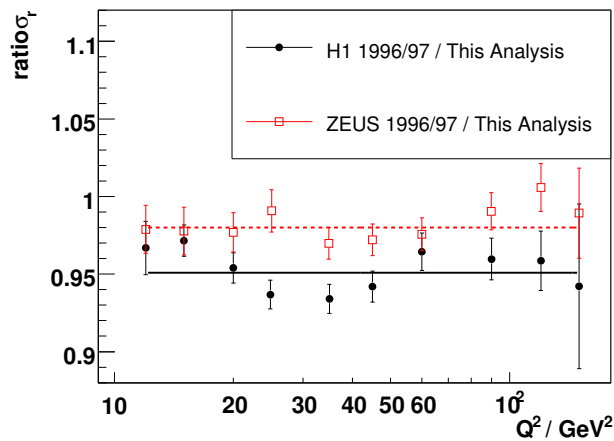
8.1 Comparison to Published Measurements

Figure 8.1(a) presents the detailed comparison of the results of this analysis to the previously published H1 [A⁺01] and ZEUS [C⁺01] measurements covering the same kinematic range. The published measurements are minimally modified to match the (x, Q^2) grid used in this work. The correction is estimated using the H1PDF2000 prediction and is typically 1 – 2% only. The centre of mass energy was slightly increased from $\sqrt{s} = 300$ GeV in 1996/97 to $\sqrt{s} = 320$ GeV in 2000. The published data is corrected for the different influence of the longitudinal structure function, which is a 1 – 2% effect at the lowest x values. The results are expected to agree within the errors. Taking the total measurement uncertainties into account, this analysis is well compatible with the ZEUS measurement. There is however a systematic deviation to the published H1 measurement, which is lower by about 5%.

To assess the effect of global normalisation uncertainties, the weighted average of all ratios at constant Q^2 is shown in figure 8.1(b). The values as well as the shown error bars are calculated ignoring the fact, that the uncertainties are partially correlated. The quoted normalisation errors for the data sets are $\sim 2.2\%$ for the ZEUS measurement, $\sim 1.7\%$ for the published H1 measurement, and $\sim 1.5\%$ for this analysis. The ZEUS measurement is seen to be overall 2.0% lower, which is covered by these uncertainties. The H1 measurement is overall 4.9% lower and some possible Q^2 dependence is observed as well. This significant discrepancy needs to be explained and will be investigated in more detail in the remainder of this chapter.



(a) Error bars correspond to the total measurement uncertainties, excluding overall normalisation uncertainties, which are typically 2% for each data set. The dashed lines indicate a deviation of $\pm 3\%$.



(b) Weighted average of the ratios shown above in figure (a) at constant Q^2 . The lines indicate the overall shift of the data sets, which is 2.0% for the ZEUS measurement, and 4.9% for the H1 measurement. The averaging is performed ignoring the fact, that the uncertainties are partially correlated.

Figure 8.1: Ratio of the new measurement (this analysis) to the ones published previously by the H1 [A⁺01] and the ZEUS [C⁺01] collaborations using data from the years 1996/97 at $\sqrt{s} = 300$ GeV corrected to $\sqrt{s} = 320$ GeV. Data at different values of Q^2 or x are shifted to the grid of this measurement using the ratio of the H1PDF2000 prediction at the old and the x, Q^2 values.

8.2 Reanalysis of the H1 1996/97 Data

This section discusses a new analysis of the data set used for the published H1 measurement [A⁺01]. In general, the same techniques as for the analysis presented above are used. Therefore only the key issues are presented here shortly. Concerning smaller corrections of less than 1%, the available information on the old analysis is used.

8.2.1 Data Sample and Event Reconstruction

The data sample used for the H1 publication was taken in the years 1996 and 1997. The run range considered is 158709 - 200407. After that period, the trigger setup was modified for a *minimum bias run*. While the publication contained this data until run 201519 with an integrated luminosity of $\mathcal{L} = 1.8 \text{ pb}^{-1}$, it is not considered here. Also the run selection was redone according to the same criteria as employed for the year 2000 data set. The main difference is, that the trigger S9 is replaced by S1 and the prescale limits on the triggers can be tightened without an effective loss of luminosity to 5 for S3 or S1, and 10 for S0. Table 8.1 lists the runs excluded and the reason. The data selected for analysis correspond to an integrated luminosity of 15.53 pb^{-1} before prescale correction.

Run Numbers	Reason for exclusion
170136 - 180931	General DAQ problems or bad data quality
164124 - 164162, 166021 - 169554, 188581 - 188637, 191687 - 191984, 192458 - 193677, 195929 - 196377	Fills with low trigger efficiency (S0)
159585 - 159602	Fill 1109 with very large yield
185721 - 185749, 186468 - 186479	Short fills 1315 and 1329 with low yield

Table 8.1: Summary of the H1 runs excluded from the analysis of the year 1996/97 data in addition to the general selection.

This run selection is slightly more restrictive than the one used for the publication and leads to about 2.8 pb^{-1} less integrated luminosity. However the differences using the original selection are of the order of less than 1%. Therefore the analysis is continued in a more independent way. The data taking stability, quantified by the event yield as in section 5.4, is very good and without significant deviations from the mean value, as can be seen in figure 8.2. The mean value is not comparable to the one from the year 2000, as the centre of mass energy and the fiducial cuts in the SpaCal are different.

As mentioned in section 5.6, the analysis of the luminosity was improved in the recent years, which leads to a change of the luminosity in the year 2000 of -1.2% w.r.t the previous value. The same reanalysis was performed for the 1996/97 run period and a small correction of -0.5% was found [Lev06], well within the systematic uncertainty of 1.5%. Nevertheless for consistency this small correction is further on applied to all results from the years 1996/97.

The H1 detector and HERA setup is mostly the same as described in chapter 3. The main difference is the smaller proton beam energy of $E_p = 820 \text{ GeV}$. Also

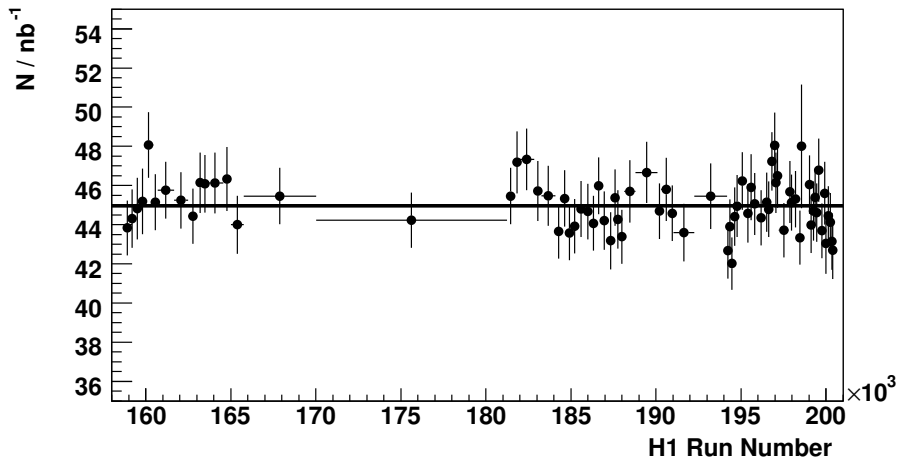


Figure 8.2: Total event yield per luminosity with the final run selection as a function of the H1 Run Number for the data taking period 1996/97. Each shown bin contains a luminosity of about 200 nb^{-1} . The line shows the average value of 44.9 events per nb^{-1} .

the BST had a smaller acceptance, was not fully operational, and is not used in the data set considered. Otherwise the event reconstruction and selection is identical to the one presented in section 5.2. A small difference is introduced in the selection of the reconstructed z position of the event vertex, which is required to be within $|z_{vtx}| < 30$ cm instead of 35 cm as for 2000. The binning uses the same x, Q^2 grid, but the special y bins at $y > 0.6$ are slightly shifted towards higher x .

In 1996 one of the two CIP layers was not operational in the limited ϕ range $4.2 < \phi < 5.2$. The consequence is, that for CIP vertices in this azimuthal range typically only one CIP pad is linked. Excluding this ϕ range is found to have no effect on the measured cross section beyond the loss of statistics.

A dedicated MC sample with 10 million events was generated with DJANGO 1.4 and simulated with H1SIM. Equivalent setup options as for the sample for 2000 are used, except for the changes related to the run period. This sample corresponds to an integrated luminosity of $\mathcal{L}_{MC} \approx 21.3 \text{ pb}^{-1}$. The γp background is estimated using the same PHOJET sample as for the year 2000 analysis. While this is not optimal, the influence is small and limited to the low x domain for low Q^2 .

8.2.2 Trigger Setup and Performance

The set of subtriggers useful for the inclusive analysis was slightly different for the older run period. It is summarised in table 8.2. The strategy, to have the full phase space covered by S0 remains. Also S3 is used similarly, the main difference here is, that the radial cut SPCL_R30 was only applied for a part of the data. In 2000 the trigger S9 with a very low energy threshold of ~ 3 GeV plus the tracking condition Ray_T0 was available with a relatively low prescale. This is not the case for this data set, but the trigger S1, which has the same energy threshold as S0, but in addition the tracking condition, is used instead.

While the available luminosity in 1996/97 is 44% lower than in 2000, the prescale corrections are smaller by 23 – 57%, which partially compensates for this loss. The triggers S1 and S3 are essentially not prescaled and S0 has an average prescale of ~ 2.1 , which is calculated separately for the two different trigger setups. In the lowest Q^2 region, which was covered by S0 only in 2000, the statistical uncertainties even improve slightly.

The analysis of the trigger efficiency is performed as described in section 5.3.2 with the help of independent subtriggers. For a good trigger performance several luminosity fills have to be excluded, because they show an abnormally low trigger efficiency of S0 even for a selection, which has typically close to 100% efficiency. This is illustrated in figure 8.3. After the full run selection the fiducial cuts are adjusted to exclude regions with low efficiency. The identified bad regions are listed in table 8.3. Eventually the overall trigger efficiency is high everywhere. The behaviour as a function of E'_e is shown in figure 8.3. The expected threshold behaviour of S0 and S3 is visible. Unlike in 2000, the trigger efficiency does not reach $> 99.9\%$, a residual inefficiency of about 0.4% in the analysis range $E'_e > 11$ GeV remains. This is not corrected for, but is in line with the uncorrelated uncertainty of 0.5% assigned in the publication.

8.2.3 BDC Efficiency Correction

In section 6.4 the BDC efficiency correction for the year 2000 was presented. The main advantage in the newer data set is, that the correction can be determined using a sample independently reconstructed by the BST, which is not possible in the older data set. A first approach was to use the same efficiency correction also for the older data. As the detector status was not changed significantly, the properties should be rather similar. In an additional step the description of the BDC efficiency is determined in data and the MC simulation by comparing the radial distributions with and without BDC requirements. This method was used already in section 7.2. The ratio of data to MC efficiency is shown in figure 8.4. Except for a small fluctuation around the $r_{Spac} = 25$ cm region, the efficiency in MC is described already on the 1% level. The residual small discrepancy is introduced as an additional efficiency reduction of 0 – 1% depending on r_{Spac} in the MC simulation.

8.2.4 Control Distributions

The remaining steps of detector calibration and alignment, as outlined in chapter 6, were performed in the same way. For the resolution optimisation of the calorimetric measurements, i.e. E'_e and the HFS measurement, the same parameters were used, which are found to be sufficient also for this data set.

Overall the control distributions in the figures 8.5 and 8.6 show a good agreement between the data and the MC simulation. Here the same structure function F_2 was used as in section 7.4. Altogether the description is on a similarly good level as for the year 2000 sample and further on the cross section measurements will be compared.

Subtrigger Name	L1 Condition	L2 Condition ($N_{run} > 198826$)	Energy Threshold
S0	SPCLe_IET>2	—	7 GeV
S1	SPCLe_IET>2&&Ray_T0	— (SPCL_R30)	7 GeV
S3	SPCLe_IET>2&&SPCLe_ToF_E_2	— (SPCL_R30)	~ 15 GeV

Table 8.2: Summary of trigger setup for the used subtriggers S0, S1, and S3. The radial cut on L2 was only introduced for the last part of the data taken.

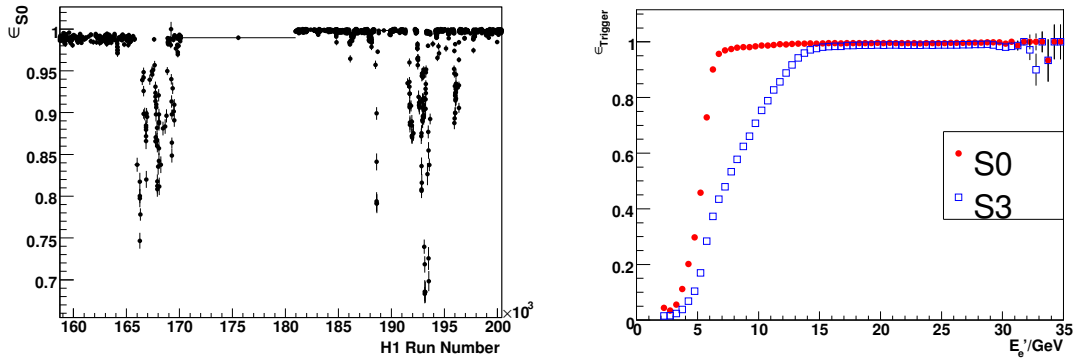


Figure 8.3: Left: S0 trigger efficiency as a function of time before the full run selection. Several run ranges have to be excluded because of abnormally low efficiency. Right: Dependence of the S0 and S3 efficiency on the energy of the scattered electron E_e' . S1 contains the same SpaCal elements as S0 and has therefore the same performance, excluding its track based trigger element.

Excluded SpaCal Cells/Regions	Reason for exclusion
Central box ($-18.5 \text{ cm} < x < 10.5 \text{ cm}$) && ($-10.5 \text{ cm} < y < 18.5 \text{ cm}$)	Not included in IET trigger (S0)
Box ($-8.5 \text{ cm} < x < 8.5 \text{ cm}$) && ($-12.5 \text{ cm} < y < -8.5 \text{ cm}$) Box ($8.5 \text{ cm} < x < 20.5 \text{ cm}$) && ($-8.5 \text{ cm} < y < 8.5 \text{ cm}$)	Extend central box because of low trigger efficiency
Box ($19.5 \text{ cm} < x < 36.5 \text{ cm}$) && ($56.5 \text{ cm} < y < 90 \text{ cm}$) Box ($27.5 \text{ cm} < x < 40.5 \text{ cm}$) && ($-36.5 \text{ cm} < y < -23.5 \text{ cm}$)	Larger regions with low trigger efficiency
Cell #89, #763, #868, #980, #952	Single cells with low trigger efficiency
$r_{Spac} > 73 \text{ cm}$	Containment of SpaCal

Table 8.3: Summary of the fiducial cuts applied in the analysis of the 1996/97 data. Single cells or clusters of cells are rejected with an additional margin of 0.5 cm around the borders. All cuts are due to low trigger efficiency.

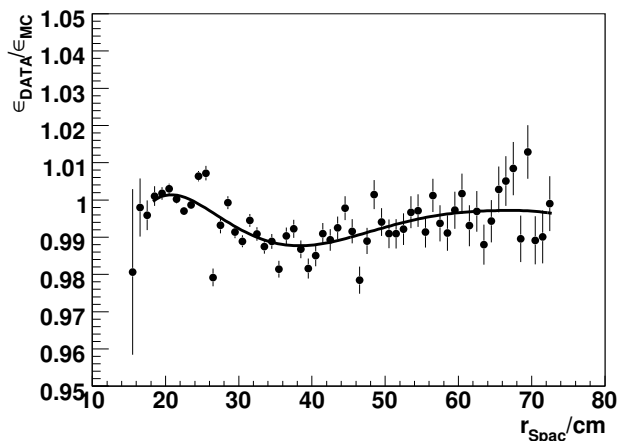


Figure 8.4: Ratio of the BDC efficiency measured in data and MC with applied correction determined for the 2000 data. The difference is parametrised by a polynomial of degree 6 and introduced as additional correction in the simulation.

8.2.5 Cross Section Result and Comparison

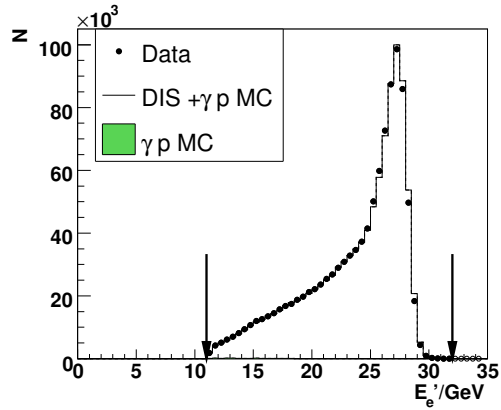
Unlike for the 2000 data a detailed determination of systematic uncertainties was not performed. For the correlated uncertainties the tests to estimate the size of the variations were repeated and a similar magnitude as for the published analysis is found. The uncertainties related to the BDC and vertex reconstruction efficiency cannot be determined the same way, but a similar size of 0.5 – 1% is reasonable.

For the online selection a small trigger inefficiency of $\sim 0.4\%$ was determined above. Furthermore the losses at trigger level L4 were determined to be $\sim 0.5\%$ for the publication [S⁺00]. These global inefficiencies are not taken into account here, but should be considered for the comparison of the cross section results.

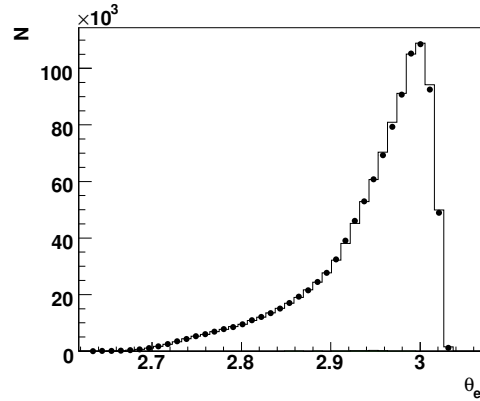
Figure 8.7(a) compares the new analysis of the 1996/97 data to the one using the data from the year 2000. Unlike the comparison to the published measurement presented before in figure 8.1(a), no large discrepancy is visible. The deviations are mostly not exceeding the 3% level, which is covered by the measurement uncertainties. The deviation is typically larger at the lowest and highest x . For low x this may be related to the treatment of γp background, which was estimated using a PHOJET sample not adapted to the running period. At large x the correlated uncertainties due to the HFS measurement and cover the differences.

For figure 8.7(b) the same weighted average of all ratios at constant Q^2 is calculated as before in figure 8.1(b) to assess global deviations. The agreement between the results using the data sets from the years 1996/97 on the one hand and the year 2000 on the other hand is very good.

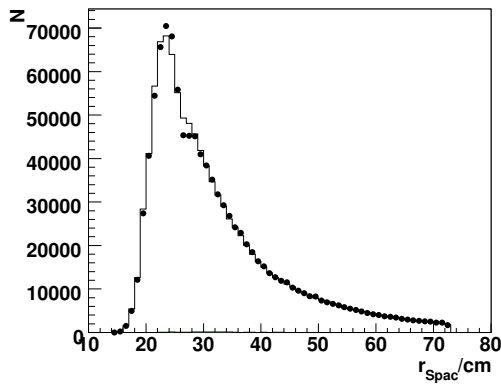
The result of the reanalysis of the older data set is, that differences between the new result presented in this work and the published H1 measurement are not due to properties of the data sets themselves. Also a large global effect, e.g. due to a wrong luminosity determination, is unlikely.



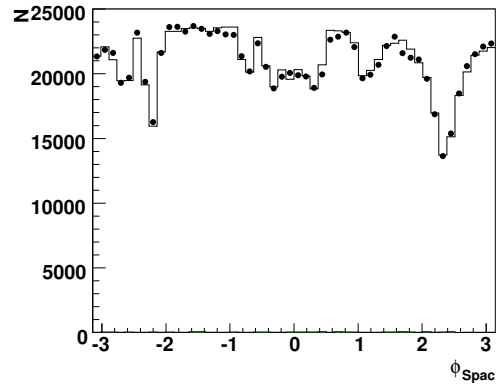
(a) Electron Energy



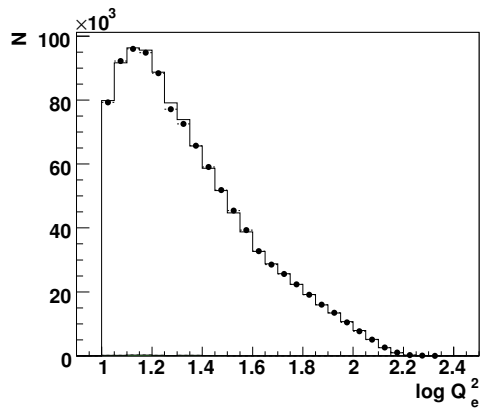
(b) Electron Polar Angle



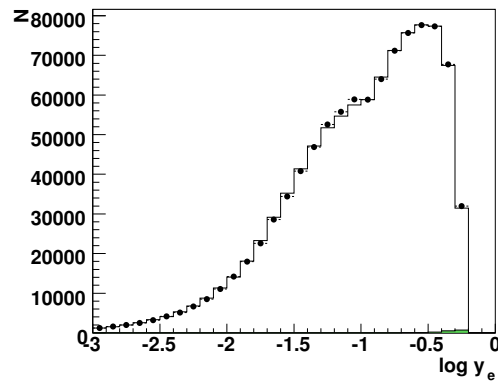
(c) Electron SpaCal Radius



(d) Electron Azimuthal Angle



(e) Q^2 from Electron Method



(f) y from Electron Method

Figure 8.5: Control plots related to the scattered electron. Dots are the data, the full histograms show the prediction of the simulation. Arrows indicate the analysis selection on E'_e . The normalisation is adjusted to the luminosity and only events within the final bin selection contribute to the plots.

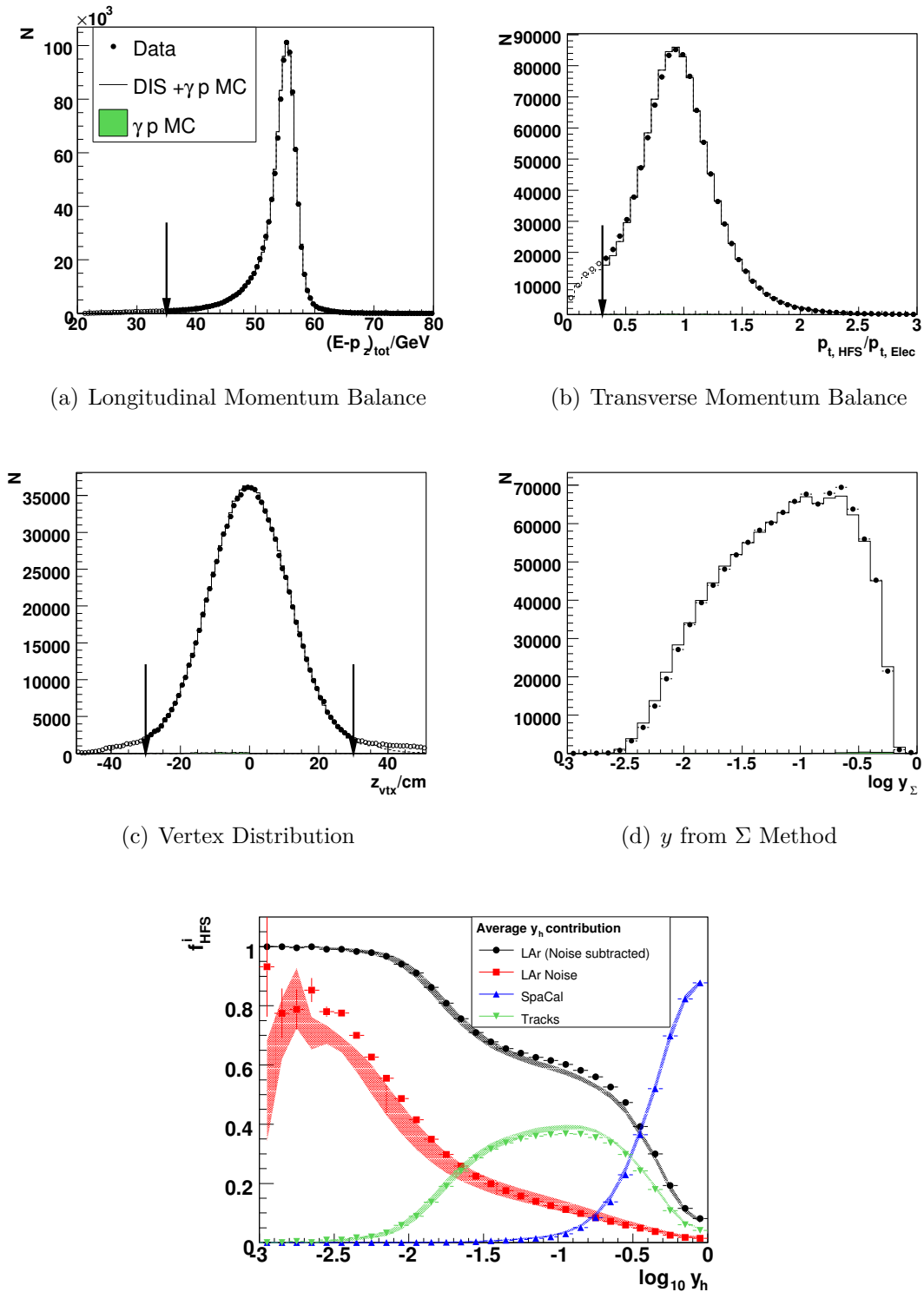
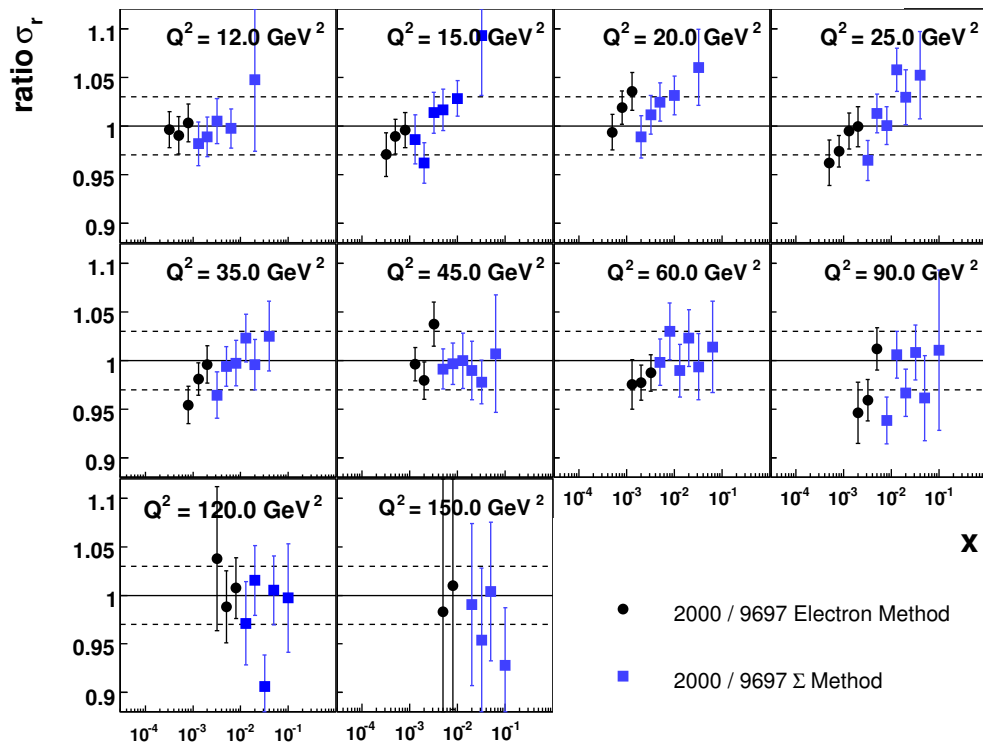
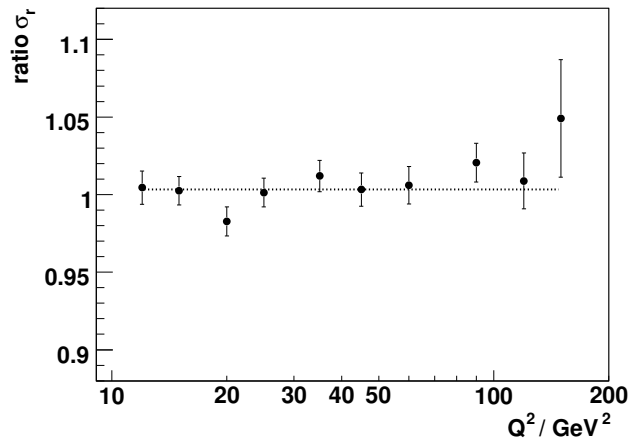


Figure 8.6: Control plots related to HFS or combined quantities. Dots are the data, the full histograms show the prediction of the simulation. Arrows indicate the analysis selection. The normalisation is adjusted to the luminosity and only events within the final bin selection contribute to the plots.



(a) The error bars correspond to the quadratic sum of individual measurement uncertainties. While for the 2000 data the systematic errors were determined, the 1996/97 errors are statistical only.



(b) Weighted average of the ratios shown above in figure (a) at constant Q^2 . There is no significant overall shift of the data sets. The averaging is performed ignoring the fact, that the uncertainties are partially correlated.

Figure 8.7: Ratio of the cross section measurements done within this work using the data sets from the years 2000 and 1996/97. A small correction to the common centre of mass energy of $\sqrt{s} = 320 \text{ GeV}$ is applied to the results from the years 1996/97.

8.3 Influence of the Monte Carlo Samples

An important tool for the determination of the cross section is the Monte Carlo simulation. Here the published analysis and the analyses presented in this thesis differ in several ways, which may hint at the reason of the differences.

First of all, the available statistics available today is much larger due to the general progress in computer technology. For the publication two samples of about 2 million events each were used, which just matched the luminosity of the analysed data sample. For the new analysis of the 2000 data on the other hand, the available sample with 50 million events is equivalent to about five times the data luminosity.

The second difference is the used Monte Carlo event generator, which is responsible for generating the correct distribution of final event states for a set of given parton densities and a certain total cross section. In all cases the DJANGO program [SS91] has been used. For the published analysis the version was DJANGO6 2.4, while for the new analyses it was DJANGOH 1.4. The more recent version has a few known improvements. Also the DJANGO options used for the old and the newer samples differ. The two most important options are the minimal Q^2 value considered for the event generation, Q_{min}^2 , and the value Q_{wgt}^2 , which effectively lowers the number of events generated for $Q^2 < Q_{wgt}^2$. This weighting option is a convenient way to distribute the events more evenly across the analysed kinematic range, as otherwise most events would be simulated at low Q^2 due to the $1/Q^4$ cross section dependence.

Furthermore the version of the simulation program H1SIM used in each case is different. These differences should however be mostly absorbed in the corrections determined on the analysis level.

The full simulation of generated events even today is a computing intensive process. Therefore many of the following tests use large samples of generated events, where many million events can be produced in just a few hours. For these, no detector level information is available. Table 8.4 summarises the MC samples used in the following tests and their basic properties.

Gen.	N_{Events} [10^6]	\mathcal{L} [pb^{-1}]	Q_{min}^2 [GeV^2]	Q_{wgt}^2 [GeV^2]	Pub.	Sim.	Label
DJ6	2.2	30.2	5	50	Yes	Yes	9697 Pub.
DJ6	1.5	2.6	0.5	—	Yes	Yes	9697 Pub. Low Q^2
DJH14	10	21.9	2	5	No	Yes	New 9697 DJH14
DJ6	40	534	5	50	No	No	Gen DJ6 WGT
DJ6	20	82.1	5	—	No	No	Gen DJ6 NOWGT
DJH14	50	102	2	5	No	No	Gen DJH14

Table 8.4: Summary of generated and simulated MC event samples and their properties, all are produced for 1996/97 settings. The generators DJANGO6 (“DJ6”) and DJANGOH 1.4 (“DJH14”) are used. Partially they were used for the publication [A⁺01] (“Pub.”), partially also reconstruction level information is available (“Sim.”). The assigned label is further on used to refer to these samples. The samples “Gen DJ6 WGT/NOWGT” were produced to study “9697 Pub.” in more detail, “Gen DJH14” is an high statistics extension of “New 9697 DJH14”.

8.3.1 Radiative Corrections

First the test for the proper description of the total DIS cross section including the *radiative corrections*, as discussed in section 4.2.4, is performed. Figure 8.8 compares the DJANGO result for the most important samples to the analytic HECTOR calculation. The expected maximal systematic deviation is 0.5%, which is the uncorrelated error quoted for this comparison.

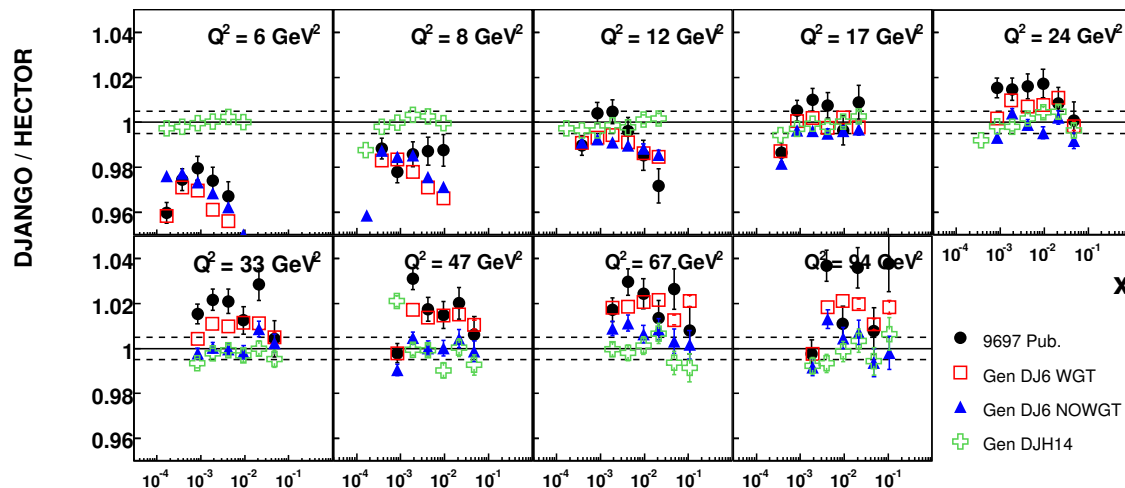


Figure 8.8: Ratio of the full DIS cross section calculated with DJANGO over the analytic HECTOR calculation for different samples. The dashed lines indicate the maximal expected systematic deviation. The binning does not correspond to the standard analysis binning.

It is observed, that the main MC sample used for the old H1 publication (sample “9697 Pub.”), exceeds the uncertainty by up to 3% in the analysis range. This behaviour can be mostly reproduced by the newly generated sample with the same settings (sample “Gen DJ6 WGT”). The problem vanishes, if the Q^2 weighting option of DJANGO is disabled (sample “Gen DJ6 NOWGT”). The new DJANGO 1.4 sample (sample “Gen DJH14”) is the only sample to agree well with HECTOR also for $Q^2 < 10 \text{ GeV}^2$. This is mostly an effect of the improved simulation at low W in the new version. These results have been confirmed by an independent analysis [SS07]. The technical reason for this DJANGO problem in connection with its weighting option is unknown so far. Similar effects have however been observed before, as mentioned in section 4.2.4. This problem was not discovered for the analysis leading to the published H1 results, as at that time extensive checks have been performed using only unweighted generated DJANGO files [S⁺00].

8.3.2 Derivation of a Correction

To compare the new measurement with the published one, a correction of the results obtained with the bad MC sample should be performed. Due to the use of the *Monte Carlo Method*, see equation 4.23, the published measurements are proportional to the ratio of the cross section to the number of reconstructed MC events in each bin, i.e. $\sigma_r \propto \sigma_r^{MC} / N_{rec}^{MC}$. This relation is independent of the used structure functions,

but was disturbed by the DJANGO generator. For these studies the same binning as originally used for the publication is employed.

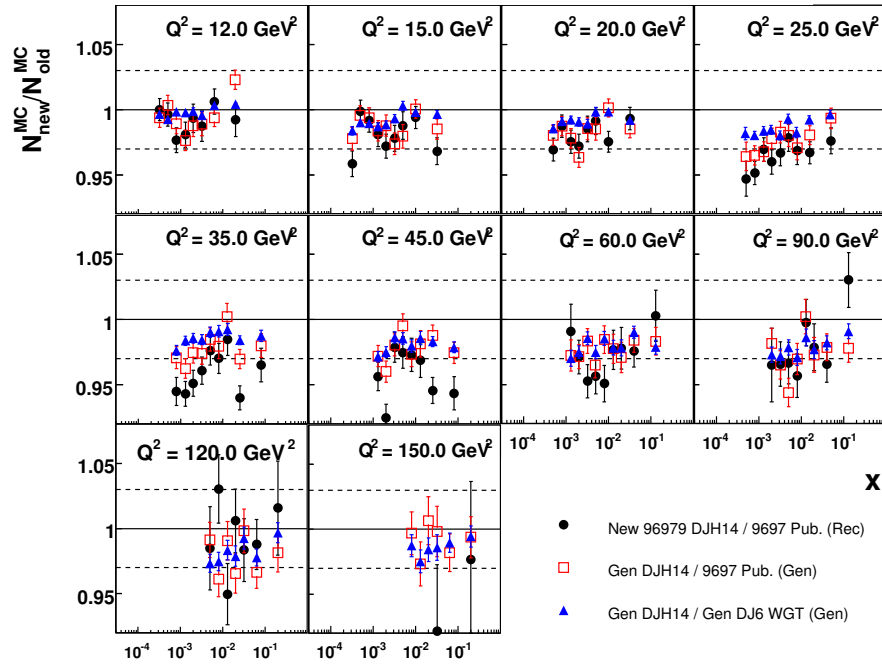
The most consistent way would be a correction at the *reconstruction level*, i.e. after the full event simulation, reconstruction, and selection. Using the same input structure functions σ_r^{MC} , the measurements should be divided by the factor $N_{rec,new}^{MC}/N_{rec,old}^{MC}$, which effectively replaces the *old* MC sample by the *new and correct* one. As the old analysis is not available in detail, one would have to assume, that the ratio $N_{rec,new}^{MC}/N_{rec,old}^{MC}$ is mostly independent of smaller analysis details. The statistical precision for this correction is limited by the available samples. It is executed using the event samples “9697 Pub.” and “New 9697 DJH14”. The results are shown in figure 8.9(a) on the top in detail. The correction is similar to the disagreement seen in figure 8.8 and reaches up to 5% in some bins.

An incorrect number of events in a certain analysis bin N_{gen}^{MC} on the *generated level* will translate to a corresponding disagreement on the reconstruction level N_{rec}^{MC} . Therefore another option is to perform the correction using generator level information only. This way, the large generated event samples can be used. One then has to assume, that the ratio $N_{rec,new}^{MC}/N_{rec,old}^{MC}$ can be reliably reproduced using $N_{gen,new}^{MC}/N_{gen,old}^{MC}$. As well one has to assume that the newly generated files reproduce the behaviour of the old ones. To improve the agreement between the generated and the reconstruction level, some additional selection criteria are introduced. An approximate $(E - p_z)_{tot} > 35$ GeV selection is performed by rejecting ISR events with a large radiative photon energy E_γ by requiring $2(E_e - E_\gamma) > 35$ GeV. The analysis selection $p_{t,HFS}/p_{t,e} > 0.3$ is mostly equivalent to requiring $W_{gen} > 20$ GeV. These additional selections as well as the method for determining the *generated event kinematics* have an influence of typically less than 0.5% on the size of the correction factors. In figure 8.9(a) the results derived using the large *correct* “Gen DJH14” sample and two different *wrong* DJANGO6 samples are shown.

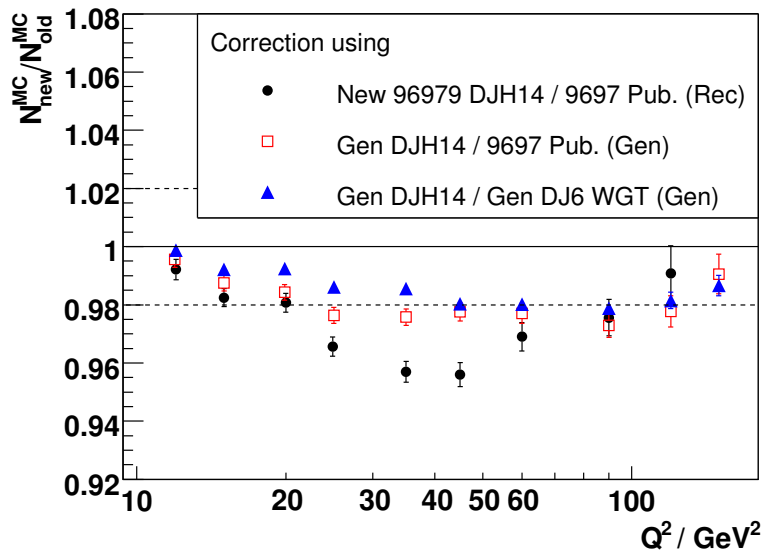
Systematic differences of 1 – 2% between the different correction factors are observed. This is especially evident, if the weighted average over all correction factors for the same Q^2 is formed, which is shown in figure 8.9(b). This simplified dependence on Q^2 only is justified by the behaviour of the high statistics samples.

One significant difference is observed between the corrections on the reconstruction and the generated level in the range $25 \text{ GeV}^2 \leq Q^2 \leq 45 \text{ GeV}^2$. This behaviour was traced to a different description of the selections on the logarithmic cluster radius r_{log} and the BDC information. Most probably differences in the H1 simulation program are responsible for this. Thus the reconstruction level correction option is discarded for now.

The second significant, albeit smaller, difference is observed between the corrections on the generated level using different DJANGO6 samples. In the domain $20 \text{ GeV}^2 \leq Q^2 \leq 35 \text{ GeV}^2$ the correction using obtained with the MC sample employed for the publication “9697 Pub.” gives a correction about 1% larger than the new generated sample “Gen DJ6 WGT”. The statistical significance of this difference after the Q^2 averaging is about 3σ . As a consequence the correction using the larger “Gen DJ6 WGT” sample is discarded, because it does not well represent the MC sample used for the publication. The reason may be just a statistical fluctuation.



(a) Error bars correspond to the statistical uncertainties. The dashed lines indicate a correction of $\pm 3\%$.



(b) Error bars correspond to the statistical uncertainties of the weighted mean. The dashed lines indicate a correction of $\pm 2\%$.

Figure 8.9: Comparison of three options for the correction of a measurement bias introduced in the published H1 measurement [A⁺01]. In (a) the bin wise dependence is shown, while for (b) the weighted average for each Q^2 is shown. The options considered are commented in detail in the text. They are using selected events with reconstructed (“Rec”) or generated (“Gen”) kinematics. Eventually the correction shown in the open symbols and labelled with “Gen DJH14 / 9697 Pub. (Gen)” is used.

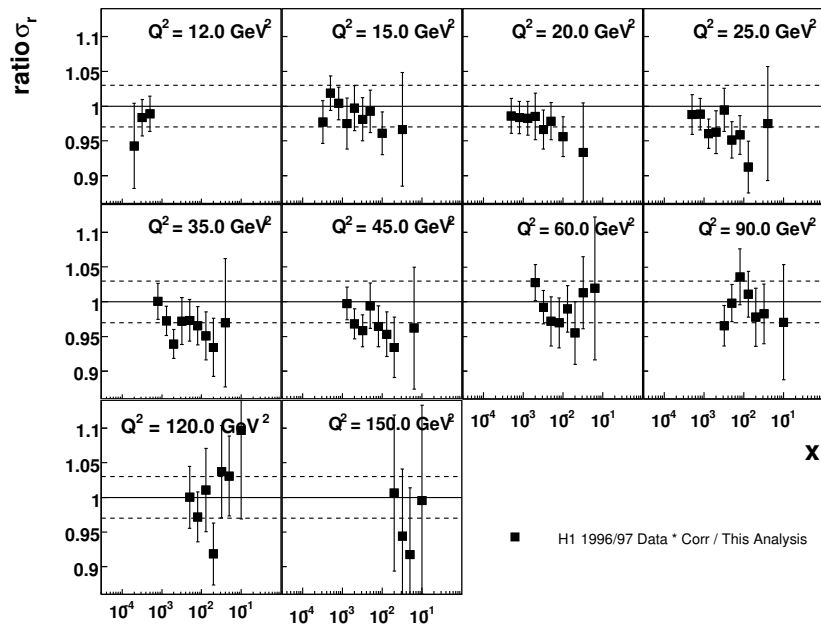
8.3.3 Final Comparison of the Cross Section Measurements

Finally the new cross section measurement is compared to the published H1 results corrected for the effect of the incorrectly generated MC sample. In addition the small 0.5% effect from the luminosity reanalysis is included. Above it was shown, that the derivation of a correction is difficult and the best scheme to use is still under discussion. The correction applied here is determined on the generated level with the help of a large sample of correct DJANGO1.4 and the sample used for the published results, labelled with “Gen DJH14 / 9697 Pub. (Gen)” in figure 8.9. The correction factors are averaged for each Q^2 bin to reduce statistical fluctuations. A value of $\lesssim 1\%$ is found at $Q^2 \leq 15 \text{ GeV}^2$ which grows to $\sim 2\%$ at larger Q^2 . The systematic uncertainty of the correction estimated from figure 8.9(b) is of the same order of magnitude as the correction itself.

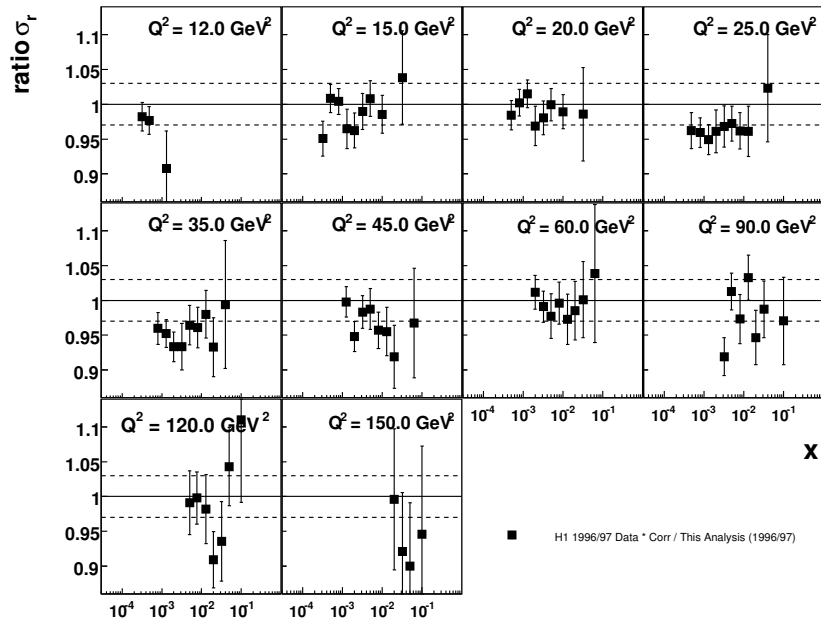
In figure 8.10(a) the deep-inelastic cross section measurement obtained in this work with the data from the year 2000 is compared to the corrected published H1 results. The correction improves the agreement significantly. In most bins the ratio is now compatible with 1. The largest disagreement is found in the bins with $25 \text{ GeV}^2 \leq Q^2 \leq 45 \text{ GeV}^2$, where the new measurement is still $\sim 3\%$ higher than the published one.

In addition figure 8.10(b) shows the comparison of the published and the new analysis of the 1996/97 data. After correcting the older results, the agreement between these two is essentially on the same level as commented above.

For figure 8.11 the weighted average of all ratios at constant Q^2 is formed again. Here the main result of this analysis, the new measurement using the year 2000 data, is compared to the published H1 result before and after applying the discussed corrections. The improved agreement after the correction is apparent. Still the new measurement tends to be larger by 2% overall. This is covered by the normalisation uncertainties of both samples, which are 1.5% and 1.7% for the old and new sample respectively. The residual deviations are typically within the quoted uncertainties.



(a) Comparison of the new measurements of this analysis using the data from the year 2000 to the corrected H1 publication



(b) Comparison of the new measurements of this analysis using the data from the years 1996/97 to the corrected H1 publication

Figure 8.10: Comparison of the new measurements presented in this work to the one published previously by the H1 [A⁺01] corrected for the effect introduced by the MC event sample. In addition, the published measurements are shifted by +0.5% due to the new determination of the luminosity. Data taken at different values of x are shifted to the grid of this measurement using the ratio of the H1PDF2000 prediction at the old and the x, Q^2 values. Effects of different centre of mass energies are corrected for. Overall the agreements of the two new measurements to the published one are similar.

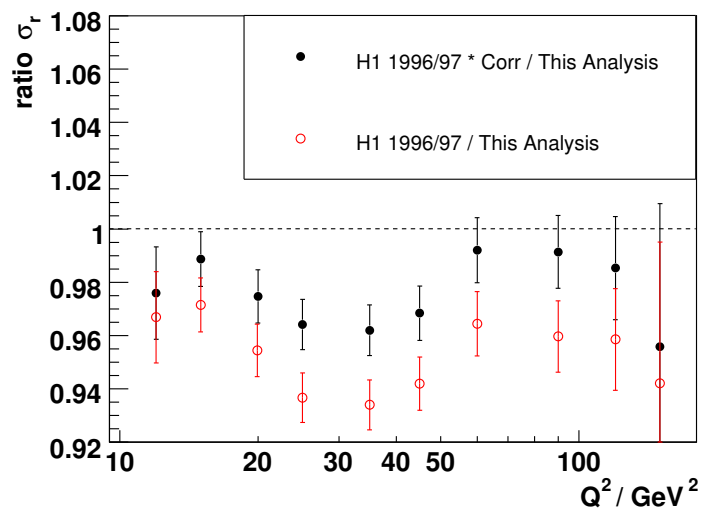


Figure 8.11: Comparison of the new measurement using the year 2000 data to the published H1 result before and after applying the discussed corrections. The weighted average is calculated from the ratios at constant Q^2 shown in figure 8.10(a). The shown error bars are calculated ignoring the fact, that the measurement uncertainties are partially correlated.

Chapter 9

Summary

The goal of this work was to perform a new measurement of the inclusive deep-inelastic electron-proton scattering cross section using the data taken with the H1 experiment in the year 2000. The measurement was restricted to the region of low and intermediate inelasticities y , where the background is low. In this domain the measured reduced cross section is also nearly identical to the proton structure function F_2 . About one order of magnitude in the photon virtuality, $10 \text{ GeV}^2 < Q^2 < 180 \text{ GeV}^2$, and three orders of magnitude in the Bjorken scaling variable, $1.3 \cdot 10^{-4} < x < 0.15$, are covered.

Results using the data from the years 1996/97 were published before, so the main goal was to reduce the uncertainties of the measurement. This was eventually accomplished and a self consistent measurement was presented. The results were also reproduced in an independent analysis. The errors of the new measurement are typically in the range of 1.3–2.0%, which means a 30% improvement in accuracy over the previously published results. None of the considered systematic error sources dominates the total uncertainty in the bulk of the measurement. Only at the highest x values, or equivalently lowest y , the measurement is limited by the achieved control over the measurement of the hadronic final state.

An unexpected but nevertheless important result is the observed discrepancy between the measurement and the previously published H1 results. In turn both, the data set and the Monte Carlo samples used for the older measurement, were tested carefully. The new analysis of the data set from the years 1996/97 showed no disagreement beyond the expected uncertainties. However, it was possible to prove, that assumptions made for the simulated event sample were wrong. The bias in the cross section measurement is difficult to quantify, but an approximate correction of the published data leads to a reasonable agreement of the old and the new measurement within their respective uncertainties.

In the future, the new results will have a strong impact on QCD analyses, which will be able to determine the parton distribution functions of the proton with improved precision. These analyses will also challenge our understanding of the DGLAP evolution and precisely determine the strong coupling constant α_s . The outcome of the QCD fits will be a valuable input to measurement at the forthcoming proton-proton collider LHC.

List of Figures

2.1	Lowest order Feynman diagram describing deep-inelastic electron-proton scattering	3
2.2	The Quark Parton Model interpretation of DIS	6
2.3	Diagrams for the lowest order splitting functions for the DGLAP equations.	9
2.4	Data on F_2 from fixed target experiments and the HERA collider experiments together with a NLO QCD fit	10
2.5	The exponent $\lambda(Q_2)$ describing the rise of F_2 for low $x < 0.01$	11
2.6	Lowest order diagrams for the process $ep \rightarrow eX\gamma$	12
2.7	Kinematic (x, Q^2) plane covered by fixed target, the HERA and Tevatron collider experiments, and the forthcoming LHC	14
3.1	The HERA accelerator facility and its 4 experiments	18
3.2	Schematic drawing of the H1 detector	19
3.3	View of the central tracking detectors in the xy -plane	20
3.4	View of the LAr calorimeter in the rz -plane	22
3.5	Cut on the rz -plane of the H1 backward region	23
3.6	Technical drawing of the whole SpaCal and the insert section	24
3.7	Three-dimensional view of a section of the BDC illustrating the layer structure and the drift cell geometry.	25
3.8	Schematic layout of the H1 Backward Silicon Tracker (BST)	26
3.9	Two types of silicon sensors used in the BST: r and u -sensor	27
3.10	A schematic overview of the H1 Luminosity System	28
3.11	The four trigger levels of H1	29
4.1	The kinematic (x, Q^2) plane for the DIS process $ep \rightarrow eX$ at the Born level and low Q^2	34
4.2	Material distribution in the backward region of the H1 detector	37
4.3	Comparison of the total DIS cross section including all radiative corrections between the HECTOR prediction and the DJANGO generator	38
4.4	Acceptance of the Electron Tagger for photoproduction events as a function of the inelasticity	40
4.5	Energy spectra in tagged γp events of the scattered electrons in the ET and the falsely identified electron in the SpaCal	41
4.6	Some key distributions of events selected for e -pilot bunches compared to the whole set of selected data events	43
4.7	Reconstruction bias and resolution from the Electron Method as a function of the position on the kinematic plane	45

4.8	Reconstruction bias and resolution from the Sigma Method as a function of the position on the kinematic plane	47
4.9	Acceptance of this analysis in the kinematic plane due to selection criteria imposed on the data	48
4.10	Displays of two DIS events as seen by the H1 detector	50
5.1	Integrated luminosity \mathcal{L} recorded by H1 differentiated by the applied prescale on the trigger conditions S0, S3, S9	55
5.2	Basic SpaCal cluster properties and selection cuts imposed for background rejection	57
5.3	Operation principle of the z -Vertex-Trigger visualised in the rz -plane	61
5.4	Efficiency of the SpaCal L1 and L2 elements of the used subtriggers S0, S3, and S9 as a function of the selected electron energy E'_e and its radius on the SpaCal plane r_{Spac}	62
5.5	Efficiency of the SpaCal elements of the S9 subtrigger as a function of the H1 Run Number	63
5.6	Efficiency of the Ray_T0 condition provided by the proportional chambers	64
5.7	Subdivision of the event sample into subsets corresponding to events triggered by one, two, or all three subtriggers	65
5.8	Final results for the trigger efficiency measured with the reference sample defined by the offline analysis cuts and non-SpaCal reference triggers as a function of technical variables and the reconstructed kinematics	66
5.9	Total event yield per luminosity with the final run selection as a function of the H1 Run Number	68
5.10	Mean and spread of the vertex distributions determined by Gaussian fits for each luminosity fill	70
5.11	The function used to reweight the MC vertex distribution to the one observed in data and comparison of the analysis vertex distributions in data and the reweighted MC	70
5.12	Determination of the S0 global option efficiency in the year 2000 done with the help of Bethe-Heitler events and S91 trigger	72
5.13	Distribution of reconstructed z_{vtx} values of DIS events with a special selection to assure an equalised acceptance	74
6.1	Comparison of the absolute energy scale given by the MC generator and measurements by the Double Angle Method and the SpaCal . . .	77
6.2	Number of effective calibration events available for the determination of the cell calibration constants as a function of the cell number . . .	78
6.3	Deviation of the SpaCal energy measurement from the calibration scale E_{DA} before and after the application of the cell calibration constants	80
6.4	Deviation of the SpaCal energy measurement from the calibration scale E_{DA} as a function of the cluster barycentre relative to the centre of the hottest cell	80
6.5	Deviation of the SpaCal energy measurement from the calibration scale E_{DA} as a function of the total integrated H1 luminosity	81

6.6	SpaCal calibration correction for energy loss in dead material as a function of the impact position on the SpaCal plane	83
6.7	Deviation of the SpaCal energy scale from E_{DA} before and after the dead material corrections as a function of r_{box}	84
6.8	Comparison of the scattered electron energy in the kinematic peak region for Data and MC with different corrections applied	85
6.9	SpaCal energy smearing in the MC and correction of the data energy scale for nonlinear effects at low energies	86
6.10	Illustration of the two adjustments of the HFS contribution given by the SpaCal	87
6.11	LAr calibration constants determined with the Lagrangian Method .	89
6.12	Tests of the HFS Energy scale and resolution in data and MC simulation using the transverse momentum balance	90
6.13	Assigned uncertainty on the hadronic energy scale	92
6.14	Contributions to y_h from different detector components	93
6.15	Dependence of the relative CIP misalignment $\Delta\theta = \theta_{CT} - \theta_{CIP}$ on ϕ_e	94
6.16	BDC efficiency in data and MC before and after applying the efficiency correction; BDC efficiency correction functions measured with a sample reconstructed by the BST	95
7.1	Distributions for the basic selection criteria for the BST reference sample	98
7.2	Difference of the event vertex position reconstructed by the BST and the CT or CIP	99
7.3	Vertex reconstruction efficiency by the CT or CIP as a function of y_Σ in data and MC	99
7.4	Vertex reconstruction efficiency in the selected analysis bins	101
7.5	Efficiency of the cluster based DIS event selection with the standard PHOJET normalisation and with specially adjusted PHOJET normalisation before and after the selection	102
7.6	Efficiency of the BDC based DIS event selection with the with specially adjusted PHOJET normalisation before and after the selection	102
7.7	Efficiency of the QED Compton rejection cut	103
7.8	Efficiency of the momentum balance selections in data and MC . . .	103
7.9	Purity and Stability for the chosen analysis binning for both the Electron and the Σ Methods	105
7.10	Control plots related to the scattered electron	107
7.11	Control plots related to HFS or combined quantities	108
7.12	Reduced cross section measured with the Electron and the Σ Method and the most important measurement uncertainties for three Q^2 bins	111
7.13	Cross checks of the reduced cross section measured with partial event or data samples compared to the nominal analysis	115
7.14	Total measurement uncertainties for three Q^2 bins using a combination of the Electron and the Σ Method and the $e\Sigma$ and the PT Method	116
7.15	Comparison of the new measurements to other published data	117

7.16	Total measurement uncertainties for three Q^2 bins for this analysis and the published measurements	118
8.1	Ratio of the new measurement to the published results	120
8.2	Total event yield per luminosity with the final run selection as a function of the H1 Run Number for the data taking period 1996/97 .	122
8.3	S0 trigger efficiency as a function of time before the full run selection and dependence of the S0 and S3 efficiency on the energy of the scattered electron	124
8.4	Ratio of the BDC efficiency measured in data and MC with applied correction determined for the 2000 data	125
8.5	Control plots related to the scattered electron for the 1996/97 data .	126
8.6	Control plots related to HFS or misc. quantities for the 1996/97 data	127
8.7	Ratio of the cross section measurements done within this work using the data sets from the years 2000 and 1996/97	128
8.8	Ratio of the full DIS cross section calculated with DJANGO over the analytic HECTOR calculation for different samples	130
8.9	Comparison of three options for the correction of a measurement bias introduced in the published H1 measurement	132
8.10	Comparison of the new measurements to the one published previously by the H1 corrected for the effect introduced by the MC event sample the new determination of the luminosity	134
8.11	Comparison of the new measurements to the one published previously by the H1 corrected for the effect introduced by the MC event sample the new determination of the luminosity	135
A.1	Cell numbering scheme of the SpaCal calorimeter. The cell numbers zero to three correspond to the veto cells.	145

List of Tables

4.1	Summary of the additional selection criteria for tagged γp events . . .	41
4.2	Summary of the average number of different bunch types, the number of DIS events selected and the effect on the analysis results	42
4.3	Standard bin boundaries and central values in Q^2 and x	51
5.1	Summary of the H1 runs excluded from the analysis of the year 2000 data	56
5.2	Summary of the cuts on reconstructed quantities applied to select DIS events in the phase space of interest	57
5.3	Summary of trigger setup for the used subtriggers S0, S3, and S9 . .	61
5.4	Summary of the fiducial cuts applied in the analysis	63
5.5	Summary of the corrections applied to the luminosity value as calculated by standard H1 Luminosity tools.	71
6.1	Split of the data sample into four periods for cell wise calibration . .	79
6.2	CIP alignment constants in data and MC	94
7.1	Table of sources of systematic uncertainties considered for the cross section measurement	109
7.2	Systematic shifts in units of standard deviations of the assigned uncertainty fitted to improve the agreement of the cross section measured by the Electron and the Σ Methods.	113
8.1	Summary of the H1 runs excluded from the analysis of the year 1996/97 data	121
8.2	Summary of trigger setup for the used subtriggers S0, S1, and S3 . .	124
8.3	Summary of the fiducial cuts applied in the analysis of 1996/96 data .	124
8.4	Summary of generated and simulated MC event samples for 1996/97 settings	129

Appendix A

SpaCal Cell Numbers

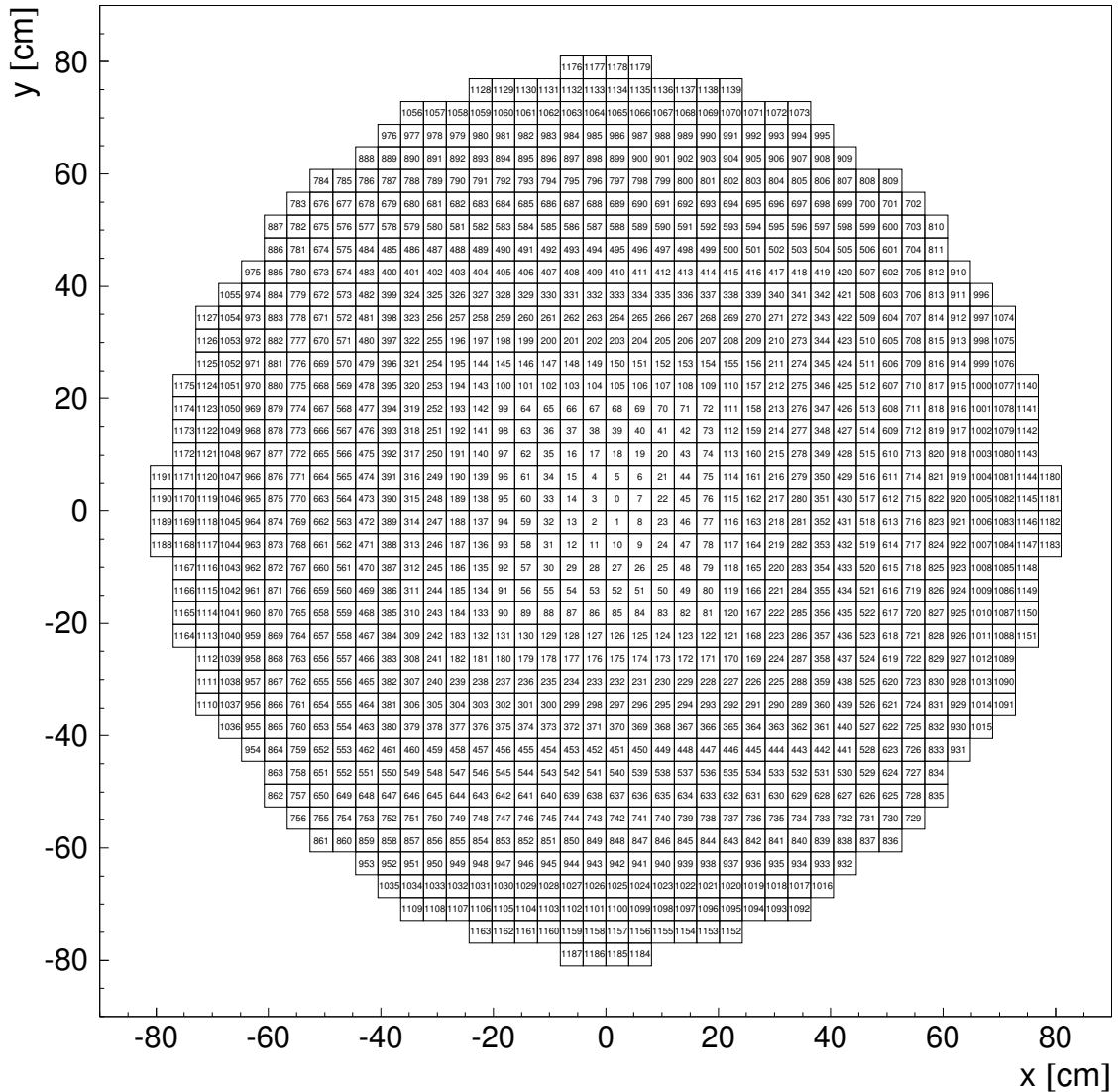


Figure A.1: Cell numbering scheme of the SpaCal calorimeter. The cell numbers zero to three correspond to the veto cells.

Appendix B

Cross Section Results

The following table summarises the results of the analysis presented in this work. The main result is the measured reduced cross section σ_r together with its detailed information of measurement uncertainties. Also results on the structure function F_2 are presented, which are essentially equal to σ_r plus a small correction due to the influence of the longitudinal structure function F_L , which is performed according to equation 4.24. The prediction for F_L , or equivalently $R = F_L/(F_2 - F_L)$ is taken from the modified QCD fit, as explained in section 7.4.

The columns of the table contain (from left to right):

- the kinematic variables Q^2 , x , and y at the bin centres,
- the measured reduced cross section σ_r , the R value used for the extraction of F_2 , and the structure function F_2 itself,
- the total uncertainty of the measurement δ_{tot} and its components, i.e. the statistical error δ_{sta} , the cumulated uncorrelated systematic uncertainties δ_{unc} , and the cumulated correlated systematic uncertainties δ_{cor} ,
- the individual components of the total correlated systematic uncertainty from the uncertainty on the electron energy scale $\delta_{E'_e}$, electron polar angle δ_{θ_e} , hadronic energy scale of LAr calorimeter and Central Tracker δ_{LAr} , noise in the LAr calorimeter δ_{Noise} , hadronic energy scale of the SpaCal calorimeter δ_{HSpa} , and PHOJET normalisation $\delta_{\gamma p}$.

All quoted errors are relative uncertainties in per cent. The normalisation uncertainties, i.e. the global 1.5% uncertainty due to the determination of the luminosity, is not included in these errors.

Q^2 [GeV ²]	x	y	σ_r	R	F_2	δ_{tot} [%]	δ_{sta} [%]	δ_{unc} [%]	δ_{cor} [%]	$\delta_{E'_e}$ [%]	δ_{θ_e} [%]	δ_{LAR} [%]	δ_{Noise} [%]	δ_{HSpa} [%]	$\delta_{\gamma p}$
12.0	$2.00 \cdot 10^{-4}$	0.591	1.345	0.252	1.431	2.8	1.2	1.3	2.1	-0.7	-0.3	0.2	-0.2	-0.3	-2.0
12.0	$3.20 \cdot 10^{-4}$	0.369	1.259	0.253	1.285	1.8	0.9	1.3	0.8	-0.6	-0.3	0.2	-0.2	0.0	-0.3
12.0	$5.00 \cdot 10^{-4}$	0.236	1.173	0.247	1.181	1.8	1.0	1.3	0.8	-0.6	-0.4	0.2	-0.1	0.0	0.0
12.0	$8.00 \cdot 10^{-4}$	0.148	1.071	0.242	1.074	1.8	0.9	1.3	0.9	-0.8	-0.4	0.1	-0.1	0.0	0.0
12.0	$1.30 \cdot 10^{-3}$	0.091	0.934	0.248	0.935	2.1	1.0	1.3	1.4	0.1	-0.4	-0.2	-0.8	1.1	0.0
12.0	$2.00 \cdot 10^{-3}$	0.059	0.842	0.247	0.842	1.9	1.1	1.3	0.9	0.0	-0.4	-0.5	-0.3	0.5	0.0
12.0	$3.20 \cdot 10^{-3}$	0.037	0.765	0.239	0.765	2.0	1.3	1.3	0.8	0.0	-0.5	-0.4	-0.2	0.5	0.0
12.0	$6.31 \cdot 10^{-3}$	0.019	0.634	0.237	0.635	1.9	0.9	1.3	1.1	-0.2	-0.3	-0.8	0.6	0.1	0.0
12.0	$2.00 \cdot 10^{-2}$	0.006	0.503	0.193	0.503	6.9	1.2	2.4	6.4	-0.6	0.7	-1.4	6.1	0.3	0.0
15.0	$3.20 \cdot 10^{-4}$	0.462	1.354	0.253	1.401	2.0	0.8	1.3	1.3	-0.6	-0.3	0.2	-0.2	-0.1	-1.1
15.0	$5.00 \cdot 10^{-4}$	0.295	1.232	0.256	1.246	1.6	0.7	1.3	0.7	-0.5	-0.3	0.2	-0.1	0.0	-0.1
15.0	$8.00 \cdot 10^{-4}$	0.185	1.132	0.247	1.136	1.7	0.8	1.3	0.8	-0.7	-0.4	0.2	-0.1	0.0	0.0
15.0	$1.30 \cdot 10^{-3}$	0.114	1.012	0.243	1.014	2.5	0.8	1.3	1.9	0.7	-0.4	0.2	-1.4	1.1	0.0
15.0	$2.00 \cdot 10^{-3}$	0.074	0.883	0.250	0.883	2.0	0.9	1.3	1.3	0.6	-0.4	0.0	-1.0	0.5	0.0
15.0	$3.20 \cdot 10^{-3}$	0.046	0.803	0.238	0.803	1.9	1.1	1.3	0.9	0.5	-0.4	0.0	-0.6	0.3	0.0
15.0	$5.00 \cdot 10^{-3}$	0.030	0.726	0.228	0.726	1.9	1.2	1.3	0.8	0.6	-0.5	-0.1	-0.3	0.1	0.0
15.0	$1.00 \cdot 10^{-2}$	0.015	0.609	0.212	0.609	1.7	0.9	1.3	0.6	0.3	-0.2	0.0	-0.4	0.2	0.0
15.0	$3.20 \cdot 10^{-2}$	0.005	0.477	0.155	0.477	5.6	0.9	2.4	5.0	0.0	0.2	0.0	5.0	0.4	0.0
20.0	$5.00 \cdot 10^{-4}$	0.394	1.343	0.255	1.374	1.6	0.7	1.3	0.7	-0.5	-0.3	0.2	-0.2	0.0	-0.3
20.0	$8.00 \cdot 10^{-4}$	0.246	1.227	0.248	1.237	1.6	0.6	1.3	0.6	-0.5	-0.3	0.1	-0.1	0.0	0.0
20.0	$1.30 \cdot 10^{-3}$	0.151	1.102	0.241	1.105	1.7	0.7	1.3	0.8	-0.8	-0.3	0.1	0.0	0.0	0.0
20.0	$2.00 \cdot 10^{-3}$	0.098	0.974	0.240	0.975	2.0	0.7	1.3	1.4	0.7	-0.3	0.0	-0.9	0.8	0.0
20.0	$3.20 \cdot 10^{-3}$	0.062	0.866	0.232	0.866	1.8	0.7	1.3	1.0	0.5	-0.3	0.0	-0.7	0.3	0.0
20.0	$5.00 \cdot 10^{-3}$	0.039	0.780	0.221	0.780	1.7	0.8	1.3	0.8	0.5	-0.3	-0.2	-0.5	0.1	0.0
20.0	$1.00 \cdot 10^{-2}$	0.020	0.652	0.202	0.652	1.8	0.6	1.3	1.1	0.5	-0.4	0.2	-0.9	0.1	0.0
20.0	$3.20 \cdot 10^{-2}$	0.006	0.498	0.144	0.498	3.6	0.6	2.4	2.6	0.3	-0.5	0.5	2.4	0.4	0.0
25.0	$5.00 \cdot 10^{-4}$	0.492	1.424	0.254	1.482	1.7	0.9	1.0	1.0	-0.7	-0.2	0.2	-0.2	-0.2	-0.7
25.0	$8.00 \cdot 10^{-4}$	0.308	1.300	0.248	1.317	1.3	0.7	1.0	0.5	-0.4	-0.3	0.1	-0.1	0.0	0.0
25.0	$1.30 \cdot 10^{-3}$	0.189	1.171	0.239	1.175	1.3	0.7	1.0	0.6	-0.5	-0.3	0.1	0.0	0.0	0.0
25.0	$2.00 \cdot 10^{-3}$	0.123	1.054	0.232	1.056	1.5	0.7	1.0	0.9	-0.8	-0.4	0.1	0.0	0.0	0.0

continued on next page

Q^2 [GeV ²]	x	y	σ_r	R	F_2	δ_{tot} [%]	δ_{sta} [%]	δ_{unc} [%]	δ_{cor} [%]	$\delta_{E'_e}$ [%]	δ_{θ_e} [%]	δ_{LAR} [%]	δ_{Noise} [%]	δ_{HSpa} [%]	$\delta_{\gamma p}$
25.0	$3.20 \cdot 10^{-3}$	0.077	0.910	0.230	0.911	1.5	0.7	1.0	1.0	0.5	-0.3	0.0	-0.7	0.3	0.0
25.0	$5.00 \cdot 10^{-3}$	0.049	0.816	0.218	0.817	1.4	0.7	1.0	0.8	0.5	-0.3	-0.1	-0.4	0.2	0.0
25.0	$8.00 \cdot 10^{-3}$	0.031	0.712	0.208	0.712	1.5	0.8	1.0	0.8	0.5	-0.3	0.0	-0.5	0.2	0.0
25.0	$1.30 \cdot 10^{-2}$	0.019	0.650	0.182	0.650	1.9	1.1	1.0	1.2	0.6	-0.5	0.0	-1.0	0.2	0.0
25.0	$2.00 \cdot 10^{-2}$	0.012	0.585	0.162	0.585	2.1	0.8	1.0	1.7	0.5	-0.5	0.6	-1.4	0.3	0.0
25.0	$3.98 \cdot 10^{-2}$	0.006	0.495	0.123	0.495	4.0	0.7	2.2	3.3	0.6	-0.9	0.3	3.1	0.2	0.0
35.0	$8.00 \cdot 10^{-4}$	0.431	1.409	0.247	1.449	1.5	0.8	1.0	0.7	-0.6	-0.2	0.2	-0.2	0.0	-0.3
35.0	$1.30 \cdot 10^{-3}$	0.265	1.255	0.241	1.266	1.3	0.8	1.0	0.4	-0.2	-0.3	0.0	0.0	0.0	0.0
35.0	$2.00 \cdot 10^{-3}$	0.172	1.132	0.231	1.136	1.4	0.8	1.0	0.6	-0.6	-0.3	0.0	0.0	0.0	0.0
35.0	$3.20 \cdot 10^{-3}$	0.108	0.991	0.223	0.992	1.8	0.8	1.0	1.2	0.8	-0.3	0.0	-0.8	0.5	0.0
35.0	$5.00 \cdot 10^{-3}$	0.069	0.869	0.215	0.869	1.6	1.0	1.0	0.9	0.7	-0.3	0.0	-0.4	0.0	0.0
35.0	$8.00 \cdot 10^{-3}$	0.043	0.767	0.199	0.768	1.6	0.8	1.0	0.9	0.5	-0.2	-0.1	-0.8	0.1	0.0
35.0	$1.30 \cdot 10^{-2}$	0.027	0.677	0.179	0.677	1.8	1.1	1.0	0.9	0.6	-0.3	-0.2	-0.6	0.1	0.0
35.0	$2.00 \cdot 10^{-2}$	0.017	0.614	0.155	0.614	1.8	0.9	1.0	1.2	0.5	-0.4	0.2	-1.0	0.2	0.0
35.0	$3.98 \cdot 10^{-2}$	0.009	0.512	0.117	0.512	3.0	0.8	2.2	1.9	0.5	-0.8	0.1	1.5	0.6	0.0
45.0	$8.00 \cdot 10^{-4}$	0.554	1.513	0.237	1.591	2.4	2.0	1.1	0.6	-0.3	-0.1	0.2	-0.2	-0.2	-0.3
45.0	$1.30 \cdot 10^{-3}$	0.341	1.329	0.238	1.350	1.4	0.9	1.0	0.4	-0.3	-0.2	0.1	0.0	0.0	0.0
45.0	$2.00 \cdot 10^{-3}$	0.222	1.178	0.233	1.184	1.4	0.8	1.0	0.5	-0.4	-0.2	0.0	0.0	0.0	0.0
45.0	$3.20 \cdot 10^{-3}$	0.138	1.051	0.218	1.053	1.6	1.1	1.0	0.6	-0.5	-0.2	0.0	0.0	0.0	0.0
45.0	$5.00 \cdot 10^{-3}$	0.089	0.902	0.213	0.903	1.8	0.9	1.0	1.2	0.8	-0.2	0.5	-0.7	0.0	0.0
45.0	$8.00 \cdot 10^{-3}$	0.055	0.792	0.197	0.793	1.8	0.9	1.0	1.1	0.8	-0.3	-0.4	-0.6	0.0	0.0
45.0	$1.30 \cdot 10^{-2}$	0.034	0.700	0.175	0.700	1.9	1.3	1.0	0.9	0.5	-0.3	-0.2	-0.6	0.4	0.0
45.0	$2.00 \cdot 10^{-2}$	0.022	0.616	0.156	0.616	2.0	1.0	1.1	1.3	0.6	-0.3	-0.2	-1.1	0.2	0.0
45.0	$3.20 \cdot 10^{-2}$	0.014	0.537	0.130	0.537	1.9	1.1	1.1	1.1	0.5	-0.5	0.1	-0.5	0.7	0.0
45.0	$6.31 \cdot 10^{-2}$	0.007	0.447	0.091	0.447	5.2	1.1	2.3	4.6	0.8	-0.9	-1.1	4.2	0.3	0.0
60.0	$1.30 \cdot 10^{-3}$	0.454	1.403	0.234	1.446	1.8	1.3	1.1	0.6	-0.5	-0.1	0.2	-0.2	-0.1	0.0
60.0	$2.00 \cdot 10^{-3}$	0.295	1.251	0.228	1.265	1.4	1.0	1.0	0.3	-0.2	-0.2	0.0	0.0	0.0	0.0
60.0	$3.20 \cdot 10^{-3}$	0.185	1.092	0.218	1.096	1.5	1.0	1.0	0.5	-0.5	-0.2	0.0	0.0	0.0	0.0
60.0	$5.00 \cdot 10^{-3}$	0.118	0.953	0.207	0.955	2.0	1.5	1.1	1.0	0.7	-0.2	-0.2	-0.6	0.0	0.0
60.0	$8.00 \cdot 10^{-3}$	0.074	0.852	0.186	0.853	2.5	2.1	1.1	0.9	0.6	-0.3	0.1	-0.6	-0.1	0.0

continued on next page

Q^2 [GeV ²]	x	y	σ_r	R	F_2	δ_{tot} [%]	δ_{sta} [%]	δ_{unc} [%]	δ_{cor} [%]	$\delta_{E'_e}$ [%]	δ_{θ_e} [%]	δ_{LAR} [%]	δ_{Noise} [%]	δ_{HSpa} [%]	$\delta_{\gamma p}$
60.0	$1.30 \cdot 10^{-2}$	0.045	0.710	0.175	0.710	1.8	1.1	1.1	0.9	0.8	-0.3	0.0	-0.3	0.1	0.0
60.0	$2.00 \cdot 10^{-2}$	0.030	0.643	0.149	0.643	2.5	1.7	1.1	1.5	0.7	-0.3	-0.3	-1.2	-0.2	0.0
60.0	$3.20 \cdot 10^{-2}$	0.018	0.546	0.128	0.546	2.2	1.2	1.1	1.4	0.5	-0.3	0.0	-1.1	0.7	0.0
60.0	$6.31 \cdot 10^{-2}$	0.009	0.439	0.090	0.439	4.1	1.2	2.3	3.2	0.4	-0.4	-1.2	2.8	1.0	0.0
90.0	$2.00 \cdot 10^{-3}$	0.443	1.326	0.223	1.363	2.2	1.8	1.2	0.4	-0.3	-0.1	0.0	0.0	0.0	0.0
90.0	$3.20 \cdot 10^{-3}$	0.277	1.188	0.207	1.198	1.6	1.2	1.1	0.2	0.0	-0.2	0.0	0.0	0.0	0.0
90.0	$5.00 \cdot 10^{-3}$	0.177	1.035	0.196	1.038	1.6	1.2	1.1	0.4	-0.3	-0.2	0.0	0.0	0.0	0.0
90.0	$8.00 \cdot 10^{-3}$	0.111	0.843	0.194	0.844	2.1	1.2	1.1	1.3	1.0	-0.1	0.4	-0.6	0.0	0.0
90.0	$1.30 \cdot 10^{-2}$	0.068	0.744	0.168	0.744	1.9	1.3	1.1	0.8	0.6	-0.2	-0.2	-0.4	-0.1	0.0
90.0	$2.00 \cdot 10^{-2}$	0.044	0.653	0.147	0.653	2.0	1.3	1.1	1.0	0.4	0.0	-0.2	-0.8	0.0	0.0
90.0	$3.20 \cdot 10^{-2}$	0.028	0.568	0.121	0.568	2.3	1.4	1.2	1.3	0.5	-0.3	-0.2	-1.1	0.5	0.0
90.0	$5.00 \cdot 10^{-2}$	0.018	0.475	0.099	0.475	2.4	1.6	1.2	1.3	0.6	-0.3	-1.0	-0.3	0.4	0.0
90.0	$1.00 \cdot 10^{-1}$	0.009	0.391	0.059	0.391	7.1	1.7	2.4	6.5	0.7	-0.3	-2.2	6.0	1.1	0.0
120.0	$2.00 \cdot 10^{-3}$	0.591	1.133	0.269	1.210	23.4	20.4	10.6	4.4	-3.9	2.0	0.0	0.0	0.0	0.0
120.0	$3.20 \cdot 10^{-3}$	0.369	1.230	0.203	1.250	4.4	3.8	2.1	0.3	-0.3	0.0	0.0	0.0	0.0	0.0
120.0	$5.00 \cdot 10^{-3}$	0.236	1.041	0.198	1.047	2.6	2.2	1.4	0.3	-0.3	-0.2	0.0	0.0	0.0	0.0
120.0	$8.00 \cdot 10^{-3}$	0.148	0.888	0.184	0.890	2.2	1.8	1.3	0.4	-0.3	-0.2	0.0	0.0	0.0	0.0
120.0	$1.30 \cdot 10^{-2}$	0.091	0.757	0.165	0.758	3.9	1.8	1.3	3.2	2.3	-0.1	1.0	-1.9	-0.6	0.0
120.0	$2.00 \cdot 10^{-2}$	0.059	0.676	0.140	0.676	2.9	1.7	1.2	2.0	1.7	-0.2	0.2	-0.9	-0.4	0.0
120.0	$3.20 \cdot 10^{-2}$	0.037	0.553	0.122	0.553	2.9	1.8	1.3	2.0	1.4	-0.2	0.4	-1.1	0.6	0.0
120.0	$5.00 \cdot 10^{-2}$	0.024	0.494	0.093	0.494	2.7	1.9	1.3	1.4	0.9	0.0	-0.6	-0.9	0.4	0.0
120.0	$1.00 \cdot 10^{-1}$	0.012	0.382	0.058	0.382	5.2	1.9	1.3	4.6	1.1	-0.2	-2.2	3.9	0.6	0.0
150.0	$5.00 \cdot 10^{-3}$	0.295	1.130	0.182	1.140	18.9	16.0	9.9	1.7	-1.7	0.0	0.0	0.0	0.0	0.0
150.0	$8.00 \cdot 10^{-3}$	0.185	1.024	0.157	1.027	8.6	7.4	4.1	1.6	0.8	-1.4	0.0	-0.2	0.0	0.0
150.0	$1.30 \cdot 10^{-2}$	0.114	0.714	0.177	0.715	6.3	5.5	2.8	0.8	-0.8	0.0	0.1	0.0	0.0	0.0
150.0	$2.00 \cdot 10^{-2}$	0.074	0.715	0.131	0.715	6.9	4.2	2.4	4.9	3.5	0.3	3.2	-1.2	-0.4	0.0
150.0	$3.20 \cdot 10^{-2}$	0.046	0.591	0.112	0.591	6.4	3.9	2.1	4.7	3.5	-0.3	0.7	-2.9	-0.8	0.0
150.0	$5.00 \cdot 10^{-2}$	0.030	0.497	0.091	0.497	5.5	3.9	2.1	3.3	2.6	-0.2	0.5	-1.7	0.9	0.0
150.0	$1.00 \cdot 10^{-1}$	0.015	0.398	0.054	0.398	5.2	3.5	1.9	3.3	2.9	-0.4	-1.1	1.0	0.4	0.0

Bibliography

- [A⁺92] Awes, T. C.; et al.: A Simple Method of Shower Localization and Identification in Laterally Segmented Calorimeters. In: *Nucl. Instrum. Meth.*, volume A311:pp. 130–138, 1992.
- [A⁺93a] Abt, I.; et al. (H1): Measurement of the Proton Structure Function $F_2(x, Q^2)$ in the low x Region at HERA. In: *Nucl. Phys. B*, volume 407:p. 515, 1993.
- [A⁺93b] Andrieu, B.; et al. (H1 Calorimeter Group): Results from pion calibration runs for the H1 liquid argon calorimeter and comparisons with simulations. In: *Nucl. Instrum. Meth.*, volume A336:pp. 499–509, 1993.
- [A⁺93c] Andrieu, B.; et al. (H1 Calorimeter Group): The H1 liquid argon calorimeter system. In: *Nucl. Instrum. Meth.*, volume A336:pp. 460–498, 1993.
- [A⁺96] Appuhn, R. D.; et al. (H1 SpaCal Group): Hadronic response and e/pi separation with the H1 lead/fibre calorimeter. In: *Nucl. Instr. and Meth. A*, volume 382:p. 395, 1996.
- [A⁺97a] Abt, I.; et al. (H1): The H1 detector at HERA. In: *Nucl. Instr. and Meth. A*, volume 386:p. 310, 1997.
- [A⁺97b] Abt, I.; et al. (H1): The Tracking, calorimeter and muon detectors of the H1 experiment at HERA. In: *Nucl. Instr. and Meth. A*, volume 386:p. 348, 1997.
- [A⁺97c] Adloff, C.; et al. (H1): Diffraction Dissociation in Photoproduction at HERA. In: *Z. Phys.*, volume C74:pp. 221–236, 1997. [hep-ex/9702003](#).
- [A⁺01] Adloff, C.; et al. (H1): Deep-Inelastic Inclusive ep Scattering at Low x and a Determination of α_s . In: *Eur. Phys. J. C*, volume 21:p. 33, 2001. [hep-ex/0012053](#).
- [A⁺03a] Abramowicz, H.; et al.: A New Experiment for the HERA Collider, Expression of Interest, 2003. MPP-2003-62, <http://wwwhera-b.mppmu.mpg.de/hera3>.
- [A⁺03b] Adloff, C.; et al. (H1): Measurement and QCD analysis of neutral and charged current cross sections at HERA. In: *Eur. Phys. J.*, volume C30:pp. 1–32, 2003. [hep-ex/0304003](#).
- [A⁺03c] Alexopoulos, T.; et al.: Electron-Deuteron Scattering with HERA, a Letter of Intent, 2003. DESY 03-194, <http://hep.ph.liv.ac.uk/~green/HERA3>.
- [A⁺04] Aktas, A.; et al. (H1): Measurement of the proton structure function F_2 at low Q^2 in QED Compton scattering at HERA. In: *Phys. Lett.*, volume B598:pp. 159–171, 2004. [hep-ex/0406029](#).

- [ABB⁺96] Arbuzov, A.; Bardin, Dmitri Yu.; Bluemlein, J.; Kalinovskaya, L.; Riemann, T.: HECTOR 1.00 - A program for the calculation of QED, QCD and electroweak corrections to ep and IN deep inelastic neutral and charged current scattering. In: *Comput. Phys. Commun.*, volume 94:pp. 128–184, 1996. [hep-ph/9511434](#).
- [AC99] Abramowicz, H.; Caldwell, A.: HERA collider physics. In: *Rev. Mod. Phys.*, volume 71:pp. 1275–1410, 1999. [hep-ex/9903037](#).
- [AGIS83] Andersson, Bo; Gustafson, G.; Ingelman, G.; Sjöstrand, T.: Parton Fragmentation and String Dynamics. In: *Phys. Rept.*, volume 97:p. 31, 1983.
- [AGLP89] Andersson, Bo; Gustafson, Gosta; Lonnblad, Leif; Pettersson, Ulf: Coherence Effects in Deep Inelastic Scattering. In: *Z. Phys.*, volume C43:p. 625, 1989.
- [AGS83] Andersson, Bo; Gustafson, G.; Söderberg, B.: A General Model for Jet Fragmentation. In: *Z. Phys.*, volume C20:p. 317, 1983.
- [AP77] Altarelli, G.; Parisi, G.: Asymptotic Freedom In Parton Language. In: *Nucl. Phys. B*, volume 126:p. 298, 1977.
- [Ark00] Arkadov, V.: *Measurement of the Deep-Inelastic ep Scattering Cross Section using the Backward Silicon tracker at the H1 Detector at HERA*. Ph.D. thesis, Humboldt-Universität zu Berlin, 2000.
- [Arn95] Arndt, C.: *Kalibration des H1 Spaghetti Kalorimeters mit Halo Myonen*. Ph.D. thesis, Universität Hamburg, 1995.
- [B⁺69a] Bloom, E. D.; et al.: High-Energy Inelastic ep Scattering at 6 degrees and 10 degrees. In: *Phys. Rev. Lett.*, volume 23:p. 930, 1969.
- [B⁺69b] Breidenbach, Martin; et al.: Observed Behavior of Highly Inelastic electron-Proton Scattering. In: *Phys. Rev. Lett.*, volume 23:pp. 935–939, 1969.
- [B⁺87] Brun, R.; et al.: GEANT3 User's Guide. CERN, 1987. [CERN-DD/EE84-1](#).
- [B⁺96] Beck, H.; et al.: Principles and Operation of the z-Vertex Trigger. Internal Note H1-05/96-479, 1996.
- [B⁺00] Breitweg, J.; et al. (ZEUS): Measurement of the proton structure function F_2 at very low Q^2 at HERA. In: *Phys. Lett. B*, volume 487:p. 53, 2000. [hep-ex/0005018](#).
- [BB95a] Bassler, U.; Bernardi, G.: H1KINE : Reconstruction of Kinematic Variables inside H1REC: User's Guide. H1 Software Note 51-06/95, 1995.
- [BB95b] Bassler, Ursula; Bernardi, Gregorio: On the kinematic reconstruction of deep inelastic scattering at HERA: The Sigma method. In: *Nucl. Instrum. Meth.*, volume A361:pp. 197–208, 1995. [hep-ex/9412004](#).
- [BB99] Bassler, Ursula; Bernardi, Gregorio: Structure function measurements and kinematic reconstruction at HERA. In: *Nucl. Instrum. Meth.*, volume A426:pp. 583–598, 1999. [hep-ex/9801017](#).

-
- [Beh06] Behrendt, O.: *Measurement of the Proton Structure Function F_2 at Low Q^2 at HERA*. Ph.D. thesis, Universität Dortmund, 2006.
- [BEK92] Bentvelsent, S.; Engelen, J.; Kooijman, P.: The Double Angle Method. In: Buchmüller, W.; Ingelman, G., editors, *Proceedings of the Workshop Physics at HERA, vol. 1*, p. 23. 1992.
- [BH34] Bethe, H.; Heitler, W.: On the Stopping of fast particles and on the creation of positive electrons. In: *Proc. Roy. Soc. Lond.*, volume A146:pp. 83–112, 1934.
- [Bjo69] Bjorken, J. D.: Asymptotic Sum Rules at Infinite Momentum. In: *Phys. Rev.*, volume 179:pp. 1547–1553, 1969.
- [BL78] Balitsky, I. I.; Lipatov, L. N.: The Pomernanchuk Singularity in Quantum Chromodynamics. In: *Sov. J. Nucl. Phys.*, volume 28:p. 822, 1978.
- [Blo] Blobel, Volker: MILLEPEDE. A program description and the code are available via <http://www.desy.de/~blobel>.
- [C⁺01] Chekanov, S.; et al. (ZEUS): Measurement of the neutral current cross section and F_2 structure function for deep inelastic e^+p scattering at HERA. In: *Eur. Phys. J. C*, volume 21:p. 443, 2001. [hep-ex/0105090](#).
- [C⁺03] Chekanov, S.; et al. (ZEUS): A ZEUS next-to-leading-order QCD analysis of data on deep inelastic scattering. In: *Phys. Rev. D*, volume 67:p. 012007, 2003. [hep-ex/0208023](#).
- [C⁺04] Chekanov, S.; et al. (ZEUS): High- Q^2 neutral current cross sections in e^+p deep inelastic scattering at $\sqrt{s} = 318$ GeV. In: *Phys. Rev. D*, volume 70:p. 052001, 2004. [hep-ex/0401003](#).
- [C⁺05] Chekanov, S.; et al. (ZEUS): An NLO QCD analysis of inclusive cross-section and jet-production data from the ZEUS experiment. In: *Eur. Phys. J.*, volume C42:pp. 1–16, 2005. [hep-ph/0503274](#).
- [CG69] Callan, Jr., Curtis G.; Gross, David J.: High-energy electroproduction and the constitution of the electric current. In: *Phys. Rev. Lett.*, volume 22:pp. 156–159, 1969.
- [CSDdR98] Cooper-Sakar, A. M.; Devenish, R. C. E.; de Roeck, A.: Structure Functions of the Nucleon and their Interpretation. In: *Int. J. Mod. Phys. A*, volume 13(20):pp. 3385–3586, 1998. [hep-ph/9712301](#).
- [CSS88] Collins, John C.; Soper, Davison E.; Sterman, George: Factorization of Hard Processes in QCD. In: *Adv. Ser. Direct. High Energy Phys.*, volume 5:pp. 1–91, 1988. [hep-ph/0409313](#).
- [D⁺93] Derrick, M.; et al. (ZEUS): Measurement of the Proton Structure Function F_2 in ep Scattering at HERA. In: *Phys. Lett. B*, volume 316:p. 412, 1993.
- [Dir96] Dirkmann, M.: Calibration of the SpaCal with Cosmics. H1 Internal Note H1-05/96-477, 1996.
-

- [Dok77] Dokshitzer, Yu. L.: Calculation Of The Structure Functions For Deep Inelastic Scattering And e^+e^- Annihilation By Perturbation Theory In Quantum Chromodynamics (In Russian). In: *Sov. Phys. JETP*, volume 46:p. 641, 1977.
- [E⁺97a] Egli, S.; et al.: Calculating Event Weights in Case of Downscaling on Trigger Levels 1-4. Internal Note H1-04/97-517, 1997.
- [E⁺97b] Eick, W.; et al.: Development of the H1 backward silicon strip detector. In: *Nucl. Instr. and Meth. A*, volume 386:pp. 81–86, 1997.
- [Eck02] Eckstein, D.: *Messung der Longitudinalen Strukturfunktion $F_L(x, Q^2)$ mit dem HERA-Experiment H1*. Ph.D. thesis, Humboldt-Universität zu Berlin, 2002.
- [ER96] Engel, R.; Ranft, J.: Hadronic Photon-Photon Interactions at High Energies. In: *Phys. Rev.*, volume D54:pp. 4244–4262, 1996. [hep-ph/9509373](#).
- [F⁺74] Fox, D. J.; et al.: Test of Scale Invariance in High-Energy Muon Scattering. In: *Phys. Rev. Lett.*, volume 33:p. 1504, 1974.
- [Fer01] Ferencei, J.: Collaboration internal communication, 2001.
- [Fey69] Feynman, Richard P.: Very high-energy collisions of hadrons. In: *Phys. Rev. Lett.*, volume 23:pp. 1415–1417, 1969.
- [FGML73] Fritzsche, H.; Gell-Mann, Murray; Leutwyler, H.: Advantages of the Color Octet Gluon Picture. In: *Phys. Lett.*, volume B47:pp. 365–368, 1973.
- [GL72a] Gribov, V. N.; Lipatov, L. N.: Deep inelastic e p scattering in perturbation theory. In: *Sov. J. Nucl. Phys.*, volume 15:p. 438, 1972.
- [GL72b] Gribov, V. N.; Lipatov, L. N.: e^+e^- pair annihilation and deep inelastic e p scattering in perturbation theory. In: *Sov. J. Nucl. Phys.*, volume 15:p. 675, 1972.
- [GL96] Gogitidze, N.; Levonian, S.: An Offline Luminosity Determination for the 1995 e^+p Data. H1 Internal Note H1-02/96-471, 1996.
- [Gla98] Glazov, A. A.: *Measurement of the Proton Structure Function F_2 and F_L with the H1 Detector at HERA*. Ph.D. thesis, Humboldt-Universität zu Berlin, 1998.
- [Gla06] Glazov, A. A.: Veto inefficiency estimation using SAVEË. Presentation at the H1 Trigger meeting, Dec 2006.
- [Gla07] Glazov, A. A.: private communication, 2007.
- [GM64] Gell-Mann, Murray: A Schematic Model of Baryons and Mesons. In: *Phys. Lett.*, volume 8:pp. 214–215, 1964.
- [GP88] Gustafson, Gosta; Pettersson, Ulf: Dipole Formulation of QCD Cascades. In: *Nucl. Phys.*, volume B306:p. 746, 1988.
- [GRP90] Grindhammer, Guenter; Rudowicz, M.; Peters, S.: The Fast Simulation of Electromagnetic and Hadronic Showers. In: *Nucl. Instrum. Meth.*, volume A290:p. 469, 1990.

-
- [GW73] Gross, D. J.; Wilczek, Frank: Asymptotically Free Gauge Theories. 1. In: *Phys. Rev.*, volume D8:pp. 3633–3652, 1973.
- [GW98] Glazov, A. A.; Wallny, R.: Presentation at the ‘H1 Thursday Meeting’, 22.01.98, 1998.
- [H⁺98] Haynes, W. J.; et al.: The H1 silicon tracker data acquisition system. In: *Nucl. Instr. and Meth. A*, volume 403:pp. 313–325, 1998.
- [H1p07a] H1prelim-07-042 (H1): Inclusive ep Scattering Cross Section at low Q^2 and high y , 2007. Presented at DIS 2007, Munich, Germany, available at <http://www-h1.desy.de/h1/www/publications>.
- [H1p07b] H1prelim-07-045 (H1): Measurement of the Inclusive ep Scattering Cross Section at low Q^2 and x at HERA, 2007. Presented at DIS 2007, Munich, Germany, available at <http://www-h1.desy.de/h1/www/publications>.
- [H1p07c] H1prelim-07-144 (H1): Inclusive ep Scattering Cross Section at high Q^2 and high y , 2007. Presented at EPS 2007, Manchester, United Kingdom, available at <http://www-h1.desy.de/h1/www/publications>.
- [Hab06] Habib, S.: Veto conditions in S67. Presentation at the nELAN meeting, June 2006.
- [Han63] Hand, L. N.: Experimental investigation of pion electroproduction. In: *Phys. Rev.*, volume 129:pp. 1834–1846, 1963.
- [Hoe92] Hoeger, K. C.: The Double Angle Method. In: Buchmüller, W.; Ingelman, G., editors, *Proceedings of the Workshop Physics at HERA, vol. 1*, p. 43. 1992.
- [J⁺95] Janoth, J.; et al.: An Algorithm to Calibrate the New H1 Backward Calorimeter ‘SPACAL’ Using the Kinematic Peak. H1 Internal Note H1-11/95-464, 1995.
- [JB79] Jacquet, F.; Blondel, A.: Report from the study group on detectors for charged current events. In: Amaldi, U.; et al., editors, *Proceedings, Study Of An ep Facility For Europe*, pp. 377–414. 1979.
- [Kat97] Katzy, J. M.: *Messung der Strukturfunktion F_2 bei kleinen Bjorken- x und kleinen Impulsüberträgen am H1 Experiment bei HERA*. Ph.D. thesis, Universität Heidelberg, 1997.
- [KLF76] Kuraev, E. A.; Lipatov, L. N.; Fadin, V. S.: Multi-Reggeon Processes in the Yang-Mills Theory. In: *Sov. Phys. JETP*, volume 44:p. 443, 1976.
- [KLF77] Kuraev, E. A.; Lipatov, L. N.; Fadin, V. S.: The Pomeranchuk Singularity in Nonabelian Gauge Theories. In: *Sov. Phys. JETP*, volume 45:p. 199, 1977.
- [KSM92] Kwiatkowski, A.; Spiesberger, H.; Mohring, H.-J.: HERACLES: an event generator for ep interactions at HERA energies including radiative processes. In: *Comp. Phys. Comm.*, volume 69:p. 155, 1992.
- [Laš04] Laštovička, T.: *Measurement of the Inclusive Deep Inelastic Scattering Cross Section at Low Q^2* . Ph.D. thesis, Humboldt-Universität zu Berlin, 2004.
-

- [Leh98] Lehner, F.: *Bestimmung und QCD-Analyse der Protonstrukturfunktion $F_2(x, Q^2)$ bei kleinen Bjorken- x und Q^2 mit Hilfe des verbesserten Rückwärtsbereichs des H1-Detektors*. Ph.D. thesis, Universität Hamburg, 1998.
- [Len01] Lenderman, V.: *Measurement of the QED Compton Scattering Cross Section with the H1 Detector at HERA*. Ph.D. thesis, Universität Dortmund, 2001.
- [Lev06] Levonian, S.: Status of the offline lumi corrections for ELAN samples. Presentation at the nELAN meeting, October 2006.
- [Lev07] Levonian, S.: The status of H1 luminosity precision. Presentation at the H1 Physics Plenary, February 2007.
- [LMGL05] Laštovička-Medin, G.; Glazov, A. A.; Laštovička, T.: Precision Limits for HERA DIS Cross Section Measurement. In: *HERA and the LHC - A workshop on the implications of HERA for LHC physics: Proceedings Part A*, pp. 79–83. 2005. [hep-ph/0601012](#).
- [Lön92] Lönnblad, Leif: ARIADNE Version 4: A Program for Simulation of QCD Cascades Implementing the Color Dipole Model. In: *Comput. Phys. Commun.*, volume 71:pp. 15–31, 1992.
- [LP95] Levonian, S.; Panitch, A.: Treatment of the Proton Satellite Bunches in 1994 Data. H1 Internal Note H1-09/95-454, 1995.
- [MER⁺00] Mücke, A.; Engel, Ralph; Rachen, J. P.; Protheroe, R. J.; Stanev, Todor: Monte Carlo Simulations of Photohadronic Processes in Astrophysics. In: *Comput. Phys. Commun.*, volume 124:pp. 290–314, 2000. [astro-ph/9903478](#).
- [Mer05] Merkel, J.: Systematische Studien zur Ausrichtung der rückwärtigen Detektoren von H1 für die Messung der Protonstrukturfunktion F_2 . Diploma Thesis, Universität Dortmund, 2005.
- [Mey96] Meyer, A.: Adjustment of the High Voltage for the H1 Spacal. H1 Internal Note H1-08/96-486, 1996.
- [MRST02] Martin, Alan D.; Roberts, R. G.; Stirling, W. J.; Thorne, R. S.: MRST2001: Partons and $\alpha(s)$ from precise deep inelastic scattering and Tevatron jet data. In: *Eur. Phys. J.*, volume C23:pp. 73–87, 2002. [hep-ph/0110215](#).
- [MVV04] Moch, S.; Vermaseren, J. A. M.; Vogt, A.: The three-loop splitting functions in QCD: The non-singlet case. In: *Nucl. Phys.*, volume B688:pp. 101–134, 2004. [hep-ph/0403192](#).
- [N⁺96] Nicholls, T.; et al. (H1 SpaCal Group): Performance of an electromagnetic lead/scintillating-fibre calorimeter for H1 detector. In: *Nucl. Instr. and Meth. A*, volume 374:p. 149, 1996.
- [New04] Newman, P.: Deep inelastic lepton nucleon scattering at HERA. In: *Int. J. Mod. Phys.*, volume A19:pp. 1061–1073, 2004. [hep-ex/0312018](#).
- [P⁺00] Pitzl, D.; et al.: The H1 silicon vertex detector. In: *Nucl. Instrum. Meth.*, volume A454:pp. 334–349, 2000. [hep-ex/0002044](#).

-
- [P⁺02] Pumplin, J.; et al.: New generation of parton distributions with uncertainties from global QCD analysis. In: *JHEP*, volume 07:p. 012, 2002. [hep-ph/0201195](#).
- [PB00] Plathow-Besch, H.: PDFLIB: Proton, Pion and Photon Parton Density Functions, Parton Density Functions of the Nucleus, and α_s Calculations. User's Manual - Version 8.04, W5051 PDFLIB, CERN-ETT-TT 200 0.04.17, 2000.
- [Pet07] Petrukhin, A.: private communication, 2007.
- [Pös96] Pöschl, R.: Untersuchung der Ortsauflösung des H1-Spaghetti-Kalorimeters unter besonderer Berücksichtigung großer Einschlußwinkel der Primärteilchen. Diploma Thesis, Universität Dortmund, 1996.
- [Rai04] Raičević, N.: Bulk 1999/2000 Status - PHOJET Problem. Presentation at the nELAN meeting, January 2004.
- [S⁺] Spiesberger, H.; et al.: Radiative corrections at HERA. Contribution to the Workshop on Physics at HERA, Hamburg, Germany, Oct 29-30, 1991.
- [S⁺00] Shekelyan, V.; et al.: T0 Talk for 'Deep inelastic ep Scattering at Low Q^2 at HERA'. Presentation at the H1 Plenary, 14.7.2000.
- [Sch96a] Schleif, S.: SpaCal Reconstruction. H1 Software Note 56-03/96, 1996.
- [Sch96b] Schwab, B.: *Das Rückwärtsdriftkammersystem des H1-Experiments*. Ph.D. thesis, Universität Heidelberg, 1996.
- [Sie99] Sievers, P.: Untersuchungen zur Verbesserung der Energiemessung im Rückwärtsbereich des H1-Experimentes. Diploma Thesis, Universität Heidelberg, 1999.
- [Sir80] Sirlin, A.: Radiative corrections in the $su(2)_L \times u(1)$ theory: A simple renormalization framework. In: *Phys. Rev.*, volume D22:pp. 971–981, 1980.
- [Sjö94] Sjöstrand, Torbjörn: High-Energy Physics Event Generation with PYTHIA 5.7 and JETSET 7.4. In: *Comput. Phys. Commun.*, volume 82:pp. 74–90, 1994.
- [Spi92] Spiesberger, H.: Monte Carlo treatment of radiative corrections at HERA. In: *Nucl. Phys. Proc. Suppl.*, volume 29A:pp. 221–228, 1992.
- [SS91] Schuler, G. A.; Spiesberger, H.: DJANGO: The Interface for the event generators HERACLES and LEPTO. In: Buchmüller, W.; Ingelman, G., editors, *Physics at HERA, vol. 3*, pp. 1419–1432. 1991.
- [SS07] S. Shushkevich, V. Shekelyan: Radiative Corrections in Django NC. Presentation at the ELAN Meeting, 18.09.2007.
- [SZ96] Shekelyan, V.; Zhokin, A.: Presentation at the meeting 'Towards F_2 ', 7.5.1996.
- [Urb05] Urban, K.: Triggerstudien für eine Messung der Protonstrukturfunktion F_2 bei H1. Diploma Thesis, Universität Dortmund, 2005.
-

- [Var06] Vargas, A.: *Determination of the Energy Scale Uncertainty for the Measurement of F_2 at Low Values of Q^2 with the H1 Detector*. Ph.D. thesis, Universität Dortmund, 2006.
- [VMV04] Vogt, A.; Moch, S.; Vermaseren, J. A. M.: The three-loop splitting functions in QCD: The singlet case. In: *Nucl. Phys.*, volume B691:pp. 129–181, 2004. [hep-ph/0404111](http://arxiv.org/abs/hep-ph/0404111).
- [VVM05] Vermaseren, J. A. M.; Vogt, A.; Moch, S.: The third-order QCD corrections to deep-inelastic scattering by photon exchange. In: *Nucl. Phys.*, volume B724:pp. 3–182, 2005. [hep-ph/0504242](http://arxiv.org/abs/hep-ph/0504242).
- [Wei73] Weinberg, Steven: Nonabelian Gauge Theories of the Strong Interactions. In: *Phys. Rev. Lett.*, volume 31:pp. 494–497, 1973.
- [WH01] Willeke, F.; Hoffstaetter, G.: Talks at the Workshop on the Future of DIS, Durham, 2001. <http://hep.ph.liv.ac.uk/~green/HERA3/>.
- [WRB⁺90] Whitlow, L. W.; Rock, Stephen; Bodek, A.; Riordan, E. M.; Dasu, S.: A Precise extraction of $R = \sigma_L/\sigma_T$ from a global analysis of the SLAC deep inelastic e-p and e-d scattering cross-sections. In: *Phys. Lett.*, volume B250:pp. 193–198, 1990.
- [YYG90] Yuille, A. L.; Yang, T.; Geiger, D.: Robust Statistics, Transparency and Correspondence. Harvard Robotics Laboratory Technical Report 90-7, 1990.

Acknowledgements

I would like to thank Peter Kostka for all his support throughout my time in H1 and Zeuthen. Many thanks go also to Prof. Hermann Kolanoski who took the responsibility for this thesis and had always time, when I had questions. I want to express my gratitude to Prof. Max Klein, who had a steady interest in my work and supported me in many ways in the last years. Prof. Thomas Lohse was patient enough to carefully read through the many pages of my work and I wish to thank him for that.

From a professional point of view this work would not have been possible without the help, ideas, and contributions from Sasha Glazov and I wish to thank him for his support. I also want to thank Alexey Petrukhin for his large contribution to these results. I am also indebted to many PhD and former Diploma students from the Dortmund group, Andrea Vargas, Olaf Behrendt, Jesko Merkel, and Klaus Urban for their direct and indirect help. Thanks to all these people there was always a good working atmosphere in our group and I enjoyed the work¹. I also want to thank Vladimir Shekelian, who has helped the progress of the work in the later stages as a referee and expert for the published H1 data.

Next I want to thank the crew from the FST and BST repair(s), which are Mirek Nožička, Peter Kostka, Ivan Glushkov, Anja Sandmann, Jürgen Pieper, Igor Ivanovič, Ilya Tsurin, Achim Meißner, Uli Harder, Hans Henschel, and Wolfgang Lange. Despite the hard work it was at times, it was a good experience and in the end we succeeded.

In addition to the people mentioned above, many thanks go to the other people of the H1 Zeuthen group that helped to make my time in Zeuthen and Hamburg a good one: Carmen Diez, Peter Steinbach, Thomas Naumann, Sergey Gorbounov, and Sebastian Piec. I would like to thank many of the students of the Amanda/IceCube group in Zeuthen, especially Markus Ackermann, Sebastian Böser, Stefan Klepser, and Bernhard Voigt, for their company in the S-Bahn, at lunch, in Berlins bars, or at their parties. In general I also enjoyed my time in the H1 Collaboration and I have to thank many of its members for that.

I want to thank my parents, grand parents, and friends for the good time I had in the last years. I spent a large part of my time working and unfortunately didn't have as much left to spend with them as I would have liked.

Finally many thanks to my sunshine Tina for her support of my work, her love and belief in me.

¹most of the time at least

Selbständigkeitserklärung

Hiermit erkläre ich, die vorliegende Arbeit selbständig ohne fremde Hilfe verfasst und nur die angegebene Literatur und Hilfsmittel verwendet zu haben.

Jan Kretzschmar
Berlin, den 31.10.2007